UNIVERSITY OF SOUTHAMPTON

FACULTY OF PHYSICAL SCIENCES & ENGINEERING

Electronics and Computer Science

Nanodielectrics for Machine Insulation

by

Van Truc Nguyen

Thesis for the degree of Doctor of Philosophy

May 2013

UNIVERSITY OF SOUTHAMPTON

ABSTRACT

FACUTY OF PHYSICAL SCIENCES & ENGINEERING

Electronics and Computer Science

Doctor of Philosophy

NANODIELECTRICS FOR MACHINE INSULATION

by Van Truc Nguyen

Thanks to the development of nanotechnology, epoxy nanocomposites have been expected to be potential candidates to replace the base resin, due to their superior properties. However, the effects of nano-fillers have been controversial, in both positive and negative ways. There are two main factors, comprising of stoichiometry and the nature of interfacial areas of nano-sized fillers, which are expected to contribute to the final properties of epoxy nanocomposites. The chosen stoichiometry is important in determining the nature of the polymer network that forms. A stoichiometric formulation with the optimal chemical balance between reactants will introduce good performance. However, incorporation of nano-fillers with large interfacial areas into epoxy matrices may modify the cure behaviour of the system, through introducing additional chemical reactions between moieties on the nano-filler surfaces and reactants, thereby altering the rate and sequence of the possible chemical reactions that occur during curing. These effects change the chemical balance of the original base resin system. As a result, the nature of the cross-linked network that forms may be altered.

An investigation into the effects of stoichiometry and the nature of the interfacial surface of treated nanosilica particles of various sizes on properties of epoxy-based systems has been conducted, using the differential scanning calorimetry, space charge and ac breakdown measurements, and the dielectric spectroscopy. The introduction of nanosilica has induced changes in curing mechanisms and led to different impacts on systems of different resin stoichiometry. In addition, the investigation has revealed a key role of the characteristic interaction between the nanoparticle surface and the resin matrix in determining material properties, rather than the filler size. Weak interactions have produced negative impacts on material properties. The addition of nano-silica particles into conventional microcomposites has suggested the possible synergetic effects due to the presence of both nano and micro fillers.

Furthermore, the long-term performance of the unfilled epoxy and its nanocomposites has been explored. Open branch trees with the faster propagation rate have been observed in nanocomposites, compared to the unfilled epoxy. The material degradation during partial discharge activities has also been evinced using the confocal Raman microprobe spectroscopy.

Table of Contents

List of figures

List of tables

DECLARATION OF AUTHORSHIP

I, Van Truc Nguyen, declare that the thesis entitled

'Nanodielectrics for Machine Insulation'

and the work presented in the thesis are both my own, and have been generated by me as the result of my own original research. I confirm that:

- this work was done wholly or mainly while in candidature for a research degree at this University;
- where any part of this thesis has previously been submitted for a degree or any other qualification at this University or any other institution, this has been clearly stated;
- where I have consulted the published work of others, this is always clearly attributed;
- where I have quoted from the work of others, the source is always given. With the exception of such quotations, this thesis is entirely my own work;
- I have acknowledged all main sources of help;
- where the thesis is based on work done by myself jointly with others, I have made clear exactly what was done by others and what I have contributed myself;
- parts of this work have been published as:

- Van Nguyen, A S Vaughan, P L Lewin, A Krivda, *Effects of nanoparticle and stoichiometry on properties of an epoxy system*. Dielectrics, 2011.

- V Nguyen, A S Vaughan, P L Lewin, A Krivda, *Stoichiometry and Effects of Nano-sized and Micro-sized Fillers on an Epoxy based system.* IEEE Conference on Electrical Insulation and Dielectric Phenomena, 2011.

- V Nguyen, A S Vaughan, P L Lewin, A Krivda, *On the stoichiometry with space charge and breakdown behaviour of an epoxy based system with nano-sized and micro-sized fillers.* IEEE Conference on Electrical Insulation and Dielectric Phenomena, 2012.

Signed: ……..

Date:…….

Acknowledgements

Firstly, I would like to thank my supervisors, Professor Alun Vaughan and Professor Paul Lewin for their patience, guidance, continued support and critical discussion throughout my PhD. Without their help, finishing this thesis would not have been possible.

I would also like to acknowledge ABB Switzerland Ltd., Corporate Research Center, for financial support to the majority of this thesis. In particular, I am also grateful to Dr Andrej Krivda at ABB Research Center, Switzerland, for his valuable advices and discussions.

I would like to further my gratitude to the members of the Tony Davies High Voltage Laboratory who provided advices and interesting discussions during my research, in particular, to Mike and Brian for their technical support. Special thanks also go to Dr Gabriele Gherbaz, Dr Ian Hossier, Dr Martin Reading, Dr Nicola Freebody, Ms Celia Yeung; their help was greatly appreciated.

Finally to my family including my mother, father, brother, and especially to my husband, Dr Long N Dao, I will be forever in your debt. Thank you so much for being there with me throughout the good and hard times which are inevitable during my study. Without your love, support and encouragement, I could not finish this thesis.

To you all I will be forever grateful!

Definitions and Abbreviations

AC - Alternating current

AEW - The anhydride equivalent weight

CNT - Carbon nanotubes

CRMS – Confocal Raman microprobe spectroscopy

DC - Direct current

DETA - Diethylenetriamine

DGEBA - Diglycidylether of bisphenol A

DSC - Differential scanning calorimetry

EEC - 3,4-epoxycyclohexyl-3’4’-epoxycyclohexane carboxylate

EEW - Epoxide equivalent weight

EM - Electromagnetic

FT - Fourier transform

FTIR - Fourier transform infrared

HN - Havriliak and Negami

HV - High voltage

IR - Infrared

LDPE - Low density polyethylene

LFD – Low frequency dispersion

LIPP - Laser-induced pressure pulse

LV - Low voltage

MDSC - Modulated differential scanning calorimetry

MMT - Montmorillonite

MWS - Maxwell-Wagner-Sillars

NMA - Nadic methyl anhydride

PE - Polyethylene

PEA - Pulsed electroacoustic

PMA - Poly(methyl acrylate)

PMNA - Poly(methyl methacrylate)

PPG - Poly(propylene glycol)

PVA - Poly(vinyl alcohol)

PVDF – Polyvinylidene Fluoride

PWP - Pressure wave propagation

SEM - Scanning electron microscopy

TEM - Transmission electron microscopy

TEOS - Tetraethylorthosilicate

TSM - Thermal shock method or Thermal step method

XLPE - Crosslinked polyethylene

Chapter 1 Introduction

1.1 Basic problems

Commercial epoxy resins were first introduced into the market in the 1940s, although similar products had been patented as early as the 1930s [1]. Epoxy resins are synthesized by the reaction of a base resin and a hardener, with or without a catalyst, and different reactive components. The chemistry of epoxies and the range of commercially available inclusions allow cured polymers to be produced with a broad range of properties, such as excellent adhesion, chemical and heat resistance, good mechanical properties and, of particular relevance here, very good electrical insulating properties. Therefore, the applications of epoxy-based materials are extensive, including adhesives, coatings, aerospace, electronic and electrical industries, etc [1-2].

The global demand for energy has been increasing rapidly as a result of dramatic population growth and the continuous development of the worldwide economy and of technology. High voltage electrical systems with high power have been developed, which require very good insulating materials in terms of mechanical, electrical, and thermal properties. Epoxy resins are indeed excellent candidate materials for use in a wide range of different electrical power generation and transmission applications including indoor, outdoor and enclosed apparatus, which require high thermal endurance as well as good dielectric properties; examples include solid insulated switchgear, generators, transformers, and bushings [3-7]. The epoxy formulations and the processing procedures have evolved continuously to the current state where high quality products can be produced economically. In addition to providing excellent electrical and mechanical functions, epoxy systems offer several advantages such as light weight; they are easy to cast into complicated shapes, and exhibit good impact and seismic resistance when compared to other insulating materials such as porcelain. Moreover, compared to other composite insulators such as fiber glass core and elastomer housing, epoxy systems also eliminate interfacial problems that are associated with the different materials in the composites. Employing epoxy-based devices in

electrical systems also limits problems relating to oil, leakage and maintenance. Although 2009 was the most difficult year for the epoxy industry due to the global economic crisis, the worldwide demand was estimated at roughly US$15.8 billion. It is forecast, thanks to the strong signals of recovery, that the market will reach US$21.35 billion by 2015 with the annual growth rate being 3.5-4% [8].

Epoxy resins and resulting composites have become an interesting and competitive research area for both science and industry. The inclusion of mineral fillers such as silica, alumina, etc. within epoxy matrices has been proven to reduce the material cost, improve fire resistance as well as mechanical properties such as tensile strength and, consequently, both the science and technology of epoxy-based composites filled with micro-sized and/or nano-sized particles have attracted considerable attention. For example, previous research has found that the thermal conductivity of composites increases with micro-filler content [9] and that composites containing a high percentage of micro-fillers can exhibit thermal expansion coefficients comparable to aluminium or copper [10]. Another example was the work done by Hyuga et al. [11] in which samples containing high microfiller loading levels exhibited low electrical conductivity, low dielectric constant and low dielectric loss factor at temperatures higher than the glass transition temperature. A number of studies on nanocomposites have also shown that the addition of a small amount of nano-scale fillers significantly increases the partial discharge resistance of epoxy-based systems [12-15]. In the work for Haque et al. [16] involving the investigation on the mechanical and thermal properties of glass/epoxy nanocomposites filled with nanoclays such as MMT, significant improvements in mechanical properties were found with the addition of 1 wt% organo silicate nanoparticles. In another investigation conducted by Chiang et al. [17], epoxy nanocomposites filled with silica exhibited much improved thermal stability at higher temperatures and excellent flame retardance. Many other instances exist where epoxy nanocomposites have showed improved properties compared with unfilled and conventional microfilled systems [18-22]. Such positive results have fuelled a great increase in research into the dielectric response of nanocomposites – so-called nanodielectrics. A key aspect of nanodielectrics is thought to concern the role of interfaces and the formation of interphases located between the nanofiller and the unperturbed matrix. Indeed, for an interphase region of thickness 10 nm, this component will dominate for particles less than about 100 nm in diameter [23] and, consequently,

many studies of nanocomposite interfaces and matrix filler interactions have been undertaken. X-ray photoelectron spectroscopy has, for example, revealed evidence for hydrogen bonding between the carbonyl groups of the polymer and hydroxyl groups on the filler in a poly(methyl methacrylate)/kaolinite system [24], while the electron spin resonance spectroscopy response of a poly(methyl acrylate) (PMA)/synthetic fluoromica nanocomposite was interpreted as providing evidence of a rigid interphase region 5-15 nm in thickness [25].

Nevertheless, there are also a number of investigations showing negative influences on material properties upon the incorporation of nano-fillers and the underlying mechanisms are not adequately understood [26-30]. The dispersion and the surface of nano-sized fillers are believed to be key factors in realising optimum material properties. The surface treatment of fillers has been proven to be an effective method to produce a well-dispersed nanostructured matrix. For example, Maity et al. [31] observed that the inclusion of alumina nano-fillers lowered the effective real and imaginary permittivity of the composite at low temperatures. However, at higher temperatures, the work revealed that only those composites prepared with silane-functionalised nanoparticles showed the low permittivity. For the convenience of processing, some manufacturers, such as Nanoresin, and 3M, have produced premixed epoxy resin systems in which nanometric fillers are claimed to be surface-treated and well-dispersed into the resin. Due to their convenience and commercial availability, such master-batch systems are widely used in a number of industries.

1.2 Epoxy structure and property dependence

In general, a complete epoxy system possesses a 3-D crosslinked network resulting from the reactions of an epoxy resin monomer or epoxy mixture, a curing agent or hardener, a catalyst, fillers, and other additives. An epoxy system can offer the user a wide diversity of characteristics and varying end properties by using different types of resin and hardener or adjusting their reactive concentrations. Epoxy resins are often modified with other resins to enhance certain properties, as required by a particular application. A proper formulation of the epoxy resin requires an understanding of the chemical structures of the resin and curing agent, as well as the chemical reactions

leading to polymerisation, because it determines the chemical and physical properties of the final product.

Epoxy monomers are organic compounds characterized by one or more reactive oxirane or epoxy rings. That is, a 3 member ring formed between 2 carbon atoms and 1 oxygen atom, as shown in Figure 1-1, which can react with hardeners or be catalytically homopolymerised to become a crosslinked thermosetting structure with higher molecular weight. This atomic arrangement produces better reactivity than the common ethers. Due to the different electronegativity of C and O atoms, the carbon atoms of the ring become electrophilic, and hence, the ring opening can be achieved by reactions with nucleophiles. The epoxy groups can be situated internally, terminally, or on a cyclic structure. The number of epoxy groups per molecule is referred to as the functionality of the resin [32].

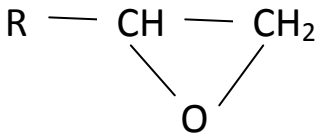

Figure 1-1 The oxirane ring

There are mainly two families of epoxies, including the glycidyl epoxies, such as diglycidylether of bisphenol A (known as DGEBA), and aliphatic epoxy resins such as 3,4-epoxycyclohexyl-3'4'-epoxycyclohexane carboxylate (ECC). Their structures are shown in Figure 1-2. A general formula for an epoxy resin can be represented by a linear polyether with terminal epoxy groups and secondary hydroxyl groups located along the molecular chain [32]. The epoxy resin structure exerts certain influences on the properties of the final product, an example is shown in Figure 1-3:

- Due to the secondary hydroxyl groups, the epoxy resin exhibits good adhesion;
- Aromatic rings along the epoxy resin backbone provide good heat and chemical resistance;
- The epoxy groups and hydroxyl groups provide high reactivity;
- No small molecules are liberated during the curing process, thus low shrinkage occurs and low internal stresses are formed during curing.

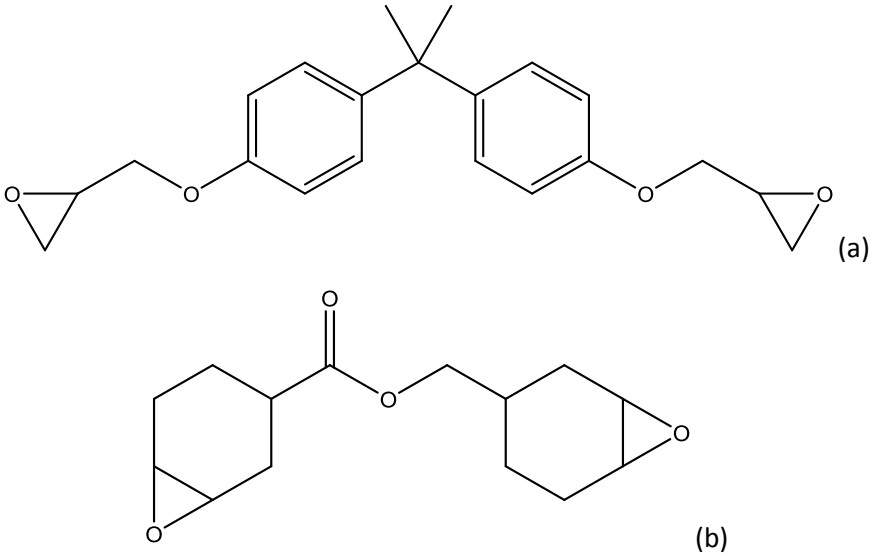

Figure 1-2 Chemical structure of (a) DGEBA and (b) ECC

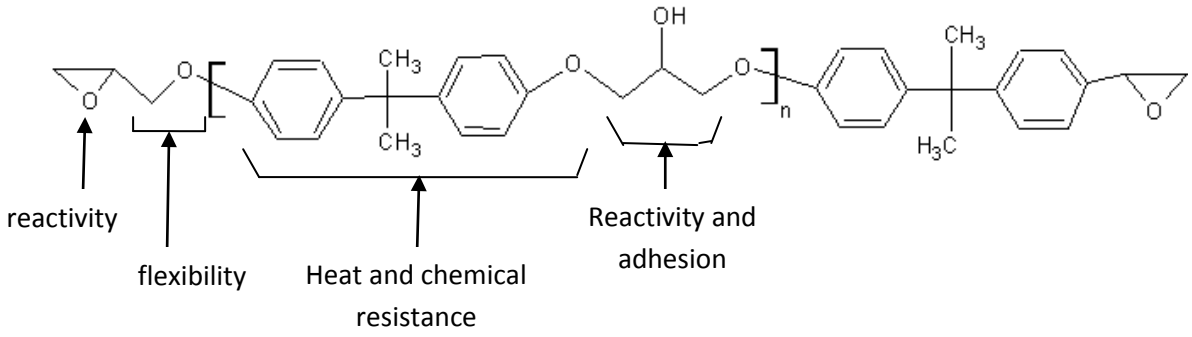

Figure 1-3 Dependence of property on structure of a DGEBA-type resin

The value of n in Figure 1-3 above determines the number of hydroxyl groups in the molecular structure and the molecular weight. Commercial epoxy resins are mixtures of molecules of different molecular weights and chemistry. They can be low-viscosity liquids or hard solids, depending on the molecular weight. In addition, commercial epoxy resins can possess a certain amount and degree of branching with terminal groups being either epoxy or hydroxyl. The differences in the chemical structure can be considered as the consequences of the manufacturing process. The ratio of reactants involved in the synthesis of epoxy resins determines not only the extent of reactions, and the molecular weight, but also the chemical structure of the monomers that are formed.

The process by which an epoxy resin is converted to a hard, rigid thermoset is usually carried out by using an appropriate crosslinking agent to connect the epoxy monomers together by a ring-opening mechanism to form a 3-D crosslinked structure. This process is referred to as curing. There are two primary types of epoxy curing reactions, including polyaddition and homopolymerisation. Both reactions are exothermic and the rate of reaction increases with temperature. The polyaddition is based on the reaction of epoxy molecules with other kinds of reactive monomers, which are termed curing agents or hardeners [33]. This is the most commonly used reaction for curing an epoxy resin. The hardeners participate in the crosslinking reaction at certain ratios, to ensure the chemical balance of reactive sites between the hardener and the resin, depending on their functionalities. This is called the stoichiometric ratio. The functionality of epoxy resins can be determined by the epoxide equivalent weight (EEW) [33]. The epoxy equivalent weight (EEW) is an important concept used in formulating the epoxy compositions and is defined as the weight of resin in grams that contains the equivalent of one mole of oxirane rings. The EEW is then used to determine the curing agent concentration for a theoretically optimal formulation. In general, the higher the molecular weight and EEW of the epoxy resin, the less curing agent is required. Homopolymerisation is the reaction of only epoxy resin molecules via the hydroxyl groups in the reacting systems to create ether linkages. It is also called the etherification reaction and usually requires an elevated temperature cure [32]. Catalytic curing agents do not participate in polymerisation reactions, but act as initiators and promoters of curing reactions. Therefore, the properties of cured products depend on the nature of the epoxy resin and hardener only. However, the pot-life, curing temperature and time, and processability are mainly determined by the catalysts. The most popular catalysts include tertiary amines, imidazoles, etc. Sometimes, a small amount of the catalyst is added as an accelerator to cure the epoxy more effectively. The required concentration of catalyst is usually determined experimentally, because the catalyst does not react stoichiometrically. Excess leads to poor properties of the end material.

The reactions that occur between the resin with the curing agent and/or catalyst are complex. A number of side reactions can occur at different rates and sequences, depending on the materials used and the imposed curing conditions. For example, an epoxy system cured at two successive temperatures will provide a final network structure that is significantly different in chemistry, and hence, properties, from an

isothermally cured system. Therefore, the practical mixing ratio of the resin to the curing agent is not usually the stoichiometric one. The stoichiometry is nevertheless important in defining a safe resin/hardener ratio for the formulators to generate initial mixtures. Then, necessary adjustments can be carried out on the basis of the ultimate performance that is required for the material end requirements. In addition, when the filler is introduced to the resin composition, the surfaces will contain moieties, such as hydroxyl groups, which can take part in resin curing. In the case of nanocomposites, the surface area is extremely large; the introduction of nanoparticles can therefore change the chemical balance in the system, such that the ratio of resin to hardener to accelerator must be adjusted to compensate.

Obviously, the properties of a material depend on its composition and structure. This strong dependence highlights the importance of the presence of fillers within composites. It is well known that the properties of composites can change depending on the dispersion of fillers, their geometric shape, surface chemistry, particle size and particle size distribution. A poorly dispersed composite will exhibit a larger variation in properties [34-35]. An example is the work conducted by Lianhua et al. [36], which showed that severe filler settling can cause cracks and reduce the reliability of the system. Conversely, good dispersion can improve properties further [37]. In the investigation done by Ramanathan et al. [38], the well dispersed graphite/PMMA composites showed better mechanical, thermal and electrical properties. Vaughan et al. [39] found an enhanced nucleation for the well-dispersed MMT-polyethylene composites.

When nanosilica is dispersed into an epoxy matrix, at short ranges, particle surfaces are surrounded by epoxy monomers and hardener molecules. Compared to the bulk epoxy phase, this interphase region is not of continuous structure. If the interaction between particle surface and liquid molecules in this short-range region is much stronger than the one between particles, good stability of dispersion can be obtained. For filled epoxy resins, the compatibility of resin/curing agent and fillers is an important factor. The polarity and hydrophilic nature of the hardener will influence the filler dispersion within the material. For epoxy nanocomposites, if the particles are well wetted by the polymer, the force between the particles and polymer can be stronger than that between the particles, so leading to stable dispersions. In the epoxy/filler system, there is a region in

the vicinity of the interface that is referred to as the interphase region; this exists between the filler particles and the polymer matrix [40]. For good bulk properties, strong interfacial interactions between the filler and the polymer matrix are required, such that stresses can be uniformly transferred throughout the composite structure. Electrically, it has been reported that the degree of nano filler dispersion and the use of coupling agents have a great influence on the long-term treeing breakdown and partial discharge resistance of epoxy composites [41]. Conversely, unsatisfactory nano-scale filler dispersion may reduce the treeing breakdown lifetime, whereas coupling agents will lead to increased interfacial interactions, so improving performance. Some surface treatment methods have proved effective in enhancing the dielectric properties of nanocomposites [42-43]. Also, the size of nano-scale fillers has been found to be related to the breakdown time, since there is a tendency for the formation of interfacial gaps between the filler and epoxy, i.e. voids or cavities, if the filler size is large enough. The gaps became widened with increasing filler size [44].

1.3 Aims of the Thesis

In addition to the traditional factors that can affect the properties of an epoxy system, including the type of epoxy resin, the hardener, the resin/hardener ratio, and the curing cycle, the introduction of fillers increases the complexity in the matrix chemistry. Besides the formation of interphase regions and the large interfacial areas associated with nanoscopic fillers, in the case of matrices such as epoxies that are formed by some chemical reactions, the nature of the surface of nano-sized fillers may also serve to alter the chemical balance of the base resin system by introducing additional reactions between surface moieties and the reactive components and/or changing the existing reaction conditions, particularly where a number of different chemical pathways may exist. Since the chosen stoichiometry plays an important role in determining the structure of the cross-linked network that forms within the polymer matrix, additional reactions involving nanoparticle surface chemistry will affect the macroscopic properties of the final products. It has been concluded that only stoichiometric formulations with an optimum chemical balance of reactants provide optimal performances. For example, in the study of CNT-based epoxy systems by Miyagawa et al. [45], the carbon nanotubes had such a marked influence on the effective stoichiometry of the resin that the glass transition temperature was found to fall by 30

^{o}C on their introduction. To compensate for this, it was necessary to reduce the anhydride content from 91 parts per hundred (phr) to 66 phr – a major change.

While many studies have considered the effect of the large interfacial areas associated with nanoscopic fillers on material properties [46-50], few have examined system stoichiometry upon introducing nanoscopic fillers [51]. The focus of this research is therefore not only to investigate the effects of introducing silica particles into an epoxy-based system in terms of various loading percentages and sizes ranging from nanoscopic to microscopic scales, but also to combine this with a study of resin stoichiometry. The resin used in this study was based on a diglycidyl ether of bisphenol-A (DGEBA), which was cured using an anhydride-based hardener coupled with a tertiary amine accelerator. Epoxy resins cured by anhydrides are usually less poisonous and exhibit better properties than those cured with amines, including higher glass transition temperatures, higher moisture resistance, and reduced heat generation during curing and low reaction shrinkage [52-53]. In addition, without catalysers such as tertiary amines or other strong Lewis bases, epoxy-anhydride systems possess a very low reactivity and, hence, longer pot life for processing at room temperature. Therefore, this system is one of the most commonly used in industry, especially for rotating machines, due to its excellent thermal and mechanical properties. In addition, as mentioned above, one of the most important factors that affect the properties of a composite is the dispersion of the fillers that are present. Therefore, this study has concentrated on fillers commonly used in industry, including two commercial epoxy master-batch systems, both of which are claimed to contain well-dispersed nanoscopic silica particles, together with microscopic silanated, ultra-fine silica flour.

The goals set for this research were to:

- Establish the conditions to produce a good dispersion of nanosilica fillers in samples;
- Establish the resin stoichiometry to obtain the optimum performance for the unfilled epoxies and nanocomposites;
- Evaluate the effects of the characteristic interactions between the nanoparticle surfaces with the resin matrix on system performance;

- Explore the effects of adding nanosilica fillers into conventional microcomposites;
- Investigate a practical application about electrical insulation of epoxy-based systems where the long-term degradation can occur and perform chemical analysis of electrical trees in the unfilled epoxy resin and its nanocomposite.

1.4 Thesis Contents

Chapter 1 provides a basic introduction to epoxy nanocomposites, their structure and property dependence.

Chapter 2 provides the background relating to the thermal, dielectric and insulation properties of materials, as well as the theory behind all the experimental techniques used.

Chapter 3 provides details on the material used and experimental procedures, followed by the preliminary experimental data and experimental conditions chosen.

Chapters 4-5 contain the experimental results on chemical analysis, examination of the dispersion of nanofillers, as well as the thermal, dielectric, and electrical performances of different unfilled epoxy and epoxy nanocomposite systems, comparison to previous work by other authors, along with theories for the behaviour observed and general analysis.

Chapter 6 contains the experimental results on chemical analysis, examination of filler dispersion and the thermal, dielectric and electrical performances of epoxy-based systems with a large amount of micro-silica, along with general analysis.

Chapter 7 contains an optical and chemical analysis of electrical trees grown in some typical transparent epoxy-based systems, including the unfilled epoxy and its nanocomposites, and comparison to the previous work by other authors.

Chapter 8 generalises the common factors that affect the system performance.

Chapter 9 summarises all the findings from this research and draws conclusions and suggestions for further study.

Chapter 2 Theory

This chapter sets out is to outline the basic theories on the material properties, and the experimental techniques involved in this work.

2.1 Chemical structure and thermal properties

Depending on the crosslinking degree during the reactions, the presence of polyfunctional groups in a reactive system results in the formation of structures of macroscopic dimensions, and therefore produces a 3-D network during curing. The full characterisation of the curing process involves a number of factors. The chemical reactions that occur during the polymerisation process are associated with phenomenological changes, such as macroscopic gelation and vitrification.

2.1.1 Chemical structure and croslinking

Epoxy resins are network-structured thermosets that evolve through crosslinking reactions. Curing thermosetting polymers generally involves the transformation of low molecular weight liquids to amorphous networks of macroscopic molecules. The state of the material depends on the chemical conversion and temperature. The curing process is associated with exothermic chemical reactions and resulting chemo-rheological changes. The uncured epoxy resins are mixtures of small reactive molecules and curing is usually thermally activated. Through the application of heat, the mixture viscosity drops initially and the monomers readily react to each other to form oligomers. As the chemical reactions proceed, the average length of molecular chains and the degree of branching and crosslinking accelerate. This means that there is an increase in the molecular weight and, thus, viscosity. The formed microgel particles are dispersed in the low molecular weight phase, which is considered the continuous phase. This process continues and chains become linked together until the microgels constitute the continuous phase and the original phase of low molecular weight particles is entrapped in the matrix of the new phase. At this point, a continuous 3-D network is formed. This stage is termed gelation [54-55]. It is an irreversible transformation from a highly viscous liquid to an elastic gel or rubber. Based on the macroscopic development of

network formation, the gel point is defined as the point at which the viscosity approaches infinity and a mechanical modulus is produced as shown in Figure 2-1 [56].

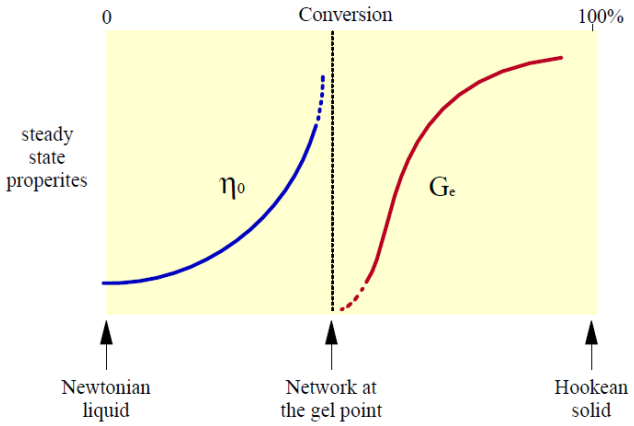

Figure 2-1 Macroscopic development of network formation [reprinted from 56]

Gelation is an important characteristic of an epoxy in term of processability. It is the incipient formation of a crosslinked network. Before gelation, the system is relatively mobile while, above the gel point, the material loses its ability to flow due to a significant increase in viscosity, its microstructure is fixed and self diffusion is drastically limited. For instance, the investigation by O'Brien et al. [57] indicated that small changes in cure state caused dramatic effects on relaxation, especially near gelation. As the material approached gelation, the relaxation slowed significantly. Due to its importance, determining the gel point of an epoxy resin has been standardised. An example is the work conducted by Halley et al. [58] to find the gel point by various rheological methods. Beyond the gel point, the reaction continues to form a 3-D fully cured network with a high crosslinking density and high glass transition temperature (T_g). The glass transition temperature, T_g, describes a transition during which an amorphous thermoset is converted from the glassy state to rubber-like form with the characteristics of a rubber/highly vicous liquid. Figure 2-2 illustrates the curing process of a thermoset from the uncured state to the fully cured one.

In principle, during the cure to full conversion, the glass transition temperature T_g of the reacting system increases from the a value T_{g0} of the uncured monomer mixture to the fully cured value $T_{g\infty}$. Vitrification is the transition from a liquid/rubbery state into a glassy one when T_g increases from below the curing temperature (T_{cure}) to T_{cure}, i.e. $T_g = T_{cure}$ [60-62]. At this point, the mobility of the reactive groups is hindered and

severely limited due to the reduction in free volume and, therefore, the rate of reaction drops drastically. Chemical kinetics in the region near vitrification become diffusion and/or mobility controlled [61, 63]. The final conversion is usually lower than unity, due to diffusion limitations. Even in the absence of any diffusion hindrance, topological limitations can lower the ultimate conversion, due to the fact that the remaining reactive groups cannot meet and react with each other [64]. Vitrification is reversible by heating to devitrify the partially cured resin. Then, chemical control of cure can be re-established. Therefore, it is usually necessary to increase the temperature after vitrification to complete curing, i.e. a post-cure at an elevated temperature is usually required.

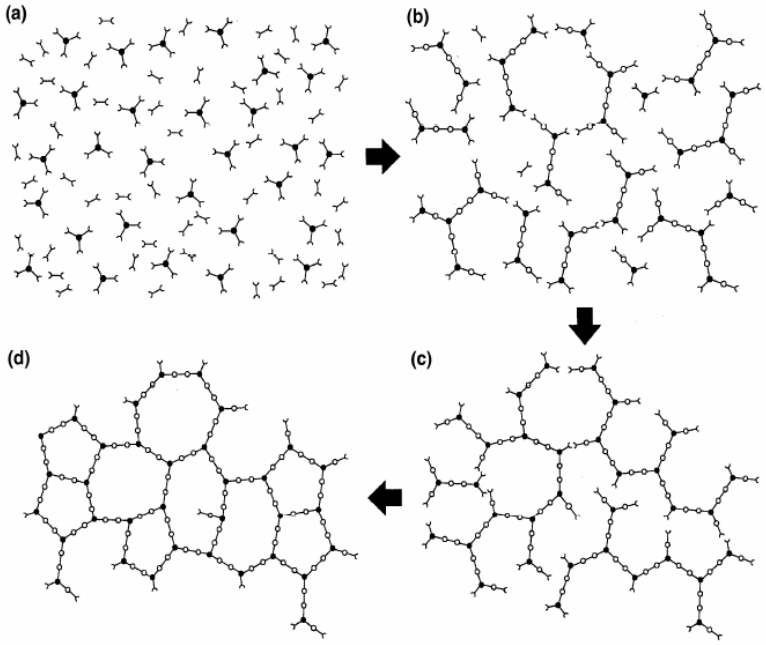

Figure 2-2 The curing process of a thermoset [reprinted from 59]

Many changes in the physical state, and hence properties of a reacting system, take place during the curing process. As a result, the cure kinetics of a thermosetting material can be determined by various techniques. The viscoelastic properties of an epoxy resin during cure have attracted a lot of interests. For example, Shimazaki et al. [65] followed the change in viscoelastic properties of an epoxy resin-acid anhydride system with a dynamic viscoelastometer. This study revealed that the viscosity increased with curing time through two inflection points. The first point was defined as the termination of the initial stage of the curing reaction. The second point coincided with the gel point, which

was determined by the torsion method. In another study by Kortaberria et al. [66], gelation and vitrification times obtained by rheological measurements of viscoelastic behaviour showed a good agreement with those obtained from dielectric spectroscopy. The free volume, which is considered as the unoccupied space between molecules resulting from their thermal motions and steric hindrance effects, is also used to determine gelation and vitrification. Khoun et al. [67] successfully measured the shrinkage to describe the volumetric effects of an epoxy system during cure. This work showed a rapid increase in the shrinkage percentage after gelation up to the full cure. Similarly, Yu et al. [68] characterised the gelation and vitrification of a thermosetting material using cure shrinkage measurements. Among those techniques that are commonly employed, differential scanning calorimetry (DSC) and modulated differential scanning calorimetry (MDSC) are suitable, because calorimetric measurements provide quantitative information to calculate the activation energy, rate of conversion as well as extent of reaction. An example of this is the work performed by Thomas et al. [69]. In this work, the degree of conversion and rate of conversion during the cure reaction at different temperatures were determined from DSC measurements, and hence, the activation energy was derived using the autocatalytic model [70]. In another study, Van Assche et al. [64] showed the possible benefits in using MDSC to study the isothermal cure of thermosets.

2.1.2 Thermal properties

The glass transition temperature leads to a change in the local degree of freedom of materials. Below the glass transition temperature, the thermal energy available is not enough to allow rotation about the single bonds in the polymer backbone and, therefore, segmental motions of molecular chains are severely hindered. Consequently, it requires quite a long time for molecular relaxation processes to occur. The material possesses hard and brittle qualities at these temperatures. Conversely, the rubber state above the glass transition temperature facilitates these long-range molecular cooperative motions. Within the glass transition temperature range, the behaviour of materials, such as heat capacity, free volume, dielectric constant and so on changes markedly. Therefore, depending on the specific application, a system with an appropriate value of T_g should be chosen, such that it exists in the desired state. In addition, the temperature range over which the glass transition take places is considered to be associated with the crosslink

heterogeneity of the local material environment [71-72]. Indeed, Alves et al. [73] observed a broadening of the temperature range of the glass transition as the crosslink density increased. They claimed that this phenomenon could be due to several factors: a broad distribution of relaxation times; the low apparent activation energy around the glass transition temperature; the compositional heterogeineity of the materials.

It is well known that phase transitions are accompanied by significant changes in material properties, such as heat flow, heat capacity, etc. The transition from a glassy state to a rubber/viscous liquid in an epoxy resin causes a stepwise increase in heat flow and heat capacity, which involve the molecular mobility. The decrease in heat capacity at T_g, $\Delta C_p(T_g)$, is attributed to the decrease in mobility imposed by the crosslink density. Montserrat et al. [74] employed the DSC and temperature modulated DSC to study vitrification during the isothermal curing of an epoxy-amine system. This work revealed an abrupt decrease in the heat capacity when the system became vitrified due to a significant decrease in the number of molecular configurational states. The results obtained using DSC also showed a good agreement with dielectric data obtained by dielectric relaxation spectroscopy. This stepwise increase in degree of freedom of configurational states between the glass and rubber state can often be readily detected by differential scanning calorimetry (DSC) [75].

Differential Scanning Calorimetry (DSC)

DSC is a thermoanalytical technique that measures the difference in the amount of heat required to control the temperature of a sample and a reference as a function of temperature or time. The basic principle for the operation of a DSC is that both the sample and reference are always held at the same temperature throughout the test. Therefore, when the sample undergoes a phase transition, it will require more or less heat than the reference to maintain the temperature equality.

The reference can be an inert material, or just an empty aluminium pan. In this study, the temperature of the sample and reference were increased at a constant rate. The calorimeter is comprised of two holders, one for the sample and another for the reference, as shown in Figure 2-3.

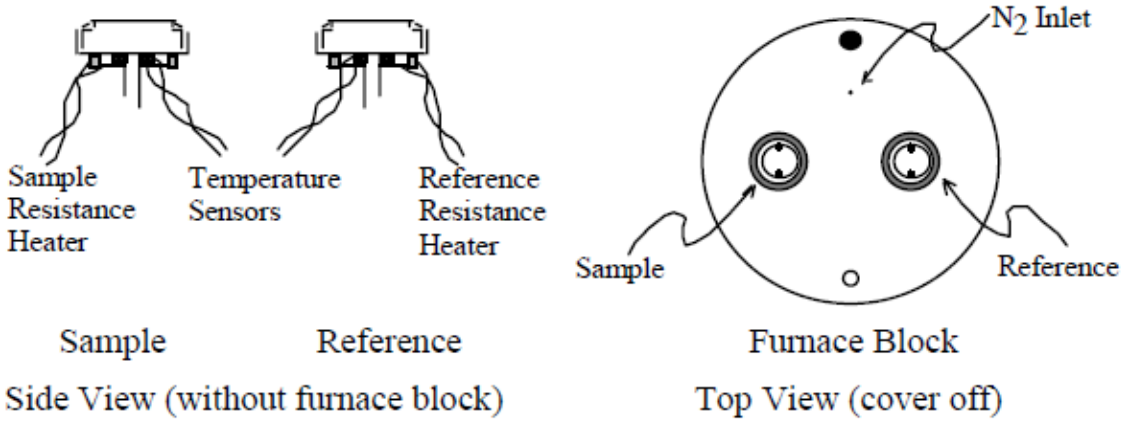

Figure 2-3 The DSC calorimeter [reprinted from 76]

Currents are applied to the resistance heaters to increase the temperatures at a specific rate. Based on the difference in power supplied to the holders to keep them at the same temperature, a heat flow diagram as a function of temperature can be obtained. Nitrogen is necessary to maintain a reproducible and dry atmosphere and improve the temperature control, as well as to eliminate oxidation at high temperatures.

The DSC technique provides quantitative and qualitative information about physical and chemical changes of materials. Therefore, it has been used extensively to characterise thermosets through the evaluation of the chemical kinetics associated with the cure reactions during the heat cycle, in which the glass transition temperature is of great importance.

2.2 Electric polarisation phenomena and dielectric permittivity

2.2.1 Electric polarisation phenomena

Epoxy resins constitute a popular class of dielectric insulators, and so it is important to investigate the behaviour of permanent dipole moments present in the material under an applied electric field. Dielectric spectroscopy measures the electric polarisation of materials as a function of frequency, or temperature. The overall polarisation from the electrode blocking layers, dipolar relaxation, and migrating charge carriers are monitored and the characteristic features of polymer materials such as thermal transition, or molecular relaxation are investigated. The method is based on the application of an ac voltage to the material and monitoring its electric response in terms of the resulting current over a wide frequency spectrum. The response is converted to

the corresponding dielectric properties, e.g. dielectric constant and loss. Despite a long development history, such as works by Von Schweidler [77], Benedict [78], or Dissado and Hill [79], there is still much to learn.

Electric polarisation can be considered as the charge redistribution in a material caused by an external electric field. The work done and energy loss due to the charge redistribution processes are obtained from the potential energy released. The total potential energy of the system in an electric field becomes smaller after polarisation.

A dielectric material is polarised under an electric field and the basic mechanisms of electric polarisation include electronic, atomic or ionic, orientational or dipolar and space charge polarisations.

a. Electronic polarisation (also called optical polarisation)

Under an applied electric field, the symmetrical distribution of electron clouds is deformed or displaced with respect to nuclei to form an electric dipole.

b. Atomic or ionic polarisation

This polarisation occurs in materials where the molecules contain two or more different kinds of atom. The electron distribution in these molecules is not symmetrically shared. The electric field causes the displacement of the relative positions of the atoms or ions, leading to the distortion of the normal lattice vibration.

Both the above-mentioned types of polarisation are mainly due to the elastic displacement of electron clouds within atoms or molecules. They are therefore intramolecular effects. There is always a restoring force against the displacement to bring the molecules back to their thermal equilibrium. These polarisation processes are largely independent of temperature.

A displacement of ions is always accompanied by the translation of electron clouds. Therefore, the distinction between the above polarisation processes is not clear. The time required to cause these polarisation processes is very short, typically about 10^{-15} s for electronic polarisation and about 10^{-13} s for atomic one. Therefore, resonance phenomena occur at very high frequencies and these polarisation processes are considered instantaneous in dielectric spectroscopy.

c. Orientational polarisation

This polarisation occurs only in materials consisting of molecules with a permanent dipole moment. Under an applied electric field, these dipoles orient themselves along the direction of the field.

The orientation of a dipole in a material under an electric field requires an amount of energy to overcome the resistance due to thermal agitation, which will bring the molecules back into random orientation, and the resistance of the surrounding molecules. This polarisation is an intermolecular interaction and is strongly dependent on temperature.

In solids, the dipoles cannot rotate freely. The rotation is determined by the interaction of the dipole with neighbouring ones, and constrained to a few discrete orientations.

d. Space charge polarisation

This polarisation is associated with mobile and trapped charges in a dielectric material. Under an electric field, charge carriers (electrons, holes, or ions), which may be injected from the electrical contacts or generated internally, may be trapped in the bulk at structural inhomogeneity or at interfaces to form space charge. The field distribution will be distorted. This is space charge polarisation. There are two possible ways to cause this polarisation.

Hopping transport

In a dielectric material, the charges such as ions, electrons or holes can move freely from one site to another for only a short time, and then they become trapped in the localised states. However, under an electric field, some localised charges can surmount a potential barrier to hop from one site to a neighbouring site. This phenomenon is probabilistic and only preferred in the low frequency range.

Interfacial polarisation

This polarisation is produced by the transport of mobile positive and negative charge carriers under an electric field. This causes the formation of positive and negative space charge in the bulk of the material at the inner boundary of discontinuous regions or at

the interfaces between different materials. This polarisation is also known as Maxwell-Wagner-Sillars (MWS) polarisation. If the accumulation of ions is at the polymer-electrode interface, it is also called electrode polarisation. For a multi-component system, this interfacial polarisation should be considered to be due to the non-uniformity within samples or to impurities associated with raw materials. Cracks or voids within samples produce a decrease in relative permittivity, whereas impurities may contribute an increase in permittivity due to their higher permittivity and the interfacial polarisation [80].

Both hopping transport and interfacial polarisation are related to the movement of charged particles, and therefore it is difficult to distinguish between them. Both processes contribute a sharp step increase in the real part, ε'_r, and imaginary part, ε''_r, of the relative permittivity with decreasing frequency.

There is another phenomenon that occurs in a dielectric material under an applied electric field, namely ionic conductivity. Thermosets often contain free ions as a result of the weak dissociation of the crosslinking agent or the residuals species from the synthesis of the resin or hardener. The migration of mobile charges within the material gives rise to dc conductivity. Unlike space charge polarisation, pure conduction manifests itself as an increase in the imaginary part of the relative permittivity with a slope of -1 in a log-log plot against frequency, while the real part stays unchanged over the low frequency range.

All types of polarisation require time to occur, and each of them takes different periods of time. The polarisations due to the elastic displacement of electron clouds or lattice vibration need very little time, while others due to the inelastic movement of particles such as the orientation of permanent dipoles and the migration of charge carriers require much longer times.

When a time-varying electric field is applied across a parallel-plate capacitor, the total current density J_T is given by:

$$J_T = J_0 + \frac{dD}{dt} = J_0 + \varepsilon^* \frac{dE}{dt} \qquad Equation\ 2-1$$

in which J_0 is the conduction current density and D is the flux density which relates to the displacement current. The complex permittivity ε^* can be defined as

$$\varepsilon^* = \varepsilon_r^* \varepsilon_0 = (\varepsilon'_r - j\varepsilon''_r)\varepsilon_0 \qquad Equation\ 2-2$$

in which ε'_r and ε''_r are the real and imaginary parts of the complex relative permittivity ε_r^* respectively, whereas ε_0 is the permittivity of vacuum. The imaginary part is introduced to allow for the dielectric losses due to dissipation processes without the effect of dc conductivity.

When a sinusoidal electric field $E = E_m e^{j\omega t}$ is applied, the total current density will be:

$$J_T = \sigma E + j\omega(\varepsilon'_r - j\varepsilon''_r)\varepsilon_0 E = (\sigma + \omega\varepsilon''_r\varepsilon_0)E + j\omega\varepsilon'_r\varepsilon_0 E \qquad Equation\ 2-3$$

In Equation 2-3, the term σE on the right involves the dc electric conductivity σ. It is a loss component due to the inelastic scattering of conducting charge carriers by scatterers during their migration. The term $(\omega\varepsilon''_r\varepsilon_0)E$ is also a loss component due to the resistance during the polarisation processes. The remaining term $\omega\varepsilon'_r\varepsilon_0 E$ is a lossless component which relates to the stored energy in the material.

For dielectric materials with sufficiently low conductivities so that the contribution of the first term can be neglected, then the loss tangent or dissipation factor can be expressed as

$$tan\delta = \varepsilon''_r/\varepsilon'_r \qquad Equation\ 2-4$$

There are several mathematical models which have been proposed to analyse the dynamic polarisation in the materials. Although the mathematical approach of those models is beyond the scope of this overview, it is useful briefly to summarise some typical results. The classic Debye equations for the dynamic polarisation with one relaxation time τ_0 can be generalised as follows:

$$\varepsilon_r^* = \varepsilon_{r\infty} + \frac{\varepsilon_{rs} - \varepsilon_{r\infty}}{1 + j\omega\tau_0} \qquad Equation\ 2-5$$

$$\varepsilon'_r = \varepsilon_{r\infty} + \frac{\varepsilon_{rs} - \varepsilon_{r\infty}}{1 + \omega^2 {\tau_0}^2} \qquad Equation\ 2-6$$

$$\varepsilon''_r = \frac{\varepsilon_{rs} - \varepsilon_{r\infty}}{1 + \omega^2 {\tau_0}^2}\omega\tau_0 \qquad Equation\ 2-7$$

$$tan\delta = \frac{\varepsilon''_r}{\varepsilon'_r} = \frac{(\varepsilon_{rs} - \varepsilon_{r\infty})\omega\tau_0}{\varepsilon_{rs} + \varepsilon_{r\infty}\omega^2 {\tau_0}^2} \qquad Equation\ 2-8$$

in which, ε_{rs} and $\varepsilon_{r\infty}$ are the static dielectric constant and the permittivity at very high frequencies respectively, whereas ω is the angular frequency. The maximum value for ε''_r occurs at $\omega\tau_0 = 1$ and $tan\delta$ becomes max when $\omega\tau_0 = (\varepsilon_{rs}/\varepsilon_{r\infty})^{1/2} > 1$.

Eliminating $\omega\tau_0$ from equation of real and imaginary permittivity and rearranging the equation we have the relation between ε'_r and ε''_r:

$$\left(\varepsilon'_r - \frac{\varepsilon_{rs} + \varepsilon_{r\infty}}{2}\right)^2 + {\varepsilon''_r}^2 = \left(\frac{\varepsilon_{rs} - \varepsilon_{r\infty}}{2}\right)^2 \qquad Equation\ 2-9$$

This is the equation of a semi-circle with the centre at $\left(\frac{\varepsilon_{rs}+\varepsilon_{r\infty}}{2},\ 0\right)$ and radius of $\left(\frac{\varepsilon_{rs}-\varepsilon_{r\infty}}{2}\right)$.

The Debye equations are only valid for a single relaxation time. However, in practice, due to intermolecular interaction, a distribution of relaxation times is necessary to interpret experimental data. In most cases, compared to the Debye semi-circle, the loss peaks have been found to be much broader and asymmetric with a high frequency tail. A number of empirical model functions have been proposed to describe such broadened and/or asymmetric loss peaks.

The Cole-Cole function has been proposed as a generalisation of the Debye dielectric equation:

$$\varepsilon_r^* = \varepsilon_{r\infty} + \frac{\varepsilon_{rs} - \varepsilon_{r\infty}}{1 + (j\omega\tau_0)^{1-\alpha}} \qquad Equation\ 2-10$$

in which α represents the effect of a distribution of relaxation times around the most probable value and is determined empirically. When α = 0, equation 2-10 is reduced to the Debye equation.

The Cole-Davidson equation is used for an asymmetric model function:

$$\varepsilon_r^* = \varepsilon_{r\infty} + \frac{\varepsilon_{rs} - \varepsilon_{r\infty}}{(1 + j\omega\tau_0)^{\beta}} \qquad Equation\ 2-11$$

where β describes an asymmetric broadening of the relaxation function.

Havriliak and Negami have proposed a more general model function (HN equation) which, in fact, is the combination of the Cole-Cole and Cole-Davidson equations:

$$\varepsilon_r^* = \varepsilon_{r\infty} + \frac{\varepsilon_{rs} - \varepsilon_{r\infty}}{(1 + (j\omega\tau_0)^{\alpha})^{\beta}} \qquad Equation\ 2-12$$

where α and β are determined empirically from dielectric data.

If dc conductivity is not ignored, it will contribute to the loss component of the complex permittivity such that:

$$\varepsilon_r^* = \varepsilon'_r - j\left(\varepsilon''_r + \frac{\sigma}{\omega}\right) \qquad Equation\ 2-13$$

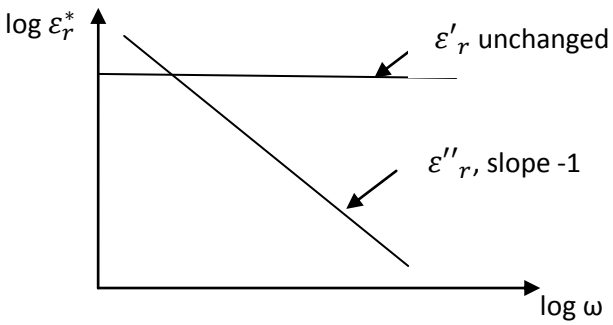

Figure 2-4 Complex permittivity behaviours as a function of frequency in pure dc conductivity mechanism

The energy absorbed or lost due to dc conductivity depends on the frequency. At low frequencies, where the ions can easily follow the applied electric field, the loss factor is mainly due to ionic conduction.

When the ionic conduction is high enough, the ions are collected at the polymer/electrode interface during one-half cycle of the oscillating electric field. The

accumulation of ions at the interface forms a charge layer, giving rise to the capacitive component of the permittivity. In the low frequency range, the ionic conduction becomes dominant, and then the contribution of the electrode polarisation to the permittivity would become maximum.

As mentioned above, in heterogeneous systems with multi-components, the MWS should be considered. For a model based on a two-component dielectric, the real and imaginary parts of relative permittivity can be expressed as follows:

$$\varepsilon'_r = \varepsilon_{r\infty} + \frac{\varepsilon_{rs} - \varepsilon_{r\infty}}{1 + \omega^2 {\tau_0}^2} \qquad Equation\ 2-14$$

$$\varepsilon''_r = \frac{1}{\omega C_0 (R_1 + R_2)} + \frac{\varepsilon_{rs} - \varepsilon_{r\infty}}{1 + \omega^2 {\tau_0}^2} \omega \tau_0 \qquad Equation\ 2-15$$

where C_0 denotes the capacitance of a vacuum condenser, while R_1 and R_2 are resistance components of the two constituent dielectrics respectively. The plot of $\varepsilon'_r(\omega)$ is similar to that of a Debye plot, whereas in $\varepsilon''_r(\omega)$, the second term is identical to that of the Debye model, but the additional first term is proportional to ω^{-1}. The MWS effect can be characterised in Figure 2-5. In practice, due to the "fractal nature of surfaces", the MWS polarisation often exhibits $\varepsilon''_r \sim \omega^{-s}$ $(0 < s < 1)$ [81].

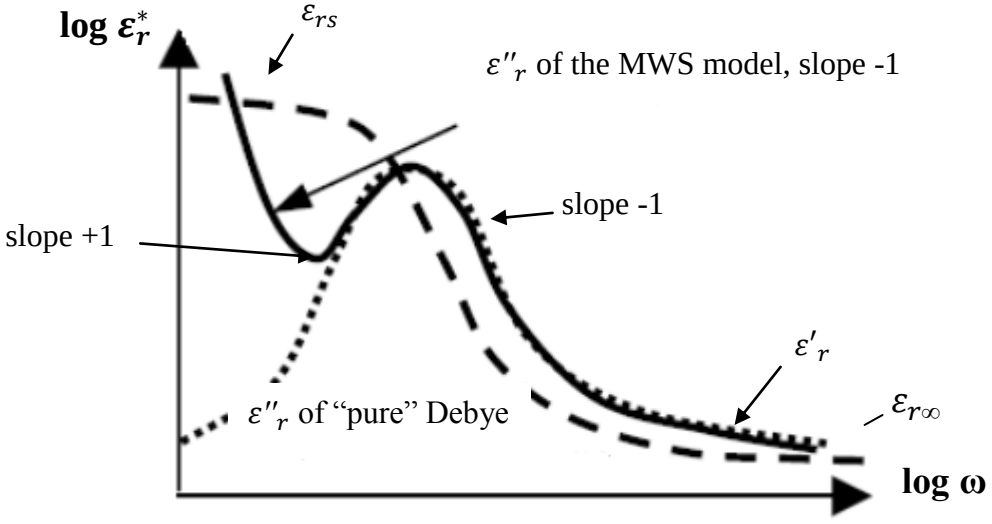

Figure 2-5 Characteristics plot of the MWS effect

The dependence of permittivity of a dielectric material on the frequency of the applied electric field is referred as the dielectric dispersion. If a polarisation process loses its

response to the change of field, the permittivity will decrease. Figure 2-6 shows a dielectric dispersion as a function of time.

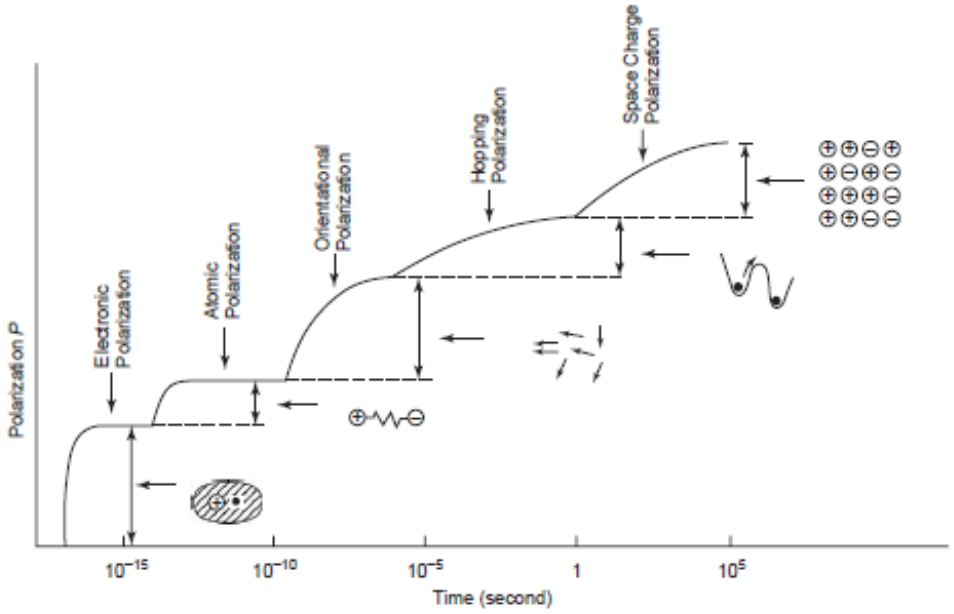

Figure 2-6 The dielectric dispersion of a dielectric material [reprinted from 82]

Dielectric spectroscopy has been used as an in-situ monitoring method for the curing process. This technique is based on changes in the relaxation phenomena upon applying an electric field. The dominance of ionic conductivity at the beginning of curing or the α-relaxation associated with the vitrification has been described successfully in numerous studies [83-84]. For instance, Nixdorf et al. [85] observed that the dielectric spectrum was completely dominated by conduction at the beginning of the cure process. However, as curing proceeded, a progressive decrease in conductivity indicated the progress of the reaction and the glass transition process was observed as a broad maximum in the dielectric loss factor. The relaxation peak shifted to lower frequencies with increasing cure time, corresponding to an increase in relaxation time. Nunez et al. [86] analysed the dielectric α-relaxation process; T_g was observed to be associated with the maximum of the ε'' versus T plot. The presence of nanofillers has been shown to affect the curing behaviour of nanocomposites. Kortaberria et al. [66] performed "real-time" experiments to follow the curing reaction of mixtures of a diglycidyl ether of bisphenol-A epoxy resin and 4,4-methylene bis(2,6-diethylaniline) hardener containing an organically modified nanoclay. Gelation and vitrification times for nanocomposite systems were found to be lower than for the unfilled epoxy. This indicates the catalytic

effect of the nanoclay on the curing reactions. Also, in this work, the presence of clays caused a sharp increase in conductivity, masking the dipolar component and increasing the frequency of a peak corresponding to the main relaxation. Puglia et al. [87] claimed an acceleration effect of single wall carbon nanotubes on the early stage of cure process in a DGEBA/DETA epoxy system. The modification of curing reactions and crosslinking density by the presence of nanofillers has also been reported elsewhere [88-89]. Different experimental techniques have pointed out that two main contradictory effects of nanofillers on chain dynamics may be considered [90]. Due to constraints imposed by the rigid nanoparticles, dynamics may be slower near the interface; at the same time, dynamics may become faster as a result of more free volume produced by loosened molecular packing of the chains. Kyritsis et al. [91] studied polymer dynamics in epoxy/alumina nanocomposites by various techniques. In this work, five relaxations were considered, including the secondary γ, β, and ω relaxations in the glassy state, the segmental α relaxation, which is associated with the glass transition, and the interfacial MWS relaxation associated with the heterogeneous structure. The investigation revealed a correlation between an increase in the real part of the dielectric permittivity, a decrease of storage modulus and an increase in ductility upon incorporating nanoparticles.

2.2.2 Dielectric mixing laws

A number of theoretical approaches have been developed to predict the effective dielectric constant of polymer composites, such as the mean field theory [92] and the effective medium theory [93]. Much theoretical hypothesis has also taken account for the role of the interface between the filler and polymer matrix, such as the interphase power law model developed by Todd et al. [94], or the model developed by Vo et al. [95] which considered the matrix-filler interaction strength.

Among the proposed dielectric mixing rules, the Lichtenecker [96] and the Maxwell-Garnett [97] are usually applied to estimate the effective macroscopic permittivity, ε_{eff}, of a heterogeneous system.

- Lichtenecker rule:

$$log\varepsilon_{eff} = V_m log\varepsilon_m + V_p log\varepsilon_p \qquad Equation\ 2-16$$

- Maxwell-Garnett rule:

$$\varepsilon_{eff} = \varepsilon_m + 3V_p\varepsilon_m \frac{\varepsilon_p - \varepsilon_m}{\varepsilon_p + 2\varepsilon_m - V_p(\varepsilon_p - \varepsilon_m)} \qquad Equation\ 2-17$$

where V_m and V_p are the volume fractions, while ε_m and ε_p are the permittivities of the base resin and the spherical particle filler respectively.

2.3 Electrical ageing and breakdown phenomena in insulating materials

Most electrical failures in the power engineering industry result from electrical ageing, partial discharge, or breakdown in insulating materials. Due to the defect density of the solid insulator, dielectric breakdown can cause mechanical damage, electrical conduction and, finally, the failure of the whole system.

2.3.1 Electrical ageing

When a solid dielectric material is continually subjected to high electrical stress, the material is said to undergo an irreversible process termed electrical ageing. The ageing process is a gradual degradation leading to the destructive breakdown of the material. Therefore, electrical ageing is always of great concern to industry.

At high fields, electrons may be injected into an insulator by a thermionic emission process or by an electron tunnelling process. In dielectric materials, there is a high concentration of localised gap states, especially near the injecting electrode and, therefore, these injected electrons quickly become trapped after a few scattering events. These trapped electrons will create a negative homo-space charge near the cathode (for the case of injecting electrons), and hence reduce the effective field and suppress further electron injection. In addition, in the nonradioactive transition from an upper to lower energy state due to trapping or recombination, an amount of energy which is equal to the energy difference between the two states will be released. The energy evolved at each trapping or recombination event is of the order of 3-4 eV or greater for deep traps and recombination centres [82]. Kao [82] has supposed that this amount of energy can be dissipated directly, causing structural damage in the microregion around the sites where the electrons are trapped, or by transfer to another electron. This second electron may become hot and have enough energy to break molecular bonds upon bombardment.

The term “hot electron” is introduced to describe electron distributions describable by the Fermi-Dirac function but with an elevated effective temperature. To become “hot”, an electron must gain sufficient kinetic energy to overcome a potential barrier necessary to break molecular bonds. Conversely, a “cold electron” describes a thermal equilibrium electron. The molecule is ruptured into free radicals, which constitute new traps. These new defects or traps can capture ‘cold’ electrons and new energy is released which may be transferred to a third electron. This process will continue in a chain reaction such that more radicals are produced. Finally, low density regions with traps can be formed, leading to the degradation of the material. The probability of creating hot electrons depends on the concentration of injected electrons. Therefore, the concentration of hot electrons and hence new traps is higher near the injecting contact and increases with the applied electric field.

In general, the ageing process involves bond scission, and space charge formation. It is a long and continuous process occurring at the molecular scale throughout the whole service life of the material. Therefore, it is not easily observed. Some models have been developed to predict the degree of electrical ageing and, hence, the lifetime of insulating materials. The lifetime of an insulating material can be defined as the time for a destructive breakdown to occur at a particular electrical stress. The higher the electric field applied to the material, the shorter the lifetime is. Each model has been proposed on the basis of different mechanisms, such as space charge accumulation, or changes of the morphology of the material during ageing. Due to the limited data obtained, it is difficult to determine which model is better.

2.3.2 Electrical breakdown

Breakdown phenomena in gases have been relatively well defined. However, this is not the case for solid dielectrics. Solid dielectrics are usually used as insulators and mechanical support for the conducting parts of the electrical systems. The breakdown process of a solid is influenced by many factors, both external ones, such as temperature, humidity, pressure, the applied voltage, electrode configuration and materials, and internal ones such as imperfections, defects, impurities, and the morphology of the material. In solid dielectrics, in addition to the migration of the electronic and ionic charge carriers, the orientation and interfacial polarisation are also considered to be mechanisms for charge transport. Based on the time required for the

occurrence of breakdown, a number of different breakdown mechanisms have been proposed, as shown in Figure 2-7 [98]. Electrical breakdown, such as intrinsic, avalanche and electromechanical breakdown, is due to electronic process, while thermal breakdown is a result of the thermal instability due to Joule heating and thermal excitation. Electrochemical erosion processes are usually referred to as pre-breakdown phenomena, and include partial discharges, water treeing and electrical treeing. Such processes cause changes in the chemical structure of the material and gradually lead to destructive breakdown. The most common mechanisms for the electrical breakdown of solids are supposed to be intrinsic, thermal and avalanche mechanisms [99, 100].

In general, electrical breakdown is ultimately due to thermal instability, which leads to the destruction of the material. When a solid dielectric is subjected to an electric field, the electrical conduction and polarisation continuously cause Joule heating within the material. If this heat cannot be dispersed quickly enough into the environment by thermal conduction, thermal instability results and the material is said to undergo thermal breakdown. This failure occurs due to the localised, non-uniform fields at a critical current density. Dielectric losses which generate heat in the material are much greater under ac fields than under dc fields. Consequently, the thermal breakdown strength is lower for ac fields. This is the reason why the loss tangent should be kept as low as possible for applications involving ac fields.

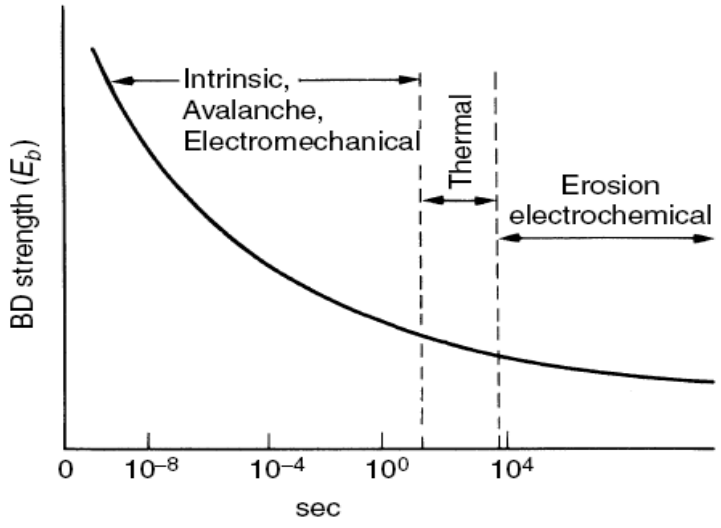

Figure 2-7 Breakdown in solid insulation against time [reprinted from 98]

For thermal breakdown process, carrier multiplication is due to mutual feedback between the temperature rise caused by Joule heating and thermal excitation. However, for electrical breakdown, carrier multiplication occurs and is mainly due to electronic processes. A number of theories have been proposed in an attempt to explain breakdown phenomena such as intrinsic breakdown, in which instability occurs when the energy of electrons gained by the applied field exceeds the energy lost by electron-phonon scattering event, or avalanche breakdown, in which the electrons gain sufficient energy to cause impact ionisation, or electromechanical breakdown, in which the mechanical deformation due to the electrostatic pressure exceeds the mechanical modulus of the material [98]. The avalanche mechanism was originally proposed by Seitz [100], in which breakdown in solids and gases are similar. This breakdown phenomenon was explained in term of lattice ionisation and formation of an electron avalanche under an applied electric field. However, in practice, a solid dielectric material has the following features [82]:

- The number of atoms or molecules per cm^3 is about 10^{22} - 10^{23}, that is, 10^3 times larger than the number of molecules in the same volume of a gas;
- Electron-phonon scattering can be considered a major interaction;
- Due to impurities, structural defects, or dislocations, the concentration of localised gap states is much larger than that of thermal equilibrium carriers;
- The mean free path is extremely small (l= 5-20 Å);
- The energy band gap is large (E_g > 4 eV);
- The carrier effective mass m* is large and mobility is low;
- The lifetime of carriers is much smaller than the dielectric relaxation time.

Consequently, in reality, it is almost impossible for carriers to gain sufficient energy from the applied field to become hot electrons to cause structural changes or to cause impact ionisation. It is unlikely that the injected electrons have enough time to be excited to a high mobility state before being trapped. One approach to explain this phenomenon has been proposed [101]. This proposal claimed that electrode defects and structural defects are the causes that enable breakdown to occur. The heterogeneity in the polymer structure leads to a non-uniform voltage drops and hence, non-uniform local electric fields within the polymer due to the different conductivities of

heterogeneous regions. A detailed account of breakdown processes in polymers can be found in [102].

Kao [82] also developed a model for breakdown in solid insulators, in which electrical breakdown was first considered to involve the formation of low density domains or regions in the bulk, by the trapping or recombination of charge carriers injected from the electrical contacts. Each trapping or recombination will evolve energy of the order of 2-5 eV, depending on the trap energy levels, while for condensed insulating materials, bond dissociation energies, E_d, are usually only about 3 eV. For example, E_d for C-C, C-H, CH_3-CH_3, Si-H, and Si-O bonds are 3.5, 3.55, 3.6, 3.05, and 3.8 eV respectively [82]. Therefore, the energy released from the trapping events was used up to break molecular bonds. Subsequently, low density domains are formed with large mean free paths. The breakdown was considered to be initiated by impact ionisation within such low density domains, followed by carrier multiplication and extension of the regions to form highly conducting channels, leading to the final destructive breakdown. This model can explain the dependence of the breakdown strength on the ramp rate of the applied voltage, as well as on the sample thickness. However, it is necessary to assess how large the mean free path is to cause impact ionisation. For example, the energy band gap is about 9 eV [103] or 6.9-7.4 eV [104] for polyethylene. This is the energy required for impact ionisation. Assuming this energy to be 9 eV and that the applied electric field that relates to service conditions is in the range from 10-100 kV/mm, then the mean free path required to cause impact ionisation is about 90-900 nm, which is much larger than the distance between atoms in a dielectric. This means that breakdown will not be initiated until low density regions with such large mean free paths are created. However, polymeric materials always contain defects in terms of buried loops of chain ends or microvoids, which act to increase unit cell dimensions and specific volume. Microvoids can be formed by evaporation of volatile decomposition products, imprurities or auxiliaries, which can decompose, and migrate, and gases that have not diffused out of the system. For example, Steven et al. [105] found that an epoxy resin that was prepared under extremely stringent degassing conditions still contained 10^{12}–10^{13} voids m^{-3} with diameter of 200 – 600 nm. Typically, microvoid diameters fall into the range 10-300 nm, but they can grow under mechanical and electrically-caused mechanical stresses. On the other hand, as mentioned above, the bond energies in condensed insulating materials usually fall in the range of 3-4 eV. The

energy released by the trapping or recombination events at least needs to be of the same order to break molecular bonds. Obviously, this energy depends on the trap energy level. In other words, this energy depends on the trap distribution inside the material. Two issues need to be addressed here concerning the trap distribution. The first relates to the formation of traps and their associated energy levels. For example, which factors determine the trap formation and its nature, or what is the probability of traps of the required energy level existing inside a dielectric? A high probability is necessary for the formation of the low density regions. The second concerns the spatial distribution of traps, which is whether the traps of the required energy levels are near the electrodes or in the bulk of the material. According to the model proposed, these traps need to be near the electrode such that the injected electrons can be trapped or recombined to release the energy. In general, it is essential to provide strong evidence in order to draw a sound conclusion about the application of this model. Space charge measurement may be a useful tool to describe the trap distribution inside the material qualitatively. However, quantitative evaluation also plays a key role in this model.

The electromechanical mechanism was based on the compression force due to the electrostatic attraction of opposite electric charges at electrodes in contact with the dielectric. This force is restrained by elastic force. The material will collapse when this electrostatic force exceeds its mechanical compression strength. In addition, due to heterogeneity in the structure, the material can experience a shear force as well. A dielectric contains a number of domains with heterogeneous structures. The domain boundaries can be considered as weak regions within the material. A shear force may produce “cracks” within the material, where the breakdown phenomenon is initiated.

2.3.3 Statistical analysis of breakdown data

Electrical breakdown voltage, as measured in practice, is subject to random variances. The breakdown phenomenon is a system failure which occurs when a weak link in the system fails. The distribution of structural defects within polymers is random, and therefore, each sample may undergo breakdown at different fields even though in principle, the samples are of the same material. As a result, it is necessary to analyse the breakdown data statistically. Although a number of statistical distribution functions can be applied to electrical breakdown, such as the Gumbel and Lognormal [106], the

Weibull distribution is the most common function used for the analysis of small or large data sets.

Assuming that the random breakdown process follows the Weibull distribution, the Weibull probability density fucntion *f(x)* indicates the probability of the breakdown phenomenon at an applied field *x*. The overall probability of electrical breakdown of a sample under an applied field less than or equal to *x* can be expressed by the cumulative distribution function:

$$F(x) = \int_0^x f(u)du = 1 - \exp\left(-\frac{x}{\alpha}\right)^{\beta} \qquad Equation\ 2-18$$

where the scale parameter α is the electric field at which the failure occurs for 63.2% of the samples. The shape parameter β indicates the scattering of the data. The higher the β, the lower the scatter. To plot the failure probability as a function of the breakdown strength, Benard's approximation of median rank [107] is usually applied to evaluate the unreliability of each failure and provide a 50% confidence interval of the true i^{th} failure among *n* samples. This method will rank the breakdown data in an increasing order before plotting. This approximation is given by:

$$f(i,n) = \frac{i-0.3}{n+0.4} \qquad Equation\ 2-19$$

2.4 Space charge formation and the pulsed electroacoustic technique (PEA)

In practice, all solid dielectrics are imperfect. Polymeric materials usually contain impurities, and/or physical and chemical defects due to the manufacturing and handling processes. Such defects contribute a distribution of localised energy states within the band gap. However, these states are not extended throughout the crystal but exist in the vicinity of chemical and structural defects. These states are termed as traps because charge carriers entering these states are not available for conduction and may have to require considerable energy to be removed. The traps can be in the form of donors with energy levels immediately above the top of the valence band, acceptors with energy levels immediately below the bottom of the conduction band, or sites. Depending on the energy required to remove carriers, traps can be classified into deep and shallow traps.

When charge carriers such as electrons are trapped, space charge will be formed and the localised electric field around the trapping sites will be modified. Such field distortion can be significant. For example, Gallot-Lavallee et al. [108] considered a 1 mm thick film of relative permittivity of 2 and estimated that if the dielectric contains a charge density of 1 C/m^3 (i.e., 1 trapping site per 10^6 atom in a typical solid, equating to 1 ppm of impurities), the electric field can reach a value as high as 50 kV/mm. In reality, technical insulations usually contain more than 1 ppm of impurities [109]. The increase in the local electric field in the system will lead to a consequent decrease in the electrical performance of the material [110-111]. Dissado et al. [112] investigated the effect of space charge on the electric field distribution and suggested that space charge is the origin of material degradation.

The mechanisms of space charge formation in the bulk of a dielectric are extremely complex, involve charge injection and transport within the material and are strongly influenced by various factors, such as the applied stress, humidity, temperature, electrode materials, impurities, etc. Charge carriers may be generated inside the material by various processes, such as thermal excitation, impurities, ionisation, internal dissociation or injection from the electrodes [110]. In general, a dielectric contains only a small amount of mobile charge within its bulk. Furthermore, under a high electric stress, at the electrodes, electron injection or extraction (hole injection) can occur by either Schottky emission or quantum-mechanical tunnelling through the barrier [110]. They are referred to as homo-charges. At interfaces between the electrodes and the material, there always exists the contact potential, which is defined as the potential difference created between two dissimilar materials of different work functions when they are brought into intimate contact [110]. The potential barrier height may limit the charge transport if its value becomes too high. The magnitude and slope of potential barrier height are strongly influenced by polymer electron affinity and the ionisation potential [113]. In addition, the dissociation of intrinsic charges in the bulk can produce mobile carriers for conduction, or traps that will affect the mobility of charge carriers injected from the electrodes. Under the influence of an applied field, charge carries will drift across the material and some of them will be trapped in localised states. Therefore, the amount of charge moving will decrease. However, the electric field may also modify the potential barrier profile of a trap to liberate the trapped charges more easily, a process termed field-assisted charge generation [114]. Charge transport can be imagined

as bi-polar conduction, due to electrons from one side and positive charges from the other side of the material. Therefore, through their motion, there is the recombination of opposite charges, which results in the reduction in the amount of charge and effective charge carrier mobility. A mobile charge is associated with an effective mobility. Charge carrier mobility controls the charge carrier density that can be transported through the sample under the presence of low injection potential barriers [114]. Due to the difference in these mobility values, recombination may not occur in the middle of the bulk, but near the electrodes. The trapped charge plays an important role in the electric field distribution and therefore the electrical ageing of insulating materials [115]. Charges with the same polarity as the electrode reduce the interfacial field and, thus the injection of homo-charges, but increase the field in the bulk, and vice versa. The increase in the local field can lead to the local degradation of the material and, ultimately, to breakdown.

The principles of charge carrier injection, transport, trapping and recombination described above are modelled by Alison-Hill in a bipolar scheme, as shown in Figure 2-8. Mathematically, the model is based on the following basic equations of charge transportation in space and time:

Transport equation: $j(x,t) = \mu n(x,t)E(x,t)$ *Equation* 2 − 20

Continuity equation: $\frac{\partial n(x,t)}{\partial t} + \frac{\partial j(x,t)}{\partial x} = s$ *Equation 2 - 21*

Poisson's equation: $\frac{\partial E(x,t)}{\partial x} = \frac{\rho(x,t)}{\varepsilon}$ *Equation 2 - 22*

where μ is the mobility of carriers, which is a function of time *t*, while *n*, the density of mobile species, *j*, the current density, *E*, the electric field, and ρ, the net charge density, are all functions of time *t* and space *x* [116].

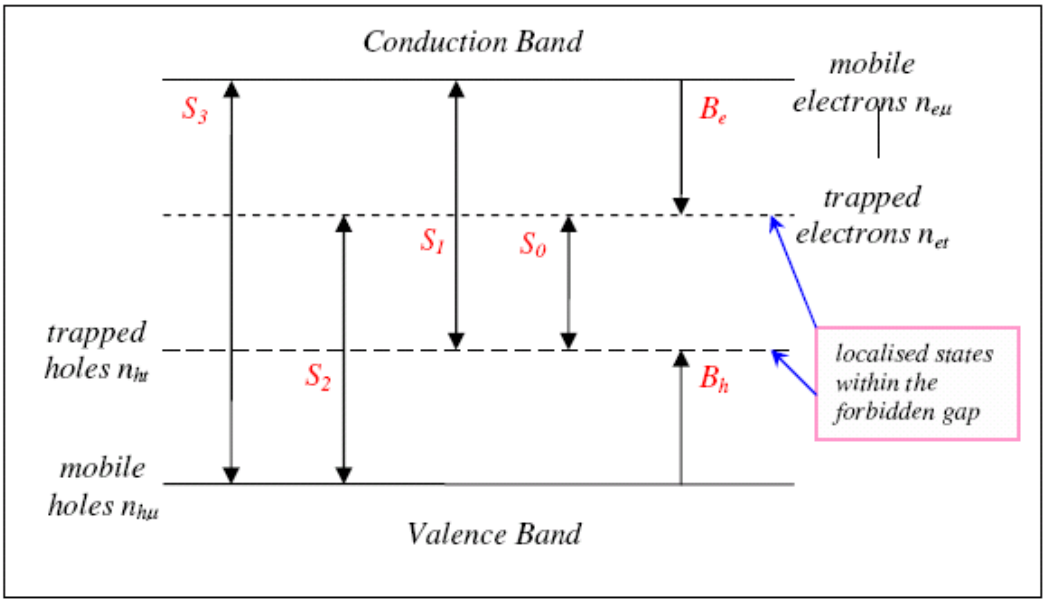

Figure 2-8 Schematic representation of the conduction and trapping model [reprinted from 116]

In principle, this model is fine, but not always applicable. In this model, there is only one single level trapping on deep centres, from which the trapped charges cannot escape [116-117]. That is, the electric field cannot modify the potential barrier sufficiently to liberate the trapped charges. Therefore, these charges can only recombine with the oppositely charged carriers. Besides, in the model, a constant effective mobility has been assumed. However, in dielectrics such as epoxy resins, there exists a distribution of trapping levels as well as a number of various charge carriers with different effective mobilities. Detrapping events can occur, that in turn, modify the effective mobility of charge carriers. Despite its simplicity, the Alison-Hill model, in principle, describes the space charge dynamics in polyethylene materials. According to the model, the transport process is dominated by electronic carriers injected from the electrodes. Only charges trapped in deep centres are introduced and there is no trap barrier modified by the applied field. The recombination is described between the opposite species (electrons and holes). Although the model is proposed with some assumptions that are impractical, such as the single trapping level and constant mobility, simulations based on it provide results that are compatible to experimental data [116-117]. Therefore, the model is a useful tool in analyzing the factors that influence space charge dynamics via numerical simulation, instead of through experimental discussions only.

In practice, the density of trap states in the energy gap can be high and the edges of the conduction and valence bands cannot be well-defined, as shown in Figure 2-9. The formation, the depths, and the concentration of traps are associated with the conditions under which the network is formed. Under the influence of an applied field, given sufficient energy, charge carriers can escape from localised states and drift to other localised states. However, such conduction in the band gap by this method depends on the inter-state distance. Further from the centre of the band gap, the distance between states is very small, so it may be possible for electrons to tunnel or hop between sites which are close to each other. However, near the centre of the gap where the concentration of states is low, it is unlikely that such a form of conduction can take place. The mobility of charge carriers in this region is extremely low and this region is referred as to the mobility gap. The concept of mobility gap is useful in separating out the extended and localised states. Obviously, the inter-state distance is a critical value for this form of conduction to occur. The probability of hopping or tunnelling between states increases quickly as this value falls below a few nanometers [118].

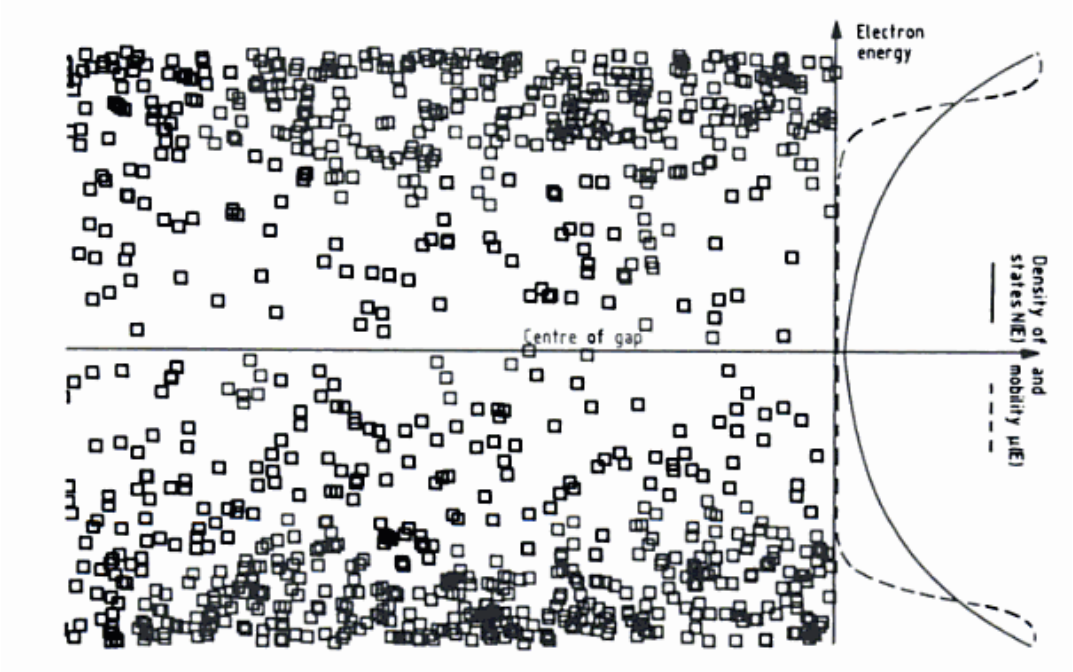

Figure 2-9 Schematic illustration of localised states (indicated by squares) as a function of electron energy, and the mobility for amorphous solids [reprinted from 118]. Overlapping squares shows states between which charge carriers can transport. Although the band edges and band gap are not well defined, a reasonable decrease in effective mobility can be detected

Because of the important influence of space charge on the performance of insulating materials, it is crucial to develop experimental techniques to facilitate the measurement of the accumulated space charge inside dielectrics quantitatively [119]. From the history of charge measurements, two classes of technique exist: destructive and non-destructive techniques.

Destructive techniques were first developed in the early days of the 20th century, and involved the use of powders, a field mill, or an electrostatic probe. However, in these methods, the dielectric had to be cut into slabs or slices, which could affect the charge distribution. This obvious disadvantage drove the discovery of non-destructive techniques.

The thermal shock method or thermal step method (TSM) was the first non-destructive, quantitative method and details of it are described in [120]. Thin electrodes are placed on both sides of a flat sample. One side of the sample is then subjected to a temperature pulse or step, which will travel as a thermal wave through the dielectric and therefore displace the space charge inside the sample slightly. This perturbs the electrode charges simultaneously, which results in a small voltage and current. The propagation of the thermal wave can be calculated. Then, using convolution techniques, the original space charge profile can be deduced. However, this method requires expensive equipment and complex mathematical calculations. The pressure wave propagation (PWP) method is used more widely [121]. The principles are similar to that of TSM but, instead of the thermal pulse, this method uses a pressure pulse of very short duration generated from a piezoelectric foil, PVDF. Moreover, as the pulse time is short, there is no need for complex convolution techniques to recover the space charge distribution and therefore it simplifies the method. The laser-induced pressure pulse (LIPP) method uses a very short laser pulse (<<1ns) to irradiate one side of the sample [122]. As a result of the energy shock at the surface, the sample generates a pulsed acoustic wave travelling through it. The principle is the same as in PWP, but the rise time is shorter.

The PEA technique is one of the most commonly used non-destructive methods for space charge measurement. In this technique, the acoustic wave is internally generated by the space charge and propagates through the material. A representation of a PEA system is given in Figure 2-10. In principle, the PEA method uses a piezoelectric transducer (PVDF foil) to detect the acoustic waves and convert them into electrical

signals. The use of a polymeric piezoelectric transducer is based on its properties, including high levels of piezo activity, wide frequency range and dynamic response, low acoustic impedance, etc [123]. The PEA system includes electrode 1, the dielectric sample, electrode 2, the transducer and acoustic absorber in sequence from right to left. An amplifier is put across the transducer to transfer the signal to an oscilloscope. A pulse source and a dc voltage source are in parallel across both electrodes.

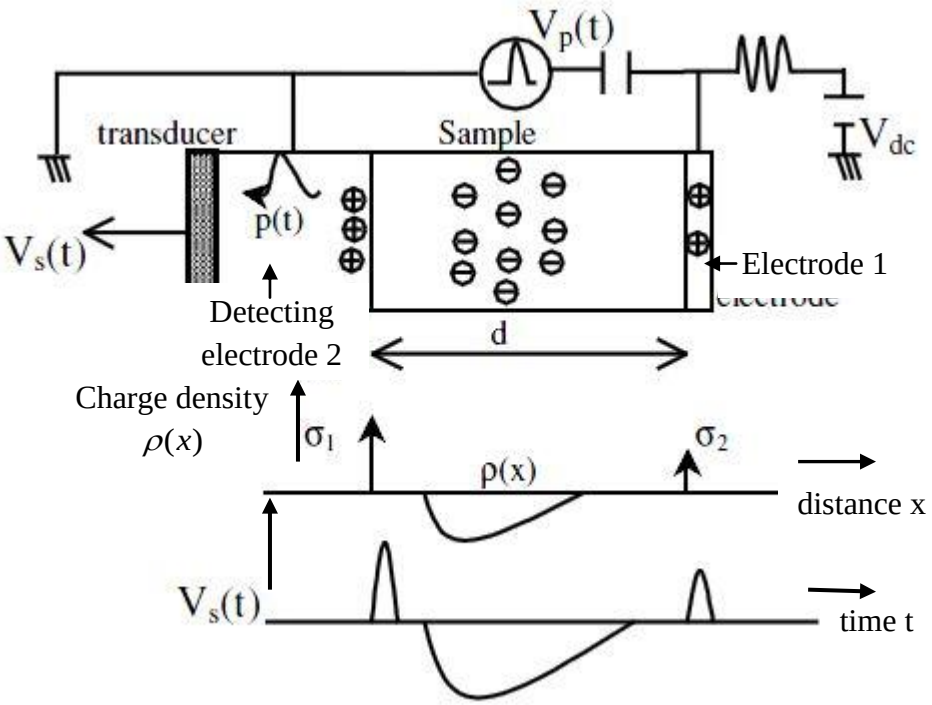

Figure 2-10 Schematic diagram of the PEA system

When a dc voltage is applied, charges are injected into the sample with total space charge density $\rho(x)$ in the bulk. The space charge distribution induces surface sheet charges of the same sign but different magnitudes on both electrodes, depending on the distance between the space charge and the electrodes. Additionally, the applied field also creates opposite charges of equal magnitude at the surfaces of both electrodes. The sums of induced charges and generated ones are the surface sheet charges σ_1 and σ_2 at the electrodes. When a short electrical pulse is put across the sample, the charges, which are the electrode charges and accumulated space charges inside the specimen, are stimulated by the pulsed field and every charge produces a pulsed electrostatic force. These forces generate pressure waves that travel as acoustic waves through the sample in two directions due to the slight movements of charges. The wave to the left will be

transmitted to electrode 2 and then to the transducer. When the acoustic wave propagates through the transducer, a surface charge is induced at the surfaces of the transducer due to the piezoelectric effect [123]. The transducer will transform this induced surface charge into an electrical voltage signal, which is amplified and shown on the oscilloscope. The magnitude of the signal is proportional to the space charge density [124]. After passing through the transducer, the wave will be absorbed by the acoustic absorber. The wave to the right will travel through the conducting layer and be transmitted to electrode 1 and then to the interface where it will be reflected back into the system to the left. After that, this wave will be transferred to the transducer later than the one to the left. Therefore, there is no overlap of the two generated pressure waves [124]. Due to its structural simplicity, ease of implementation and low cost compared to other techniques, the PEA method is used commonly to examine space charge injection and trapping in dielectric specimens.

2.5 Infra-red spectroscopy

It is well known that the energy of a molecule includes translational, rotational, vibrational and electronic contributions [125]. Translational and rotational energies involve the movement and the rotation of a molecule as a whole respectively. Vibrational energy is related to the vibration of constitutional atoms within the molecule, whereas electronic energy involves the associated energy of the electrons in the molecule. A molecule can only exist in certain discrete energy levels. There exist a number of possible vibrational energy levels at each electronic energy level, as shown in Figure 2-11. Obviously, it requires more energy to raise the electronic energy level of a molecule from the ground state to the excited state than to raise the vibrational energy levels.

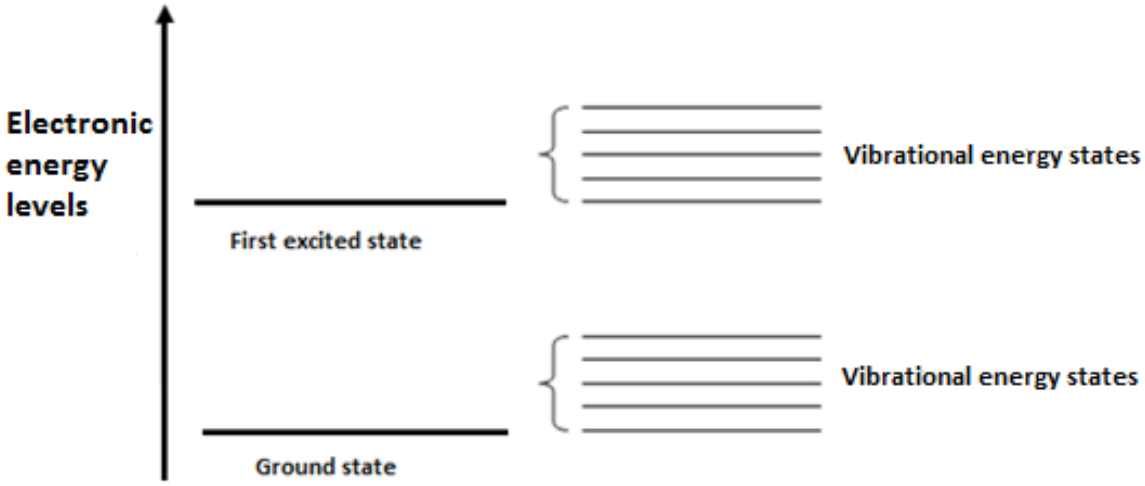

Figure 2-11 The simplified representation of the quantized electronic and vibrational energy levels of a molecule [126]

The vibrational energy of a molecule is determined by the shape of the molecule, the masses of constitutional atoms and eventually by the interaction between electronic and nuclear motions of molecules [127]. Different molecular configurations result in specific natural vibrational frequencies. For a simple diatomic molecule, only stretching vibrations can be found. For more complex molecules containing a number of alternative single and double bonds, conjugation of bonds can perturb the stretching frequency. For example, vibrational movements of atoms in simple molecular congigurations such as CH_2 groups can be classified as stretching and bending vibrations. The bending vibrations often include scissoring, rocking, wagging, and twisting as shown in Figure 2-12.

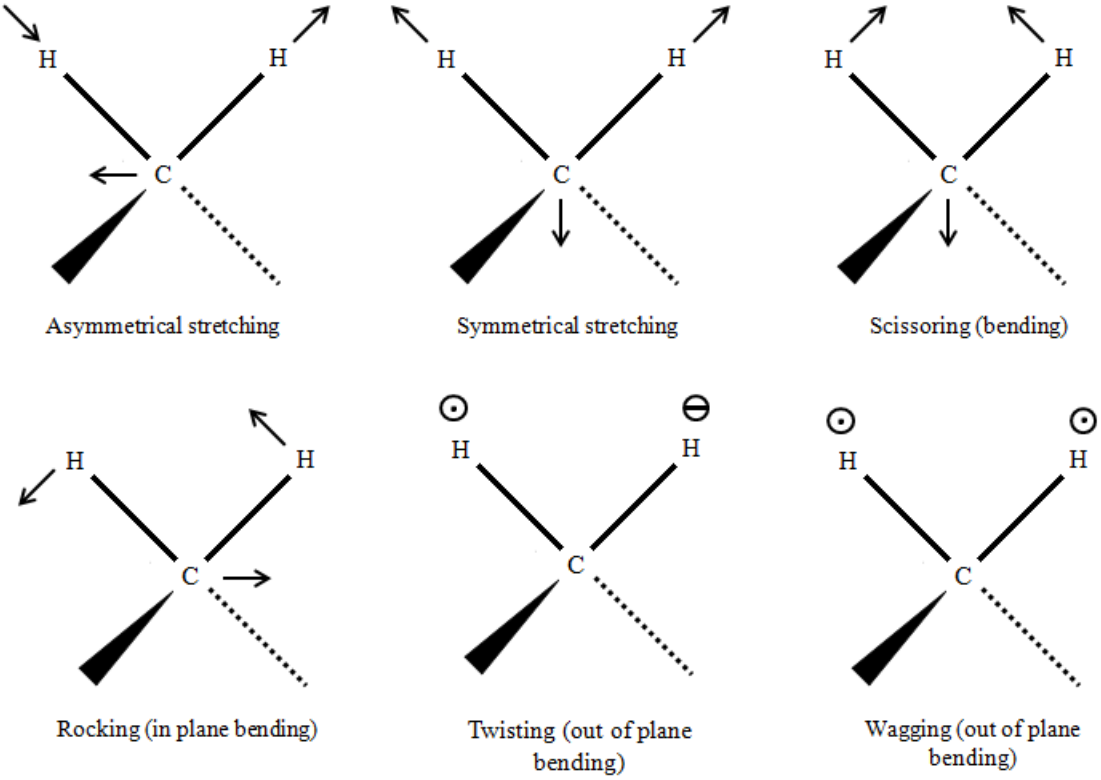

Figure 2-12 Pictorial illustration of vibrational modes detected using FTIR spectroscopy [reprinted from 128]

When electromagnetic (EM) radiation interacts with molecules, the energy of the photon can be taken up by the matter, a process termed absorption. Depending on the quantum energy of a particular frequency of EM radiation, several types of physical processes can occur, such as ionisation caused by ultraviolet radiation or electronic transitions caused by visible light. The quantum energy of infrared (IR) radiation is not sufficient to induce electronic transitions and, therefore, absorption of IR is restricted to vibrational and rotational states of a molecule, as shown in Figure 2-13. For a molecule to absorb IR, the vibrations or rotations must induce a net change in the dipole moment of the molecule. It means that only polar molecules containing permanent dipole moments can absorb IR. If the frequency of radiation matches the vibrational frequency of the molecule then radiation will be absorbed. IR absorption will increase molecular vibrational energy. The absorbed energy is quickly dissipated, in terms of kinetic energy as a result of collisions or released photons.

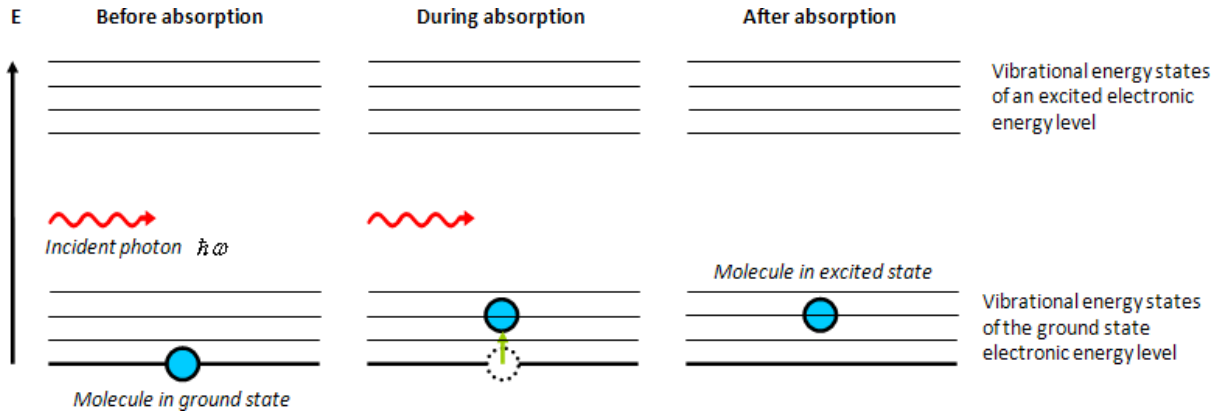

Figure 2-13 Energy levels of a molecule during absorption of a photon [reprinted from 126]

An IR spectrometer usually measures the radiation intensity as a function of the wavelength of the light incident on a sample. At the characteristic vibrational frequencies of molecules, IR absorption occurs and, the intensity of the transmitted IR will decrease. Consequently, a transmittance or absorbance spectrum plot can be obtained. Each type of bond has its own natural vibrational frequency and, so, is associated with a certain characteristic infrared absorption region. For example, absorption in the range 3000 ± 150 cm^{-1} is usually associated with C-H bonds present in the molecule. Another example is the hydroxyl group with its absorption range 3500-3000 cm^{-1}. Even two bonds of the same type in two different compounds are still in slightly different environments, and thus, no two molecules with different structures produce exactly the same infrared spectrum. Therefore, infrared spectroscopy can be used to investigate the molecular structure of samples. By combining the near (14000-4000 cm^{-1}), mid (4000-400 cm^{-1}), and far (400-10 cm^{-1}) infrared regions, the rotation or vibration of molecules, or combinations of these, can be observed and hence, a sample can be characterised and chemical bonds present in the sample can, in principle, be deduced.

In addition, IR absorption has been used successfully to determine the actual concentration of an analyte using the Beer-Lambert law [129-130]. An overview of this law can be found at [131]. This method is based on the linearly proportional relationship between peak areas in the infrared spectrum with the analyte concentration. This method requires a standard sample of known analyte concentrations for the calibration

[132]. However, this law is only restricted to circumstances where absorbance values change linearly with concentration, without any chemical effects [133].

Dispersive infrared spectrometers produce a beam of IR radiation and then split it into two separate beams of the same intensity. One of those two beams will pass through the sample and the other passes through a reference. The beams then pass into the monochromator that disperses each into a continuous frequency spectrum of IR light. The monochromator alternatively passes these two beams to a slowly rotating diffraction grating. This grating varies the frequency of radiation directing toward a detector. The detector determines the frequencies absorbed by the sample based on the ratio between the intensities of the reference and the sample beams. In Fourier transform infrared spectrometers (FTIR), the beam of IR radiation passes through an interferometer. The interferometer is used to split a beam of IR radiation into two beams which will travel different optical distances and, on recombination produce alternating interference fringes. The pattern produced contains all the frequencies of the infrared spectrum. The interferogram is a measurement of the temporal light intensity against optical path difference. Then, the returning signal undergoes FT which will convert a signal in the time domain to the frequency domain. Although the resulting spectrum should be the same from both FTIR and dispersive instrument, the FTIR can acquire the interferogram in less than a second, it offers a better signal-to-noise spectrum by operating the FT on the sum of accumulated interferograms. Because the information on all frequencies is acquired simultaneously, the FTIR provides faster method than conventional IR [132]. In addition, FTIR spectrometers are cheaper than conventional ones because it is easier to produce interferometers than monochromators. Because of these advantages, virtually, modern IR spectrometers are FTIR instruments. The big disadvantage of FTIR is atmospheric peaks, i.e. the spectrum involves the complete path length. Dispersive instruments show only the sample.

The polarity of the oxirane ring makes detection by IR spectroscopy possible. Therefore, IR spectroscopy has been used widely to characterise epoxy-based systems. For example, Zhang et al. [134] monitored the curing process of an epoxy/anhydride system at various heating rates using FTIR. In this work, changes in the concentrations of different functional groups were recorded and compared during the curing process. The results showed that etherification was not the dominant mechanism. In another

example, Preetha et al. [135] applied FTIR spectroscopy to analyse the degradation of sample surfaces due to partial discharge activity. The FTIR spectra of the aged epoxy samples demonstrated the presence of –C=O from intra molecular hydrogen bonded acids and the –CO-OOH bands of peracids.

2.6 Scanning electron microscopy (SEM)

Conventional optical microscopes operate with the limited wavelengths of light used (around 500 nm), and hence, give relatively poor resolution. In 1935, Max Knoll [136] observed the surface of a sample at nanometric scale using scanning electron microscopy (SEM). Since then, SEM has been applied frequently to investigate the morphology of many different materials. For SEM, the wavelength of electrons can be made much shorter than that of visible light, and consequently, the theoretical resolution is greatly improved. The relationship between the wavelength λ of an electron and the accelerating voltage V is presented in the equation:

$$\lambda = \frac{hc}{eV} \qquad Equation\ 2-23$$

where h is the Planck constant, c is the speed of light in vacuum, and e is the electron charge (1.602×10^{-19} C).

The SEM apparatus is enclosed in a vacuum chamber to avoid the effects of gas during operation. An electron beam, which is produced by an electron gun and accelerated through a potential difference (5-30 kV), passes through an optical system including two pairs of condenser lens and a condenser aperture. After passing through the lens, the high-angle electrons of the beam are eliminated using the aperture. The lenses are used to form a thin coherent beam passing through an objective lens which is used to focus the beam onto the selected area of the sample. The electron beam is then scanned across the surface, and the re-emitted electrons are collected by a detector. The signal from the detector is then amplified electronically and sent to a monitor screen which is scanned identically to the sample [137]. The detector signal controls the brightness while the magnification is based on the ratio of two scanning signals. The interaction between the incident electrons and those in the sample can be categorised into two main types. The first one is due to inelastic collisions, and the result is the emission of low energy secondary electrons (10-50 eV) [138]. Due to their low energy, those electrons can only

escape from regions near the surface of the sample. The second interaction involves higher energy electrons which are released from the deep regions within the sample as well as from the surface due to elastic backscattering. In order to avoid the charge accumulation at the surface, the SEM samples are usually made electrically conductive and grounded.

Chapter 3 Sample preparation and the experimental set-up

This chapter sets out to provide information about the component materials used in this work, and describes the various experimental set-ups employed to characterise the properties of the samples.

3.1 Base materials

The resin used in this study was Araldite MY 740 (Huntsman), which is based upon a diglycidyl ether of bisphenol-A (DGEBA) and has an EEW of 180-190 g/mol. This was cured using an anhydride-based hardener, coupled with a tertiary amine accelerator. The hardener used was Aradur HY 906 (Huntsman); this is methyl nadic anhydride and, as such, is a dicarboxylic anhydride. The accelerator was DY 073-1 (Huntsman), which is a modified amine complex. All these chemicals were used as received.

Table 3-1 The materials of curing system

Type	Designation	Chemical structure
Epoxy resin	Araldite MY 740	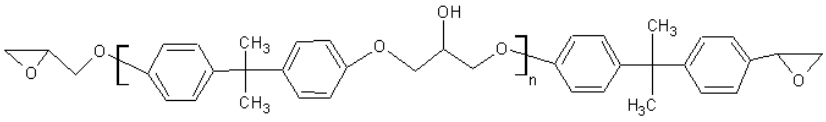
Hardener	Aradur HY 906	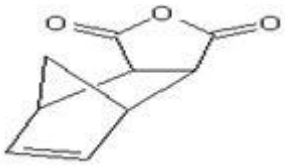
Accelerator	DY 073-1	R_3N

Table 3-1 represents the chemical structure of these organic compounds. This epoxy system is used widely in the construction of large coils for magnets and/or rotating machines due to its good mechanical and electrical properties at elevated temperatures, high thermal shock resistance and excellent radiation resistance. Typical mechanical

and electrical properties of this system are summarised in Table 3-2, based on the supplier's datasheet.

Table 3-2 Typical mechanical and electrical properties of MY 740/HY 906

Properties	Standard	Dimensions	Value
Flexural strength	ISO 178	MPa	125-135
Surface strain	ISO 178	%	4.4-5.0
Impact strength	ISO 179	kJ/m^2	15-18
Glass transition temperature (DSC)	ISO 11357-2	^oC	140-145
Breakdown strength	IEC 60243-1	kV/mm	26-30

a. Diglycidyl Ether of Bisphenol A (DGEBA)

DGEBA is the most common commercial epoxy resin monomer. The resin is synthesised from bisphenol-acetone and epichlorohydrin, as shown in Figure 3-1. The reaction is always carried out with an excess of epichlorohydrin to create terminal epoxy groups, as shown in Figure 3-2.

This excess is often associated with impurities in the resulting epoxy structure. The molecular weight of an epoxy resin can vary from low to high depending on the synthesis conditions and the amount of epichlorohydrin used, as shown in Table 3-3. The value of *n* in Figure 3-1 determines the molecular weight and the number of hydroxyl groups in the DGEBA monomers. The hydroxyl groups play an important catalytic role in the kinetics of the curing process and provide higher viscosity [139]. In general, when *n* is between 0 and 1, the resin is in the liquid phase at room temperature, but it is a rubber/solid at room temperature for values of *n* greater than 2 [32]. Commercial epoxy resins are usually a mixture of polymers, whereupon, *n* represents the average value.

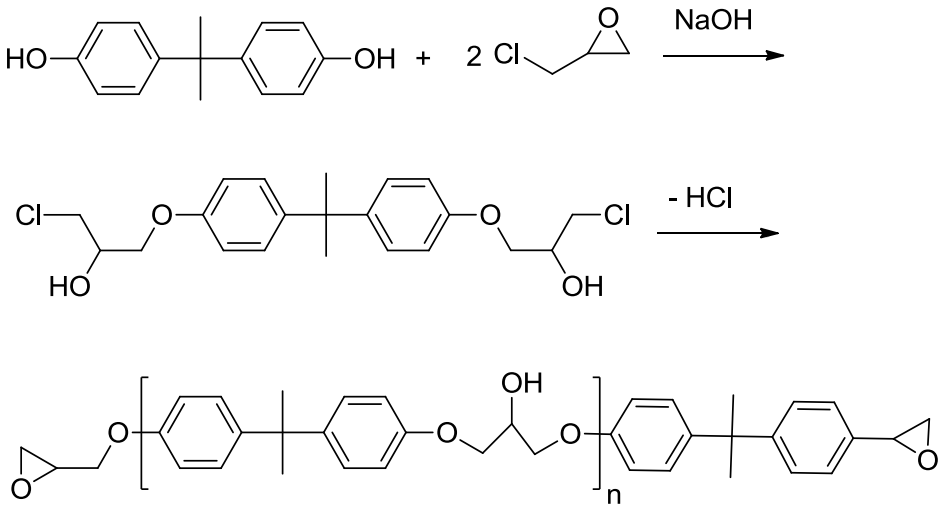

Figure 3-1 Synthesis of DGEBA resin from bisphenol A and epichlorohydrin [140]

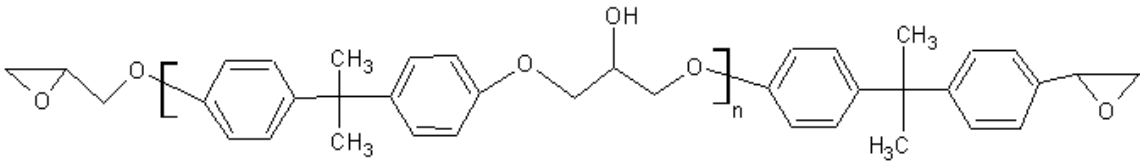

Figure 3-2 The chemical structure of DGEBA

Table 3-3 Effect of reactant ratios on molecular weight of epoxy resin [140]

Mole ratio: epichlorohydrin/ bisphenol A	Mole ratio: NaOH/ epichlorohydrin	Softerning point, ^{o}C	Molecular weight (g mol^{-1})	EEW (g mol^{-1})	Epoxy groups/ molecule
2.0	1.1	43	451	314	1.39
1.4	1.3	84	791	592	1.34
1.33	1.3	90	802	730	1.10
1.25	1.3	100	1133	862	1.32
1.2	1.3	112	1420	1176	1.21

Low molecular weight resin monomers with values of *n* ranging from 0 to 4 are of the most significance to industry, due to their ease of processing, high reactivity and high crosslinking density [140]. The cured products of these monomers possess high glass transition temperatures with good heat, chemical and solvent resistance.

b. Anhydrides [140]

In addition to amines, acid anhydrides constitute an important class of curing agents. The reaction between anhydrides and epoxy resins is extremely complex, with a number of competing mechanisms, including esterification, etherification and even reactions of nascent hydroxyl groups with epoxy rings. At low curing temperatures, ester and ether reactions occur at the same rate, while esterification becomes dominant at higher temperatures. In addition, accelerators can change the balance of ester-ether linkages, while moisture absorption can lead to the hydrolysis of anhydrides to the corresponding acids, thereby, changing the curing properties of the systems. Consequently, it is necessary to dry fillers before introducing them into an anhydride system.

c. Fillers

Nanopox E 470 (Nanoresins) was used to provide the nano-sized fillers. This commercially available material is a high performance silica reinforced bisphenol A based epoxy resin, containing a SiO_2 content around 40 wt%. The silica phase consists of surface-modified synthetic SiO_2 with an average particle diameter of 20 nm, and maximum diameter of 50 nm. According to the supplier's technical data sheet, it is an agglomerate-free colloidal dispersion of nanoparticles in the resin. Its EEW is 300 g/mol and it is stated that the nano-silica is dispersed in the resin in the form of primary particles.

In addition, a nanosilica system supplied by 3M was also used in this project; not much information exists about this product, although it is believed to include nanosilica particles with an average diameter of about 100 nm premixed in the resin at 49.8 wt%, as claimed by the supplier. Surface-treated 3M nanosilica is considered to be well dispersed in the resin.

Silbond W12 EST (Quarzwerke) was used as the micro-sized filler. This grade is a silanated, ultra-fine silica flour with an average particle diameter of 16 µm and an upper grain size of 50 µm. Due to surface-modification, such silica flours can be effectively incorporated into appropriate polymer system. Its specific surface area of 0.9 m^2/g is small. Silbond is produced from prepared natural raw minerals. Therefore, Silbond

contains only 98.5 wt% SiO_2, plus other impurities such as Al_2O_3, Fe_2O_3, CaO, MgO, Na_2O and K_2O.

3.2 Silica

Silica is the chemical name that represents a large class of materials with the general formula of SiO_2. Silica is produced by various synthesis processes, depending on the required sizes and behaviour of the filler. Silicon dioxide particles have been used widely as fillers in epoxy resins to enhance insulation properties and reduce the cost of the material. However, the addition of silica fillers into an epoxy resin can degrade material properties in the case of poor particle dispersion. Severe filler settling can cause cracks and reduce the reliability of the system [36]. Therefore, it is important to ensure a good dispersion of fillers. As a result, a fundamental understanding about surface chemistry of filler, filler dispersion and liquid-solid interactions plays an essential role in producing a good nanocomposite.

3.2.1 Silica synthesis

Naturally, silica exists in the form of flint or quartz. However, most industrial silica is a synthetic amorphous one. A number of methods are used to synthesise silica fillers, depending on the required particle size. The wet chemical route, where the silica is formed in the liquid phase, and the dry chemical route, where the silica is formed at a high temperature, are the two main ways. The two kinds of silica produced by the dry chemical route are fused silica and fumed silica. Fused silica is a noncrystalline form of quartz, with a highly crosslinked 3-D structure. It is produced by the fusion of high purity sand using an electric arc or a plasma arc furnace at about 2000 ^oC. Therefore, chemically bonded water molecules are often absent in the final forms of fused silica. Although this fusion process can produce silica particles of different sizes, ranging from nanoscopic to microscopic scales, fused silica of defined shape and geometry is usually used in the micron range size, with the thermal, mechanical and electrical properties comparable with crystalline quartz, as shown in Table 3-4 [141]. On the other hand, fumed silica is synthesised by burning $SiCl_4$ with hydrogen and oxygen in a high temperature flame, according to the reactions shown in Figure 3-3.

Table 3-4 Typical properties of silica [141]

Property	Quartz	Fused/Fumed silica
Density (g/cm^3)	2.65	2.2
Thermal conductivity ($Wm^{-1}K$)	1.3	1.4
Thermal expansion coeff. (10^{-6} K^{-1})	12.3	0.5
Tensile strength (MPa)	55	110
Compressive strength (MPa)	2070	690-1380
Poisson's ratio	0.17	0.165
Fracture toughness (MPa)	-	0.79
Melting point (^oC)	1830	1830
Modulus of elasticity (GPa)	70	73
Permittivity *	3.8-5.4	3.8
Tan (δ x 10^4) *	3	-
Loss factor *	0.0015	-
Dielectric field strength (kV/mm) *	15-25	15-40
Resistivity (Ωm) *	10^{12}-10^{16}	$>10^{18}$

***Dielectric properties at 1 MHz 25 ^oC**

$$2H_2 + O_2 \longrightarrow 2\,H_2O$$

$$SiCl_4 + 2\,H_2O \longrightarrow SiO_2 + 4HCl$$

$$\text{Or } 2H_2 + O_2 + SiCl_4 \longrightarrow SiO_2 + 4HCl$$

Figure 3-3 Synthesis of fumed silica using $SiCl_4$

Fumed white and loose silica powder has a highly disordered random network structure formed by SiO_4 tetrahedra with strong directional covalent bonds between four oxygen atoms at the corners and a silicon atom at the central, as shown in Figure 3-4 [142]. It is difficult for fumed silica to change its morphology and to crystallize, even if heated up to 1000 ^oC. The primary fumed silica particles of around 7-40 nm form a loose, non-

isolated network with about 98 vol% air through hydrogen bonds or Van deer Waals force. Due to the loose structure, the applications of fumed silica are quite different from fused silica, e.g. it cannot be used for epoxy reinforcement.

Currently, most nano-scale silica is synthesized by the sol-gel method, which is a wet chemical route. This process is based on the condensation of tetraethylorthosilicate ($Si(OC_2H_5)_4$; TEOS) in an alcoholic solution of water and ammonia. The sol-gel reactions can be considered as a two-step network forming process, including the hydrolysis of a metal alkoxide followed by a polycondensation reaction. In the case of silica, alkoxysilane such as TEOS has been widely used as a ceramic precursor in the sol-gel reactions, as shown in Figure 3-5 [143].

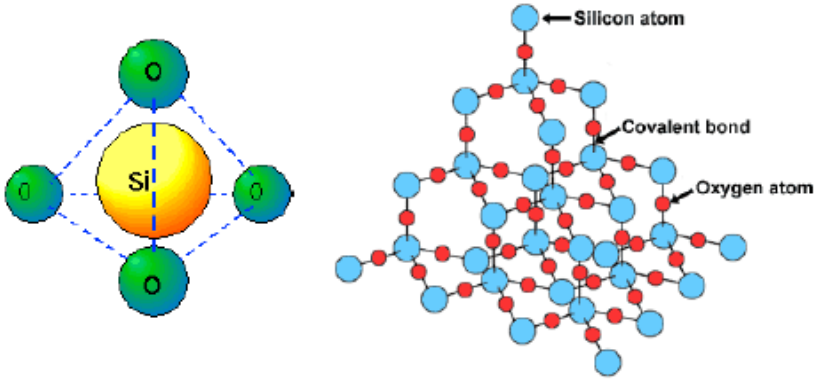

Figure 3-4 Pictorial representation of a SiO_2 atom (left), and the overall structure of silicon dioxide (right) [reprinted from 144-145]

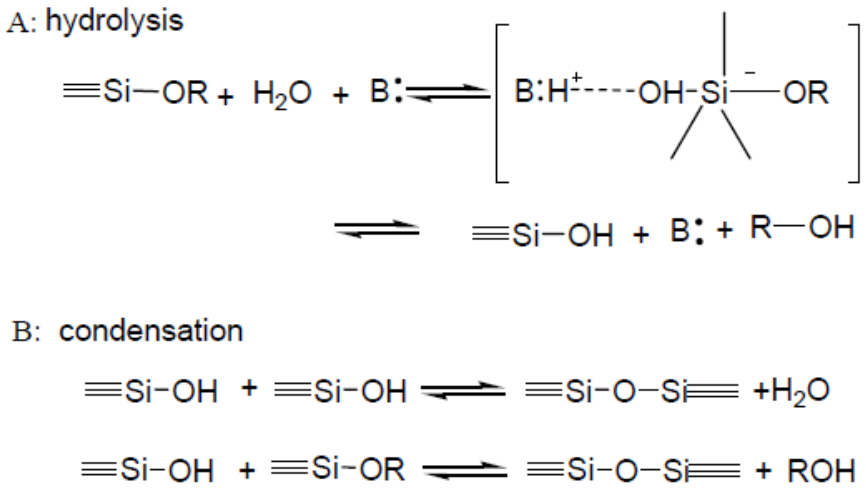

Figure 3-5 Sol-gel reactions of alkoxysilane [reprinted from 143]

There are a number of factors that influence the kinetics of the hydrolysis and condensation reactions, such as catalyst, temperature, etc. Therefore, by controlling the relative rate of these reactions in the sol-gel process, the morphology or surface nature of the silica phase can be altered, as shown in Figure 3-6 [146]. An acid or base is generally used as a catalyst to activate the sol-gel process. Acidic catalysis is found to accelerate the hydrolysis of TEOS. As a result, the hydrolysis reaction occurs at higher rate than the condensation, so leading to a weakly branched structure such that further evolution will provide a gel structure. Finally, a 3-D gel networks of the silica phase with characteristic morphological dimensions below 100 nm can be achieved [147]. In contrast, under basic catalysis, the polycondensation occurs at a higher rate than the hydrolysis. In this case, compact primary particles of highly dense networks with ring structure are formed. Further polymerisation will produce large spherical particles of highly branched clusters with dimensions much greater than 100 nm, which are generally referred to as sol structures. The sol is made of solid particles with a diameter of the order of hundreds nanometres, which are suspended in the liquid phase.

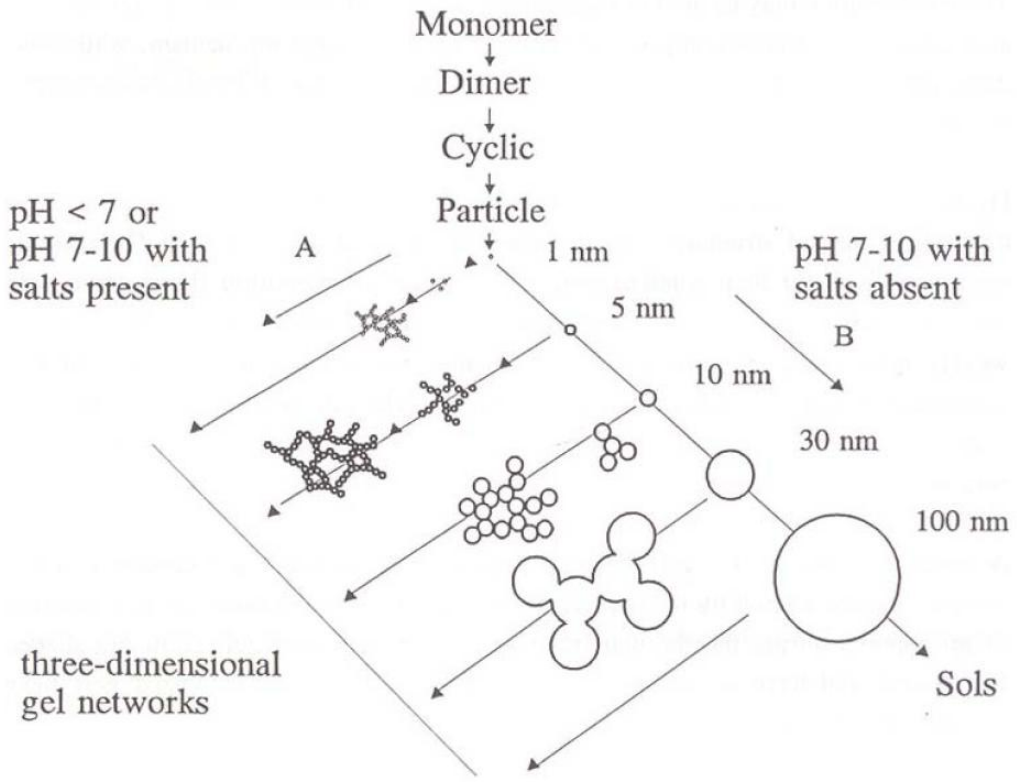

Figure 3-6 Polymerisation of silica [reprinted from 147]

Nanosilica particles produced by the sol-gel method have a large surface area, covered by silanol groups with a hydrophilic nature. Therefore, such silica particles do not exhibit good compatibility with epoxy resins. On the contrary, the particles tend to attract each other, through hydrogen bonding, to form aggregates. As a result, the material properties deteriorate, such that the nanocomposite exhibits a reduced T_g, higher moisture absorption, etc.

To achieve better compatibility and dispersion, surface modification of the particles is usually employed. The chemical treatment using silane coupling agents is preferred for silica surface modification, due to the polar function groups of the silane. Through this modification process, the hydrophilic silanol groups on the particle surface are replaced by hydrophobic groups, as shown in Figure 3-7. Consequently, better compatibility between the filler and the epoxy matrix is obtained due to the increase in the surface tension of SiO_2 through hydrogen bonding, or Van der Waals forces, etc. [148]. As a result, homogeneous dispersions of nanosilica in the polymer matrix can be produced as shown schematically in Figure 3-8.

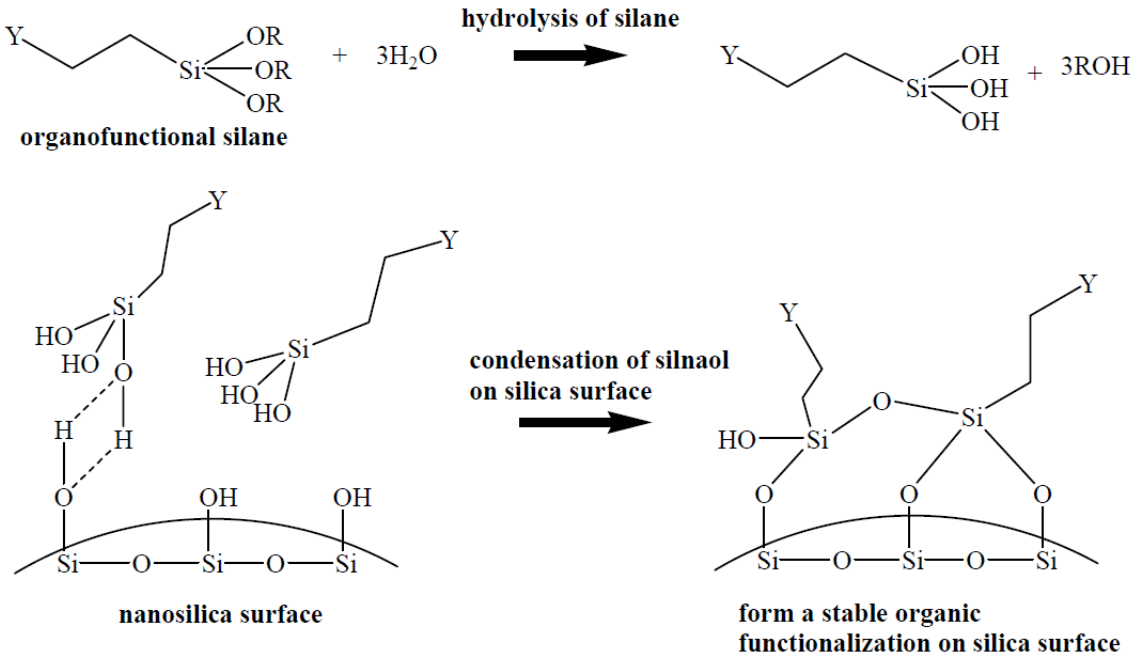

Figure 3-7 Mechanism of silane treatment to nanosilica surface [reprinted from 141]

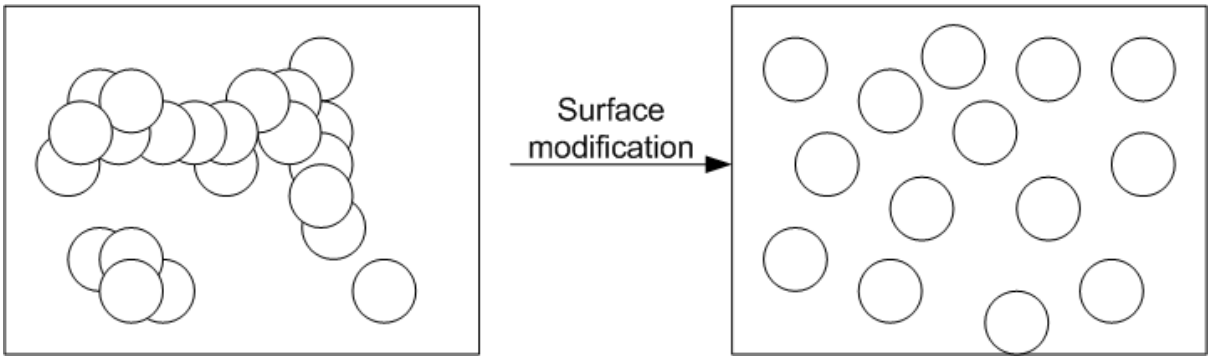

Figure 3-8 The dispersion of nanosilica before and after surface modification

3.2.2 Possible curing mechanisms

The curing process is a set of chemical reactions that lead to the formation of a highly crosslinked 3D network. A number of researchers have studied the curing of epoxy resins and anhydrides and suggested different mechanisms and kinetics. For example, Fisch and Hofmann [149] proposed that anhydride does not react with epoxy groups directly. Instead, in the absence of catalysts, the ring opening reaction between the anhydride and hydroxyl groups occurs first, followed by the reaction of the carboxyl group of the monoester with the epoxy group, resulting in a diester and a new OH group. They also noticed the reaction of epoxy groups with hydroxyls to a minor extent, and hence the anhydride requirement was only 0.5 to 0.85 mole per mole of epoxide. However, when tertiary amines or other basic catalysts were added to the reacting mixture, the authors observed that the formation of esters was accelerated while the generation of ethers was suppressed. Moreover, the ring opening reaction was found to occur at a faster rate than the others, leading to the accumulation of monoester in the reaction mixture. Fischer et al. [150] also found the same effect of catalysts. However, he did not assume that the alcoholysis reaction preceded the reaction of the epoxy groups itself due to the observation that an increase in the hydroxyl concentration did not increase the reaction rate. Similarly, Sorokin et al. [151] studied the curing of epoxy resins based on isolated reactions. This work revealed two main reactions occurring during curing with and without a catalyst, including the alcoholysis and the reaction of the nascent monoester with the epoxy group. However, in this work, he did not observe reactions between epoxy groups and hydroxyls. Later on, Kolar et al. [152] studied the curing of epoxy resins with maleic anhydride under the catalysis of N,N-dimethyl aniline based on the model reactions. He found that curing depended on the hydroxyl

content. If this was low, alcoholysis and the reaction rates of monoesters and epoxy groups were limited. Conversely, if the concentration of hydroxyls was comparable to that of epoxy groups and anhydride, the anhydride was depleted faster than the epoxy groups; hence, the kinetics depended on the reaction of monoester and epoxy groups. Based on this observation, he concluded that the hydroxyl content of the resins used determines the curing mechanism and kinetics. In addition, the work also revealed that no reaction between epoxy groups and hydroxyls took place at low temperature.

Despite such discrepancies in the proposed mechanism and kinetics, in general, three steps occur during curing of an epoxy resin and an anhydride, namely initiation, propagation and termination. The initiation step can involve the alcoholysis of anhydride. Alcoholysis is a nucleophilic reaction, and hence, the presence of tertiary amines accelerates the reaction due to the increase in the positive partial charge on the carbon next to the nitrogen atom [152], as shown in Figure 3-9. The initiation step can also involve the reaction of tertiary amines with epoxy groups, giving rise to a zwitterion as proposed by Matejka et al. [153] and Fedtke et al. [154], as shown in Figure 3-10. The resultant salt will act as the initiator for the curing process. The propagation reaction progresses as a result of transfer of the active centre between the epoxy and anhydride molecules in the fashion of chain growth polymerization through an esterification reaction, in which the CO^- group will open the anhydride ring while the COO^- group will open the epoxy ring. This reaction is considered to be the dominant curing mechanism. However, in practice, homopolymerisation/etherification also occurs to some degree during the curing process, in which the CO^- group reacts with the epoxy group and opens its ring at elevated temperatures, as shown in Figure 3-11. In other words, the curing mechanism of an epoxy-anhydride system is complicated with a number of possible competing reactions. Depending on imposed conditions, such as curing temperatures or mixing ratio, one of these reactions may become predominant and determine the final crosslinked structure, and hence, the final properties of the cured system.

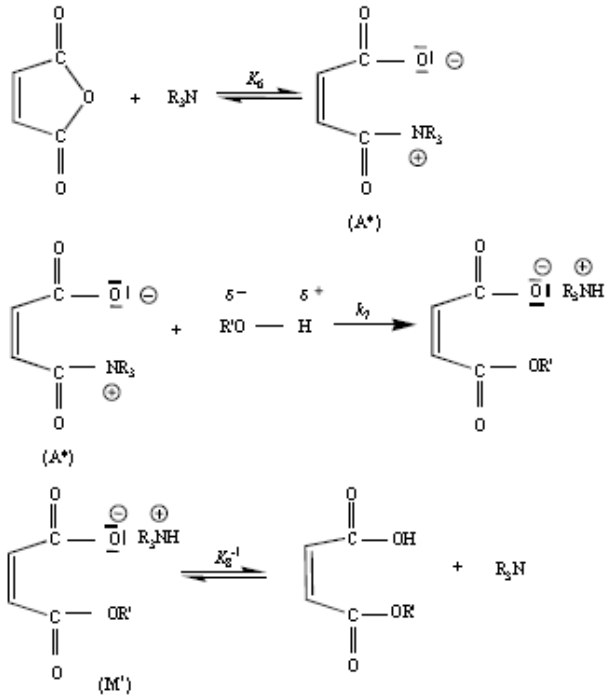

Figure 3-9 Proposed initiation step via catalytic reaction of alcoholysis [reprinted from 152]

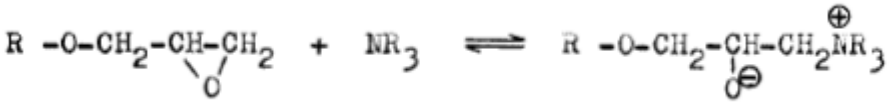

Figure 3-10 Proposed initiation step by opening epoxy ring [reprinted from 154]

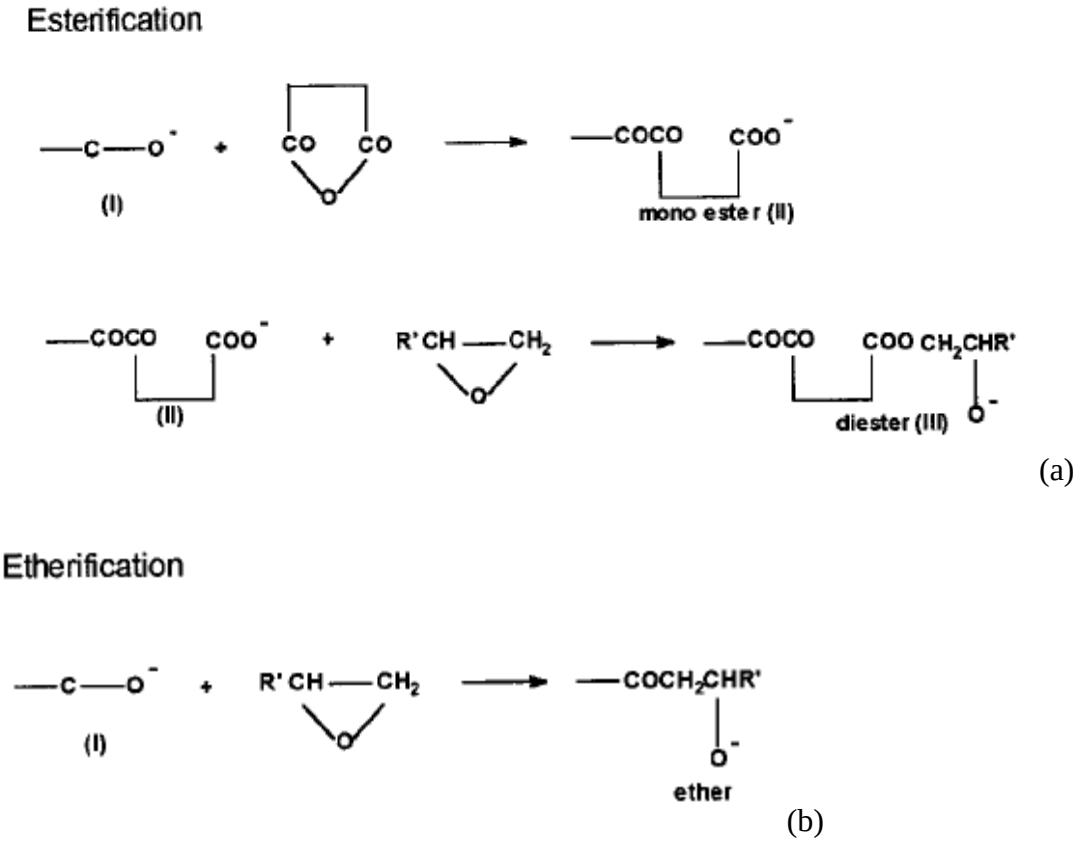

Figure 3-11 Propagation step including (a) esterification and (b) etherification [reprinted from 155]

3.2.3 Calculation of stoichiometric proportion

From the data sheets of the materials used, some important parameters can be derived as follows:

a. For the unfilled epoxy resin

- For the base epoxy resin, the average epoxy equivalent weight is EEW_{ave} = 1000/[(5.25+5.55)/2] = 185.185 g/mol.

- For the curing agent, the average molecular weight of the anhydride is MW = 178.1846 g

The anhydride equivalent weight is AEW = 178.1846 g/mol.

Based on the esterification mechanism which is favoured under the curing cycle used here, the ratio of the epoxy group to the anhydride group is close to 1:1.

Therefore, the amount of anhydride required to cure the epoxy is:

phr = (178.1846/185.185) * 100 = 96%

b. For a filled epoxy resin:

If Nanopox E 470 or the 3M system is added to the base epoxy resin, then the average epoxy equivalent weight of the mixture needs to be recalculated, because both Nanopox and 3M are silica reinforced epoxy resins with their own EEW.

The average EEW of the mixture is then calculated as follows:

$$EEW\ of\ mix = \frac{\sum_1^n W_n}{\sum_1^n \left(\frac{W_n}{EEW_n}\right)} \qquad Equation\ 3-1$$

where W_n and EEW_n are the weight and EEW of each component in the mixture.

According to the above calculation of the stoichiometric ratio for the unfilled epoxy resin, the ratio of the base resin to curing agent is 100: 96. However, the recommended ratio of the base resin to curing agent to accelerator by the supplier is 100: 80: 1. This means that the curing mechanism is not based only on esterification reactions. As mentioned in section III.2.2, etherification/homopolymerization reactions can occur simultaneously, especially at elevated temperatures. Therefore, the amount of curing agent required is reduced to obtain a chemical balance for the whole system. The optimum stoichiometry will provide good performance of the end products.

3.3 Sample preparation and experimental set-up

3.3.1 Sample preparation

Initially, the base epoxy resin, the hardener and the Nanopox E470 or 3M, as required, were warmed in an oven set to 65 ^{o}C for at least one hour to reduce their viscosity and, hence, ease mixing. The choice of 65 ^{o}C also provides the uncured epoxy system with a long pot life. Pot life is an important parameter for an uncured epoxy system in term of working life before the system becomes cured. This temperature must not be too high to avoid possible curing reactions during the mixing period.

The microscopic silica W12 EST was dried to remove physically adsorbed water. It is necessary to limit the moisture absorption as much as possible. At the moment, there is no paper which details the drying conditions of this type of micro-silica; Zhang and Stevens [156] dried nano-alumina powder at 130 ^{o}C for 4 hrs, whereas Rouyre [157] dried micro-silica powder at 130 ^{o}C for 24 hrs. The key point to note is that the micro-silica powder used here has been surface-modified, which may itself limit moisture absorption. In addition, according to the recommendations provided for this epoxy-anhydride system by the manufacturer, curing starts at 100 ^{o}C. Therefore, a temperature lower than 100 ^{o}C and a long drying time seem to be better to avoid the possibility of curing during the mixing period. The other point is that heating at a too high temperature will affect the surface functionalisation. As a result, the micro-silica was dried at 80 ^{o}C for 24 hrs.

The sample preparation processes were slightly different case by case, depending on whether it was an unfilled epoxy, a nanocomposite, a microcomposite, or a composite filled with both nano and micro silica. Nevertheless, in general, four main steps were used in the sample preparation process: mixing; degassing; casting; curing. Mixing involved using a mechanical stirrer, in combination with an ultrasonic water bath when preparing micro-composites, to obtain homogeneous mixtures. Once mixing was complete, all specimens were degassed at 65 ^{o}C at full vacuum until no new bubbles appeared. The degassing time always fell within the range 30-45 mins. After degassing, the mixtures can be considered free from bubbles. After that, the mixtures were cast into the pre-assembled moulds. Each mould is comprised of two steel plates, as shown in Figure 3-12. Due to the rigidity and crosslinked nature of the cured samples, a small amount of mould release agent QZ13 was applied to these plates prior to casting. The release agent was necessary to facilitate disassembly of the mould and sample after curing. However, in order to avoid unexpected effects on the chemistry of the samples, only an extremely small amount of QZ13 was employed. The thickness of the final sheet was controlled using Melinex spacers sandwiched between the two plates. Once assembled, the mould was closed but with two ports open on the top plate. The epoxy was poured into one side of the mould, which was tilted at an angle of about 30^{o}. The resin reached the other side due to gravity. Therefore, it was important to warm up the epoxy and the mould to retain a suitably low viscosity. The resin was initially at 65 ^{o}C, while the mould was often pre-heated to 80 ^{o}C prior to casting, due to the higher

thermal conductivity of metal compared with the epoxy. Then, the whole system was degassed again for about 15 mins until no new bubbles were observed. A four step curing cycle that is recommended by the supplier was finally used: 6h at 100 ^{o}C; 12h at 135 ^{o}C; 3h at 160 ^{o}C; the cured samples were finally allowed to cool slowly to ambient temperature within the oven before being removed from the mould.

Figure 3-12 The mould assemble for casting

For the treeing experiment, the standard mixing and degassing procedures were applied, as mentioned above. The liquid mixture then was cast into a block mould. An Ogura needle of pin tip radius 5 μm was slowly inserted into the mixture to obtain a pin to earth plane separation of ~ 2 mm. The whole system was degassed again to ensure no new bubbles prior to applying the curing cycle used above. After curing, treeing samples of pin-plane configuration were cut to the required size (6x10x15 mm).

3.3.2 Preliminary study on preparation conditions and sample quality

The unfilled epoxy resins were prepared by mixing the base resin with the anhydride hardener and the accelerator, in the required ratios, using a mechanical stirrer. The mixing time is an important factor, which determines the homogeneity of the mixture. Therefore, some experiments were conducted to optimise this parameter. Samples with different stoichiometric ratios were prepared under various mixing conditions, i.e. mixing time, as shown in Table 3-5. Here, and elsewhere, the compositions are specified relative to 100 parts by mass of resin, such that a system containing 100 parts of resin plus 70 parts of hardener plus one part of accelerator is designated 100:70:1.

Clearly, the Nanopox E470 or 3M contains both nanosilica and epoxy components; the resin component from this source has been included within the specified 100 parts of resin. To determine the appropriate mixing condition, the samples were characterised to evaluate their properties. Here, the thermal and electrical properties were chosen to be the standards for the comparison and evaluation of mixing effects.

Table 3-5 List of unfilled epoxy resin samples under preliminary study

Sample code	Stoichiometric ratio	Mixing time (mins)
Ep70-15	100:70:1	15
Ep70-30	100:70:1	30
Ep70-45	100:70:1	45
Ep80-15	100:80:1	15
Ep80-30	100:80:1	30
Ep80-45	100:80:1	45
Ep90-15	100:90:1	15
Ep90-30	100:90:1	30
Ep90-45	100:90:1	45
Ep100-15	100:100:1	15
Ep100-30	100:100:1	30
Ep100-45	100:100:1	45

3.3.2.1 Thermal characterisation - The glass transition and enthalpy relaxation

3.3.2.1.1 Experimental set-up

The samples were characterised using DSC. The equipment set-up is shown in Figure 3-13. The glass transition temperature (T_g) in this study was measured using a Perkin-Elmer DSC7 differential scanning calorimeter (DSC) operating with *Pyris* software; all samples were sealed into aluminium cans.

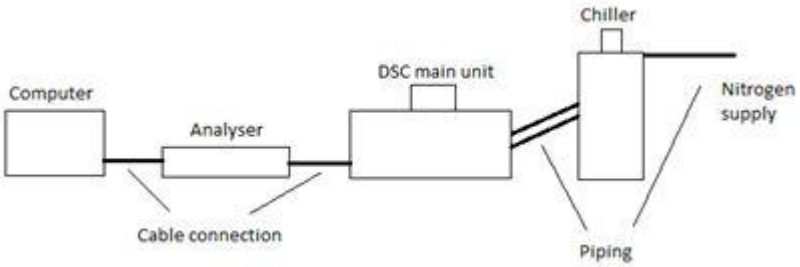

Figure 3-13 Basic set-up of DSC

The usual calibration procedure of DSC for the temperature axis, using high purity indium (the melting temperature: T_m= 156.60 ^{o}C), was followed prior to the experiments. The calibration was conducted at the same heating rate of 10 K/min as in all other runs. A water bath was used for the cooling system. Baseline correction was also applied to all the experiments described in this project. Prior to performing DSC scans of the cured epoxy samples, baseline data were collected by running a scan using an empty can of similar mass to the reference one, in the same fashion as for experiments involving epoxy-based samples. The DSC scans of epoxy-based samples comprised of three steps. First, each sample was held at 50 ^{o}C for 1 min to reduce thermal history effects. Next, a scan from 50 ^{o}C to 200 ^{o}C was conducted at the heating rate of 10 K/min. Finally, the sample was cooled down to 50 ^{o}C. In order to remove enthalpy relaxation effects, two successive scans were performed for each sample. The baseline data were then subtracted from the second scan to remove the heat capacity of the metal cans as well as other background effects. The resultant output was the heat flow and thermal characteristics of the sample. All DSC data were then further normalised, i.e. the data divided by the sample weight and the heating rate, to enable meaningful comparisons between samples. The final T_g value was determined as the mid-point of the step change in the heat flow of the normalised data.

3.3.2.1.2 Enthalpy relaxation

Figure 3-14 presents DSC heat-flow diagrams of the two successive scans for a selection of representative samples. From this, it is evident that there are differences in the heat flow diagrams from the two successive DSC scans for all the samples shown. Specially, there is an endothermic peak superimposed on the glass transition in all first runs. These endothermic peaks are ascribed to enthalpy relaxation effects, which are

also described as physical ageing [73, 158]. In addition, it is likely that the glass transition moves slightly to higher temperature upon the second scan. This suggests that post-curing occurs, leading to additional crosslinking between 150 ^{o}C and 200 ^{o}C.

Physical ageing is a structural relaxation that occurs in glassy materials. When an epoxy resin is cured, the T_g of the system increases as a result of an increase in the crosslinking degree. When T_g reaches the curing temperature, the material vitrifies. At this point, there is a physical transformation from a liquid/rubbery state to a glassy state. However, the formed glassy epoxies are in a non-equilibrium state. After curing, the samples are usually cooled down to a specific temperature for storage, e.g. the ambient temperature in this project, which can also considered as an ageing temperature, T_a, where they gradually undergo relaxation processes and approach the equilibrium state associated with the relevant molecular rearrangement. The presence of a peak after ageing at a given storage temperature reveals that some conformational motions are still possible even at temperatures much lower than the glass transition temperature.

A non-equilibrium glassy polymer possesses physical properties with higher values of enthalpy, entropy, specific volume or mechanical strength than its equilibrium state [73, 158]. Thus, it is natural that these qualities gradually approach their equilibrium values during physical ageing. Enthalpy relaxation is the physical ageing which involves changes in enthalpy *H*. During ageing, the enthalpy of the material decreases from the initial non-equilibrium value towards the equilibrium one. However, in the glassy state, the molecular mobility of the material is severely limited. Thus, enthalpy becomes nearly constant after a long period of storage. The material is then said to be in a metastable equilibrium state. When the aged material is heated up again, its molecular mobility increases and the material can reassume its equilibrium enthalpy. If the enthalpy recovery happens below T_g, it leads to a *sub-*T_g endothermic peak. Conversely, if enthalpy recovery occurs in the vicinity of T_g, a T_g*-overshoot* endothermic peak will be superimposed on the glass transition. It is worthy of note that due to the high mobility of the polymer chains, a material in the rubbery state is likely always to be close to its equilibrium state. This is the reason why the second DSC scans give heat flow diagrams without any endothermic peaks. The position and magnitude of enthalpy recovery peaks depend on the history of ageing, i.e. the ageing time and the ageing

temperature. A more comprehensive description and study of enthalpy relaxation can be found elsewhere [159-161].

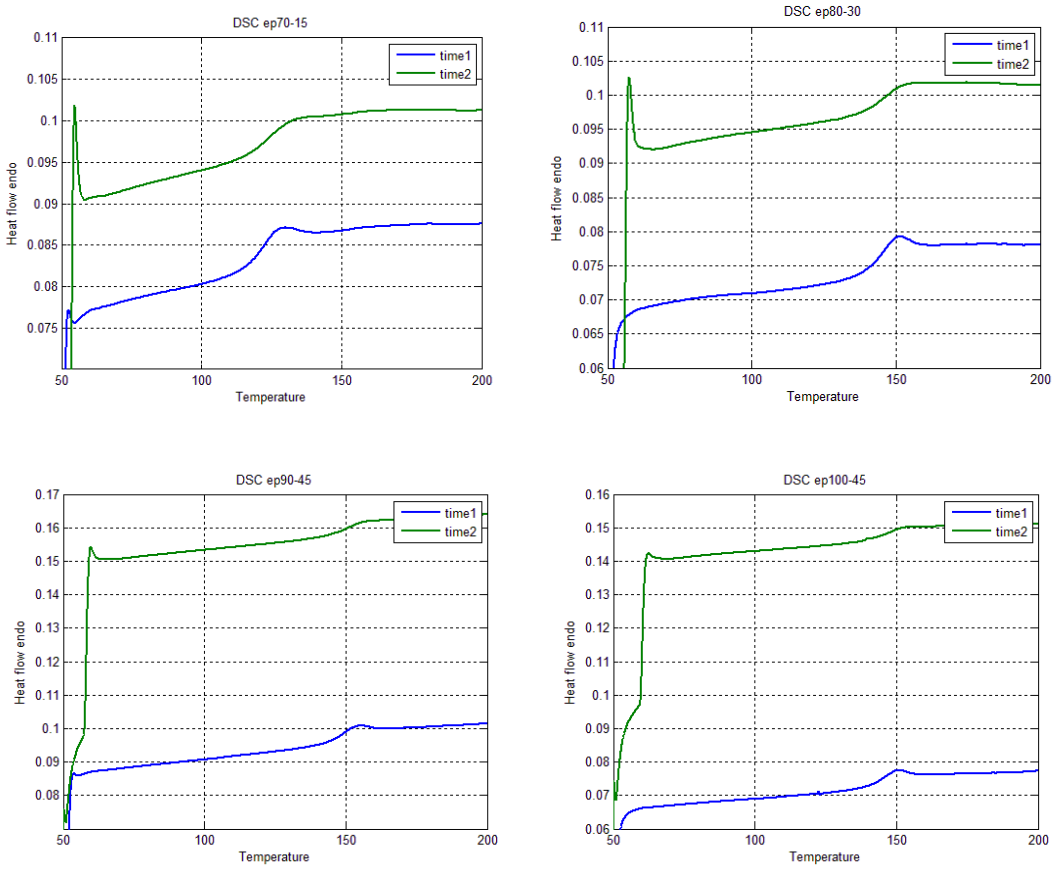

Figure 3-14 Typical DSC scans of unfilled epoxy samples (the traces are off-set)

In this project, the ageing temperature of all samples was kept nearly the same, i.e. at ambient temperature, which is much lower than their glass transition temperatures. In this case, when the ageing time increases, the endothermic peaks move to higher temperatures and their magnitude increases as well.

3.3.2.1.3 The glass transition temperature

Figure 3-15 shows DSC thermograms taken during the second scans of three samples mixed for different times. Here and elsewhere, the value of T_g is obtained as the temperature corresponding to a mid-point of the step increase in the heat flow of a normalised DSC scan. Comparison of these reveals that there is no clear difference in the glass transition between the samples formulated with same stoichimetry, indicating that the mixing time does not exert a significant impact on the obtained values of T_g. In

addition, the results show a singular transition which means that the local environment contributing to the glass transition is homogeneous. In an inhomogeneous epoxy mixture, there will be some regions that contain a high concentration of curing agent, while others contain smaller amounts of hardener. Then, the cured sample will possess a heterogeneous structure, including regions of loosely and densely crosslinked networks. This would lead to a broadening of the glass transition temperature range.

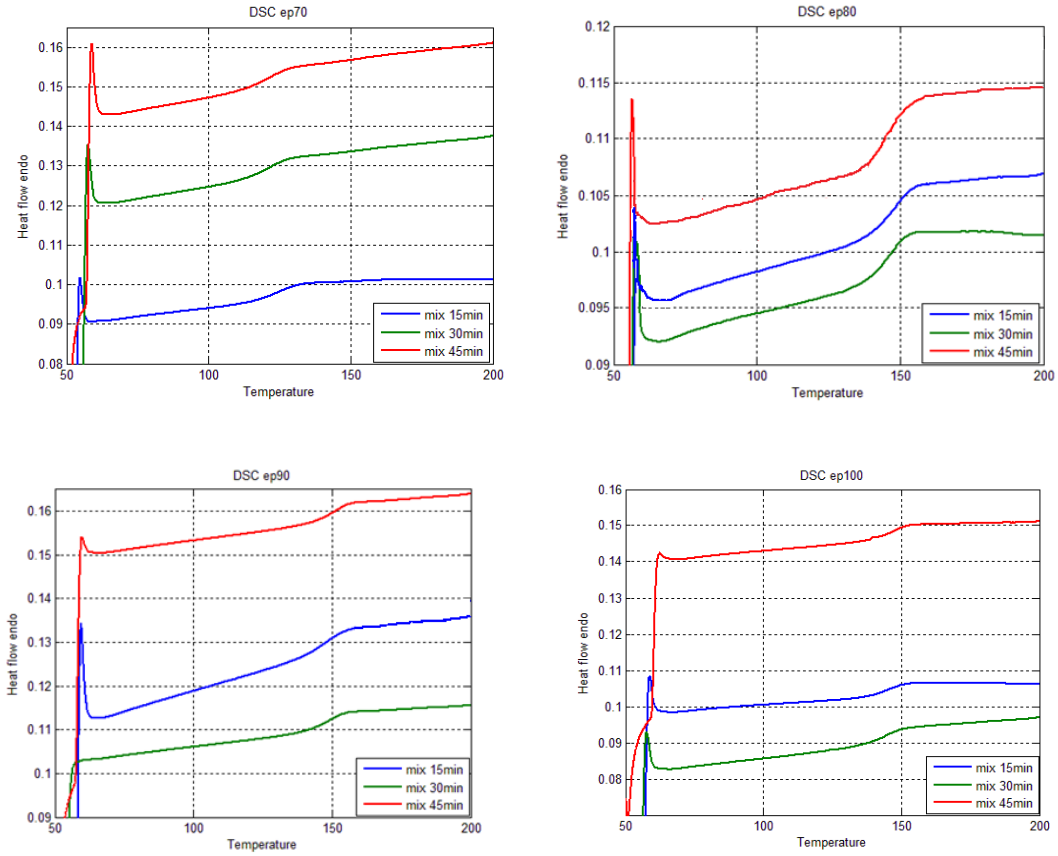

Figure 3-15 Typical DSC scans of unfilled epoxy samples for different resin/hardener ratios and different mixing times (the traces are off-set)

3.3.2.2 AC breakdown measurement

From the previous section, it would seem that a mixing time of 15 mins is likely to be effective in providing a good sample, since longer time periods did not introduce any change in T_g. However, the homogeneity of samples may not be inferred reliably from information about the glass transition. It is well known that ramp ac electrical breakdown testing can provide indirect information on the uniformity of samples and,

therefore, ac breakdown measurements were performed to evaluate the effectiveness of the imposed processing conditions.

3.3.2.2.1 Experimental set-up

AC electrical breakdown is a very common measurement, which is used to characterise the insulating properties of materials. Experimentally, this method is simple and involves the application of a linearly increasing ac voltage across the sample until failure occurs, where the failure voltage is recorded. It operates under ASTM D149-87 and IEC 60243-1 standards as well as other comparable international standards. The voltage ramp tests have the advantage of speed, but the data will be different from constant voltage tests. Although the test method used will affect the breakdown data, meaningful comparisons can still be achieved, provided that one testing method and geometry are applied throughout the whole investigation. Key parameters include ac test frequency, ramp rate, sample thickness and electrode configuration [162-163]. Breakdown strength measurements were made using a sphere/sphere electrode arrangement to avoid flashovers at the edges of the sample, as experienced with the plate-plate electrode geometry [164]. Provided that the radius of the curvature of the ball bearings is much larger than the sample thickness, then the electrode systems can be considered to be parallel plates. It is necessary to note that the electrode geometries affect the breakdown data [165-166]. Due to limitations on the voltage range of the equipment, thin film specimens ~ 70 μm in thickness were prepared for the unfilled epoxies and nanocomposites. The equipment set-up is shown in Figure 3-16. Ball bearings 6.3 mm in diameter were used as electrodes, allowing easy replacement before pitting could affect the obtained data. To avoid flashover, the sample and electrodes were fully immersed in silicone oil, which was replaced periodically to prevent contamination from affecting the results. An approximate 50 g load was applied to the upper electrode to avoid a film of oil between the ball bearing and the sample [137] and the lower electrode was connected to earth. An ac voltage applied to the upper electrode was increased at ~ 50 Vs^{-1} until failure occurred. However, for composites containing micro silica, specimens 500 μm in thickness were prepared since the size of the micro filler particles could be up to 100 μm. For those experiments, a Phenix Technologies Automated Dielectric Breakdown Test Set was employed. By utilising a Programmable Logic Controller controlled variable autotransformer, this equipment offers a

continuously varying 50 Hz output voltage from 5 kV up to 80 kV rms. The voltage applied to the sample was increased at an average of 50 Vs^{-1}, with the step voltage and dwell time set at 0.1 kV and 2 s respectively, until failure occurred. Due to such thick samples, ball bearings 16 mm in diameter were chosen and, consequently, large samples were required to avoid flashovers. The unfilled epoxies and nanocomposites usually have much higher breakdown strength than microcomposites and therefore, the use of thick samples was limited to microcomposites and only a few of unfilled epoxies and nanocomposites, for comparison.

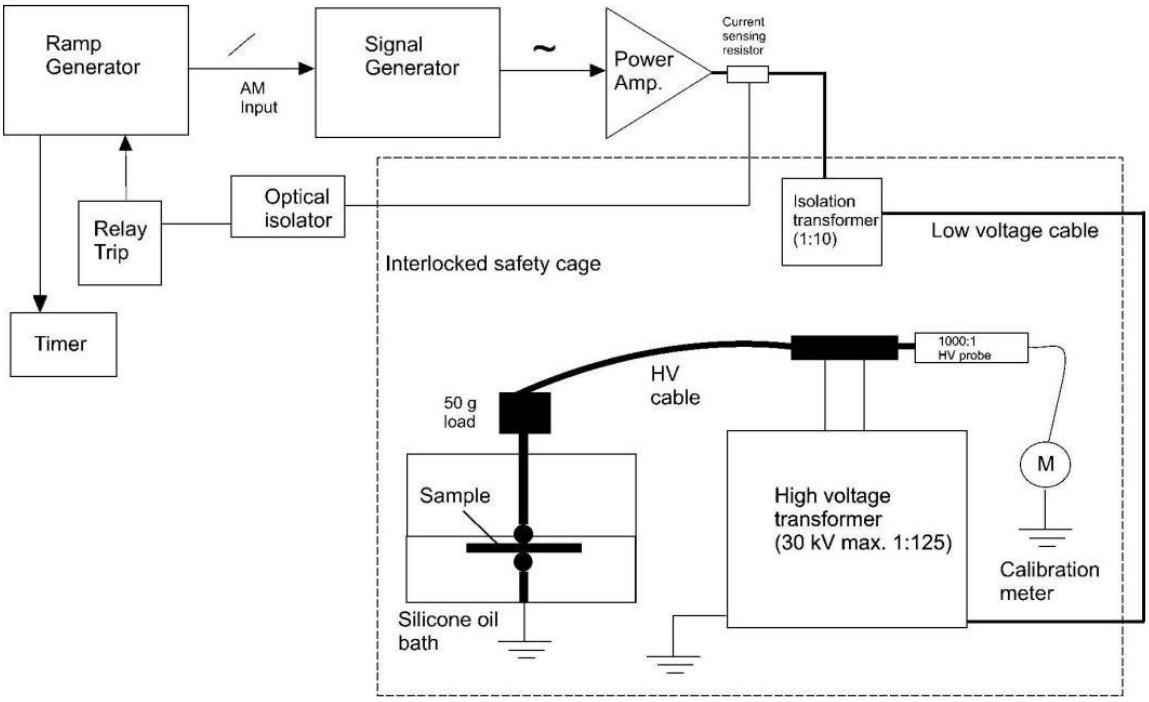

Figure 3-16 Schematic diagram of electrical breakdown equipment [reprinted from 167]

15-20 breakdown sites were chosen for each sample and the resulting data were analysed with Reliasoft Weibull 7++ software, using a two parameter Weibull distribution with 90 % maximum likelihood confidence bounds. Two sided bounds are used to indicate that the quantity of interest is contained within the bounds with a specific confidence [168]. The upper and lower confidence bounds provide more accurate method to analyse the variation in breakdown data of a set of samples [169]. Confidence bounds have been widely applied for breakdown analysis, such as by Vaughan et al. [170] and Mann et al. [171]. There are two types of confidence bounds,

including Fisher matrix and maximum likelihood. In this study, the maximum likelihood bounds were used. All measurements were conducted at room temperature and the ambient temperature during each set of tests was recorded, since the dielectric strength is significantly affected by temperature [172].

3.3.2.2.2 AC breakdown strength data

Figure 3-17 contains Weibull plots for all the samples under investigation. Unlike the glass transition temperature, breakdown measurements reveal a clear dependence of a key sample property on mixing time. For all stoichiometric ratios, it is clearly shown that there is a slight improvement in the breakdown parameters, α and β, upon increasing the mixing time, although no significant difference is observed statistically at 90% confidence limit. In other words, longer mixing times are likely to produce samples with higher breakdown strength and better uniformity.

In conclusion, based on the preliminary study on thermal and electrical properties, a mixing time of 45 mins was chosen as a standard processing condition for the unfilled epoxies used in this project.

In addition, experiments were conducted to determine the effects of sonication on the homogeneity of the samples. The unfilled system of 100:80:1 was chosen for the study. After mixing for 45 min, the resin mixture was sonicated for various periods of time, including 15 min, 30 min and 60 min using an ultrasonic water bath. Since the ac breakdown data could provide indirect information on sample quality, electrical characterisation was employed in this preliminary investigation. Figure 3-18 presents Weibull plots obtained for the samples under study. Obviously, there is no significant difference to be observed for all cases. This fact is confirmed in Figure 3-19, which compares the Weibull parameters obtained from the ac breakdown measurements of different samples. This suggests that the mixing conditions used are effective in producing homogeneous mixtures.

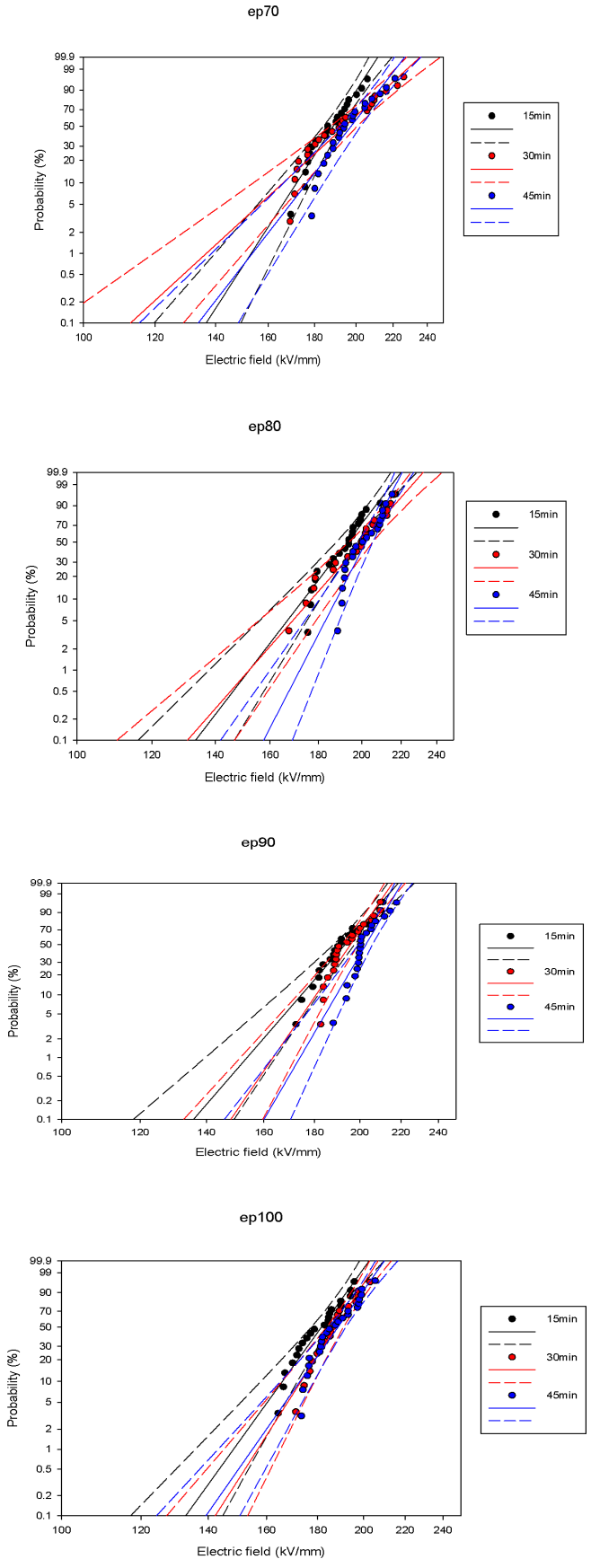

Figure 3-17 Weibull breakdown data obtained from a range of unfilled samples

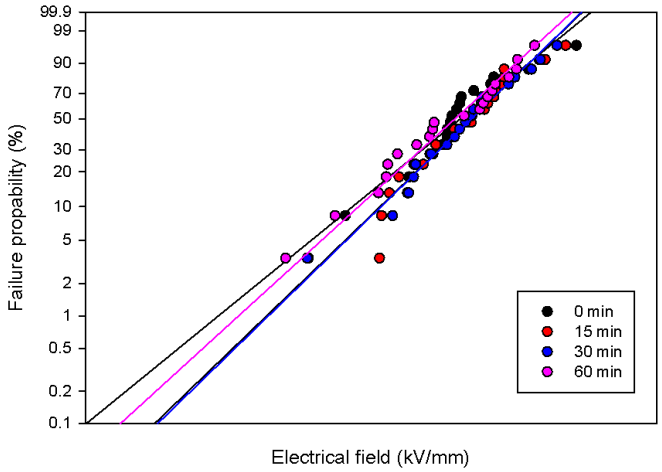

Figure 3-18 Weibull plots of AC electrical breakdown for unfilled samples of 100:80:1 resin ratio with different sonication times

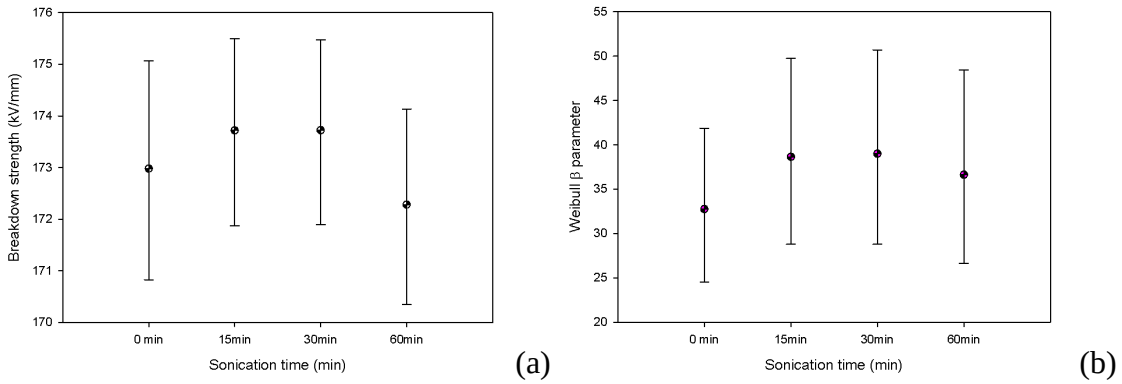

Figure 3-19 Comparison of Weibull parameters against sonication time: (a) scale parameter (b) shape parameter

Based on these preliminary studies, nanocomposites were prepared by mixing the base resin with the Nanopox or 3M system in the required proportions for 15 mins, before addition of the required quantity of hardener. This was then mixed for 30 mins to ensure the mixing time of 45 mins in total before, the accelerator was added and the complete resin mixture was stirred for another 30 mins. For composites containing a large amount of micro silica, after mixing the base resin with the Nanopox for 15 mins, the hardener and micro silica were added simultaneously. The mixture was then mixed for 15 mins by hand due to its extremely high viscosity, before using the mechanical stirrer for 30 mins. The mixture was then sonicated using the water bath for another 30 mins to

reduce the possibility of agglomeration of micro fillers. The accelerator was finally added and the mixture was mixed for another 30 mins to obtain a homogeneous system. All mixing processes were conducted at 65 ^{o}C.

3.3.3 Electrical tree growth measurement

To conduct studies of tree growth, a needle-plate electrode configuration was employed, since the resulting electric field enhancement at the needle tip reduces tree initiation times. Samples of pin-plane configuration were then immersed in a silicone oil bath and electrical trees were grown by applying an ac 50 Hz voltage between 10 to 25 kV rms to the pin tip until a tree of certain length formed or complete breakdown occurred. The plane electrode was kept at earth potential throughout. A schematic diagram of the treeing apparatus used can be seen in Figure 3-20. The initiation and propagation of electrical trees were monitored using a Prior Scientific Zoom 65 optical microscope equipped with a GXCAM-1.3 digital camera.

Prior to Raman analysis, samples containing electrical trees or breakdown channels were cut open using an RMC MT-7 ultra microtome equipped with a CR-21 cryo-system set at 0 ^{o}C. Confocal Raman microprobe spectra were collected with a Leica microscope coupled with a Renishaw Raman RM 1000 system; the exciting source was a 785 nm CW diode laser with a maximum output power of 25 mW. However, to minimise damage to tree structures [173-174], a laser power of 25 % was used. Samples were characterised at various positions around the tree/breakdown channels and all data were acquired using standard conditions of just 25 10 s extended scans between 3200 cm^{-1} and 100 cm^{-1}. After Raman analysis, sample surfaces were sputter coated with gold for SEM examination.

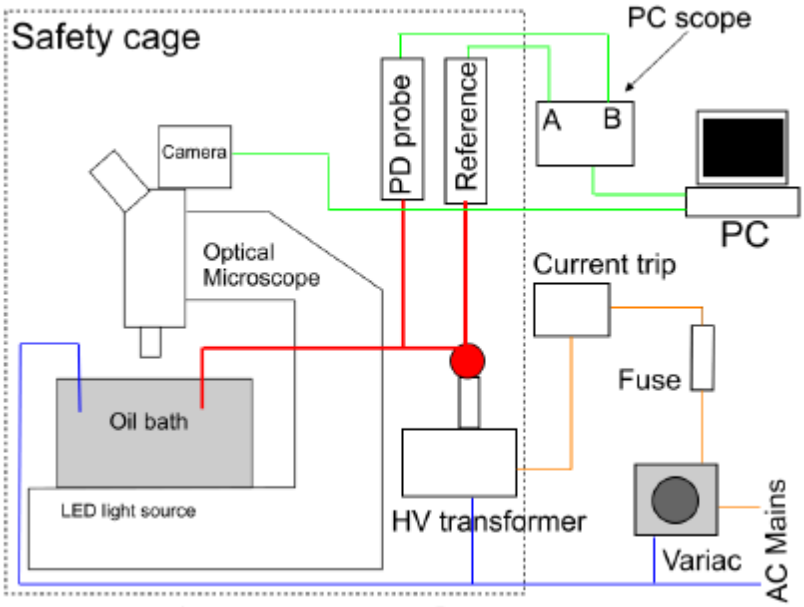

Figure 3-20 Schematic diagram of treeing apparatus [reprinted from 175]

3.3.4 Moisture absorption and drying of samples

Moisture absorption has been reported to be associated with epoxy resins and their composites [176-179]. Zhao and Li [180] reported a significant increase in dielectric constant as well as a dramatic decrease in mechanical properties with water absorption for alumina filled epoxy nanocomposites. Zou and Fothergill [47] studied the effect of water on the dielectric properties of epoxy nanocomposites. The work revealed a decrease in the glass transition temperature (T_g) by 20 ^{o}C when the huminity was increased to 100 %. It is well known that there are two kinds of moisture absorption, including physically and chemically bound water. Physically bound water involves molecules occupying network free volume or weakly attached to polymeric chains. These water molecules can be easily removed from the samples by heating for an appropriate period. Conversely, chemically bound water molecules may exist stably in an epoxy network due to their strong interaction with particular moieties. For example, for epoxy nanocomposites, there is always a certain number of hydroxyl groups located along the molecular chain. These hydroxyl groups can form hydrogen bonds with water molecules. This bonding is so strong that water molecules cannot be removed by only heating, even at 200 ^{o}C [181]. Although surface treatment of silica particles has been found to provide a considerable limitation on moisture adsorption [182-183], the presence of water molecules in epoxy resins is likely to be inevitable. It is necessary to

eliminate the effects of moisture absorption as much as possible to minimize the influence of any absorbed water on the observed behaviour.

After the curing cycle and cooling process, the samples were taken out of the moulds. Their weight was recorded. Then, the cured samples were dried at 65 ^{o}C at full vacuum for time slots of 12 hours. After each slot, the weight was recorded again. If the results showed a reduction in weight due to water loss, the drying process was continued until the weight became constant. Finally, after taking note of the weights, the dried samples were stored in desiccators with silica gel to avoid further moisture absorption. In general, the cured samples reached a constant weight after being dried at 65 ^{o}C for 2 weeks. Before conducting any characterisation experiments, the dried samples were weighed again to compare to their recorded values. If any weight change was observed, the samples were dried again.

3.3.5 Sputter coating of samples

In some characterisation experiments, such as dielectric spectroscopy, the samples needed to be coated with metal to provide good contacts between the material and electrodes. Gold sputter coating was chosen, because this is a cold coating method that does not affect the specimen. For this, an EMITECH K550X sputter coater was employed. The two opposing surfaces of each sample were initially covered by a mask of a specific diameter, so that only the desired area was gold coated. Each surface was coated at 25 mA for 3 min. The coating layer had a resistance of about 10 Ω [184].

3.3.6 Dielectric Spectroscopy

Dielectric spectroscopy provides a powerful tool for investigating a variety of dielectric processes as a function of frequency or time. It is based on the response of a dielectric to an applied electric field, and is often expressed in terms of permittivity or impedance. Unlike ac breakdown measurements, this is a non-destructive experimental method.

An SI 1260 impedance/gain-phase analyser connected to a 1296 Solartron Dielectric Interface was used in this study to provide dielectric data. To improve sample/electrode contacts, sheet samples, 460 μm in thickness, were first sputter coated with gold on both sides to a diameter of 24 mm, to match the test cell being used. Each sample was then mounted in the test cell, as shown in Figure 3-21. The test cell was enclosed in a

chamber, which was connected to a heater, to shield the sample from electrical noise. This configuration allowed temperature dependant behaviour to be investigated by controlling the voltage applied to the heater. Although a guard electrode system is efficient to eliminate surface currents, no guard ring was used due to limitations on the existing equipment.

The impedance software was employed to collect and analyse data. Although the manufacturers indicate that the maximum frequency range of this system ranges from 10^{-2} to 10^{6} Hz, in practice, the collected data became too noisy to be analysed at frequencies above 10^{5} Hz. Two measurement methods were available using this system; reference and normal. The reference method compares the dielectric response of the sample with the internal capacitor bridge and gives the best-fitted results. Alternatively, the normal method measures the dielectric data directly. The latter can be prone to errors relating to the capacitance of the cables, and as a consequence of the surrounding environment and therefore the reference method was used here to provide the required dielectric data. The real and imaginary relative permittivity, and tan delta curves were collected for all samples as a function of frequency at different temperatures up to 160 ^{0}C. Table 3-6 presents the parameters chosen for the dielectric spectroscopy experiments.

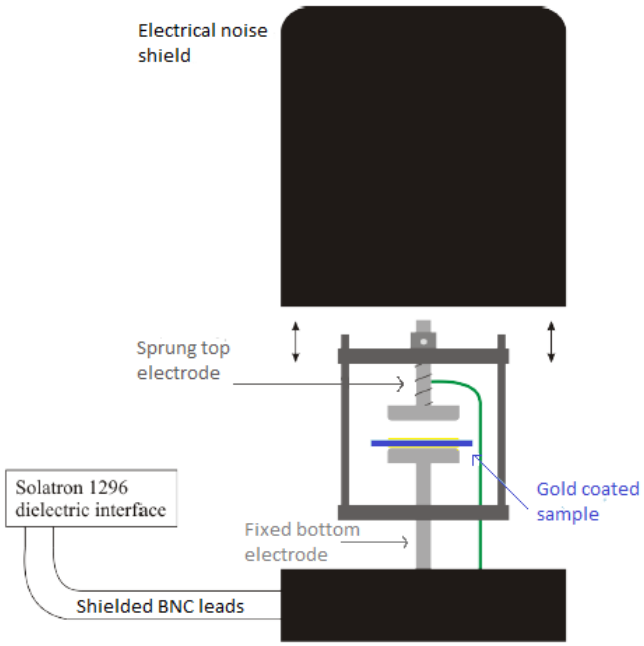

Figure 3-21 Schematic dielectric spectroscopy experiment set-up [185]

Table 3-6 Parameters used for the dielectric spectroscopy experiments

Parameter		Value or range	
Frequency		0.1* – 100,000 Hz	
AC	DC bias	4 V	0 V
Integration		V2 long**, max 50 cycles	
Sample dimension		Circular, 24 mm diameter	
Sample thickness		0.46 mm	

***Although the interfacial polarisation effects can be seen more clearly at lower frequency, i.e. 0.01 Hz, a lower frequency means a significant increase in the experimental time. The measurements were performed at high temperatures up to 160 ^{o}C. So, to avoid the possible material degradation, 0.1 Hz was chosen as the low frequency limit.**

****Auto integration averages the signals until the standard deviation reaches the target value of ± 1% of reading, ± 0.01% of full scale on analyzer for input voltage 2**

3.3.7 Space charge measurements

All space charge measurements in this study were conducted using a PEA system coupled with a user-defined acquisition and data processing LabVIEW program. The PEA setup consists of two electrodes and an enclosed polyvinylidene fluoride (PVDF) piezoelectric sensor and amplifier system, as shown in Figure 3-22. The top cylinder electrode is connected to a coupling capacitor and a resistor and all these components are embedded in epoxy insulation and surrounded by a thick copper wall to avoid flashovers. A thin layer 8 mm in diameter, of crosslinked polyethylene loaded with carbon black (semiconducting polymer or semicon) is attached to the top electrode. In practice, the use of semicon is to achieve a good acoustic wave transfer by matching acoustic impedance with the test dielectrics that should ideally be epoxy with this setup. However, due to limitations on the existing equipment in the lab, this setup was still applied to epoxy-based samples. The LV (ground) electrode is a 10 mm thick block of aluminium, to provide the signal with an acoustic time delay to reduce the interference with the oscillations from the pulse voltage. The flat sample is placed between the two electrodes and the bias dc voltage and pulse voltage are applied to it. The allowed maximum applied dc voltage is 10 kV. The pulse voltage operates at 400 Hz with a

maximum amplitude of 600 V and a duration of 2-5 ns. The acoustic wave induced by the pulse voltage is detected by a piezoelectric sensor in series with two amplifiers. The output electrical signal from the amplifiers is acquired and averaged at a sampling frequency of 2 GSs^{-1} by a digital oscilloscope. A very thin layer of silicone oil is placed on either side of the sample to minimize the reflection and attenuation of acoustic waves during propagation. In addition, an absorber is attached to the sensor to delay and suppress any acoustic reflection going back to the transducer.

An overshoot peak next to the peak that represents charges on the ground electrode, as shown in Figure 3-23(a), is usually observed in the PEA output signal. In practice, this overshoot peak is not the real charge density but a result of limitations in the frequency response of the transducer and amplifiers. Hence, a calibration process is important to transform the output signal to the charge density value and validate the quantitative charge evaluation. The calibration uses a deconvolution method to obtain the transfer function of the PEA system. More details about the theory and techniques involving the transfer function can be found in the literature [186-187]. Ideally, in a "clean" sample, if the PEA system is well constructed, the pulse voltage can be used as a calibration signal that avoids the production of bulk charges. However, in this case, the contribution to the output signal of the pulse voltage is neglected. Therefore, in the case of low dc applied voltage and high pulse voltage, it can cause a considerable error [124]. Moreover, if the PEA system is not well constructed, a poor response can occur, due to the system response and the penetration of outside noise. One solution to the problem is the application of a sufficiently low dc electric field, so that no bulk charge is produced. The electric field used for calibration needs to be determined carefully. If the electric field is too low, the resultant charge profile may be too noisy, while the use of higher electric field may produce charge injection into the sample. An example of the charge profile after calibration is shown in Figure 3-23(b).

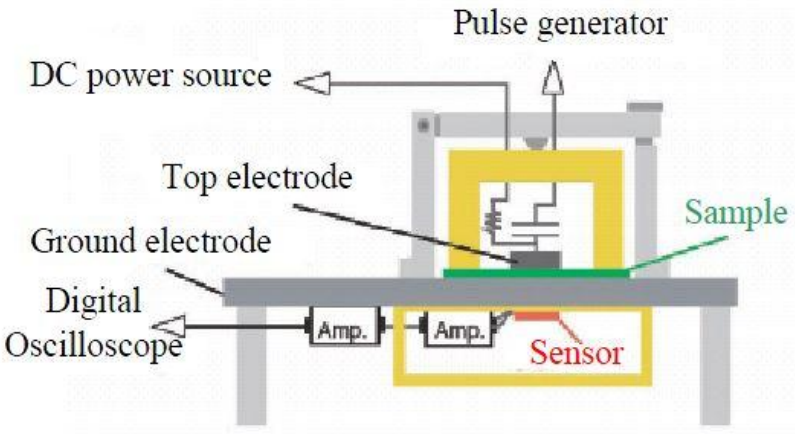

Figure 3-22 Diagram of the PEA set-up [reprinted from 188]

Previous studies on 200 μm thick LDPE samples have shown that homocharge is initiated in the samples at voltages greater than 3 kV dc [124, 189]. The signal measured at 2 kV, i.e. 10 kV/mm, has also been shown to give a good calibration for both XLPE and epoxy-based samples with no space charge build-up [190-192]. In this study, all samples for PEA were prepared to be ~ 220 μm in thickness and were examined prior to experiencing any applied fields, and, therefore, contained very small amount of bulk charge. Consequently, the above calibration method was employed at the applied dc field of 10 kV/mm prior to conducting measurements for each sample.

In the space charge mearsurements, a 600 V pulse voltage of 5 ns duration was applied to generate an acoustic wave. The samples were stressed at various dc electric fields at room temperature for 60 mins, after which the dc electric field was removed and the electrodes were short-circuited. Data were acquired throughout the poling period and for 60 mins of depolarization.

It is well-known that charge injection and trapping in polymers are significantly affected by temperature [193-194]. Therefore, care must be taken to control the experimental temperature. All measurements were conducted in the controlled environment at close to 20 ^{o}C.

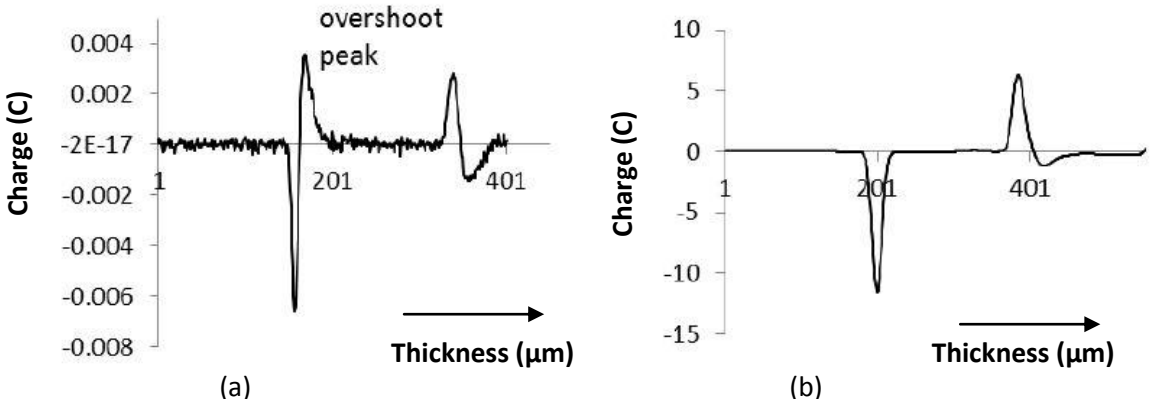

Figure 3-23 Charge profiles (a) from PEA output signal; (b) after calibration [188]

3.3.8 Fourier transform infrared spectroscopy (FTIR)

FTIR measurements were taken over the range 4000-500 cm^{-1} using a Nicolet 380 spectrometer. The FTIR data were collected using Omnic software. The sample holder arrangement is comprised of a circular crystal and a solid press tip, as shown in Figure 3-24. For each sample, 32 scans were run with the background spectra subtracted and then averaged to obtain a good signal to noise ratio. Increasing the number of scans allows the information collected by the instrument to be better differentiated from the noise randomly coming from the operation of the instrument. For solid or powder samples, a small amount of the sample was placed on the top of the circular crystal to cover the crystal completely. The black tip was used to press the powder. For liquid samples, a small amount of the sample was also used to cover the crystal completely. However, liquid samples did not require the solid press. After scanning, the data were collected in terms of transmittance and absorption as a function of wavenumbers.

Figure 3-24 FTIR sample holder

3.3.9 Scanning electron microscopy (SEM)

For SEM, cryo-fracture was employed to reveal an internal surface within each sample. The cured samples were cooled in liquid nitrogen for about 30 min before fracturing. After this, each sample was mounted on an aluminium SEM stub using doubled sided sticky tape and gold coated before being examined by a JSM 5910 SEM instrument using the JSM 5000 software. All samples were examined using an accelerating voltage of 15 kV with a spot size of 39 nm and a working distance between the samples and detector of 10 mm, since the larger the working distance, the worse the resolution. Although higher accelerating voltages and smaller spot sizes should improve the resolution, the resulting high energy/high intensity electron beam could damage the sample. This is a drawback of the SEM. Therefore, the working conditions chosen should be a compromise to provide as high a resolution as possible, without damaging the sample.

Chapter 4 Stoichiometry effects on epoxy resin and its nanocomposites

4.1 Introduction

It is well known that the chemical composition and physical structure of a material will determine its macroscopic properties. In epoxy-based systems, crosslinking reactions occur between the base resin, the curing agent and/or a catalyst and changes in the ratio of these reacting components will lead to different molecular architectures. Therefore, a detailed investigation into the relationship between the stoichiometry and material properties is crucial. Unlike for amine-cured epoxies, where the optimum stoichiometric formulation can be defined based on amine and epoxy group concentrations, complicated competitive chemical reactions occur in anhydride-cured epoxy system and, consequently, a more empirical approach is required. Although anhydride curing is thought to be mainly based on an esterification reaction initiated by the catalyst, competing etherification reactions or homopolymerisation of epoxy monomers via hydroxyl groups can also occur, which are favoured at high temperatures [5, 155]. Due to the complex and competitive curing reactions, a study of the effect of stoichiometry on epoxies and their nanocomposites can be considered as the basis for a more advanced investigation. The optimum stoichiometry is expected to provide a chemical balance in the curing system.

Although stoichiometry is not a new topic to material science, published papers on this subject have concentrated on its effects on the glass transition and the mechanical properties of the resulting materials. For example, Wingard and Beatty [195] found that the glass transition temperature and the secondary glass transition temperature were affected by non-stoichiometric curing. In the work of McCullough et al. [196], a small variation in stoichiometry led to a significant change in the elastic modulus and glass transition temperature of epoxy resins. Adachi et al. [197] investigated the effect of non-stoichiometric curing on the dynamic mechanical properties of a bisphenol A-type epoxy resin and found that the stress after yielding reduced rapidly in epoxy resins with

a lower crosslinking density and at higher strain rate. The investigation described here is to address not only the thermal but also the electrical and dielectric properties of anhydride-cured epoxies and their nanocomposites.

4.2 Samples under investigation

In order to concentrate on the stoichiometric effect, the same loading level of nano-particles was applied to all the epoxy systems under investigation, to minimise effects associated with interfacial percentages. For the purpose of comparison, unfilled epoxies with different resin ratios and the corresponding nanocomposites filled with 5 % nano-silica were prepared using the Nanopox masterbatch system. Table 4-1 lists the samples used in this investigation. The ratios specified include the resin component of the Nanopox.

Table 4-1 List of samples under stoichiometry study

Sample codes	Stoichiometric resin ratio	% nano-silica (Nanopox)
Ep40	100:40:1	0
Ep50	100:50:1	0
Ep60	100:60:1	0
Ep70	100:70:1	0
Ep80	100:80:1	0
Ep90	100:90:1	0
Ep100	100:100:1	0
Pox40-5	100:40:1	5
Pox50-5	100:50:1	5
Pox60-5	100:60:1	5
Pox70-5	100:70:1	5
Pox80-5	100:80:1	5
Pox90-5	100:90:1	5
Pox100-5	100:100:1	5

4.3 Fourier Transform Infrared Spectroscopy

Mid infrared spectroscopy has been widely employed to characterise various organic compounds and many spectral libraries have been developed [198-199]. This technique has been considered to provide reliable information not only qualitatively but also quantitatively. Although there are some limitations on the application of this technique to epoxy systems, due to the location and intensity of the oxirane ring absorptions in the IR region, it is still the most commonly used method to detect the epoxy group. In general, in the mid IR range, which runs from 4000 to 400 cm^{-1}, there are two characteristic absorptions involving oxirane rings. The first one, at about 915 cm^{-1}, is attributed to the stretching of the C-O bond of the epoxy ring [200]. The second absorption occurs at around 3050 cm^{-1} and is ascribed to the stretching of the C-H of the methylene group of the oxirane ring [200]. Although the intensity of this band is low and is usually masked by the strong O-H absorptions nearby, it can still be used as a qualitative indicative of the presence of oxirane rings from the epoxy monomers and oligomers with a low degree of polymerisation. The IR spectra associated with the epoxy resins depends on their nature. Figure 4-1 shows the FTIR spectrum of the DGEBA-type resin used in this research, MY 740.

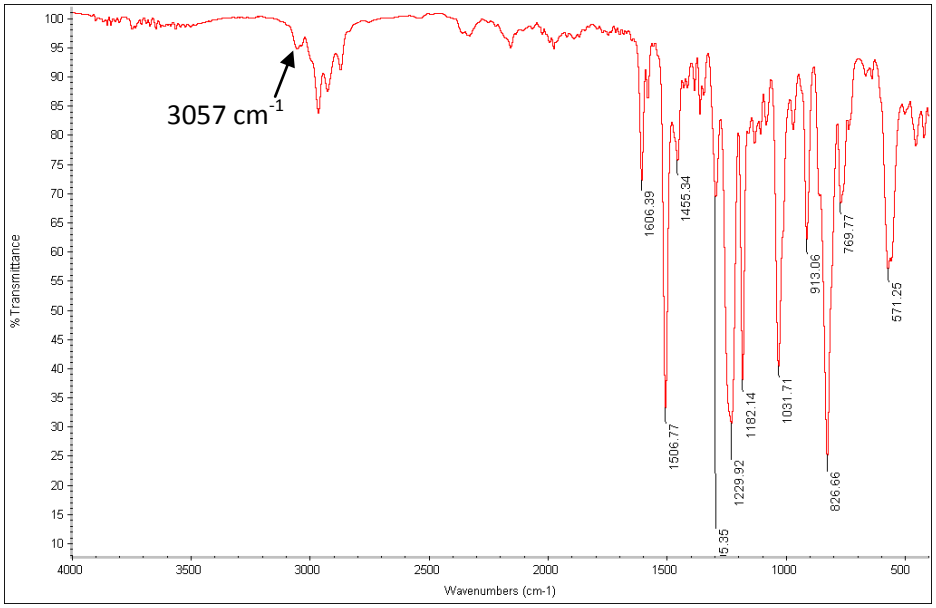

Figure 4-1FTIR spectrum of MY 740 in the mid range

It is clear from Figure 4-1 that the presence of epoxy groups is demonstrated by the sharp absorption peak at 913 cm^{-1} and the small peak located at about 3057 cm^{-1}. The presence of other C-O bonds due to ether linkages in the resin is evinced by peaks in the range of 1229-1031 cm^{-1}. The broad band located from 3800 to 3400 cm^{-1}, which is assigned to the stretching of the hydroxyl groups in the resin, reveals the presence of dimers or higher molecular weight components in the resin. Similar characteristic IR bands of other DGEBA-type resins have been reported elsewhere [199-203]. Table 4-2 summarises the main IR bands found in this resin.

Figure 4-2 shows the IR spectra of the host resin MY 740 and the Nanopox E 470. The main difference between the two resins is the presence of silica particles in the Nanopox, which introduces new chemical bonds into the molecular structure. The broad IR bands observed in the spectrum of the Nanopox E 470 around 1080 and 460 cm^{-1} are assigned to the stretching mode and the bending mode of Si-O-Si bonds respectively [204-205]. In addition, the broad peak in the range 3500-3200 cm^{-1} is, again, attributed to the intermolecular H-bonded OH groups.

During curing, the hardener also plays an important role, since the properties of the final product are determined by the chemical reactions between the hardener and the other components of the system. Therefore, it is necessary to characterise all reactive components present in the curing system. Figures 4-3 and 4-4 show IR spectra of the hardener HY 906 and the accelerator DY 073-1 respectively. The hardener HY 906 is a nadic methyl anhydride (NMA); the characteristic IR bands of the the C=O of the anhydride group can be observed at 1854 and 1770 cm^{-1}. These two bands with different intensities are characteristic of a cyclic, five-membered ring, and nonconjugated anhydride [206]. Other characteristic IR bands of the anhydride at 1220, 1077, 919 and 894 are assigned to the C-O of the anhydride group. The characteristic IR band for the accelerator DY 073-1, which is a tertiary amine, is at about 1280 cm^{-1} and is related to the stretching of the C-N [200]. Here and elsewhere, due to the background shift of the equipment, in some cases, such as in Figure 4-5, the transmittance percentage is greater than 100%. It suggests that the quantitative information is not reliable; only the qualitative information can be used for the analysis of chemical characteristics of materials. In addition, the absorption peaks in the range 2000-2300 cm^{-1}, as indicated by blue arrows in Figure 4-4, are ascribed to the carbon dioxide of the environment [207].

Table 4-2 Main characteristic IR bands of MY 740

Band (cm^{-1})	Assignment
3800-3400	O-H stretching
3057	Stretching of C-H o f the oxirane ring
2965-2873	Stretching of C-H present in aromatic and aliphatic
1606-1445	Aromatic C=C stretch
1229-1031	Stretching C-O of ethers
913	Stretching C-O of oxirane rings
826	Stretching C-O-C of oxirane rings
770	Rocking CH_2

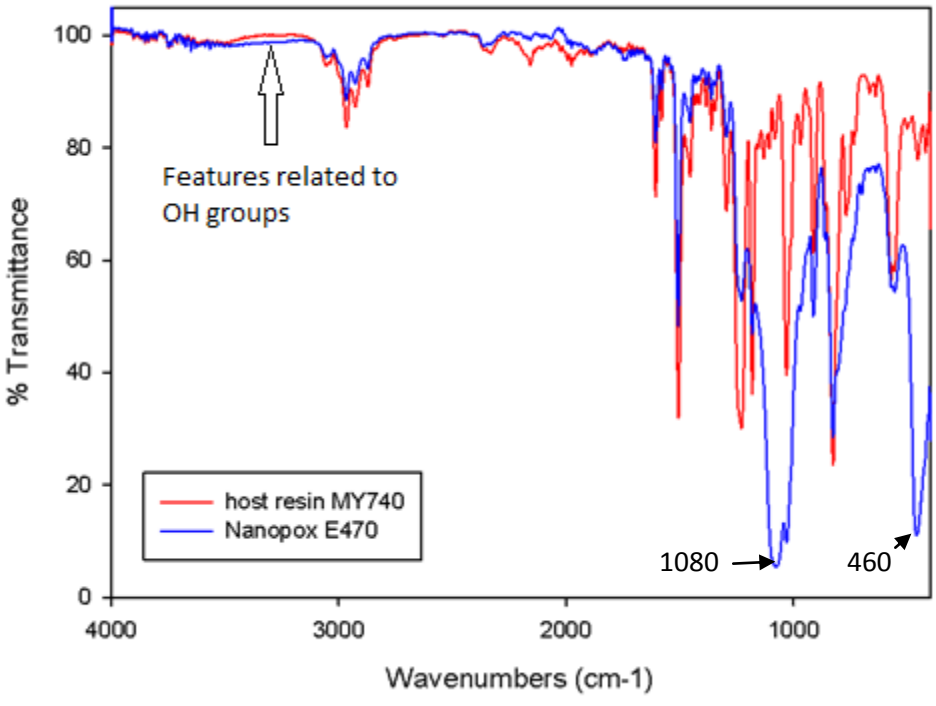

Figure 4-2 FTIR spectra of resin MY 740 and Nanopox E 470

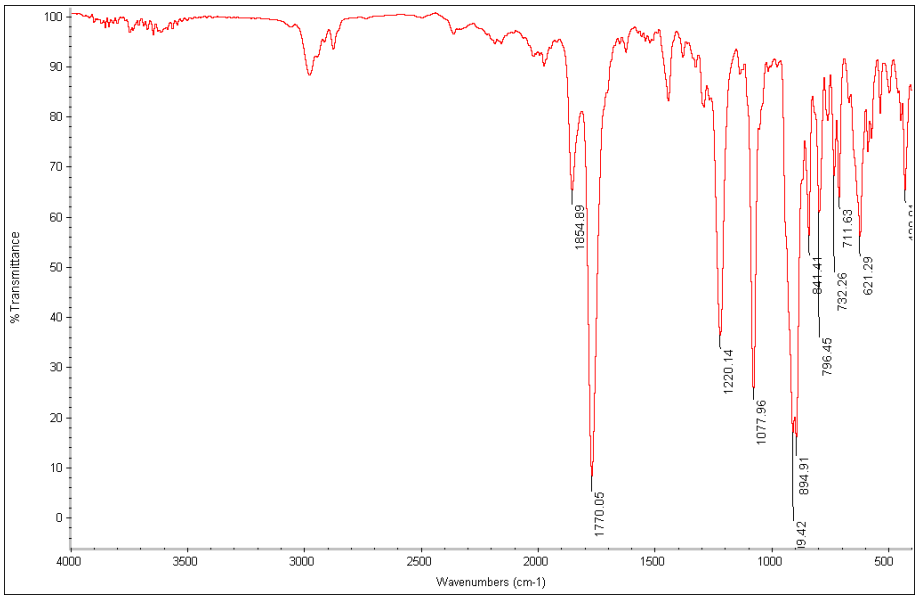

Figure 4-3 FTIR spectra of the hardener HY 906

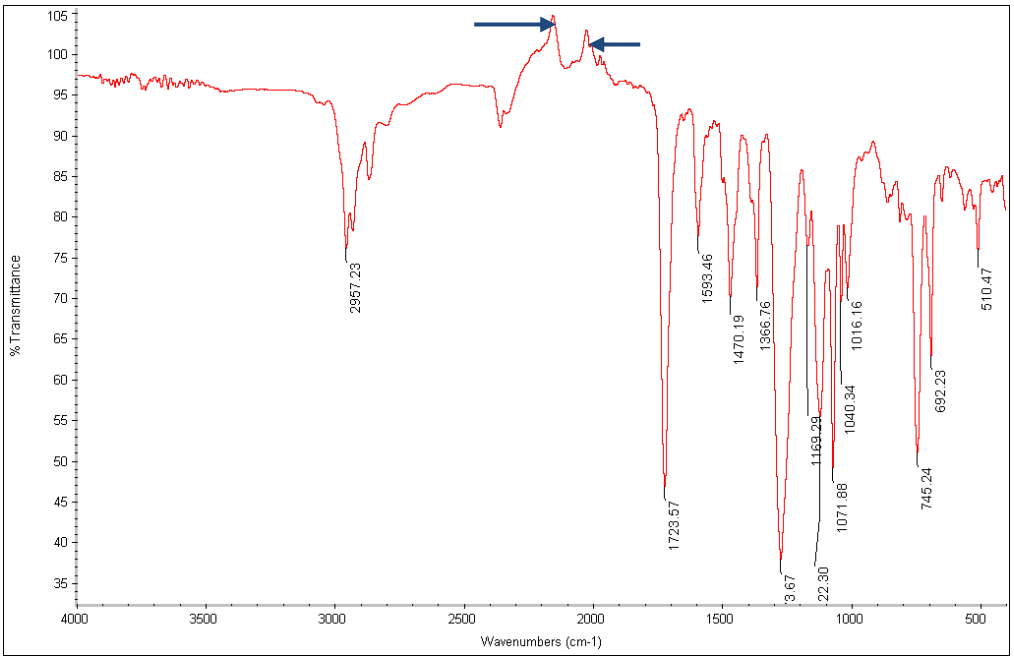

Figure 4-4 FTIR spectra of the accelerator DY 073-1

During the curing process, the associated chemical reactions result in changes in the concentration of the functional groups and introduce new chemical bonds. Figure 4-5 and Table 4-3 show the IR spectrum and some of the main characteristic IR bands of cured Ep80.

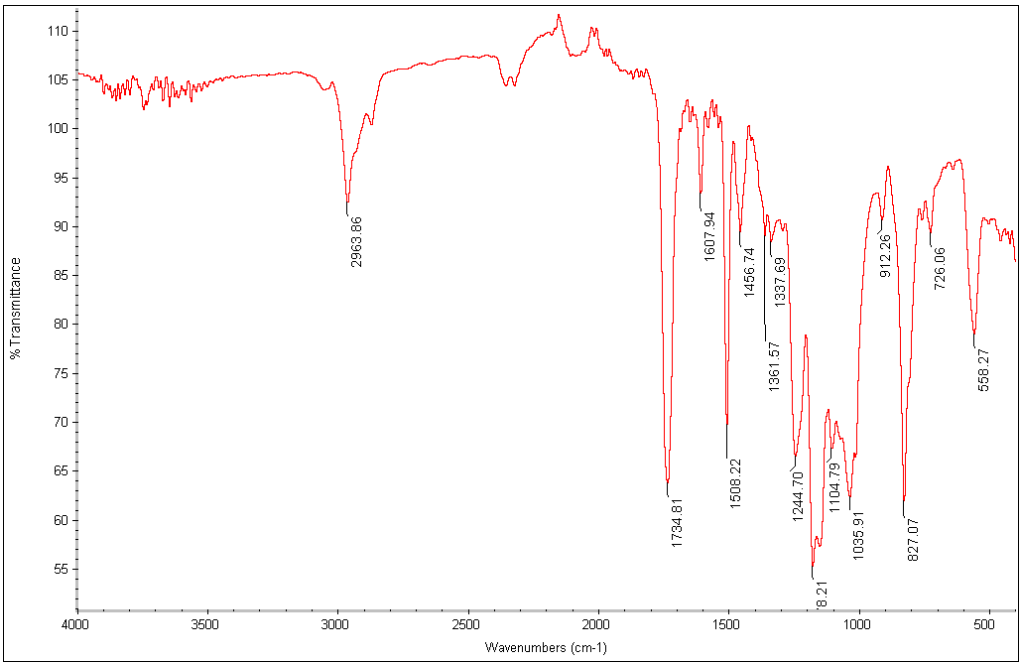

Figure 4-5 IR spectrum of cured Ep80

Table 4-3 Some main characteristic IR bands of cured Ep80

Band (cm^{-1})	**Assignment**
1734	C=O stretching of ester
1244-1035	Stretching C-O bonds
912	Stretching C-O of oxirane rings
827	Stretching C-O-C of oxirane rings

Figure 4-5 shows the FTIR spectrum of cured Ep80. From this, it is evident that the IR band at around 1734 cm^{-1} due to the C=O stretching is the result of the esterification reaction during the curing process. The peaks at 1244-1035 cm^{-1} are assigned to stretching of the ether linkages present in the epoxy resin, and the hardener, combined with any ether linkage formed by etherification reactions. It is difficult to distinguish them separately. In addition, the IR bands at 912 and 827 cm^{-1} reveal the presence of the

excess epoxy groups in the cured product. When the T_g of the product becomes higher, the molecular mobility is severely restricted and further reactions become diffusion controlled. Although the product was post-cured, it is difficult for all the epoxy and anhydride groups to diffuse towards each other, to enable esterification and/or etherification to occur to completion within the dense network. Therefore, a small amount of remnant epoxy groups remains in the cured product.

Figure 4-6 compares IR spectra obtained from cured Ep80 and cured Ep60, both of which contain excess epoxy. No marked differences in the IR spectra of Ep80 and Ep60 are evident, suggesting that the curing mechanism for both cases is comparable. It is likely that the concentration of the C=O of esters in Ep80 is higher than the one in Ep60, suggesting that a more densely crosslinked network is formed in Ep80. A higher amount of the epoxide groups in Ep60 may be attributed to the excess epoxy in the system. However, it is impossible to determine the fraction of C-O that results from etherification reactions. The quantitative information cannot be derived from these FTIR spectra, due to overlapping of the IR bands and the changes in the stoichiometric ratios. This fact can be seen more clearly in Figures 4-7 and 4-8. Figure 4-7 compares IR spectra obtained from Ep80 and Ep100. Ep100 contains an excess of anhydride and the peak at about 1780 cm^{-1} may therefore, be attributed to the C=O of the unreacted anhydride groups. This peak is observed in neither Ep80 nor Ep60. However, the increased absorption at about 1735 cm^{-1} in Ep100 contains contributions originating from the C=O in both the ester and anhydride groups; C=O stretching in anhydride groups always exhibits two bands [203]. Similarly, the increased intensities of IR bands in the range 1300-1000 cm^{-1} may be attributed to the higher concentrations of anhydride, ester groups, etc. The effect of the C=O of the unreacted anhydride groups on the IR spectrum can be seen more clearly in Figure 4-8, which compares spectra obtained from different cured epoxy systems all containing 5 wt% nanosilica. The absorption behaviour of the Si-O-Si bonds in the three systems can be assumed to be the same. However, the Pox100-5 system, which contains the excess anhydride, shows much higher absorption in the region ~ 1100-1110 cm^{-1} and at ~ 460 cm^{-1}. Therefore, it is difficult to derive quantitative information from IR spectra, due to overlapping of IR bands originating from the original reacting components and the background shift of the equipment.

Figures 4-9 to 4-11 show the effect of including 5 wt% of nanosilica within epoxy systems formulated with different resin stoichiometric ratios.

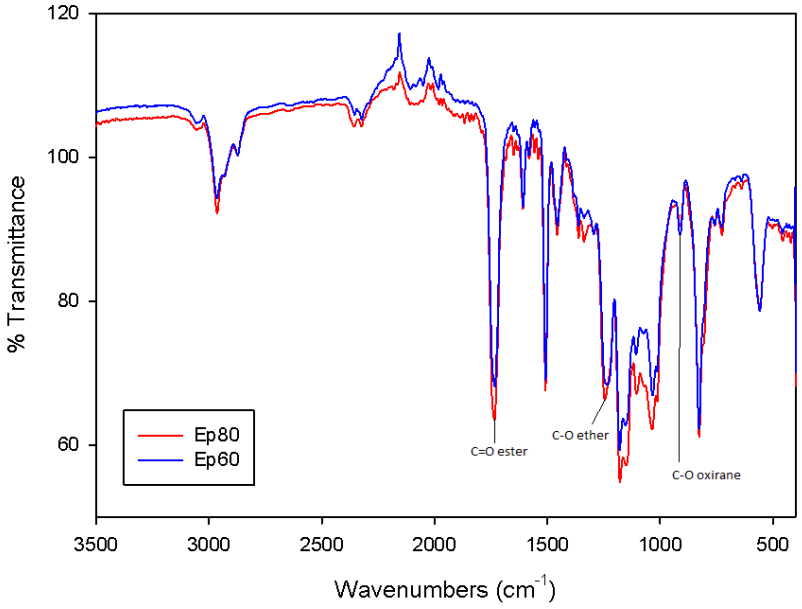

Figure 4-6 The IR spectra of Ep60 and Ep80

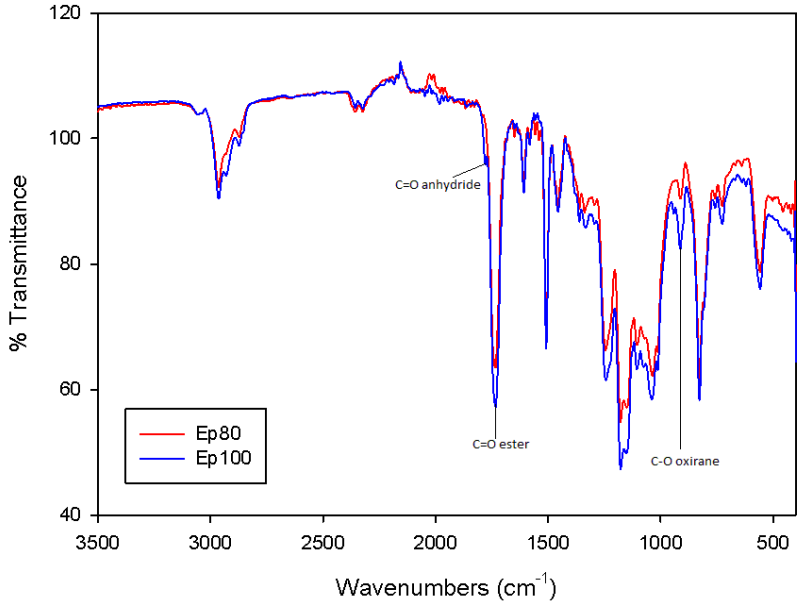

Figure 4-7 The IR spectra of Ep80 and Ep100

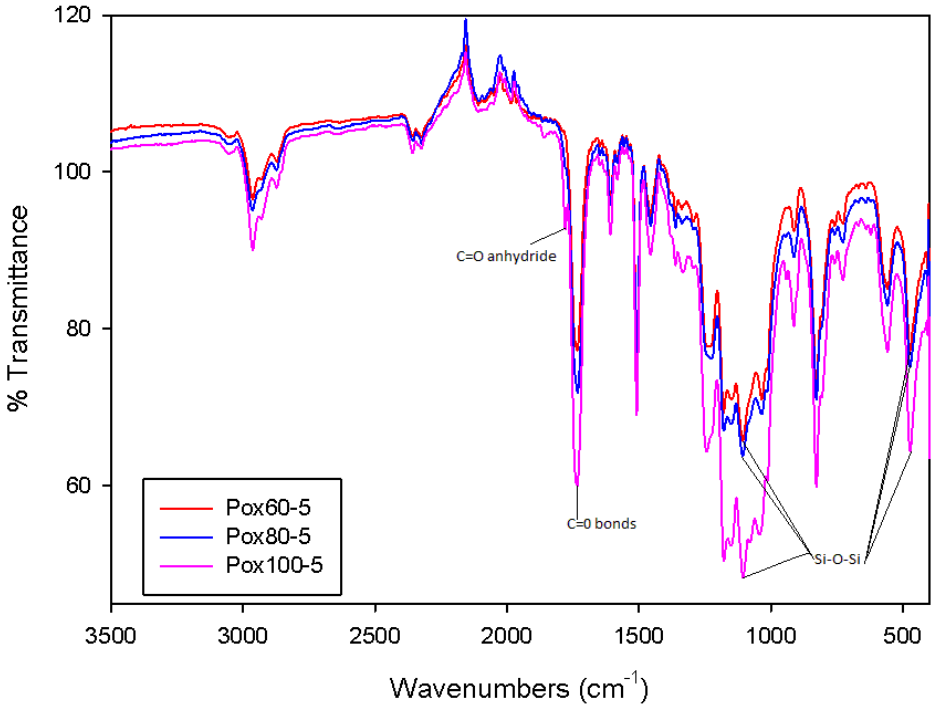

Figure 4-8 The IR spectra of epoxy systems containing 5 wt% nanosilica

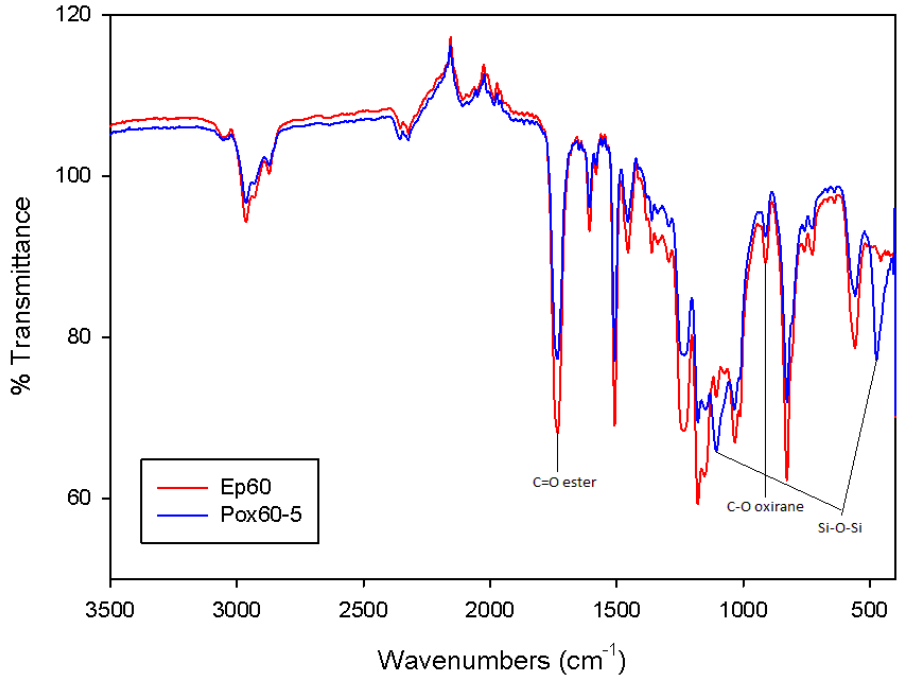

Figure 4-9 The IR spectra of epoxy system of 100:60:1 and its nanocomposite with 5 % nanosilica

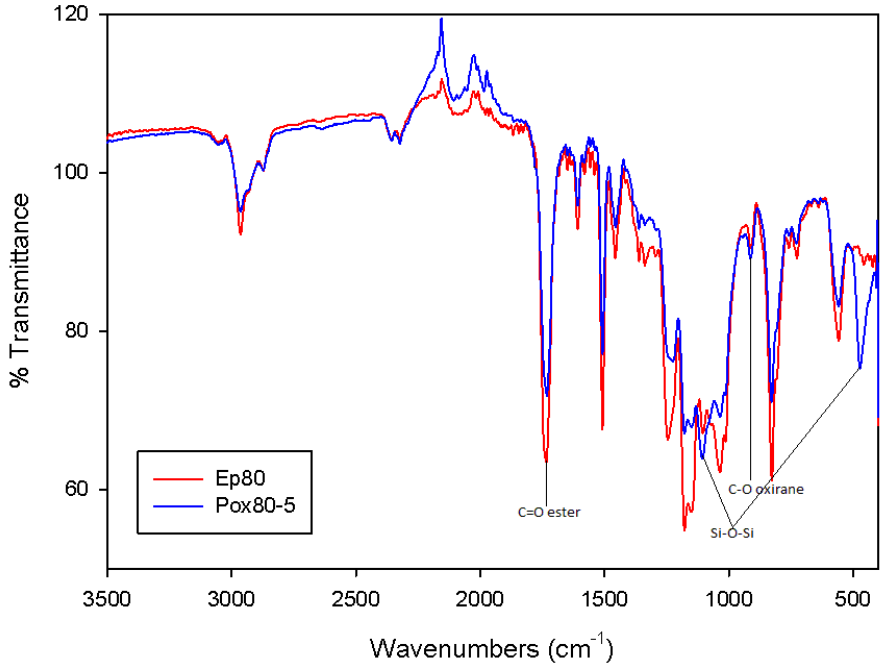

Figure 4-10 The IR spectra of epoxy system of 100:80:1 and its nanocomposite with 5 % nanosilica

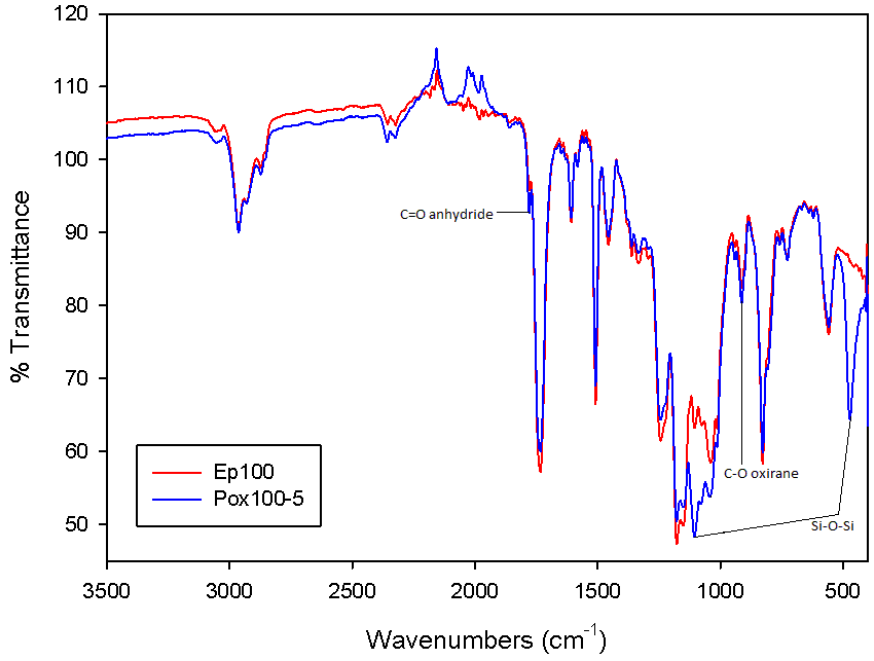

Figure 4-11 The IR spectra of epoxy system of 100:100:1 and its nanocomposite with 5 % nanosilica

From the above data, it is evident that the incorporation of nanosilica does not markedly affect the curing mechanism of the various systems. No new chemical bonds are observed within the FTIR spectra, except the Si-O-Si due to the nanosilica itself.

4.4 Scanning electron microscopy (SEM)

IR spectra can provide information about the chemical bonds present within materials, as well as effects associated with the introduction of nanosilica into the epoxy matrix in term of the changes in chemistry. However, IR spectroscopy does not reveal the dispersion of fillers in the polymer matrix. For nanocomposites, the dispersion of nanoparticles is believed to be a key factor in determining the macroscopic properties of the material [34-35, 37-38]. SEM has been widely used in the study of these materials. Although the spatial resolution obtained by the SEM cannot be compared to transmission electron microscopy (TEM), a major advantage of the SEM concerns ease of sample preparation and this has led to its widespread application. For SEM, the structure of bulk specimens of the order of millimetres in size, or larger, can be revealed using by cryo-fracturing. In contrast, sample preparation for TEM usually involves complex ultramicrotomy techniques.

Figures 4-12 (a)-(c) show low magnification images of fracture surfaces of unfilled epoxy systems with different stoichiometries. Elongated fractography features can be observed in all three unfilled epoxy specimens, but especially in the case of Ep100. Increasing the magnification reveals that the texture of the surface appears granular, as shown in Figures 4-13 (a)-(c). In general, there is no difference in the general appearance of the three systems, suggesting that the excess of anhydride groups does not affect the general matrix morphology. However, the addition of nanosilica introduces new features into the fracture surfaces. Figures 4-14 (a)-(c) present low magnification images of the surfaces of epoxy systems which contain 5 wt% nanosilica. Obviously, at this magnification, the topography of fracture surfaces in nanocomposites is different from those observed in the corresponding unfilled systems; a curved fractography feature is arrowed. A higher magnification again reveals the dramatic effects of the inclusion of nanosilica to the fracture surfaces. Figures 4-15 to 4-17 exhibit some representative images taken at various locations across the surfaces of specimens with different resin stoichiometry. If the presence of nanosilica is considered

to affect the topography of the fracture surfaces, it is reasonable to evaluate the uniformity of the dispersion based on the variability of the surface texture. It is obvious from the Figures 4-15 to 4-17 that the samples are relatively uniform at 5 %wt nanosilica loading level, although there are some variations in local concentration of nanosilica on the scale of tens to hundreds of micrometers.

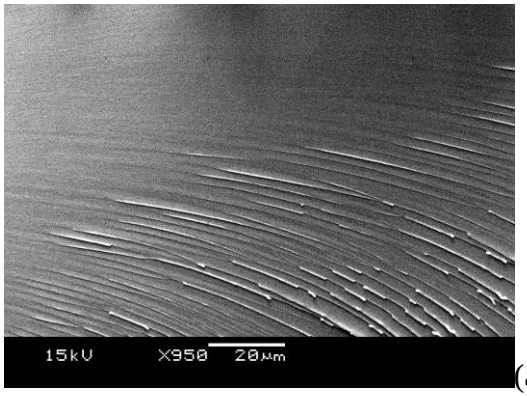

(a)

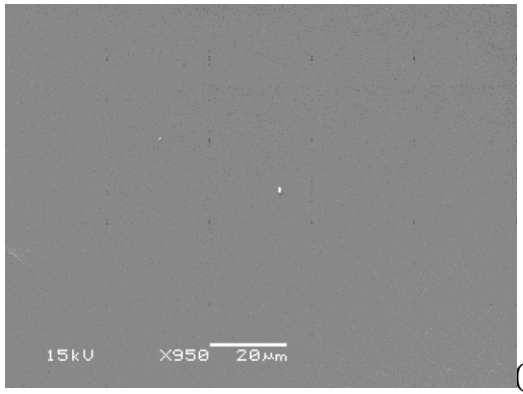

(b)

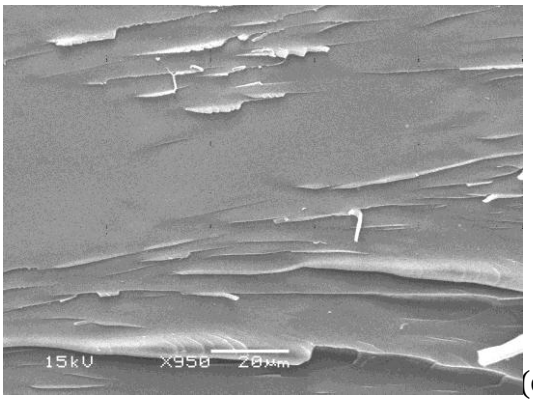

(c)

Figure 4-12 Low magnification images of unfilled (a) Ep60, (b) Ep80, (c) Ep100

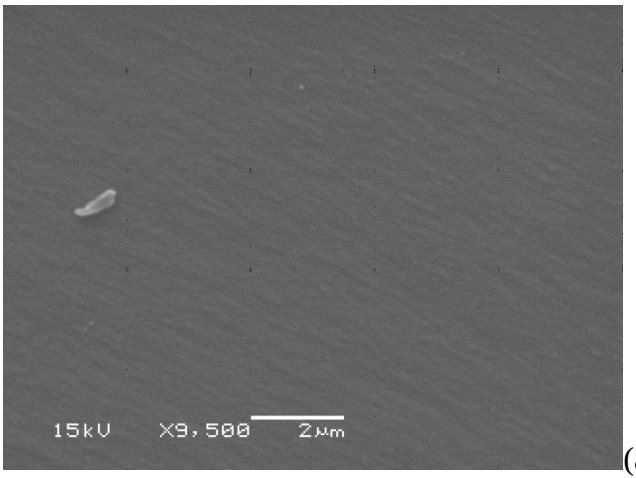

(a)

(b)

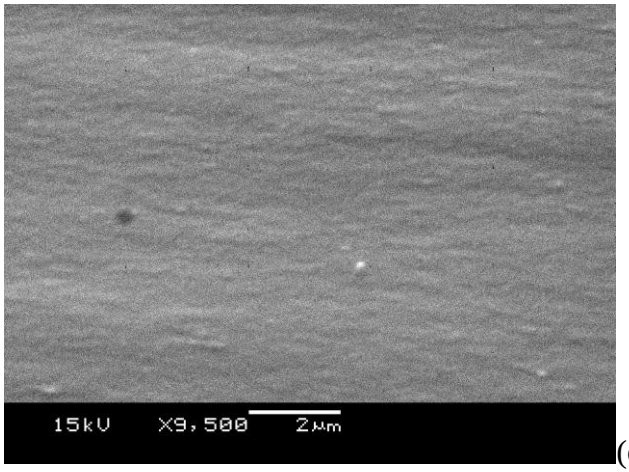

(c)

Figure 4-13 High magnification images revealing the granular structure of the unfilled systems of (a) Ep60, (b) Ep80, (c) Ep100

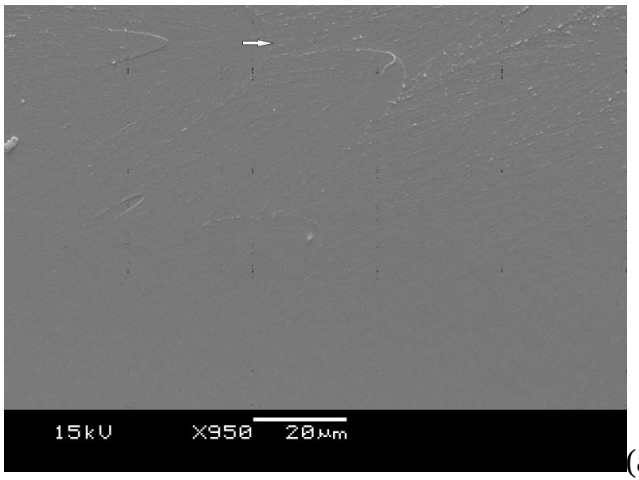

(a)

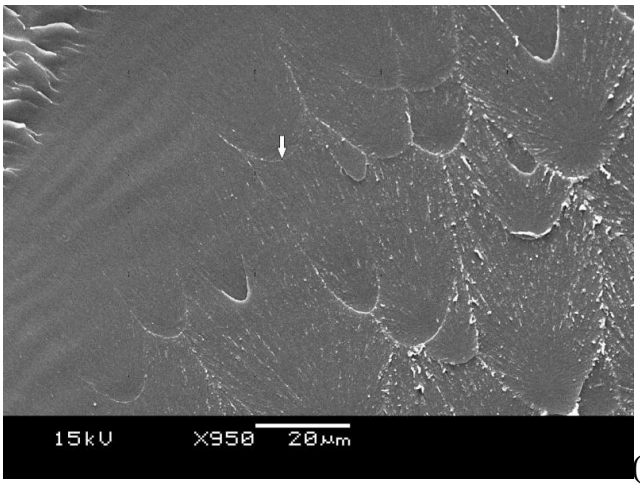

(b)

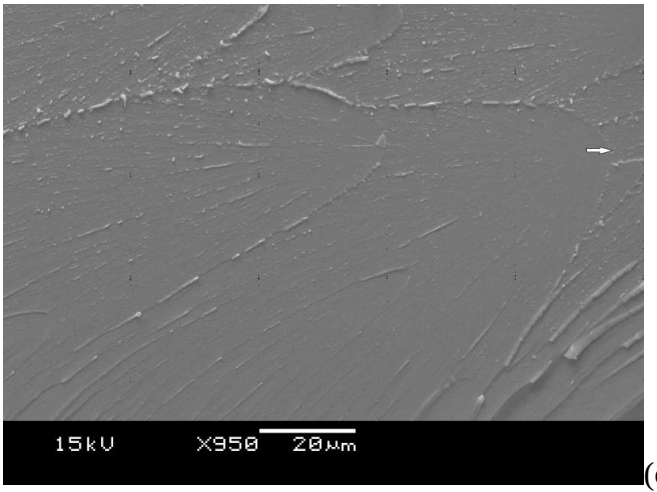

(c)

Figure 4-14 Low magnification images of nanocomposites containing 5 wt% nanosilica: (a) Pox60-5, (b) Pox80-5, (c) Pox100-5

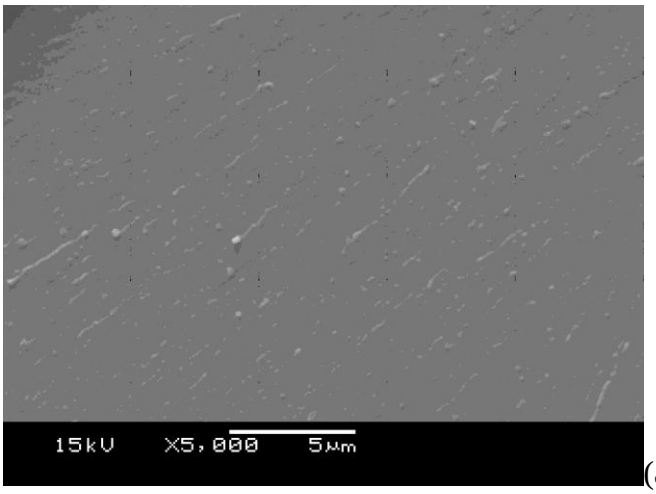

(a)

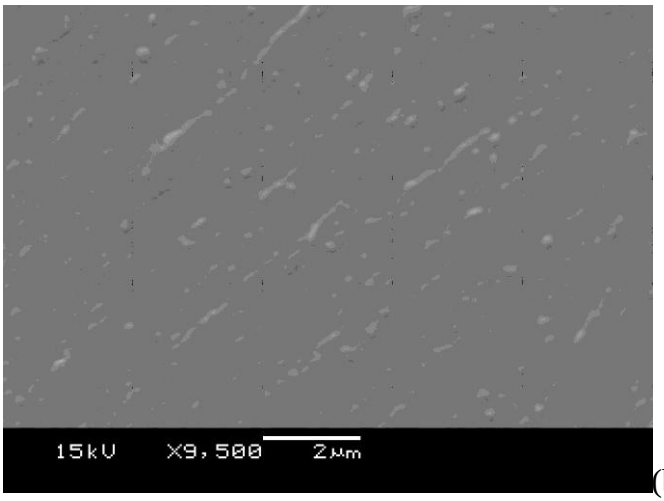

(b)

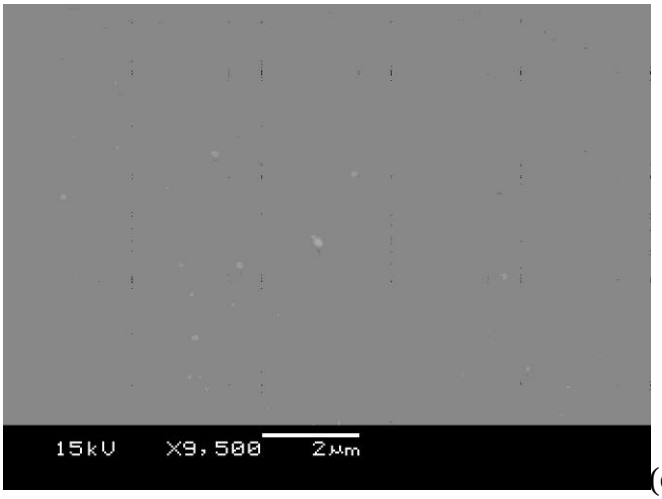

(c)

Figure 4-15 High magnification images obtained at various locations across the Pox60-5 revealing nodular inclusions

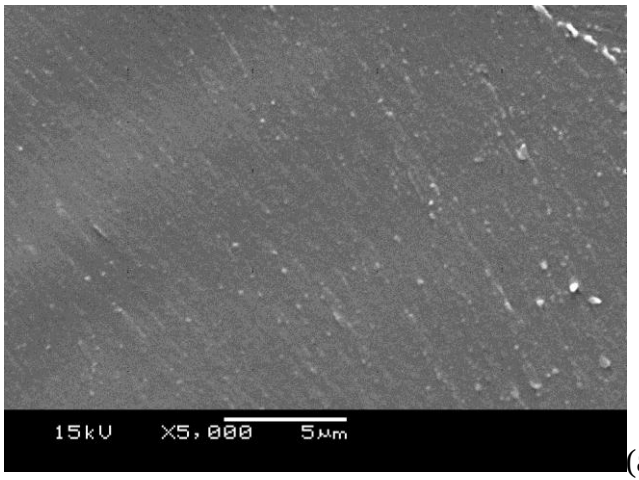

(a)

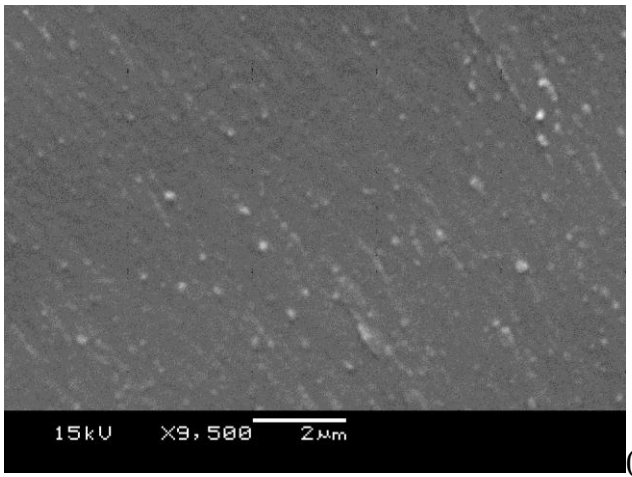

(b)

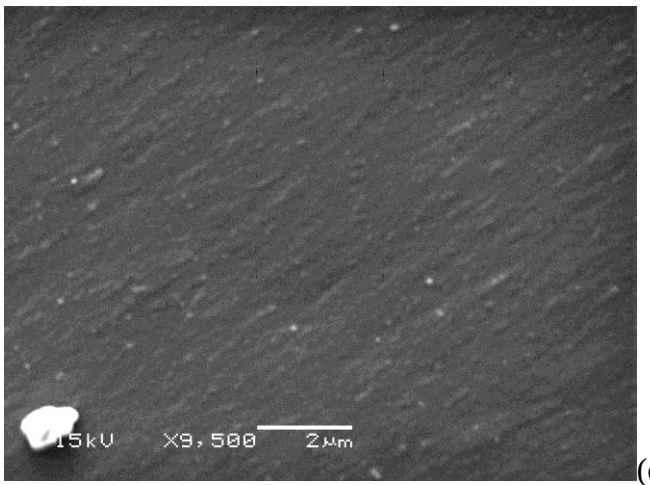

(c)

Figure 4-16 High magnification images obtained at various locations across the Pox80-5 revealing nodular inclusions

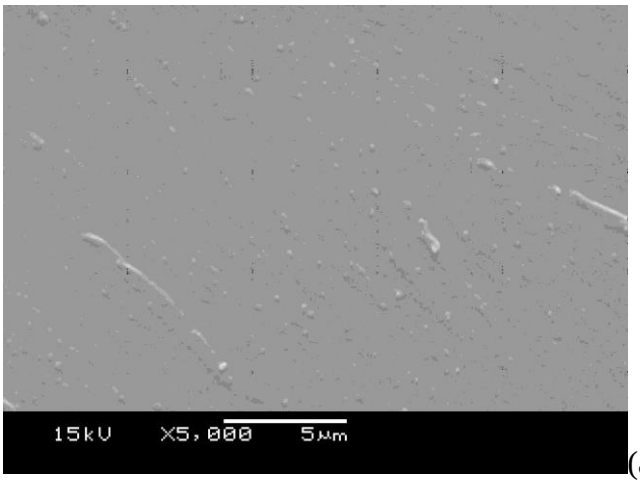

(a)

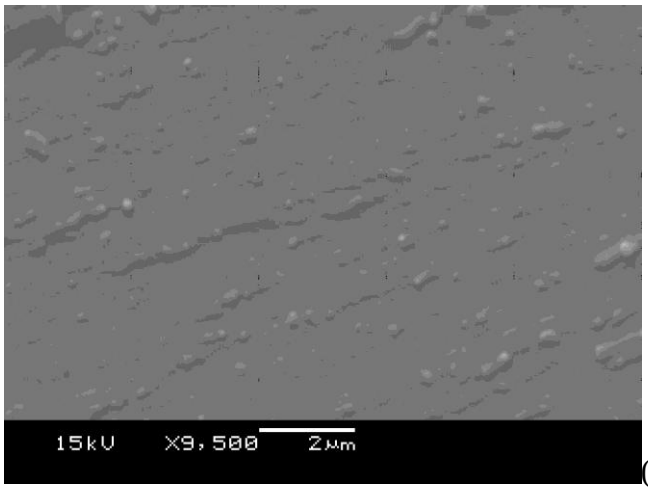

(b)

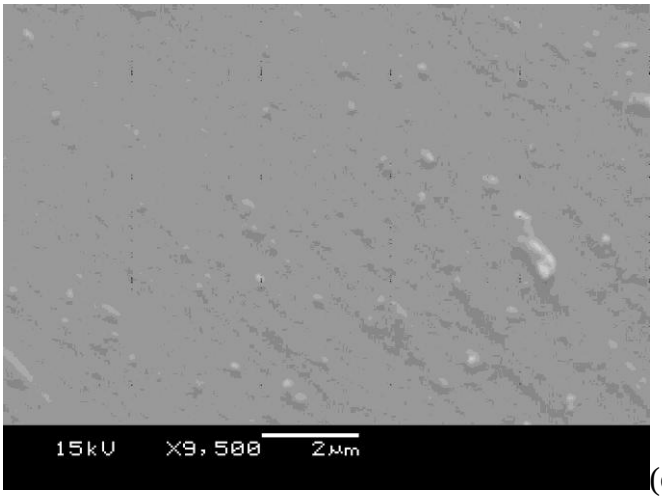

(c)

Figure 4-17 High magnification images obtained at various locations across the Pox100-5 revealing nodular inclusions

4.5 Thermal characterisation

The glass transition temperature can be considered as a basic parameter that defines the thermal properties of glassy materials, including epoxies. Previous studies on the stoichiometry of epoxy suggest that T_g can be used as a tool to evaluate the stoichiometric proportions of a curing system; a number of studies have reported that T_g reaches its highest value when the optimum stoichiometry is achieved in the epoxy matrix [208] and then falls away from its optimum on both sides, for both an amine-cured epoxy system [209] and an anhydride-cured one [210]. Research on stoichiometry effects have led to this unified conclusion about its effects on the T_g of unfilled epoxies. However, little has been extended to related nanocomposites [211].

Figure 4-18 shows typical examples of DSC thermograms obtained for the extreme cases under study. It is clear that while the temperature of the glass transition varies with system composition, there is no evidence of multiple transition temperatures or extensive broadening, suggesting that, in terms of molecular mobility, all of the systems shown are uniform. However, when the epoxy content becomes very high, the curing process is observed to be incomplete. Figures 4-18 (b)-(f) show DSC thermograms obtained from some systems containing a large excess of epoxy; that is, Ep50, Ep40 and Pox40-5. From these figures, it is obvious that after the glass transition, the heat-flow into the DSC decreases, indicating that exothermic process is occurring (additional curing), especially at about 130 ^{o}C as arrowed which could be due to both esterification and etherification reactions. Since the curing process is incomplete, the T_g of these systems are relatively low, falling below 70 ^{o}C. Therefore, the ratio of 100:60:1 is considered to be the limit to obtain full cure using the curing cycle described previously. Consequently, the characterisation of material properties shall be conducted only on systems containing 60 phr hardener and above.

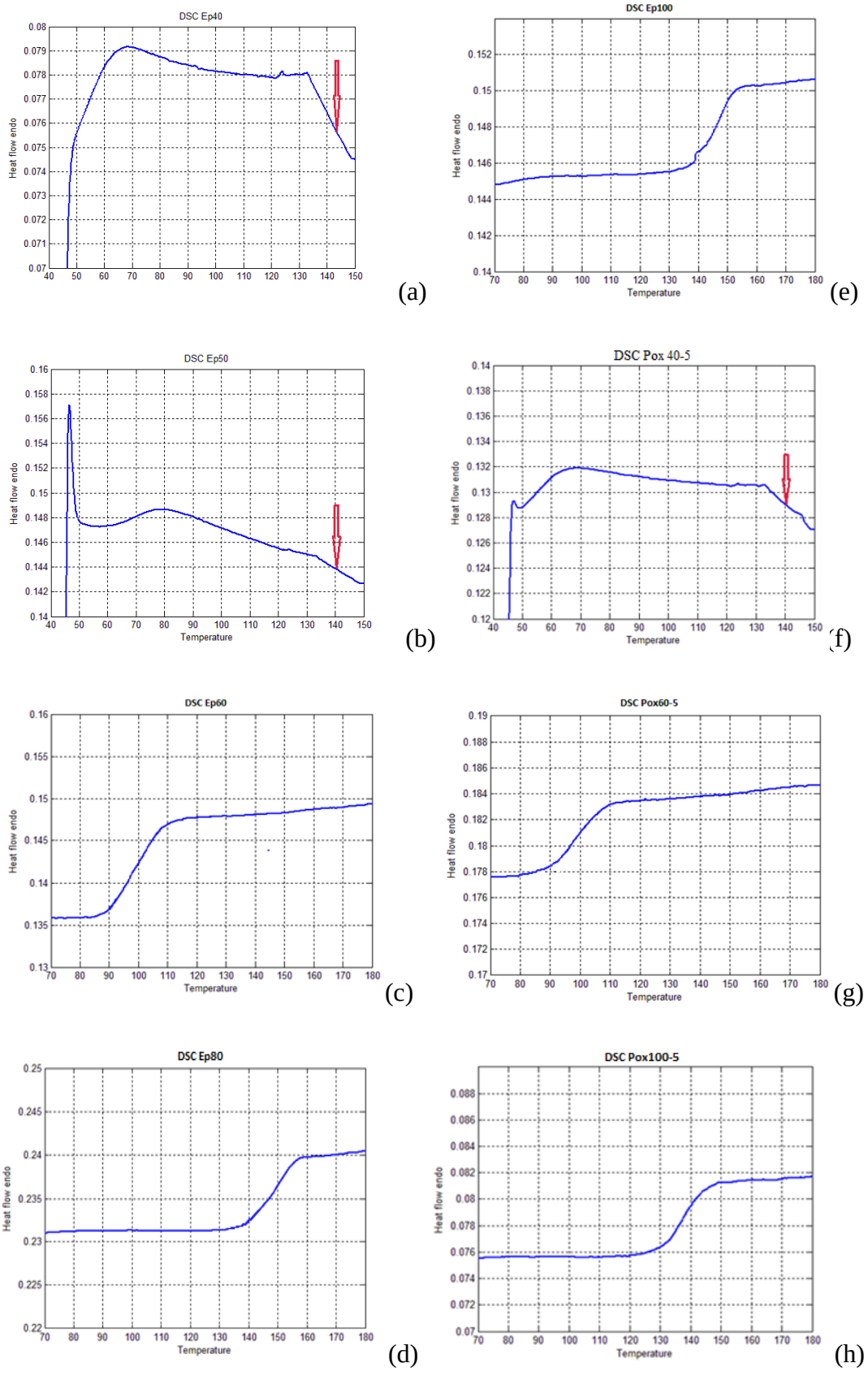

Figure 4-18 DSC scans of unfilled epoxies (a)-(e) and nanocomposites (f)-(h)

Table 4-4 summarises the main information extracted from the DSC thermograms. Although the width of the glass transition ΔT contains information relating to the heterogeneity of the samples, obviously, there is no clear trend for this quantity in the table. It is difficult to determine starting and end points of glass transition regions accurately, so a considerable uncertainty is introduced. As a consequence, although it is likely that incorporating nano-silica fillers into resin matrices introduces a broader glass transition width, a sound conclusion cannot be drawn. Nevertheless, the glass transition temperature T_g and the change in heat capacity per unit mass of polymer, ΔC_p^*, show a good agreement. Both parameters involve the molecular mobility. The decrease in T_g and the corresponding increase in ΔC_p^* suggest that a less densely crosslinked structure forms at lower hardener concentrations. This relationship has been reported elsewhere [73, 176, 212-214].

Table 4-4 Thermal characteristics of samples under stoichiometry study

Sample codes	**T_g (^{o}C) ±2 ^{o}C**	**ΔT (^{o}C) ± 2^{o}C**	**ΔC_p^* x 10^{-1}(J/g^{o}C) ±0.05**
Ep40	57	N/A	N/A
Ep50	68	N/A	N/A
Ep60	98	30	7.8
Ep70	122	26	6.5
Ep80	147	23	5.5
Ep90	146	22	5.4
Ep100	145	25	5.7
Pox40-5	58	N/A	N/A
Pox50-5	N/A	N/A	N/A
Pox60-5	99	30	7.9
Pox70-5	120	28	6.8
Pox80-5	140	25	5.9
Pox90-5	140	25	5.8
Pox100-5	138	26	6.1

Here ΔT is the width of the glass transition; ΔC_p^* is the change in heat capacity per unit mass of polymer: $\Delta C_p^* = \Delta C/(1-r)$; in which r is the wt% of filler.

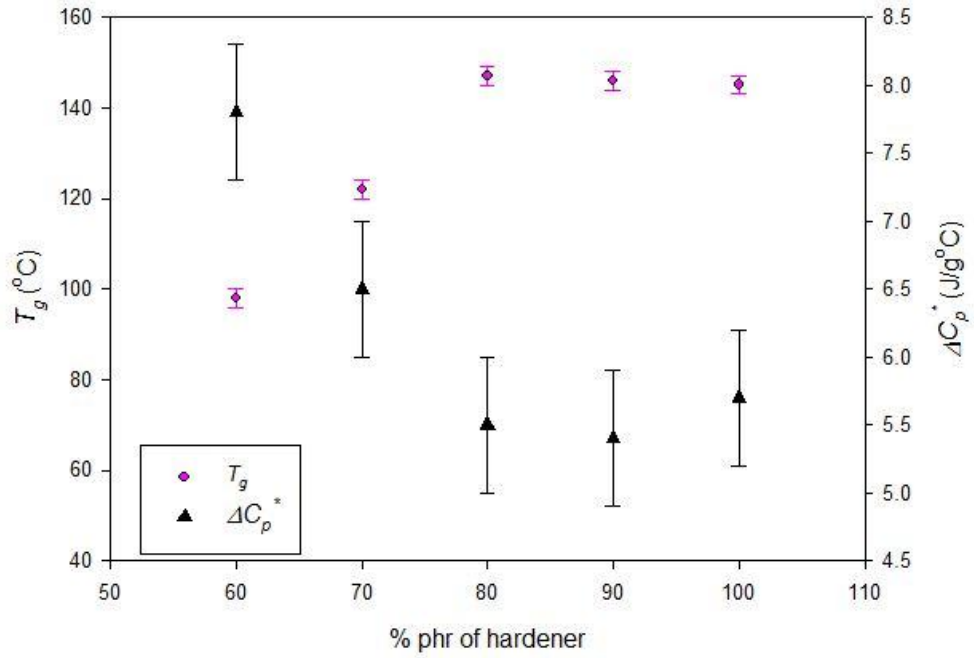

Figure 4-19 The glass transition temperature and heat capacity of unfilled samples (Standard errors based on 5 samples)

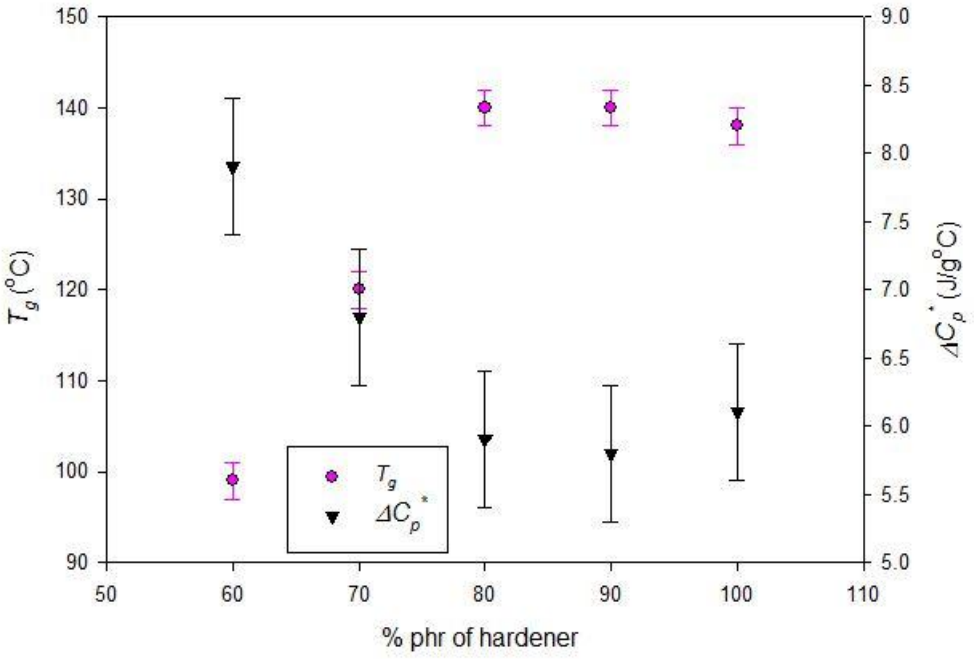

Figure 4-20 The glass transition temperature and heat capacity of samples containing 5 wt% nanosilica (Standard errors based on 5 samples)

Figures 4-19 and 4-20 present the effects of stoichiometry on T_g and ΔC_p^* of the unfilled epoxies and nanocomposites respectively. From Figure 4-19, it is evident that the highest value of T_g, which corresponds to the optimum stoichiometry for the unfilled epoxy, falls close to 80 phr hardener, although the theoretical calculation suggests that the optimum formulation is 100:96 phr hardener or 1:1 molar ratio, as mentioned in Chapter 3. This means that nearly 20 % of these epoxides are unavailable for anhydride reaction due to homopolymerisation, isomerisation or other side reactions. Similar observations have been reported by Fisch and Hofmann for the uncatalysed reactions [149]. However, the presence of tertiary amine catalysts has been reported largely or wholly to suppress the undesirable polymerisation of terminal epoxide groups during curing of anhydride-epoxy resin systems, in work conducted by the same group [150]. The decreasing requirement of anhydride quantity implies the decreasing quality of cure obtained with the resin. This suggests that the resin MY 740 used in the research may contain a number of internal epoxides and/or hydroxyl groups which enable side reactions to occur [215]. However, according to [152], the tertiary amine R_3N could open the epoxy ring and facilitate the epoxy-epoxy or epoxy-nascent hydroxyl reactions. At low elevated temperatures, both esterification and etherification reactions take place at the same rate, whereas at high temperatures, esterification happens more rapidly. The curing cycle used in this research included 3 steps: 100 ^oC for 7 hours, followed by 135 ^oC for 13 hours and then post-curing at 160 ^oC for 4 hours. Since etherification could occur during the second and final curing steps, a composition containing a slight excess of epoxy should lead to a more highly crosslinked network, as reported elsewhere [215-217]. In the optimum formulation, the anhydride and epoxy groups react together to form a network with the highest attainable degree of cross-linking, while minimising the unreacted hardener or epoxy. For compositions where the proportion of hardener is above the optimum stoichiometry, the basic curing mechanism is dominated by the esterification reactions. The homopolymerisation is likely to occur more slowly. The dominance of the esterification should favour a higher crosslinking degree in the network. However, an excess of hardener and/or both epoxide groups locating internally or terminally may increase the probability of the appearance of loops, dangling ends and sol as shown in Figure 4-21 [218]. As a consequence, such defects contribute to the free volume within the sample, and hence, lower the T_g.

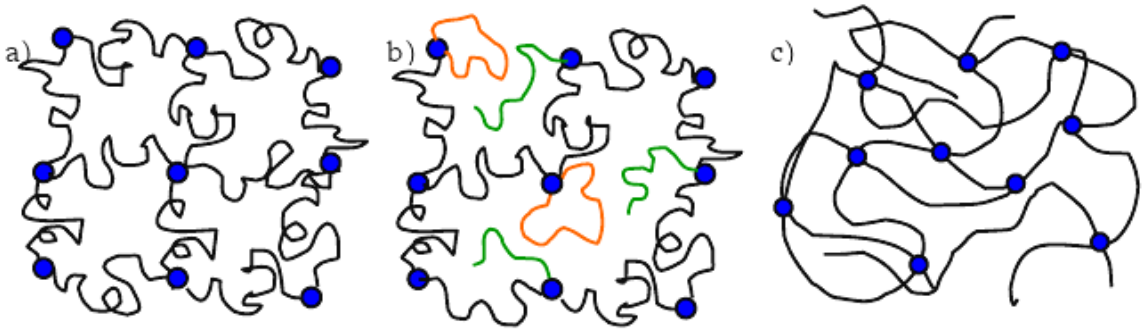

Figure 4-21 Ideal network formed after cure (a) and non-ideal network with loops, dangling ends and sol after cured (b-c) [218]

However, in cases where entanglement of very long chains with carboxyl end groups takes place, chains become constrained by their neighbours and, so physically this will behave like a crosslink. Therefore, only a small decrease in T_g is observed for compositions containing an excess of hardener. However, due to the uncertainties of measurements, this decrease cannot be concluded. When the proportion of hardener is far below the optimum, the use of excess epoxide has the advantage that the rate of esterification remains high until almost all anhydride is consumed. However, the decreasing amount of anhydride means a decrease in the crosslinking density, which leads to a decrease in T_g. Conversely, an excess of epoxy groups may lead to epoxy homopolymerisation becoming significant. The etherification reaction of epoxide groups could occur to a certain extent, especially in the presence of hydroxyl groups [139], so increasing the degree of crosskinking and, hence, T_g [73]. Epoxy homopolymerisation usually leads to a branched structure with dangling ends, and therefore, a lower crosslinking density than esterification reactions. For example, Garcia del Cid et al. [219] reported that the homopolymersation of one DGEBA-type epoxy resulted in the network having a T_g at about 88 ^{o}C, whereas curing this epoxy with a diamine hardener returned a highly crosslinked structure with T_g at about 150 ^{o}C. Obviously, the loops, dangling ends and sol (unreacted molecules) contribute more free volume to the network and lower the T_g. Indeed, Vanlandingham et al. [220] investigated the changes in microstructure and mechanical properties as a function of epoxy-amine stoichiometry. In this study, the epoxy-amine system exhibited a two-phase structure, including a hard microgel phase and a dispersed phase of soft, unreacted and/or partially cured molecules. This work found that the stoichiometric

sample possessed the highest percentage of the rigid, high density phase and the soft phase was dispersed within the microgels. Conversely, the amine-rich sample was composed of a microstructure characterised by a broader size distribution of the rigid phase, which was surrounded by a larger pool of the soft phase. On the other hand, the epoxy-rich sample was comprised of microgel regions of reduced size. The work also revealed the effects of post-curing. After post-curing, the stoichiometric sample showed the highest T_g. Etherification reactions were found to take place during post-curing, so increasing the T_g of the epoxy-rich sample. However, during post-curing, the oxidation of unreacted amine groups was also believed to take place, which resulted in changes in sample colour. Such oxidation reactions may lead to the deterioration in material properties. Depending on the amount of excess epoxy, the effective crosslinking efficiency may vary. We suggest that it is this change in the fundamental cure reaction that may be the reason why there is a difference in the decreasing rates of T_g to either side of the optimum stoichiometry. These results are in a good agreement with other observations [73, 211].

In order to investigate stoichiometry effects in nanocomposites, 5 %wt nano-silica was introduced into the unfilled epoxy matrices. Figure 4-20 shows similar behaviour in nanocomposites, compared with the corresponding unfilled epoxies. Again, it confirms the relationship between the glass transition temperature and the heat capacity with the molecular mobility. However, it is evident from Figure 4-22 that the effect of the introduction of the Nanopox into the host resin is not the same for different stoichiometric ratios. Although due to the uncertainties inherent in the measurements, an absolute conclusion cannot be drawn, it is likely that there is a reduction in T_g for the systems containing 80 phr hardener and more, while the observed T_g values stay nearly the same for those containing an excess of epoxy.

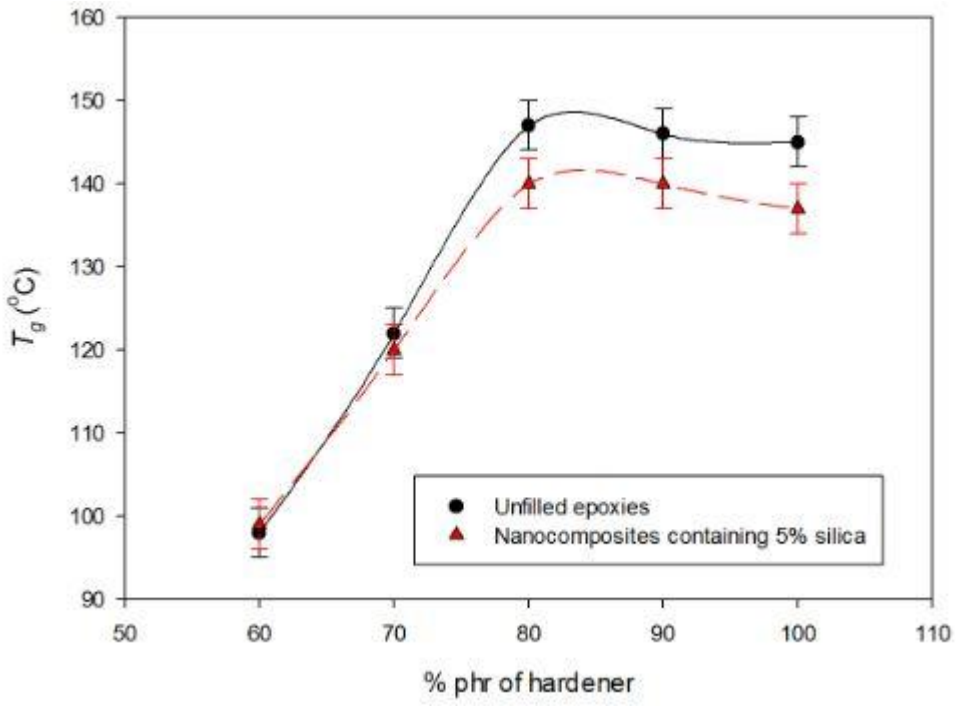

Figure 4-22 Comparison on the glass transition temperature (Standard errors based on 5 samples)

To explain this behaviour, first, we go back to the materials used in the systems. The Nanopox has its EEW of 300 with 40 wt% nanosilica. Appying equation 3-1 in Chapter 3 results in the EEW of the resin employed in the Nanopox being about 180. The EEW value of the host resin MY 740 is about 185. Therefore, in principle, these resins are supposed to have similar functionality, and hence, require the same amount of hardener in the curing reactions. The introduction of the Nanopox into the original resin system may lead to changes due to two factors, namely the resin and the nanosilica. Obviously, the resin factor can be ignored. As a result, changes in the material behaviour should be ascribed to the nanosilica, e.g. the particle surface chemistry and the particle dispersion; SEM images of the nanocomposites show a reasonably good dispersion of the filler within the resin matrix. Therefore, it is likely that the particle surface plays a key role in changes in material properties. A number of studies have claimed a reduction in T_g upon introducing nanofillers [141, 209-211]. They explained that the addition of nanofillers produced more free volume at the interface between the filler and the resin matrix, so, facilitating molecular motions in the interphase regions and thereby reducing T_g. It has also been reported that the presence of water on the nanoparticle surface could lead to a reduction in T_g [47]. Such interfacial effects will be studied in detail in the following

chapter. However, it is necessary to note that if the reduction in T_g depends only on such interfacial effects, then the similar reduction should be observed for all the samples since all contain the same proportion of nanofiller. Figure 4-22, however, shows that different behaviours are obtained by introducing 5 wt% nanosilica into systems with different stoichiometries. Therefore, there must be another additional mechanism involving the nanosilica, which leads to such a difference in system behaviour. The FTIR spectra of the MY740 and the Nanopox in Figure 4-2 show that there are H-bonded hydroxyl groups present in the Nanopox. These hydroxyl groups could catalyse epoxy homopolymerisation reactions and/or react with the epoxide groups via etherification, and hence, reduce the required amount of hardener. In addition, the synthesis of the Nanopox masterbatch using the sol-gel process involves acid or basic catalysts. The presence of such catalysts and other by-products associated with the synthesis of the Nanopox and the surface modification of the nanosilica particles could introduce changes in curing reactions. In such cases, the highest attainable crosslinking degree will be reduced, and there may be an excess of hardener for some reacting systems. The presence of excess hardener will not significantly affect T_g as discussed above. Therefore, the inclusion of nanosilica at 5 wt% can produce systems with the highest T_g of 140 ± 2 ^{o}C. The FTIR spectra in Figure 4-11 show that there is a greater excess of hardener in Pox100-5 than in Ep100. This observation is likely to support the proposed hypothesis. The remaining cases contain excess epoxy. In the presence of excess epoxy, the poly-etherification of the epoxide groups through reactions involving OH groups may become significant [139]. Xie et al. [221] also found that hydroxyl groups on the surface of multiwall nanotubes exert a catalytic effect on epoxy ring opening and this was believed to be the source of modified curing. In another study, Tao et al. [222] claimed that the high percentage of catalyst particles in the single-wall nanotubes raw material is a plausible source for the modification of cure behaviour in its early stages. Besides, due to the excess of epoxy, the esterification occurs completely. Evidently, compared with the corresponding unfilled systems, these nanocomposites contain the same amount of hardener, and hence in principle, the same crosslinking degree due to esterification. However, the catalytic effect of hydroxyl groups and/or other impurities could accelerate etherification reactions of excess epoxide-epoxide groups and epoxide-hydroxyl groups. As a result, the crosslinking density due to etherification could be higher than the corresponding unfilled systems. This positive

effect compensates for the negative impact on T_g due to the interfacial effects associated with nanofillers. Therefore, T_g stays almost the same. Similar observations were reported by Garcia del Cid et al. [219], in which the catalytic effects of organically modified clay were shown to induce changes in the required stoichiometry of the epoxy system, which manifested themselves in reduced T_g and a shift in the optimal chemical stoichiometry to a smaller amount of hardener.

4.6 Space charge behaviour

Figures 4-23 and 4-24 show space charge profiles obtained from unfilled epoxy systems of different stoichiometry, obtained by the PEA method during 1h poling time at an intermediate electric field of 30 kV/mm, followed by 1h of short-circuiting.

It is evident that there is a small amount of homocharges injected from the cathode during the 1h charging period for all the cases under investigation. The injected charges are trapped and consequently stay in the vicinity of the electrode. There is no internal space charge observed at other locations within the bulk of the samples, which implies that the injected charges cannot gain enough energy to drift to the other electrode. In addition, the quick dissipation of injected charges upon short-circuiting suggests that there is a distribution of shallow traps near the surface of the samples [223]. The presence of homocharge near the electrode reduces the field at the cathode and hence, suppresses the injection of electrons. Similar observations about the space charge behaviour of epoxy have been reported previously. For example, Iizuka et al. [224] found that there was no internal space charge in epoxy resin without fillers; charges appeared close to the electrodes. Another study by Fukunaga et al. [225] also found that homocharges were accumulated near the electrodes and that no internal space charge was observed at other locations within the bulk of the materials. The accumulation of homocharge in the vicinity of electrodes was also observed in the work of Dissado et al. [226]. It is necessary to note that all the samples under investigation possess high *Tg's* (from 100 ^{o}C upwards) while the space charge measurements are conducted at room temperature. Under this experimental condition, the materials are deep in their glassy state, and hence, molecular mobility is severely restricted; the polarisation and movement of any internal impurities present in the material will also be severely limited in such highly crosslinked structures. Furthermore, any ionic conduction is extremely

slow due to limited fluctuation of chain segments at this temperature. Therefore, the contribution of such effects to the space charge behaviour cannot be observed [227].

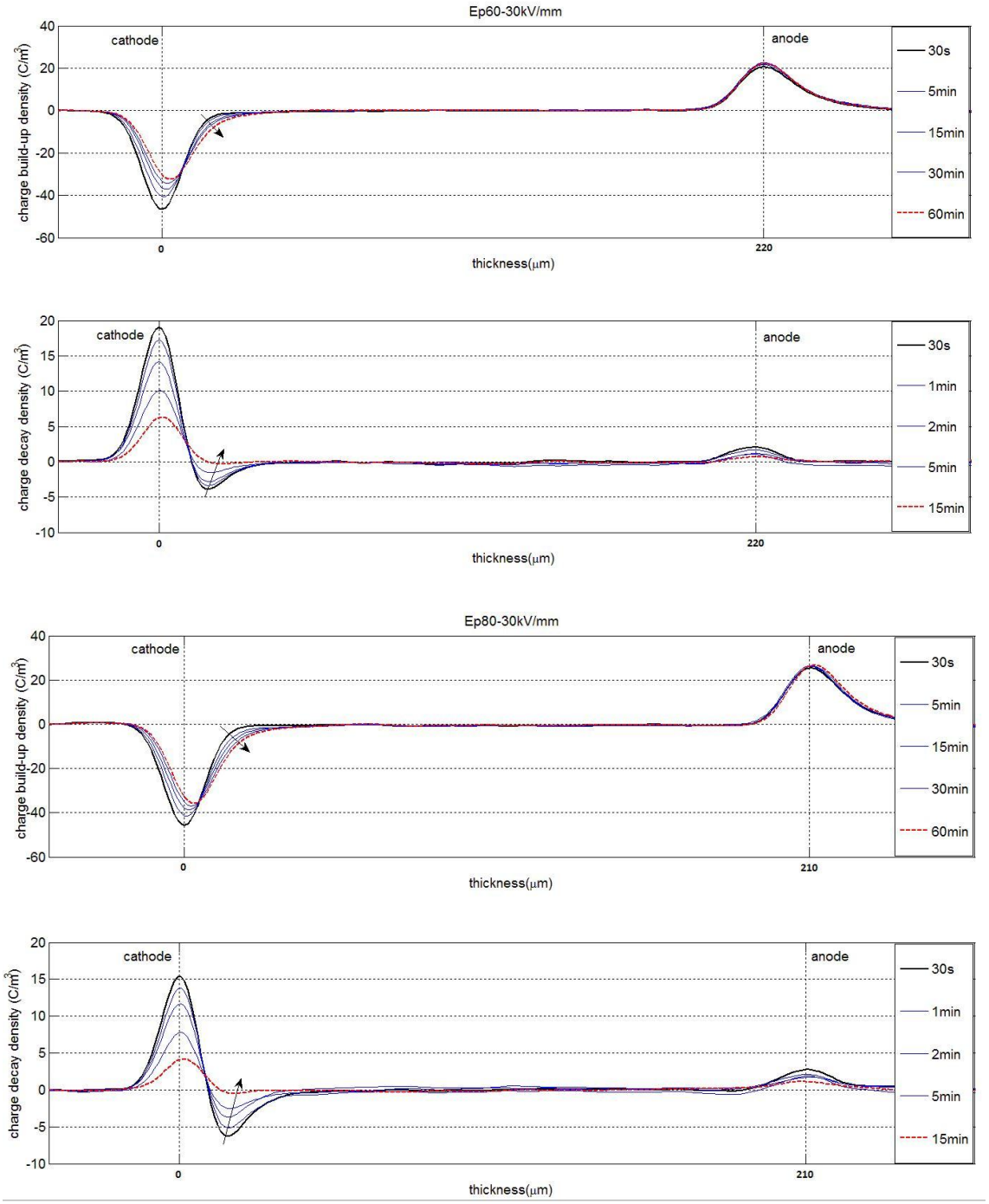

Figure 4-23 Space charge profiles of unfilled epoxies containing excess epoxy during the charging at 30 kV/mm (upper graph) and discharging (lower graph)

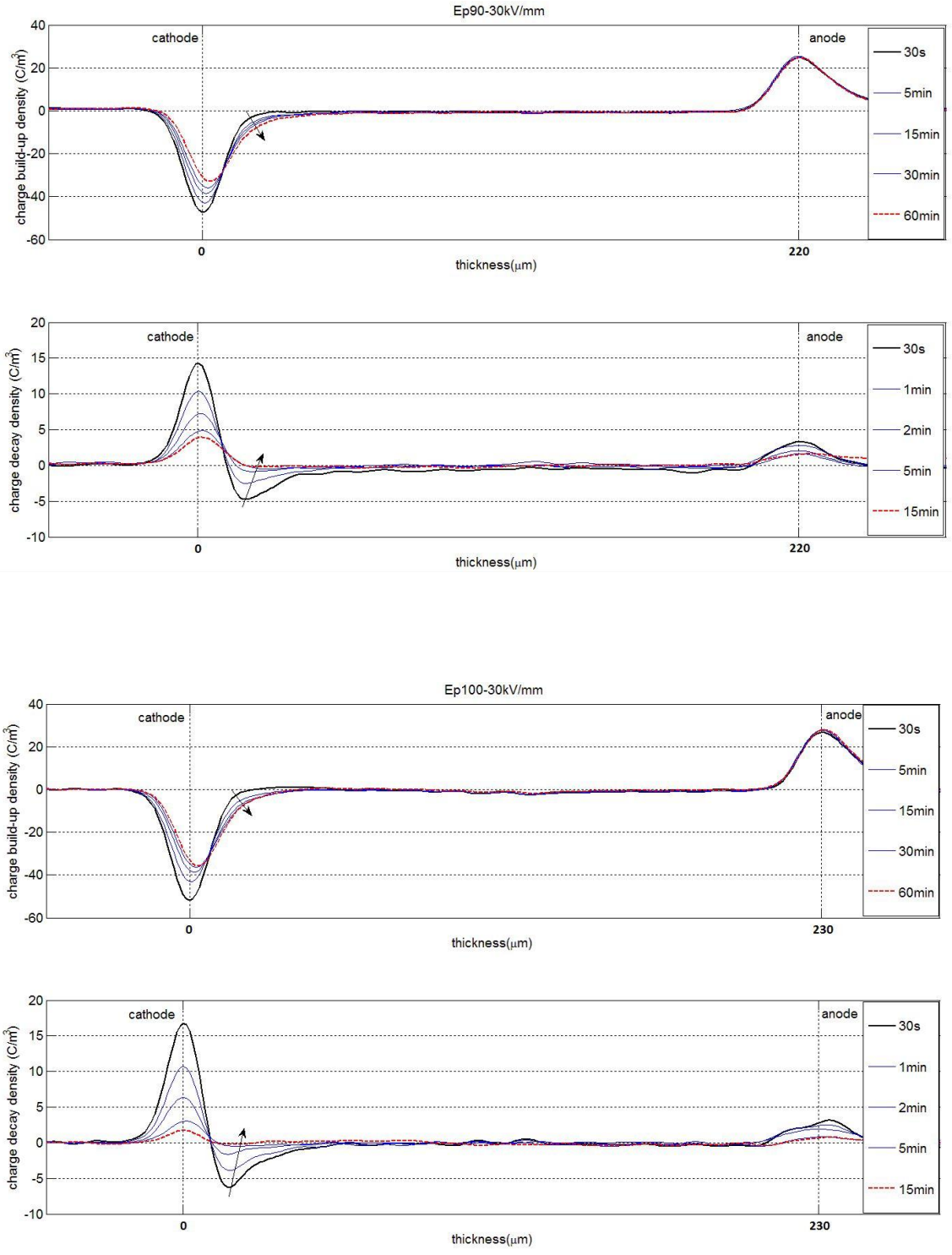

Figure 4-24 Space charge profiles of unfilled epoxies containing excess hardener during the charging at 30 kV/mm (upper graph) and discharging (lower graph)

Due to the uncertainties of the measurements and the noise during the experiments, it is difficult to draw a conclusion about the difference in the quantitative information of charge injection and trapping for samples of different stoichiometry, although significant effects related to the presence of excess anhydride and epoxy groups can be detected by FTIR or T_g. With an excess of epoxy, the polymers tend to have hydroxyl terminated end groups, while a slight excess of hardener usually produces carboxyl termination [150]. These features can contribute more trap states within the samples. Although the density of trap states in the energy gap can be higher in these cases, the inter-state distance must fall below a critical value, which can be as small as a few nanometers, for hopping or tunnelling of electrons between states to occur. In other words, the effective mobility of charge carriers is still very low in these cases. As a consequence, only a small amount of homocharge is observed near the cathode. On the other hand, the injection of charge carriers depends on the potential barrier between the electrode material and the sample. All the samples under investigation possess highly crosslinked structures, which are formed via ester and ether linkages. At room temperature, where the materials are deep in their glassy state, the potential barrier of all the samples may be very high for electrons to be injected; once, the injected electrons are trapped near the cathode, the build up of homocharge suppresses further injection.

Figures 4-25 and 4-26 present space charge profiles obtained from epoxy-based systems of different stoichiometry containing 5 %wt nanosilica. In general, there is almost no difference between the unfilled and the corresponding nanocomposite systems. The FTIR spectra of these samples reveal that there are no new chemical bonds formed by the introduction of the Nanopox, except the Si-O-Si bonds due to the silica. Therefore, in principle, the network structures are still formed through ester and ether linkages. In addition, the SEM images illustrate the good dispersion of silica fillers, and hence, with the nanosilica particles ranging from 50-200 nm in size, the host resin matrix can be considered to be continuous. As such, there is no evidence of significant variations in the chemistry or microstructure of these systems. In addition, although the introduction of Nanopox can contribute more impurities and defects, and hence, more traps in the band gap, the inter-state distance may be still quite far for hoping or tunnelling of charge carriers to occur; the mobility of charge carriers for conduction in the band gap is still very low. As a result, no changes in the space charge behaviours can be observed.

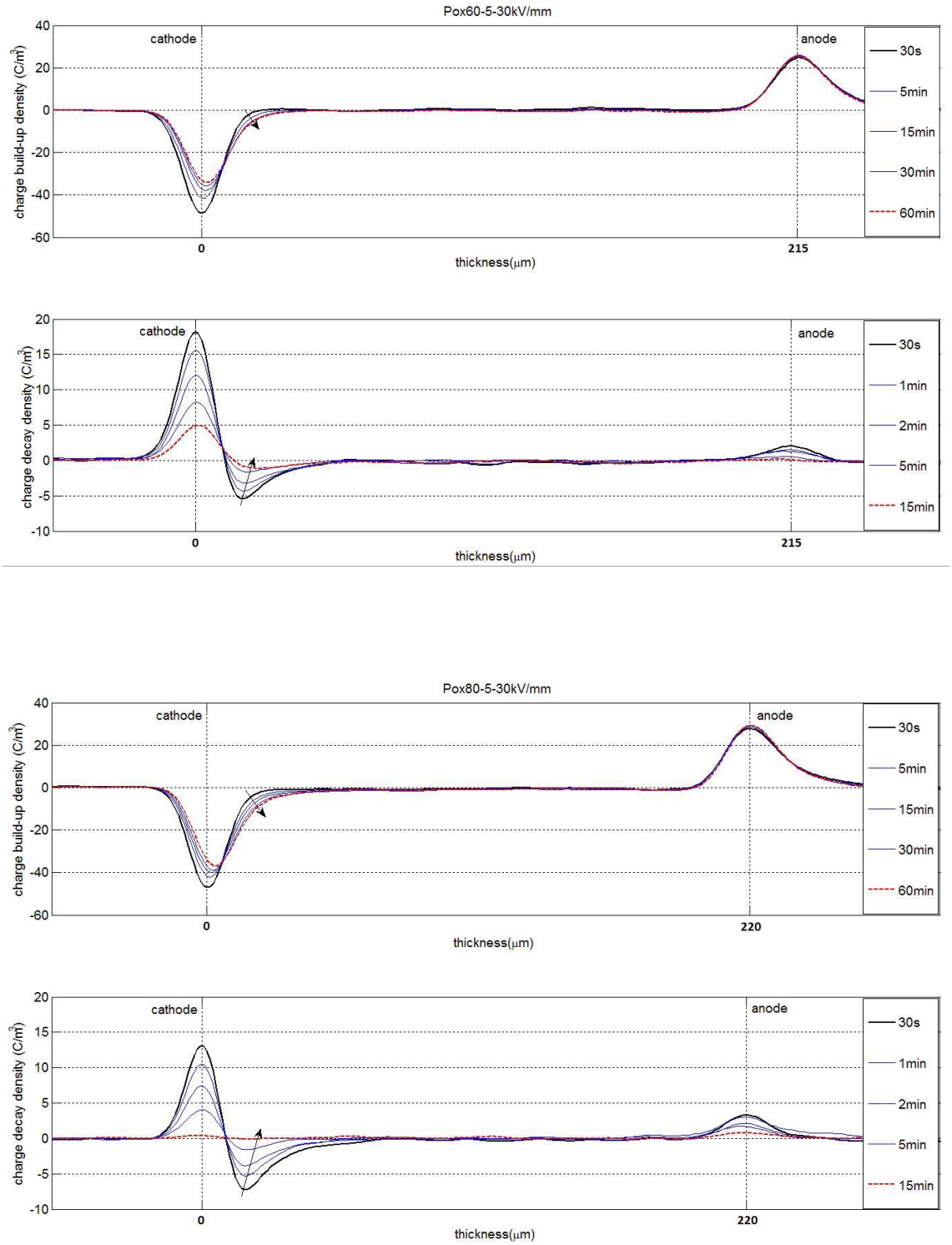

Figure 4-25 Space charge of nanocomposites containing excess epoxy plus 5 wt% nanosilica at 30 kV/mm charging (upper graph) and discharging (lower graph)

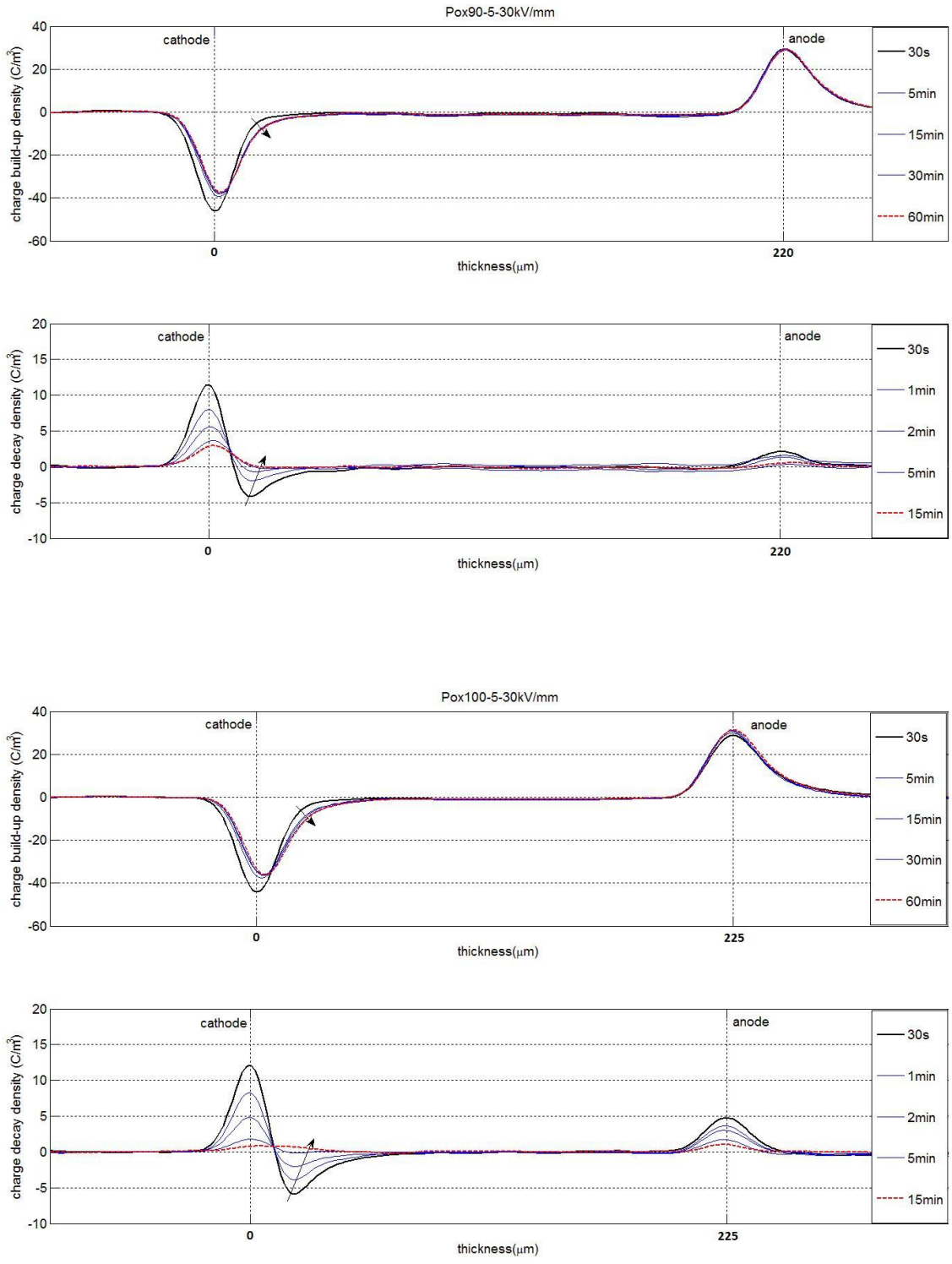

Figure 4-26 Space charge of nanocomposites containing excess hardener plus 5 wt% nanosilica at 30 kV/mm charging (upper graph); discharging (lower graph)

4.7 AC Electrical breakdown

AC breakdown measurements are commonly used to characterise electrical materials and derive the Weibull parameters, which can provide indirect information on the uniformity of samples [228]. Figure 4-27 shows representative Weibull plots illustrating the effect of resin stoichiometry on the breakdown strength, E_b, of the unfilled materials, for cases of both excess epoxy and excess hardener.

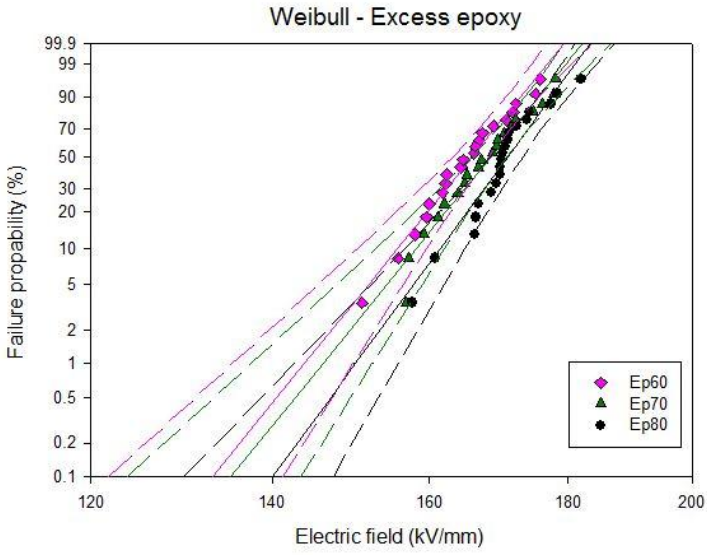

(a)

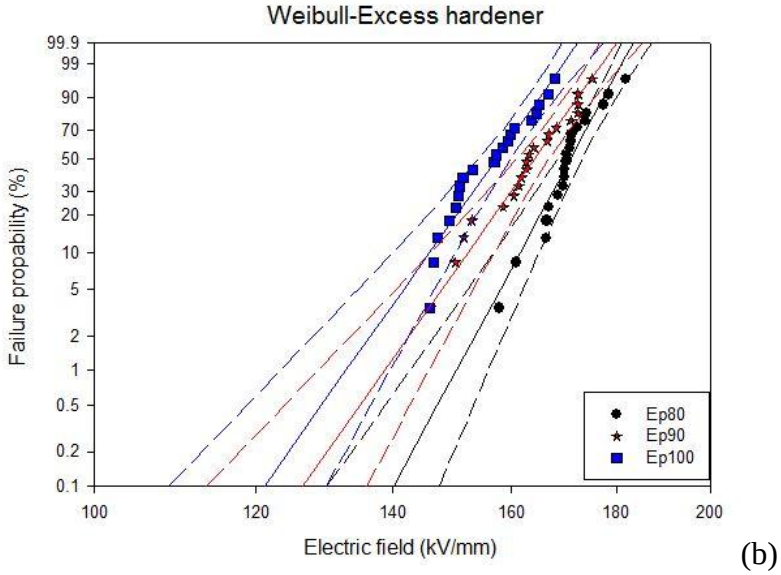

(b)

Figure 4-27 Weibull breakdown distribution of unfilled epoxies; (a) excess epoxy and (b) excess hardener

Evidently, the Weibull scale parameter, α, stays highest for the Ep80 while it is decreasing at the different rates away from this optimum ratio, as shown in Figure 4-28. In all cases, the shape parameter, β, is high (> 20), indicating low scatter in the data, as shown in Figure 4-29 and Table 4-5.

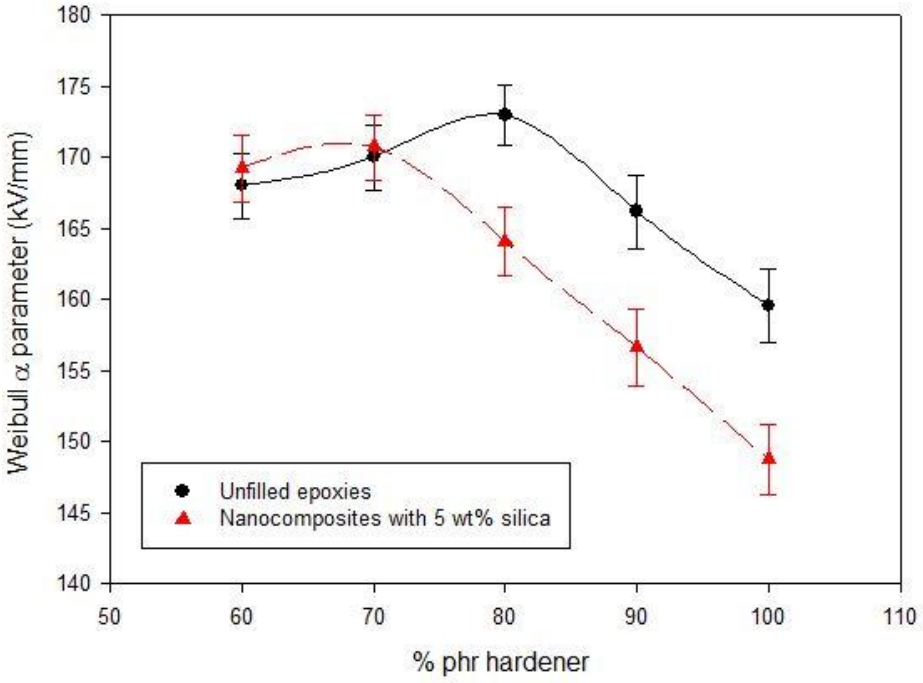

Figure 4-28 Comparison about E_b of samples (90% confidence intervals)

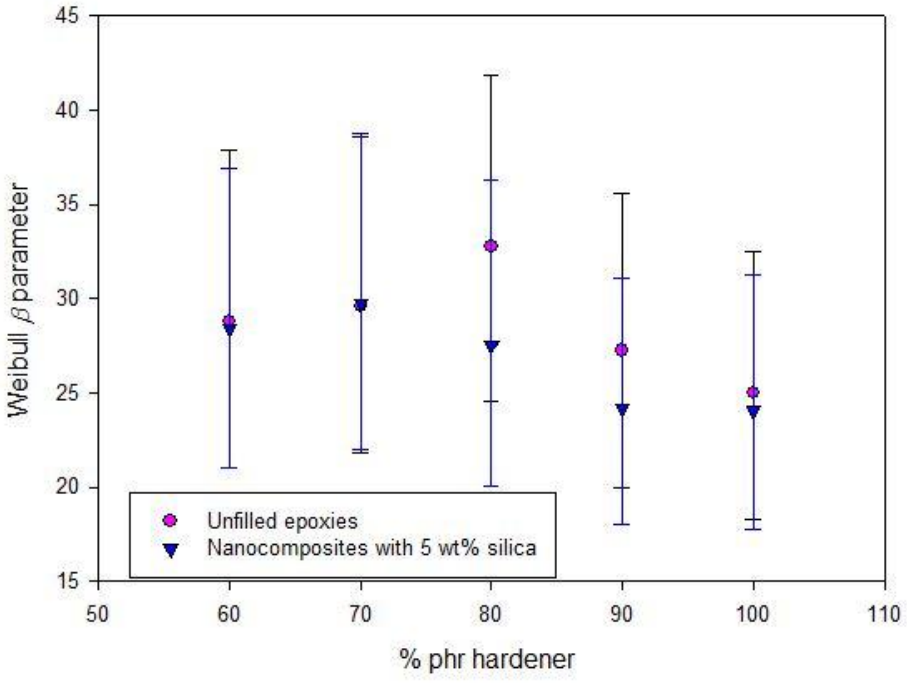

Figure 4-29 Weibull β parameter of the samples

Table 4-5 Weibull parameters of samples under stoichiometry

Sample code	α (kV/mm)	β
Ep60	168.06	28.8
Ep70	170.1	29.6
Ep80	173	32.7
Ep90	166.2	27.2
Ep100	159.6	25
Pox60-5	169.26	28.4
Pox70-5	170.7	29.8
Pox80-5	164.1	27.6
Pox90-5	156.6	24.2
Pox100-5	148.7	24

A reduction in β indicates increased scatter, which may involve an increased heterogeneity due to the excess hardener. The FTIR spectrum of Ep100 in Figure 4-7 reveals the existence of the C=O due to the excess anhydride groups in the cured product. The unreacted hardener is considered to contribute mobile moieties or defects due to the oxidation process in the network, so reducing the breakdown strength due to an increase in the local polarisation. It is well known that oxidation can lead to the degradation of materials. However, due to the uncertainties, no difference in the Weibull β parameter can be realised to be statistically significant, as illustrated in Figure 4-29. Meanwhile, excess epoxide groups can take part in etherification reactions, and hence, the amount of unreacted epoxy molecules which could also be considered to be defects is reduced, so the breakdown strength is reduced at a slower rate than that of an excess of hardener. Although the space charge profiles suggest that, at room temperature, space charge formation is not the reason for any decrease in breakdown strength and both ionic and electronic conduction are extremely low, higher fields can modify potential barriers and enable electronic conduction through energy states in the band gap. Obviously, this kind of conduction depends on the trap distribution and mobility of charge carriers. In other words, the more impurities, the higher conduction

and the lower breakdown strength are. In addition, the mechanical strain may also play an important role in the breakdown behaviour in the glassy state. According to Forthergill [229], filamentary electromechanical breakdown occurs when the strain energy released under the influence of an applied field, W_{em}, is greater than the sum of surface energy required for fracture, W_s, and plastic deformation energy, W_p, i.e. $W_{em} > W_s + W_p$. The strain energy released is proportional to the enhanced field at the crack tip and inversely proportional to the Young's modulus Y of materials, whereas the surface energy is proportional to the fracture toughness G and the plastic deformation energy is proportional to the Young's modulus Y. A filamentary electromechanical breakdown filed, E_{fem}, [229] can be defined as:

$$E_{fem} = \left(\frac{8Y\left(2G + Yr_f\right)}{\varepsilon_0^2 \varepsilon_r^2 r_f}\right)^{1/4} \qquad Equation\ 4-1$$

where ε_0 is the permittivity of free space and ε_r is the relative permittivity of the material, and r_f is the radius of a conducting tubular filamentary crack [229]. A crack may be a microvoid, an inclusion, an electrode aberration, an electrical tree or a feature of the microstructure such as the morphology [118]. For highly crosslinked networks such as epoxies, at temperatures much lower than the glass transition temperature, there is no significant difference in the Young modulus. These thermosetting polymers undergo little or no plastic deformation, as shown in Figure 4-30. For example, Hsieh et al. [230] measured the Young's modulus of various epoxy systems formed by different types of epoxy resin and hardener. He observed a broad range of the glass transition temperature of cured products which falls from 70-180 ^{o}C. However, the Young's modulus is quite similar, falling into the range of 2.9-3.1 GPa.

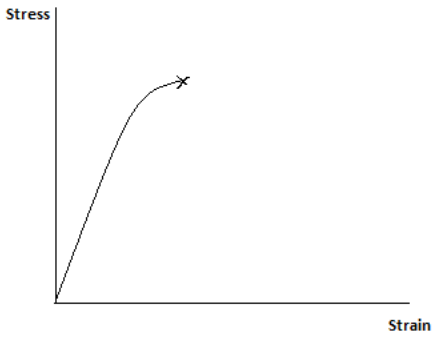

Figure 4-30 Stress-strain curve of brittle materials

It is well known that networks involving a high crosslinking degree are usually brittle. The brittleness reduces the fracture toughness, *G*, of such materials. A lower crosslinking degree may lead to an increase in the toughness, *G*. For example, Hsieh et al. [230] found that the toughness was reduced significantly with an increase in the T_g. An increase in toughness allows an increase in the plastic deformation, so reducing the stress concentration around any crack tips, and increasing the breakdown strength, as evinced by Equation 4-1. Obviously, the toughness of materials depends on their structures. A linear molecular structure possesses a high toughness (about 20 000 J/m^2 for polyethylene [118]), whereas crosslinking and branching make materials become more brittle. An excess of hardener may lead to entanglement of long molecules, such that the material becomes very brittle with a low toughness, and hence, exhibits a lower breakdown strength than systems with either the optimum stoishiometry or an excess of epoxy. However, the increase in the chain mobility could involve an increase in the conductivity or relaxation of the side chains attached to the polymer backbone, especially at high fields and high temperatures. This effect should adversely affect this electrical property. The effective breakdown behaviour is the contribution of such contradictory factors. Soft materials, therefore, exhibit poor high temperature performance due to the dominance of the latter factor. This suggests that the degree of crosslinking is not the main factor that determines the insulation strength of the materials, but rather the structural architecture. Therefore, an excess of hardener has a greater impact on the breakdown strength than does an excess of epoxy, in marked contrast to the T_g data presented above, where the glass transition was found to vary relatively little when an excess of hardener was introduced. To explore this point further, ac breakdown data for nanocomposites loaded with 5 %wt nano-silica was also considered. Figure 4-31 contains Weibull plots for such nanocomposites and Table 4-5 above summarises the derived Weibull parameters obtained for the systems under investigation. Figure 4-28 above compares the breakdown strength of the unfilled systems and nanocomposites containing 5 wt% silica.

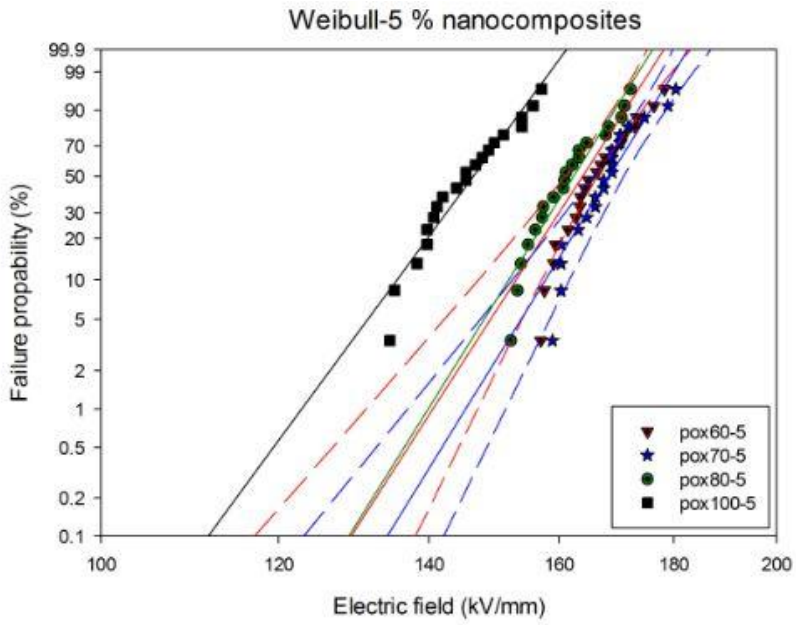

Figure 4-31 Weibull distribution of nanocomposites containing 5 wt% silica

It is evident from Figures 4-28 and 4-31 that there is a reduction in the electrical breakdown strength of the nanocomposite containing 80 phr hardener compared with the one containing 70 phr hardener. This behaviour is contrary to that seen in the corresponding unfilled systems and indicates that adding Nanopox into the unfilled system introduces changes in the reacting system. Apart from the interfacial effects, which will be investigated in the following chapter, as discussed above, the introduction of the Nanopox into the host resin reduces the hardener requirement due to the catalytic effects of the OH groups on the etherification of the epoxide groups. In such circumstances, the Pox80-5 system may have a certain amount of excess hardener. The same hypothesis is applied to the Pox90-5 and the Pox100-5 which contain a larger amount of excess hardener than their corresponding unfilled systems Ep90 and Ep100 respectively. This behaviour can be clarified in the FTIR spectra of the Ep100 and the Pox100-5 as illustrated in Figure 4-11. As a result, a significant reduction in E_b can be observed. On the other hand, the remaining systems contain an excess of epoxy. The presence of the hydroxyl groups and catalytic impurities in the Nanopox masterbatch could catalyse the etherification between epoxy-epoxy and/or epoxy-hydroxyl in the curing systems. Consequently, the amount of unreacted epoxy molecules is reduced, so, improving the E_b. Besides, a decrease in breakdown strength upon incorporating nanosilica into the polymer matrix has been reported elsewhere [30, 231-233], which

was ascribed to agglomeration of nano particles. However, the SEM images of the samples under study here show a good dispersion of nanosilica. In such cases, where the nano particles are reasonably well-dispersed, the breakdown strength has been related to the interface bonding between the silica particles and the epoxy resin, as proposed in the work done by Takahiro Imai et al. [30]. The interfacial effects of nano-fillers shall be discussed in detail in the following chapter. On the other hand, the Nanopox masterbatch can introduce more impurities and additives which are associated with the synthesis process, and hence, introduce more energy states in the band gaps and modify the trap distribution. As mentioned above, at high fields, conduction through such trap states may be possible, so, reduce E_b. The effective breakdown behaviour should be determined by a combination of stoichiometric and interfacial effects.

4.8 Dielectric response

Dielectric spectroscopy has been used extensively to analyse the dielectric behaviour of thermosets, especially to monitor the curing process of the reacting systems. However, this study concentrates on the analysis of the dielectric behaviour of fully cured epoxies, which means that the samples are at the highest obtainable crosslinking degree; that is, the samples are in the glassy state and are characterised by severely restricted molecular mobility. For solid epoxy materials, at low frequencies, two bulk effects dominate the dielectric properties: dipole orientation and ionic conductivity. At low temperatures, i.e. below the glass transition temperature, the molecules of a glassy state epoxy lose their long-range segmental mobility and, thus, dipolar relaxation cannot dominate the dielectric response. However, the dipolar orientation of short-range side groups attached to the main polymer chain can contribute to the dielectric properties. Therefore, an investigation into the temperature dependence of the dielectric response is required. As a material is heated, dipoles gain energy and mobility, such that they are progressively able to orient in the applied electric field. In addition, residual chloride ions and associated corresponding cations always exist in the epoxy, as a consequence of the synthesis process of bisphenol A epoxy. They constitute impurity ions within the system. The movement of such ions under an electric field can contribute to the ionic conductivity. It has been shown that concentrations well below 1 ppm are sufficient to cause a significant conduction [234], which increases dramatically with increasing temperature due to the increased polymer mobility. Therefore, ionic conductivity and

electrode polarisation effects usually dominate the dielectric behaviour at low frequencies and high temperatures.

Figure 4-32 shows plot of the real and imaginary parts of the permittivity for all the samples under study, at room temperature. At this temperature, all the samples are deep in their glassy state; the contributions of ionic conduction and electrode/interfacial polarisation are negligible, due to the restricted segmental motion. However, in such cases, the local orientation of polar side groups may contribute to increased permittivity. As mentioned above, the Ep80 is likely to be close to the optimum stoichiometry for an unfilled system, with the highest crosslinking degree and an extremely small amount of unreacted molecules. Therefore, it exhibits the lowest values in both real permittivity and loss factor. Conversely, an excess of either anhydride or epoxy, in terms of dangling ends, loops or sols, leads to an increase in the permittivity, due to polarisation effects associated with unreacted molecules, oxidation products and structural branches; this is related to the β-relaxation. The β-relaxation is usually observed at low frequencies and low temperatures [81]. It is likely that small peaks arrowed at ~ 0.1 Hz in the imaginary permittivity plots of all samples, except for the Ep80, are ascribed to this secondary relaxation. Lewis [235] suggested that the β-relaxation in an epoxy resin results from the motions of epoxy monomer molecules attached to the network by one end and that the magnitude of the β-peak is reduced by an increase in the crosslinking degree and a decrease in the concentration of partially reacted molecules. Pogany et al. [236] ascribed the β-relaxation in a non-stoichiometric epoxy formulation to the glass transition of a proportion of the resin that attains a low crosslinking degree. In this study, the DSC thermograms do not exhibit an intensive broad glass transition for non-stoichiometric formulations. Therefore, it is likely that the β-relaxation is due to the local orientation of polar side groups originating from unreacted and partially reacted anhydride or epoxy molecules, in response to the applied electric field. Besides, in the case of Ep60, a broad peak is observed at ~ 100 Hz in the imaginary permittivity plot (arrowed). This peak may also be due to the β-relaxation of small polar groups such as hydroxyl groups attached to the backbone of resin monomers or epoxy sols. Each type of polar groups is associated with a characteristic relaxation time, depending on the surrounding environment. The Ep60 contains a large excess of epoxy, which can lead to a considerable amount of hydroxyl groups and a low crosslinking degree. These small polar groups may orient themselves more readily than entangled anhydride/epoxy

molecules that exist in terms of dangling ends and loops. Therefore, the relaxation time of these polar groups may be shorter than that of other more bulky side groups. However, this analysis should not be taken too far, due to the uncertainties in the measurements. Kochetov et al. [237] also observed a similar broad β-relaxation ranging from 10-1000 Hz in an unfilled epoxy.

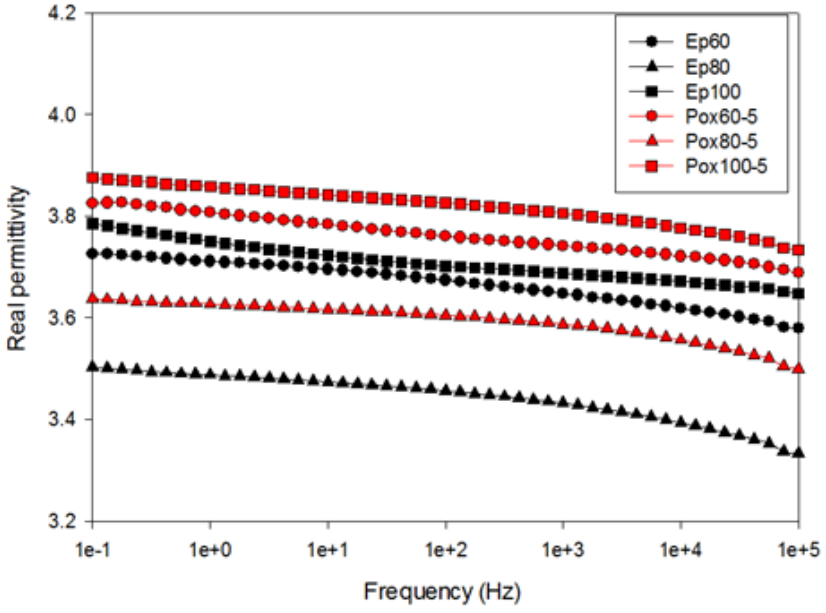

(a)

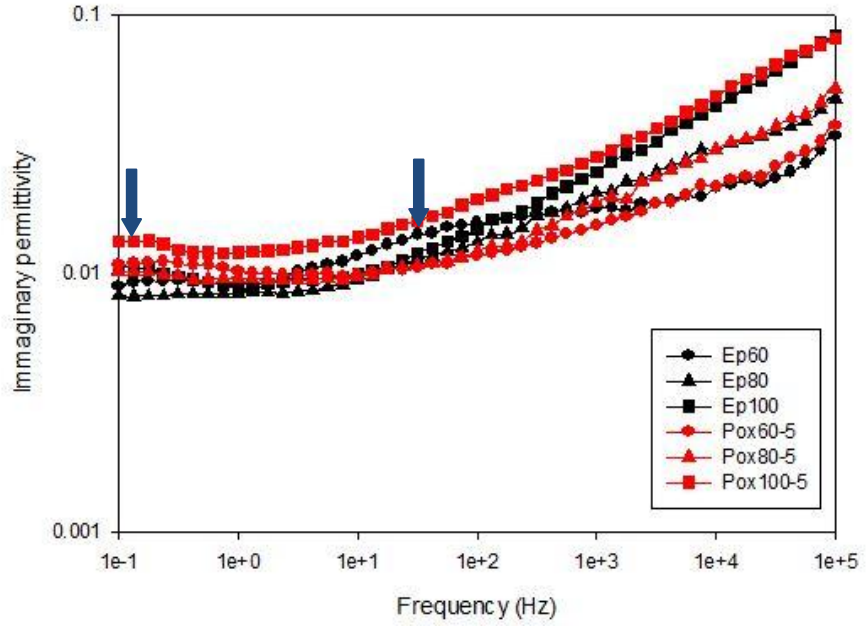

(b)

Figure 4-32 Complex permittivity plots (a) Real (b) Imaginary at room temperature

The addition of the Nanopox, which contains nanosilca fillers, could introduce more impurities/defects/additives in terms of excess hardener/epoxy molecules, or polar catalysts associated with the synthesis and the surface treatment of the nano-silica particles, and consequently, increase both the permittivity and the loss factor. Peaks observed in the imaginary plots at low frequencies are ascribed to the secondary β-relaxation, as discussed above. In the case of Pox60-5, there is no evidence of the β-relaxation peak associated with hydroxyl groups or epoxy sols, as that seen in the case of Ep60. As mentioned previously, the introduction of the Nanopox may catalyse etherification reactions between epoxy groups and hydroxyl groups attached to both the particle surface and the monomer backbone. As a result, the amount of "free" hydroxyl groups or epoxy sols is significantly reduced. In addition, the local polarisation of any loosely bound side branches in the interphase regions between the nanoparticles and the host resin matrix may contribute to this polarisation and manifest itself as a broad relaxation peak ranging from 0.1-10 Hz. Interfacial effects will be studied in detail in the following chapter. To facilitate a meaningful analysis, the temperature has been varied and Figure 4-33 shows the resulting temperature dependence of real permittivites obtained for all samples under study. It is clear that increasing the temperature leads to an increase in permittivity, due to the consequent increased mobility of the molecules in the network.

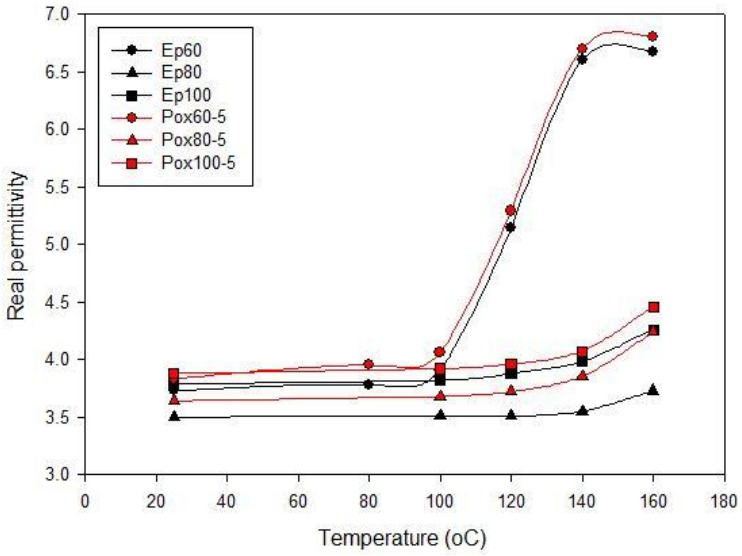

Figure 4-33 Real permittivity as a function of temperature, obtained at 0.1 Hz

Figures 4-34 to 4-36 show the real and imaginary parts of relative permittivity plots obtained for all samples at 120 ^{o}C, 140 ^{o}C, and 160 ^{o}C. At 120 ^{o}C, the systems containing 80 phr hardener and more are still in the glassy state; the real component is almost "flat" in a log-log plot and the imaginary part shows the power law behaviour in the low frequency range. Conversely, the Ep60 and Pox60-5 systems are in their rubbery state, a dramatic increase in permittivity can be observed. In addition, it is likely that a dispersion process start occurring in the range 0.1-1 Hz. It is necessary to note that, at 120 ^{o}C, there is no peak in the imaginary permittivity curves in the frequency range under study, which could be due to two reasons. The first relates to time/temperature superposition, in which variations in temperature displace relaxation processes along the frequency scale. An increase in temperature leads to an increase in molecular mobility, which facilitates polarisation and relaxation processes to occur faster, i.e. at higher frequencies. The second reason is that an increased contribution of the dispersion process at low frequencies and high temperatures may obscure the β-relaxation that manifests itself as a small and broad peak. A slight increase in the loss factor of the Pox80-5 and Pox100-5 compared to the Ep80 and Ep100, respectively, is due to the increased amount of impurities/defects/additives and a reduced crosslinking degree that is the consequence of the change in stoichiometry as proposed above. The continuous increase in temperature leads to the shift of the permittivity plots to the right due to the increase in the chain mobility of the network. At 140 ^{o}C, as the systems containing 80 phr hardener and more approach their T_gs, the power law behaviour in the low frequency range 0.1-1 Hz exhibits the slopes that are greater than those observed at 120 ^{o}C, indicating a loss process occurring at lower frequencies. Especially, at 40 ^{o}C above the T_g, the dispersion process appears more clearly in the systems Ep60 and Pox60-5. The dielectric spectra observed in the systems Ep60 and Pox60-5 reveal low frequency dispersion (LFD) and mid frequency dispersion (D). LFD occurs in carrier dominated systems where charge transport between clusters is possible [238]. However, different from dc conduction, in LFD, the charge transport is limited to the neighbouring clusters and hence, there is no complete percolation path to connect the two electrodes [239]. In addition, when the charge transport between the clusters is not possible, a loss peak (D) occurs with fractional power laws [239]. Both LFD and D dispersion are shifted to higher frequencies and become more pronounced at elevated temperatures. At 160 ^{o}C, the imaginary part observed in the systems Ep60 and Pox60-5

increase steadily at a slope of -1 at frequencies lower than the peak frequency of the dispersion D process. This behaviour, together with a sign of an increase in the real component of the relative permittivity in the same frequency range, indicates a LFD response. The slope smaller than -1 observed in the dispersion D process indicates the heterogeneity of large scale clusters and hence, a non-uniform charge transport. Moreover, the charge transport between clusters can only occur at temperatures higher than T_g, i.e. significant segmental motions are required. In addition, the dc conduction may also occur as a parallel process at high temperatures. This behaviour has been reported in the work by Dodd et al [240-241]. LFD has been considered as a bulk material property, while the dispersion D has been assumed to be an interfacial phenomenon [240]. The addition of nanosilica is likely to enhance the charge transport between clusters due to the increased cluster size and/or the increased amount of clusters. This behaviour is evinced by a broader relaxation of the dispersion D observed in the Pox60-5 or a smaller slope of the power law behaviour observed in the Pox100-5 in the low frequency range, compared to their corresponding unfilled epoxies. It is necessary to note that at low frequencies, the loss factor of the Pox60-5 is smaller than that of the Ep60, while the remaining nanocomposite systems show higher loss factors than their corresponding unfilled ones. This observation is in good agreement with the breakdown data concerning the modification of the crosslinking degree due to the catalytic effects of the hydroxyl groups or impurities on the epoxy homopolymerisation.

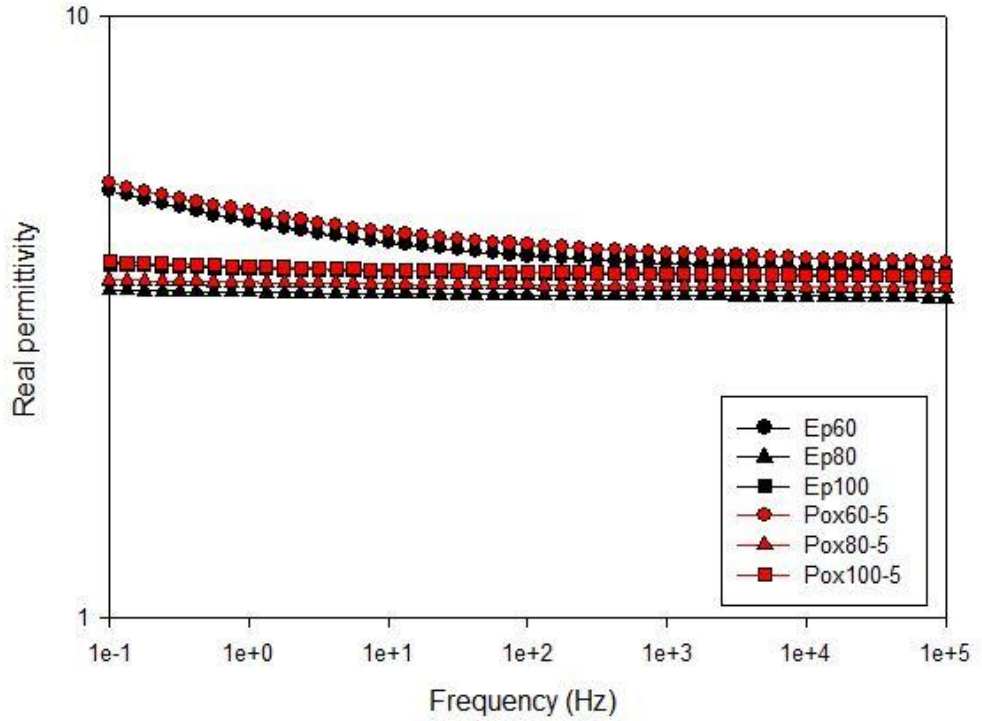

(a)

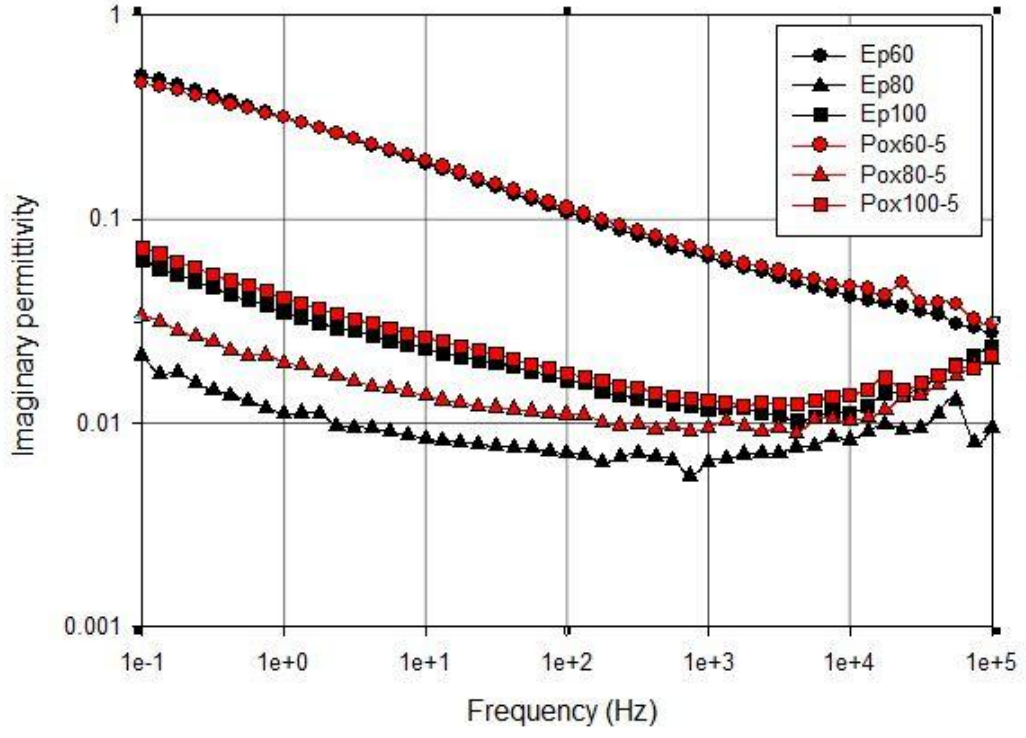

(b)

Figure 4-34 Complex permittivity plots (a) Real (b) Imaginary at 120 ^{o}C

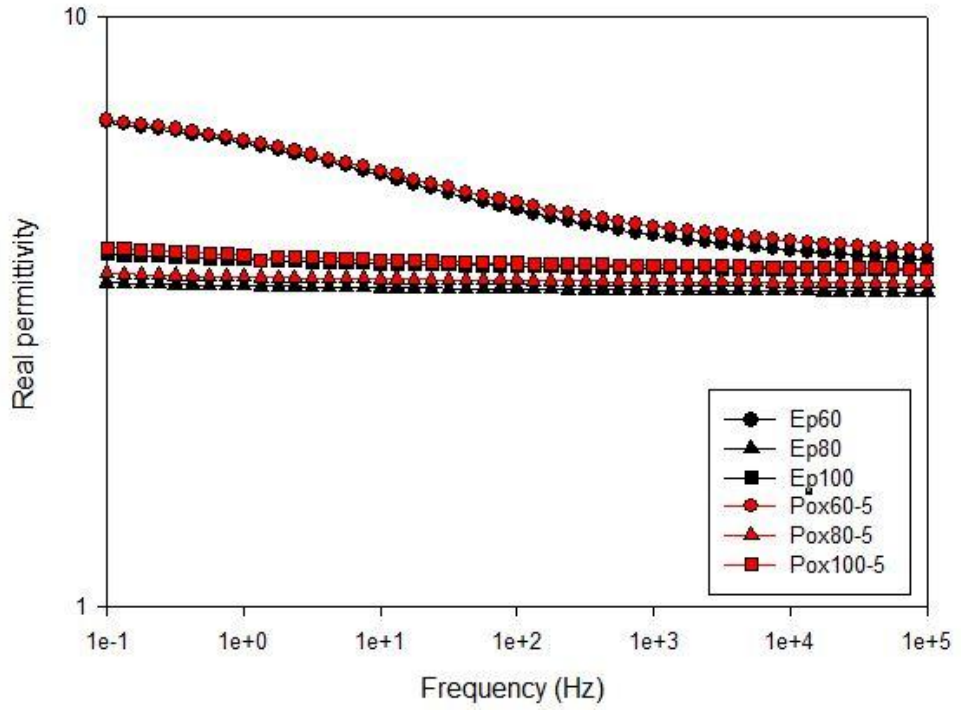

(a)

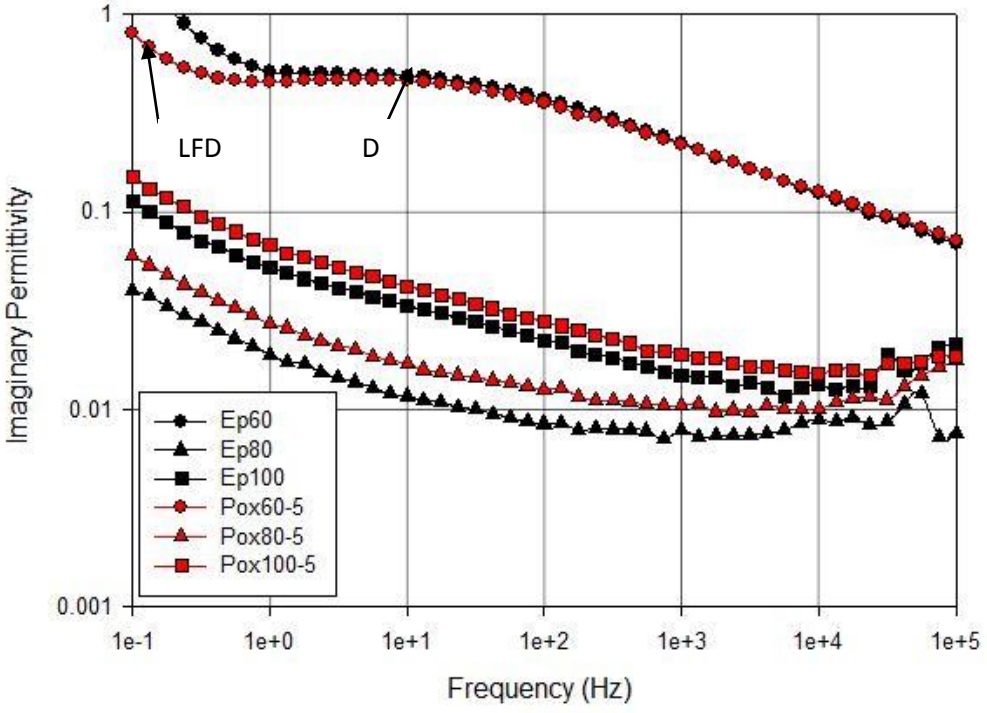

(b)

Figure 4-35 Complex permittivity plots (a) Real (b) Imaginary at 140 ^{o}C

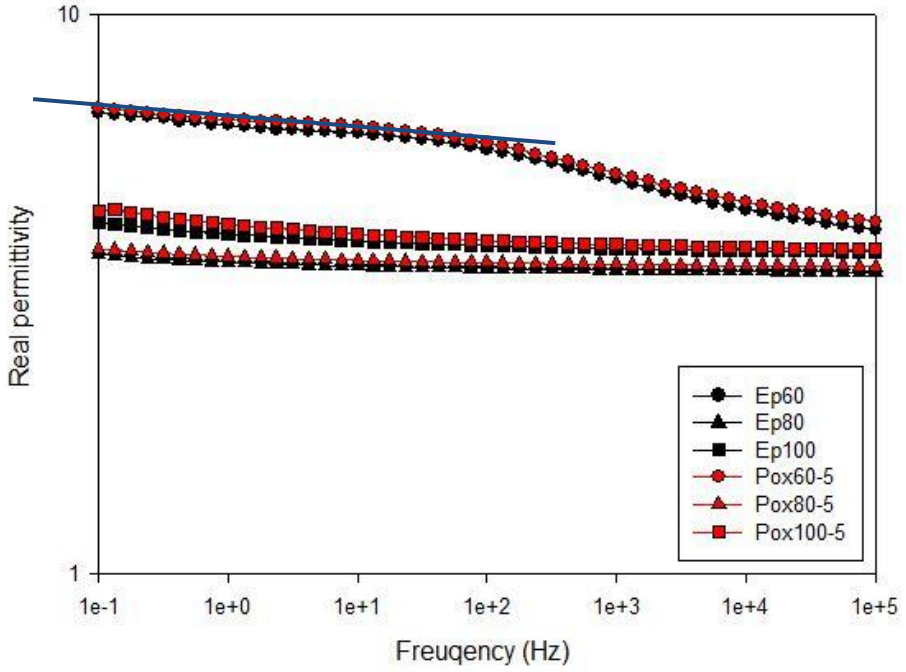

(a)

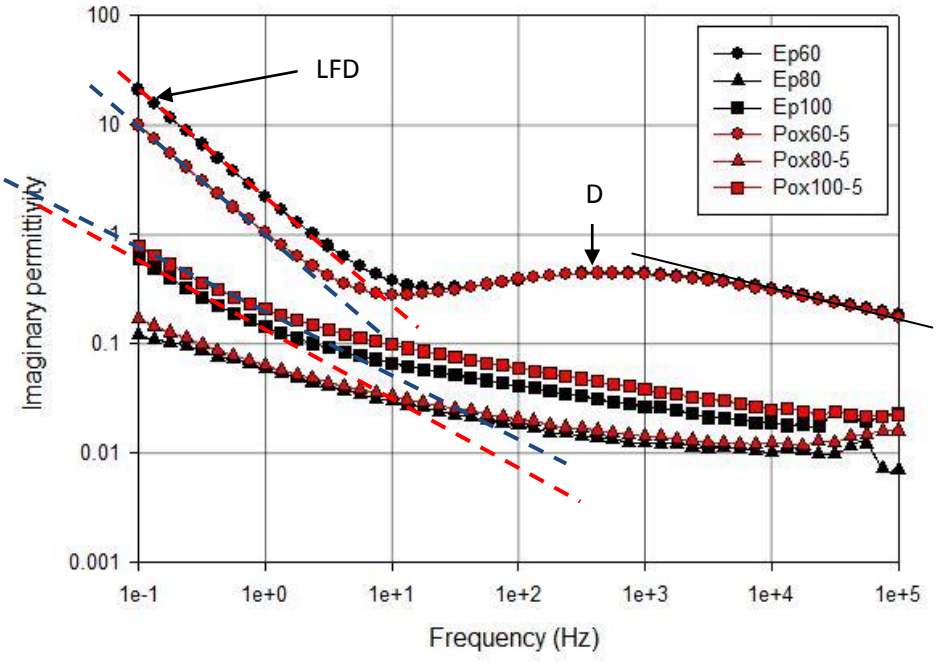

(b)

Figure 4-36 Complex permittivity plots (a) Real (b) Imaginary at 160 ^{o}C

4.9 Chapter summary

The stoichiometry markedly influences T_g and the electrical breakdown strength of the unfilled epoxies and the nanocomposites. The T_g value peaks at the optimum proportion, and decreases at different rates away from the optimum. While an excess of hardener exerts no marked effect on T_g, it leads to a dramatic decrease in E_b, probably due to oxidation of the unreacted hardener molecules. Conversely, systems containing an excess of epoxy show less pronounced effects on E_b, whereas a significant reduction in T_g can be observed when compared to the optimum system. This behaviour is shown in Figure 4-38. The introduction of Nanopox into the host resin not only increases the amount of impurities, but also induces changes in the stoichiometry of the reacting systems. As a result, for the systems containing excess epoxy, the T_g stays nearly unchanged due to the homopolymerisation reactions, while the ones containing excess hardener exhibit reduced T_g's due to the lower degree of crosslinking. In addition, changes in stoichiometry lead to changes in the electrical breakdown strength. At 5 wt% nanosilica loading, the samples show a good dispersion of nanofillers in the resin matrix, as revealed by SEM. However, the breakdown strength reduces significantly for the systems containing 80 phr hardener and more, suggesting that more excess hardener is present in these systems. The remaining systems, which contain an excess of epoxy, show almost no change in E_b due to the modification of the crosslinking degree as a result of the catalytic effects of impurities and/or hydroxyl groups located on the nanoparticle surface. There may be a small contribution of interfacial effects to the reduction in T_g and E_b upon the addition of nanosilica into the resin matrix. This interfacial behaviour of nanofillers will be discussed in the following chapter. The existence of excess hardener can be observed in the FTIR spectra.

Meanwhile, neither changes in stoichiometry nor addition of nanosilica produce a significant effect on the space charge behaviour of the samples. Only a small amount of homocharge can be observed near the cathode for all the cases, and then the injection is likely to be suppressed. No internal space charge can be observed at other locations within the bulk of the samples. Moreover, the quick decay of such injected charges suggests a distribution of only shallow traps near the sample surfaces. Therefore, one can conclude that, in the well-dispersed samples, space charge will not be a major factor in influencing electrical properties, at least at room temperature, which is far below T_g.

However, the dielectric permittivity values are affected by the stoichiometry and the presence of nanosilica. The variations of the real permittivity and loss factor support the proposed stoichiometric effect on T_g and E_b behaviours observed above. The excess hardener/epoxy systems show increased real and imaginary permittivity values. Meanwhile, the systems containing an excess hardener attain a lower crosslinking degree, and hence, a reduced T_g and a higher permittivity. The changes in the loss factor upon the introduction of the Nanopox also support this explanation about changes in stoichiometry and its impact on E_b. The higher the loss factor, the lower the E_b. At temperatures much higher than T_g, LFD behaviours can be observed in both the unfilled epoxy and nanocomposite. The LFD is shifted to higher frequencies and becomes more pronounced at elevated temperatures. In addition, it is likely that the addition of nanosilica leads to an increase in the size of clusters and/or in the amount of clusters and hence, enhances the inter-cluster charge transport.

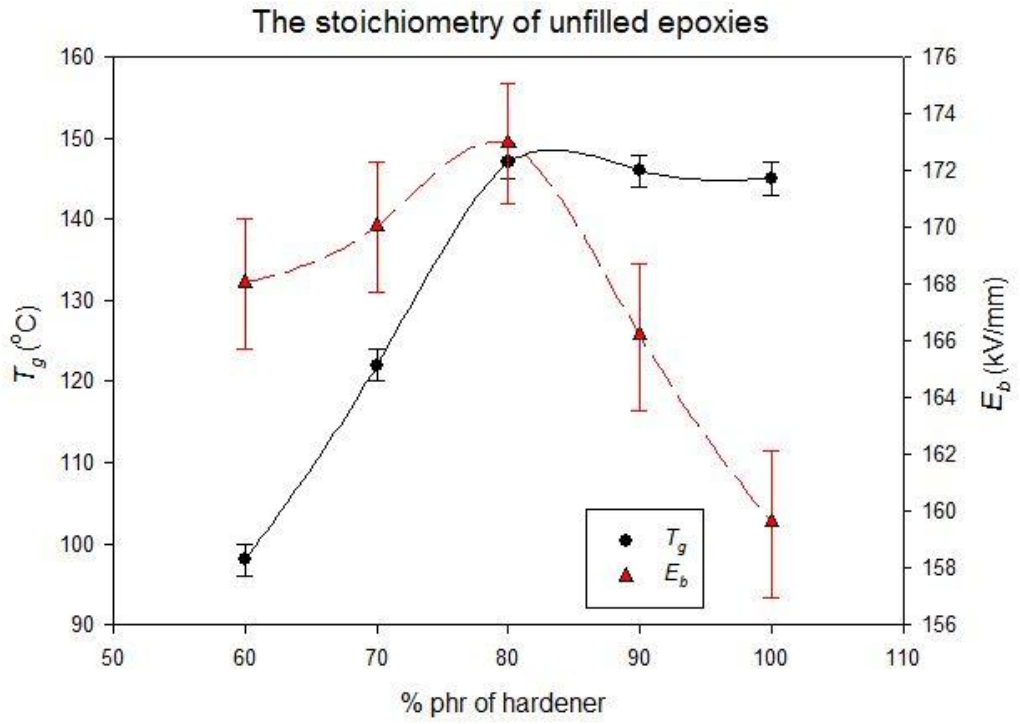

Figure 4-37 Effects of stoichiometry on T_g (standard error) and E_b (90% confidence interval) of unfilled epoxies

Chapter 5 Interfacial effects on epoxy-based composites

5.1 Introduction

In the previous chapter, the effect of stoichiometry on material properties was investigated. This work also revealed changes in the performance of unfilled systems based on different resin ratios with the introduction of the Nanopox masterbatch at 5 wt% nanosilica loading level, as a result of changes in the effective stoichiometry of the matrix due to reactions with hydroxyl groups on the particle surface and/or catalytic impurities present in the masterbatch. These hydroxyl groups and impurities are believed to modify the curing mechanism of reacting systems in such a manner so that etherification reactions are favoured. However, besides the stoichiometric effect, the incorporation of nanosilica particles could exert additional influences on material properties due to interactions at the interfaces of the nanofiller with the resin matrix. Numerous studies have been conducted with various nano-fillers, including silica, carbon nano tubes (CNT), zinc oxide (ZnO), etc. [242-244]. Such investigations have revealed that nanocomposites exhibit different behaviours than the bulk polymers and their counterpart micro-filled composites [245-246]. The specific properties of nanocomposites are believed to be largely associated with interfaces and the formation of interphases located between the nanofillers and the unperturbed matrix. Investigations have suggested that the thickness of such interphases falls in the nanoscopic scale [247-248]. Due to the small size of nanofillers, the dimension of these interphases become comparable to those of the nanofillers themselves and, consequently, govern the macroscopic properties of the material if the nanofiller concentration if sufficiently high. The inclusion of such nano-fillers within a polymer matrix could affect material properties in both positive and negative ways. For example, Tanaka et al. [249] reported an enhancement in the partial discharge resistance of epoxy clay nanocomposite compared to the unfilled system. The electric discharge endurance was also found to be improved by the presence of nanofillers [250-251]. Conversely,

Wang et al. [252] reported adverse effects on the space charge accumulation of nanocomposites filled with SiO_2 and Al_2O_3 compared to the unfilled epoxy. In this study, heterocharge was observed near the cathode. Various hypotheses have been proposed in an attempt to explain the widespread variations seen in material properties on the addition of nanofillers into the polymer matrix, such as the "multi-core model" by Tanaka [253], or the model by Lewis [254], or the "water-shell" model [255]. In all the proposed models, the role of interfaces and interactions between the polymer matrix and nanofillers are highlighted. Therefore, this chapter concentrates on interfacial effects, including the size effect, due to the incorporation of nanosilca into the epoxy matrix.

5.2 Samples under investigation

In order to study interfacial effects in epoxy nanocomposites, two kinds of nano-silica have been employed. The Nanopox specifies that the grade used here includes surface treated nano-silica with an average diameter of about 20 nm; the 3M master-batch contains surface treated particles with an average diameter of about 100 nm. It is important to note that there are several methods of surface treatment [143, 146-147] and that each method will produce nanofillers with different surface chemistry and, hence, different interfacial characteristics. For example, Wu et al. [256] compared the effect of different pre-treatments of carbon fibres and concluded that the surface functional groups on the fillers produced acceleration effects on the cure mechanism and this effect was closely related to the specific surface area of the filler. Following the studies conducted in the previous chapter, for the sake of brevity, only the resin stoichiometry of 100:80:1 was subsequently used, because this ratio was likely to be the best choice from the point of view of insulation performance among the unfilled systems. The nano-silica was incorporated into the epoxy matrix at various loading levels. In addition, microscopic silica particles were also introduced into the epoxy resin, to provide a more comprehensive understanding of the effect of filler size. Also, the 3M and Nanopox master-batches may contain different epoxy formulations, i.e. different amounts of impurities, additives, etc., that may impact on cured properties.

Table 5-1 List of samples under interfacial study

Sample code	Resin ratio	%wt micro-silica	%wt nano-silica	Type of nanosilica
Ep80	100:80:1	0	0	N/A
Pox80-1	100:80:1	0	1	Nanopox
Pox80-2	100:80:1	0	2	Nanopox
Pox80-5	100:80:1	0	5	Nanopox
Pox80-12.5	100:80:1	0	12.5	Nanopox
3M-1	100:80:1	0	1	3M
3M-2	100:80:1	0	2	3M
3M-5	100:80:1	0	5	3M
3M-12.5	100:80:1	0	12.5	3M
Ep80-5m	100:80:1	5	0	N/A
Ep80-12.5m	100:80:1	12.5	0	N/A

5.3 Fourier Transform Infrared Spectroscopy

Figure 5-1 shows IR spectra of the host resin MY 740, the Nanopox E 470 and the 3M master-batch. Again, the main difference between the spectra of the two master-batch systems and that of the host resin relates to the presence of silica particles, which introduces new chemical bonds in the molecular structure. The IR bands observed at around 1082 and 460 cm^{-1} are assigned to the stretching mode and the bending mode of Si-O-Si bonds respectively [204-205]. The 3M system contains 49.8 wt% nanosilica, while the Nanopox contains about 40 wt%. As a result, the 3M system exhibits higher absorption peaks at these IR wavenumbers than the Nanopox, as shown in Figure 5-1. The above IR peaks are not observed in the spectrum of the unfilled Ep80. In addition, the broad flat peak spanning the range from 3500-3200 cm^{-1} is attributed to the intermolecular H-bonded OH groups (arrowed). The existence of this feature indicates that more hydroxyl groups are present in the master-batch systems, which may be attached to the surface of nanosilica and/or the epoxy monomer backbones. The

presence of epoxide groups is confirmed in all the three resin systems by the sharp peaks at about 913 cm^{-1} and the small peaks at 3057 cm^{-1} due to stretching of the C-O and C-H of the oxirane rings respectively.

Figures 5-2 and 5-3 show representative FTIR spectra obtained from a number of cured nanocomposites. It is evident that the addition of nanosilica does not introduce any new curing reactions. No new chemical bonds are observed in the FTIR spectra of the nanocomposites compared to the unfilled Ep80, except the Si-O-Si feature at about 1100-1110 cm^{-1}, which is due to the presence of the nanosilica. The IR band at around 1734 cm^{-1} confirms the existence of the C=O stretching in the ester groups. Meanwhile, the bands at 1244-1035 cm^{-1} are assigned to the stretching vibration of C-O linkages present in the epoxy resin, hardener, and ester, as well as the ether linkages formed by any etherification reactions. Therefore, in principle, the curing mechanism of the unfilled epoxy system and the nanocomposites is based on the competition of esterification and etherification reactions. However, it is impossible to derive the quantitative contribution from each of these two types of reaction, due to the overlapping of different IR bands present in the spectra.

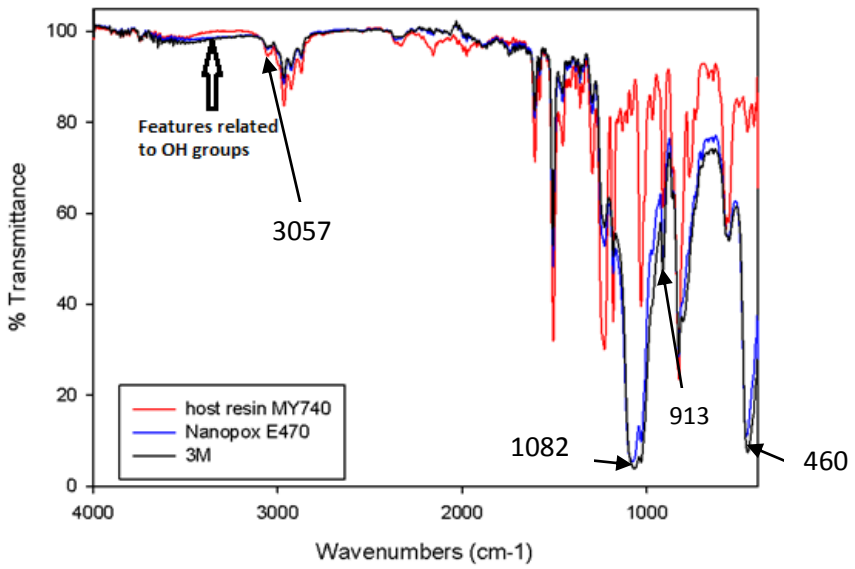

Figure 5-1 FTIR spectra of resin MY 740, Nanopox E 470 and 3M master-batch

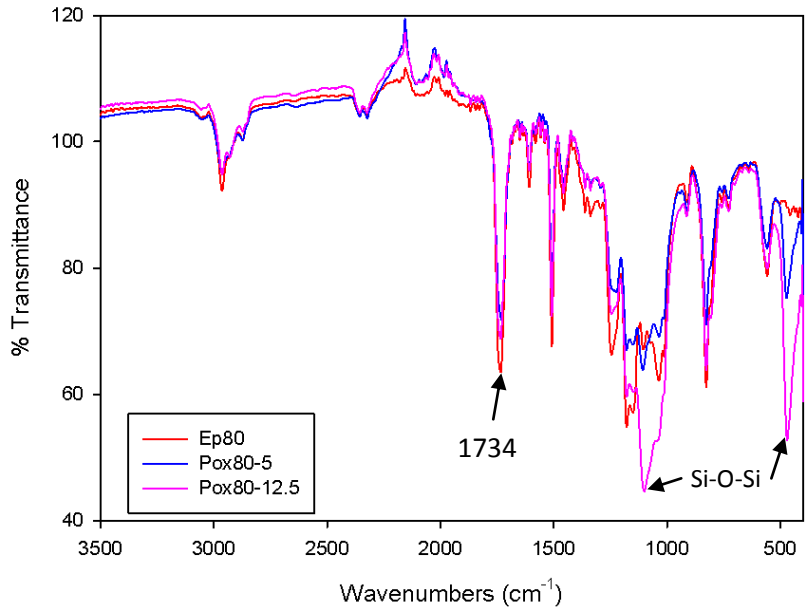

Figure 5-2 FTIR spectra of epoxy-based systems containing Nanopox

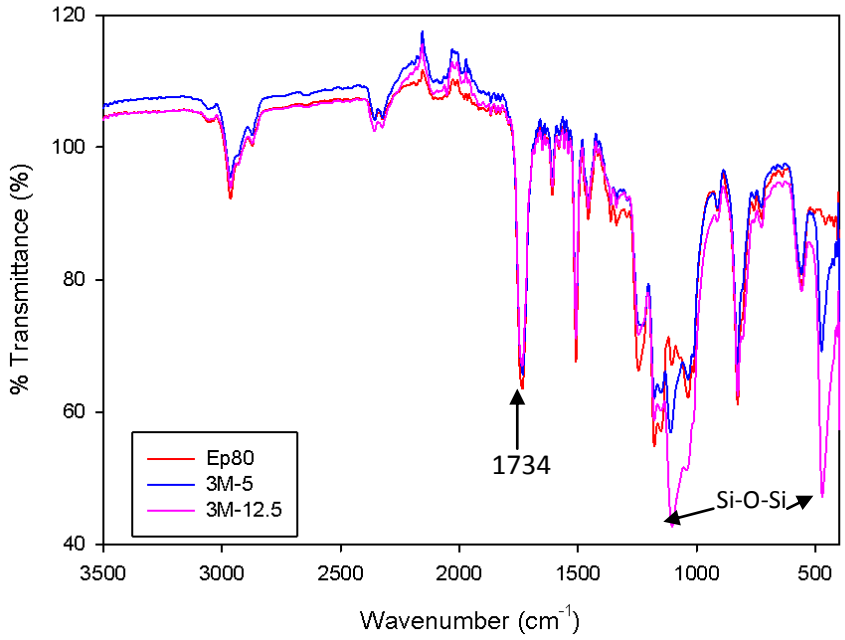

Figure 5-3 FTIR spectra of epoxy-based systems containing 3M

5.4 Scanning electron microscopy (SEM)

Figure 5-4(a) shows a low magnification image of an internal fracture surface of unfilled Ep80. The surface appears to be relatively flat. Increasing the magnification reveals the typical granular matrix structure, as shown in Figure 5-4(b). The addition of nanosilica introduces new features to the fracture surfaces. Figure 5-5 shows low magnification images of fracture surfaces of epoxy systems that contain Nanopox at different loading levels. Evidently, at this magnification, the topography of the fracture surfaces in these nanocomposites is different from those observed in the corresponding unfilled systems, with the appearance of the curved fractography features (arrowed) or rougher surfaces at higher filler loading (arrowed). The higher magnification images again reveal the dramatic effects of the inclusion of nanosilica on the texture of the fracture surfaces. If the presence of nanosilica is considered to affect the topography of the fracture surfaces, it is reasonable to evaluate the uniformity of the dispersion based on the variability of the surface texture. It is evident from Figure 5-6 that the samples are relatively uniform although there are some variations in local concentration of nanosilica on the scale of tens to hundreds of micrometers. The key point is that the surface texture gets rougher with larger scale features, which imply agglomeration. Indeed, SEM images of the Pox80-12.5 reveal such features with a size up to 500 nm, as indicated by the arrows in Figure 5-6.

The introduction of the 3M master-batch produces surfaces with fracture topographies that differ from both the unfilled system and those containing the Nanopox, as shown in Figure 5-7. Also, this figure reveals an area damaged by radiation, which is clearly visible as a darker rectangle (arrowed) in Figure 5-7(a), after focusing on the bright dust particle. However, no cracks or voids are evident in any of these samples. Increasing the magnification reveals the good dispersion of the nanosilica in both the 3M-5 and 3M-12.5, as shown in Figure 5-8. Despite the larger filler size, features less than 500 nm in size are observed. This suggests that the dispersion of nanosilica is better in the 3M systems than in the Nanopox ones.

In contrast to the systems described above, the incorporation of micro silica appears to have a dramatic effect on dispersion. The micro silica is observed to be deposited at the bottom of sample Ep80-12.5m, as shown in Figure 5-9. This indicates a very poor

dispersion of the filler within the matrix, due to the incompatibility of the fillers and the epoxy. Also, some cracks/voids can be observed in this sample (arrowed), as shown in Figure 5-9(d). Increasing the magnification reveals the same fine scale granularity in the epoxy matrix, as in the unfilled Ep80. The differences in the dispersion state of the fillers, obviously, are expected to induce different effects on the material properties.

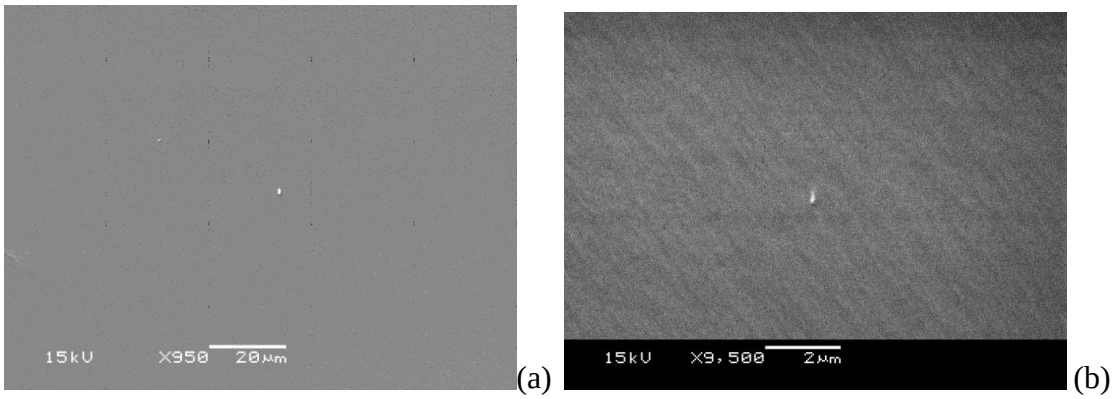

(a) (b)

Figure 5-4 SEM images of the unfilled Ep80 at (a) low maginification, (b) high magnification

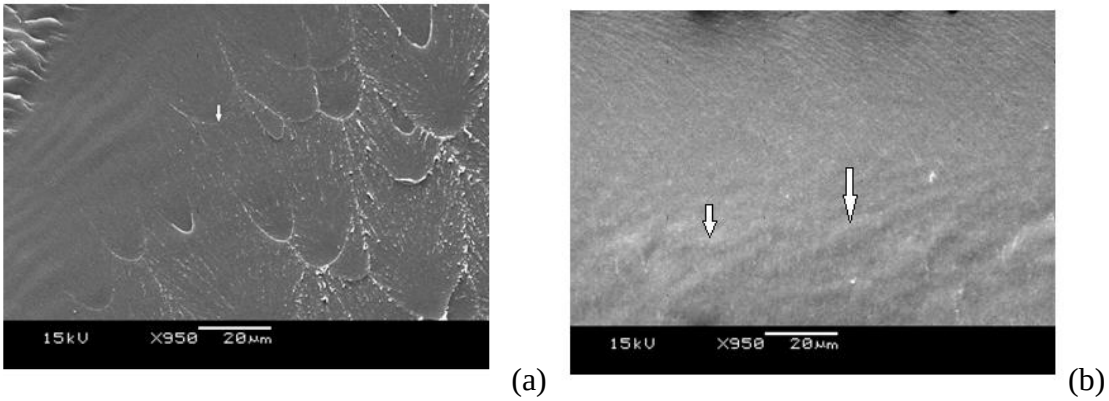

(a) (b)

Figure 5-5 SEM images at low magnification of Pox80-5 with curved fractography feature (a)) and Pox80-12.5 with rougher surface (b)

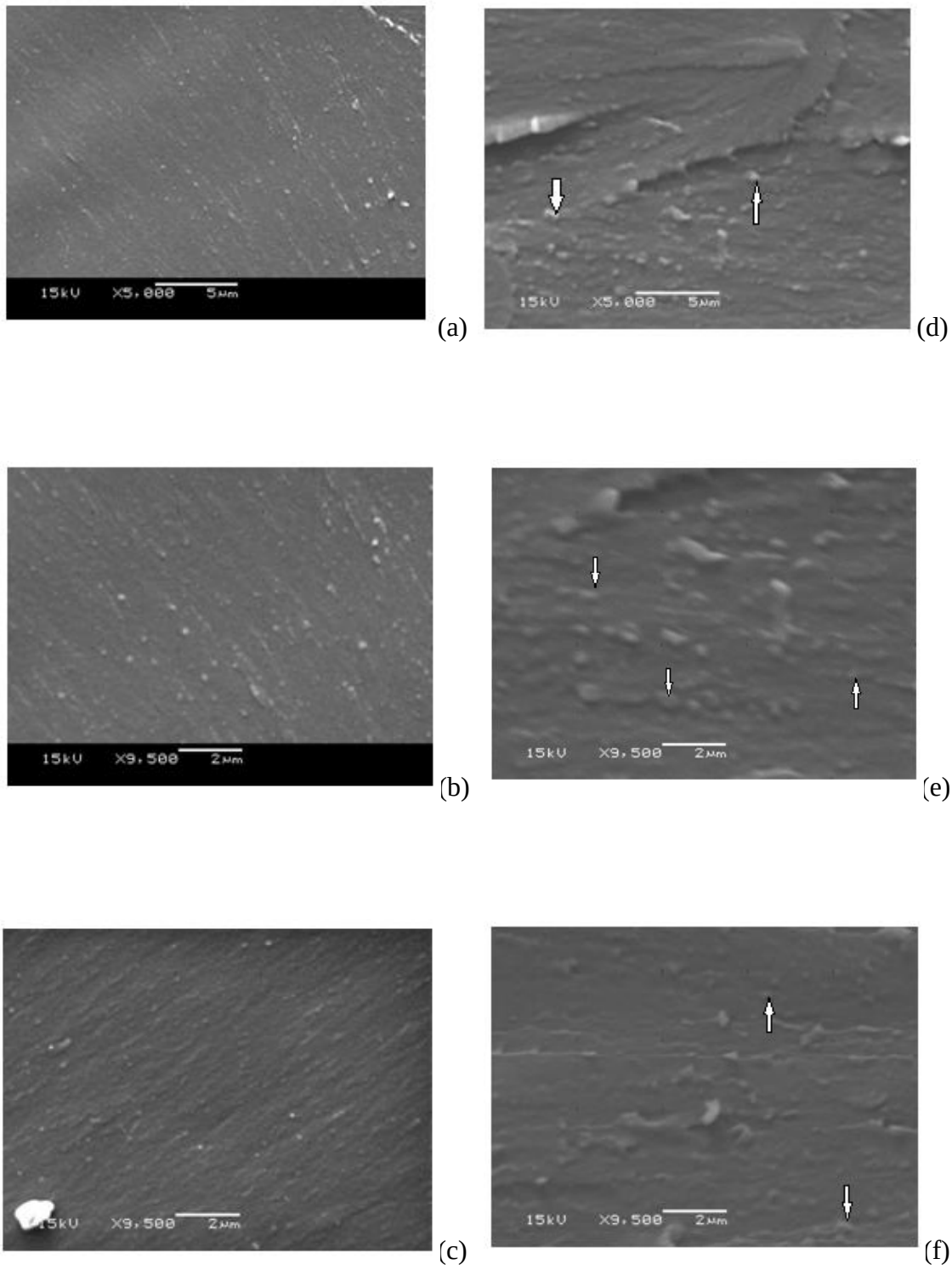

Figure 5-6 High magnification SEM images of the Pox80-5 (a)-(c) and Pox80-12.5 (d)-(f) at different locations

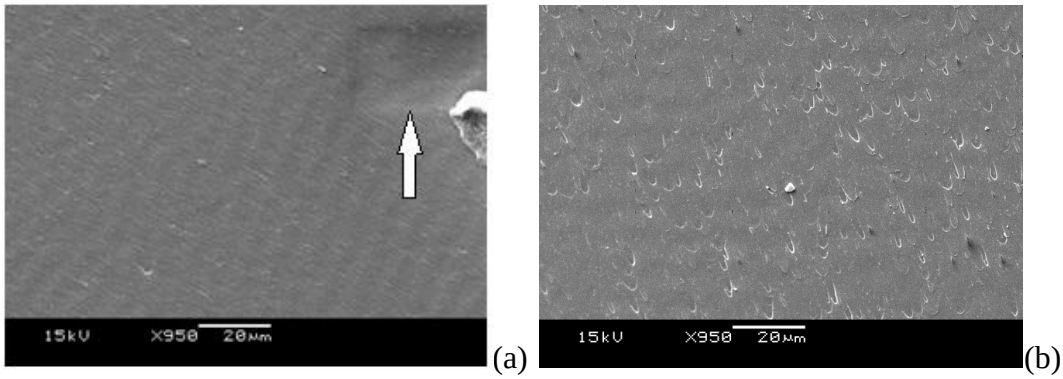

(a) (b)

Figure 5-7 SEM images at low magnification of 3M-5 (a) and 3M-12.5 (b)

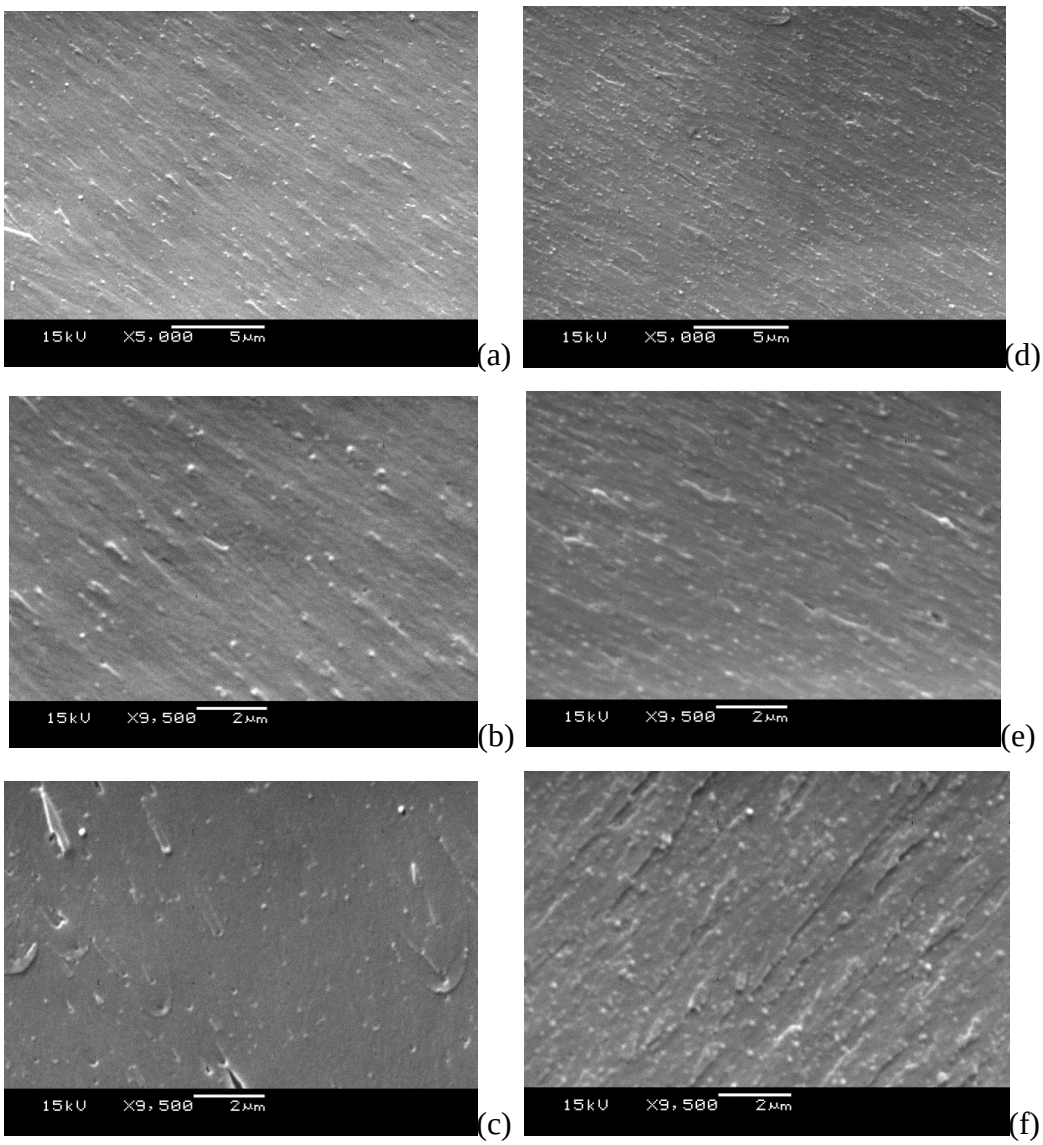

(a) (d)

(b) (e)

(c) (f)

Figure 5-8 High magnification SEM images of the 3M-5 (a)-(c) and 3M-12.5 (d)-(f) at different locations

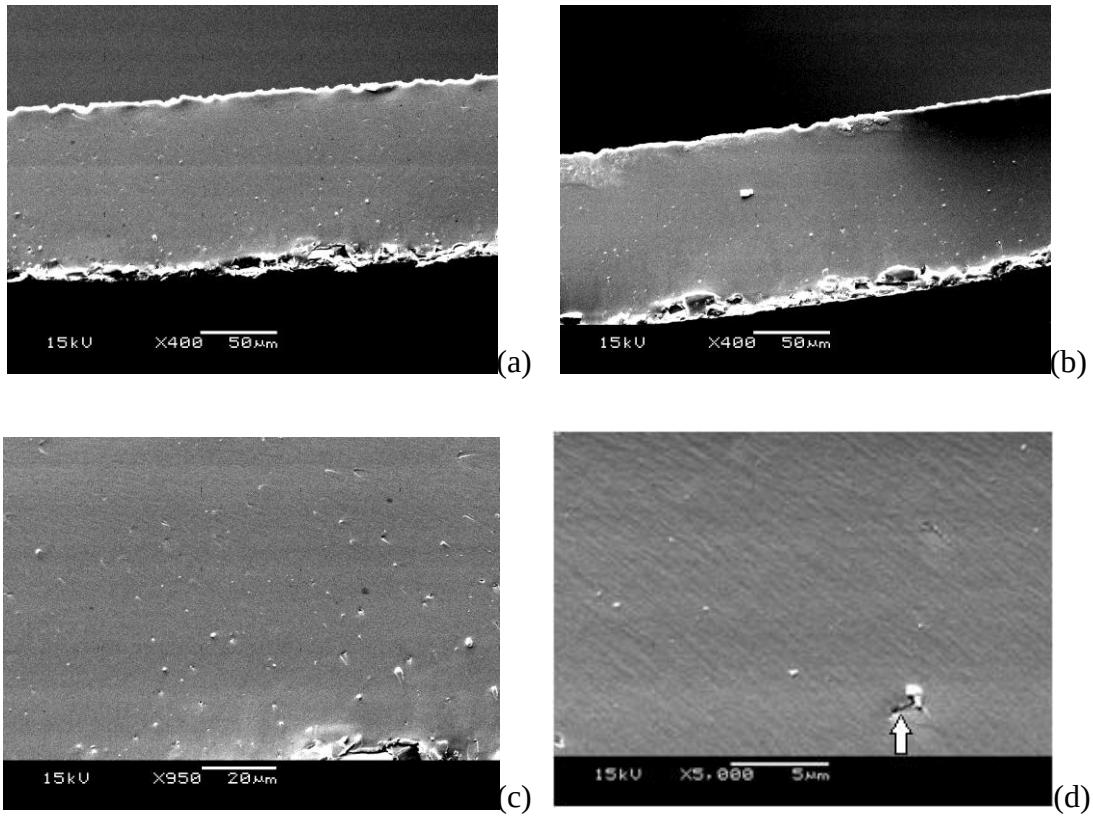

Figure 5-9 SEM images of the Ep80-12.5m at (a)-(c) low maginification, (d) high magnification at different locations

5.5 Thermal characterisation

The influence of numerous parameters on the glass transition of many different material systems has been studied and such work has suggested that, in the case of nanostructured systems, interactions at the polymer-filler interface are a key factor that affects the glass transition behaviour [257-259]. For example, dielectric studies of propylene glycol and two poly(propylene glycol)s (PPGs) of different molecular weight confined within controlled pore glasses [260] have revealed a retardation and broadening of the α-relaxation process associated with T_g, and the existence of an additional relaxation attributed to the interaction of a few layers (hydrogen bonding effect) of the confined liquid with the surface of the pore. Elsewhere, T_g has been found to vary in a non-monotonic manner [261], where T_g first decreases and then increases as the pore size is reduced, depending upon whether intrinsic size effects or interfacial interactions dominate. An initial increase in T_g followed by a reduction in T_g with higher filler percentage was observed for a poly(styrene butylacrylate) latex/nano-ZnO

composite [262]. Cases have been reported where T_g was found to increase with nanofiller loading level [263-265], whereas a decrease in T_g was observed elsewhere [266]. A study of the mechanical relaxation behaviour of poly(vinyl alcohol)(PVA)/silica nanocomposites revealed two relaxations, which were attributed to the glass transition of the PVA matrix (43 ^{o}C) and segments of PVA chains confined by the surface of silica nanoparticles (83 ^{o}C). This study went on to deduce that the thickness of the interfacial immobilised layer was 5-10 nm and dependent upon composition [267]. As the filler size is in the nanoscale range, the volume fraction of the interaction region increases with the increase in the interfacial area of the polymer and nanofillers. This is believed to be the basis for changes in many of the properties of nanocomposites.

Figure 5-10 shows typical DSC scans obtained from some extreme cases. It is evident that, while the temperature of the glass transition varies with the loading percentage of nano-silica, there is no evidence of multiple transition temperatures or extensive broadening of T_g, suggesting that, in terms of molecular mobility, all of the systems shown are reasonably uniform. Table 5-2 summarises the important information extracted from the DSC scans for the glass transition. Once again, the width of the glass transition ΔT shows no clear trend when the uncertainties in the measurements are considered, except in the case of Pox80-12.5. Therefore, any comparison should be based on other characteristics of the glass transition. The change in heat capacity per unit mass of polymer, ΔC_p^*, reveals a good correlation with the glass transition temperature T_g, as shown in Figures 5-11 and 5-12. The reduction in T_g is associated with an increase in ΔC_p^* and vice versa, which is related to the molecular mobility in the system.

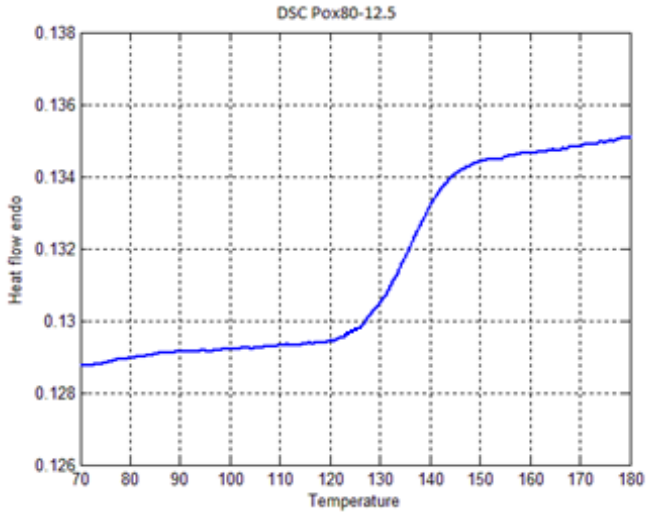

(a)

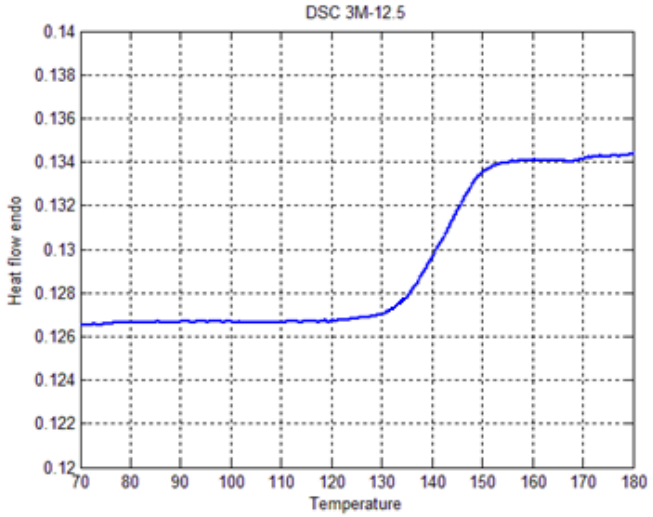

(b)

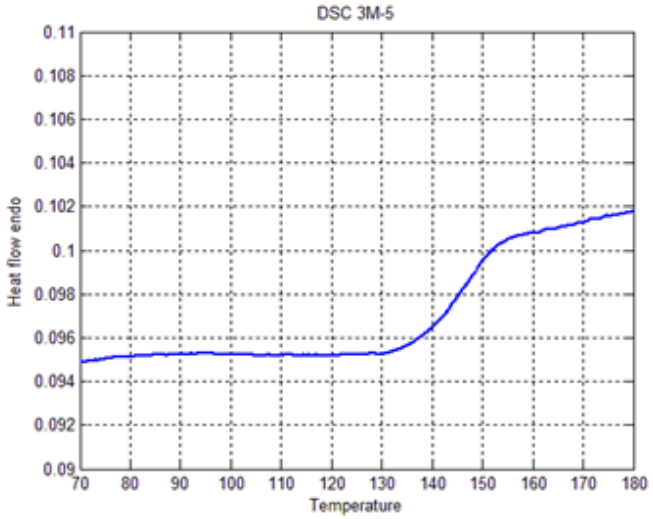

(c)

Figure 5-10 Typical DSC scans of some samples under interfacial study

Table 5-2 Thermal characteristics of samples under interfacial study

Sample codes	T_g (°C) ±2 °C	ΔT (°C) ±2 °C	ΔC_p^* x10^{-1}(J/g°C) ±0.05
Ep80	147	20	5.5
Pox80-1	146	22	5.6
Pox80-2	143	22	6.0
Pox80-5	140	25	6.5
Pox80-12.5	135	28	7.1
3M-1	146	22	5.4
3M-2	145	22	5.5
3M-5	145	23	5.6
3M-12.5	143	23	5.7
Ep80-5m	146	25	5.6
Ep80-12.5m	145	25	5.7

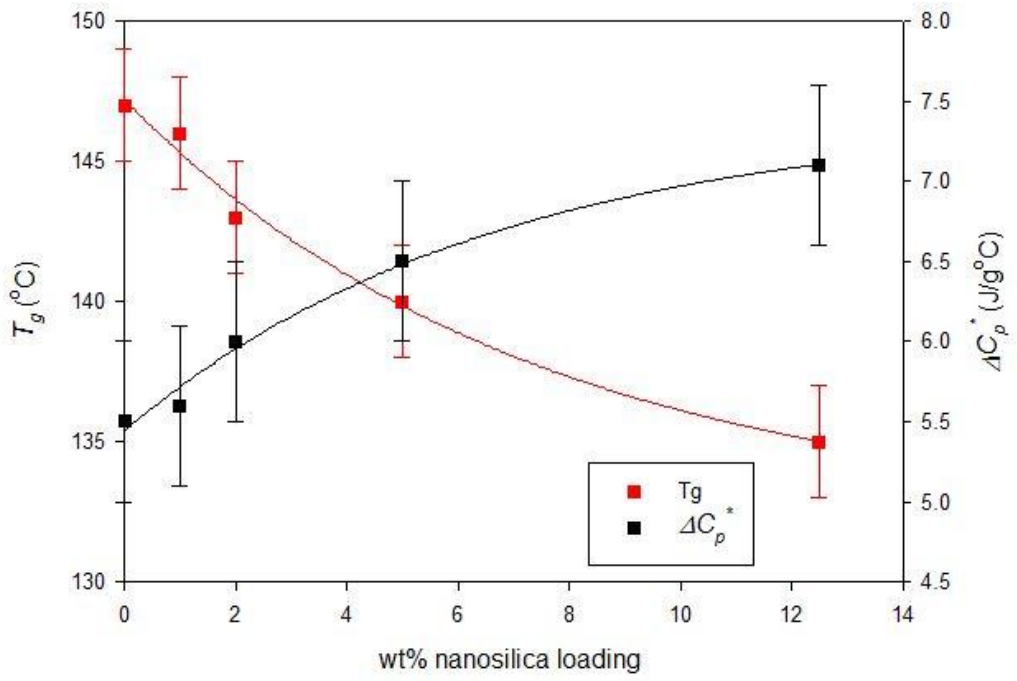

Figure 5-11 The glass transition temperature and heat capacity of Nanopox systems (standard errors based on 5 samples)

Figure 5-11 shows the effects on T_g of adding Nanopox into the epoxy system. In general, increasing the filler loading level results in a reduction in T_g. Comparable behaviour was reported by Sun et al. [182], who found a significant reduction in the T_g of nanocomposites, compared with the unfilled epoxy or counterparts filled with micro-fillers. This behaviour was explained by the surface chemistry of the nanofillers and interactions at the filler-resin matrix interfaces; the absorbed water and bonded organics on the surface of nanosilica enhanced the polymer dynamics due to the extra free volume at the resin-filler interfaces and, hence, reduced T_g and increased the dielectric loss. Tomer et al. [268] observed a systematic decrease in T_g with increasing inorganic content of both barium titanate and organically modilfied montmorillonite fillers. Such a reduction was claimed to be due to disruption of the epoxy crosslinking as a result of the fillers. It is well-known that the T_g of a polymer system depends on a number of factors, including changes in the tacticity, molecular weight, crosslinking degree and the amount of reaction residue acting as a plasticiser [269]. Taking into account the stoichiometric effects discussed in chapter 4, the introduction of nanosilica could change the chemical balance in the reacting systems due to the catalytic effect of the hydroxyl groups and/or impurities present in the Nanopox. These moieties may catalyse the etherification of the epoxide groups, so leading to an effective excess of hardener. Cheng et al. [270] found that the etherification reaction usually leads to a lower degree of curing at gelation. Therefore, homopolymerisation is supposed to produce a structure that is characterised by a higher branching degree than the esterification reaction between the epoxy and anhydride. As a result of a lower crosslinking degree, the T_g is reduced. Therefore, the effective reduction in T_g results from a combination of both factors, namely the stoichiometric effect and extra free volume introduced at interfaces. As a consequence, the rate of decrease is non-linear with the nano-filler loading percentage. Furthermore, at high filler loading levels up to 12.5 %wt, it is likely that the decrease in T_g is slowed down, possibly as a result of increasing the degree of nanoparticle interaction/aggregation. First, from the point of view of the stoichiometric effects, agglomeration of nano-particles may reduce the amount of any hydroxyl groups on the particle surface available for etherification reactions with epoxy, so leading to a reduced effective excess of hardener. As a result, the decrease in T_g due to this stoichiometric effect is smaller. Second, agglomeration of nano-particles will increase the effective filler size and, hence, the volume fraction of interphase regions will be

reduced. Therefore, the contribution of extra free volume to the reduction of T_g will be decreased. Concepts concerning extra free volume are related to the so-called "multi-core model" proposed by Tanaka [253], which suggests that the introduction of nano-fillers into a polymer matrix can create a number of distinct interphase regions, each with nanometric dimensions. First, chemical interactions between the matrix and the nanoparticle might lead to tightly bound regions, in which molecular mobility is dramatically reduced. Surrounding this, it is suggested that regions of increased free volume may exist. Evidently, from the perspective of T_g, these two factors would act in opposite senses; reference to the literature reveals examples where T_g increases on introducing nanoparticles [271], where negligible effects were observed [272-273] and where T_g was reduced [274-275]. In a study of polyurethane-based systems [276], a range of complementary techniques was used to study the glass transition in systems including montmorillonite (MMT). Agreement between the various techniques was found to be good and suggested that similar molecular dynamics occur in both the pure matrix and the nanocomposites. However, this study also showed evidence of the existence of a fraction of the polymer in each nanocomposite that made no contribution to the glass transition. Evidence for an immobilized interfacial phase that did not affect T_g has also been seen in polyamide/layered silicates systems [277-278]. In the case of epoxy based systems, Ou and Shiu [279] reported on the effect of adding silica nanoparticles of different sizes. This work revealed a pronounced increase in T_g (up to 20 ^{o}C) on adding as little as 0.3% of the nanoparticles; the smaller the nanoparticles, the greater the elevation in T_g. However, Singha and Thomas [280] reported that the addition of even small concentrations of spherical nanoparticles, (titania, alumina and ZnO), had entirely the contrary effect. In this study, a decrease in T_g of ~ 8 ^{o}C was reported on adding just 0.5% of nanofiller. Elsewhere, the addition of a functionalised MMT to an epoxy resin was shown to accelerate the curing reaction; in this case, the observed decrease in T_g was ascribed to alkylammonium cations from the clay acting as a plasticizer [281]. It is clear that the effective T_g depends on the relative contributions of those distinct phase regions. The existence of such phase regions is expected to introduce different glass transitions or, at least, an extensively broad one. However, this is not seen clearly in the DSC thermograms obtained for samples studied here. Chemically, the unfilled epoxy network was formed by a distribution of ester and ether linkages. Etherification is usually associated with the formation of more highly

branched molecular architectures than esterification, i.e. less densely crosslinked regions. The combination of these regions of different crosslinking degrees leads to a glass transition spanning ~ 20 ^{o}C, as shown in Table 5-2. The addition of nanosilica can induce tightly bonded regions and loose ones, according to the "multi-core" model. However, due to the surface treatment process, the difference in molecular mobility in these regions is small. The span of the glass transition, ΔT, of such loosely bound regions may overlap that of regions containing the unperturbed resin matrix formed mainly by etherification. Similarly, the ΔT span of tightly bound regions may also overlap that of bulk resin regions mainly by esterification reactions. As a result, compared with the unfilled Ep80, only a small difference of ~ 5 ^{o}C in ΔT is observed in the case of Pox80-5 and ~ 8 ^{o}C in the case of Pox80-12.5. However, taking into account the uncertainties in the measurements, only the Pox80-12.5 shows this difference.

The behaviour of the 3M systems, which involve 100 nm-diameter nano-silica, is rather different from the Nanopox systems, in that T_g stays unchanged or only slightly decreases on introducing the nano-silica up to 12.5 %wt, as shown in Figure 5-12.

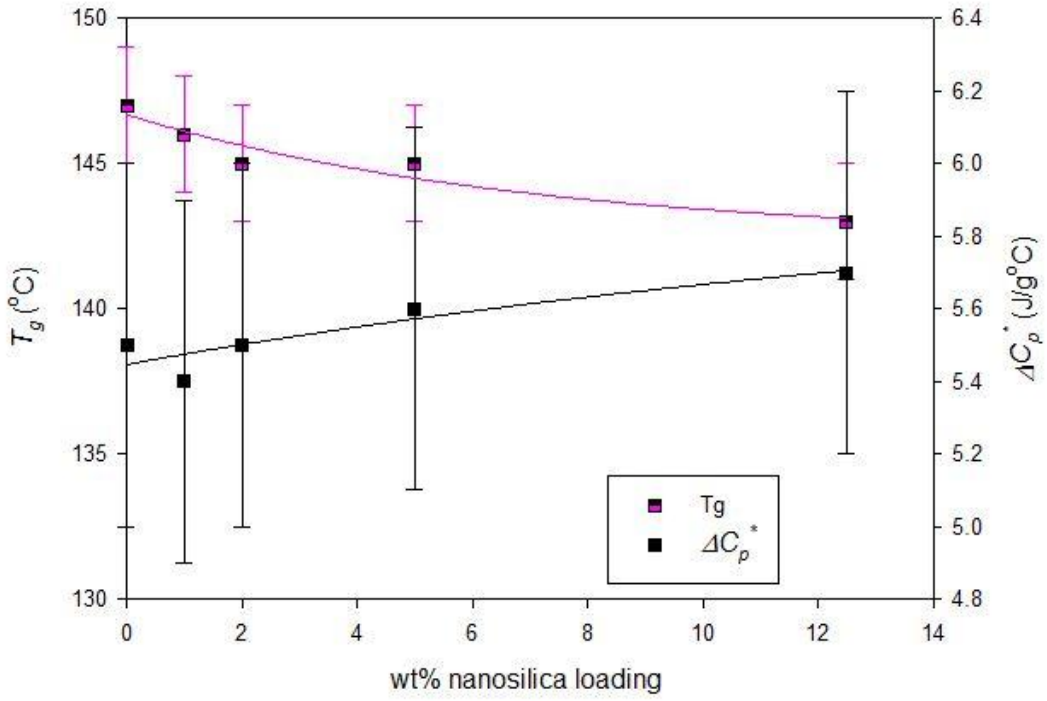

Figure 5-12 The glass transition temperature and heat capacity of 3M systems (standard errors based on 5 samples)

For this system, SEM images show a good dispersion of nanosilica in the matrix. In addition, the FTIR spectra of the Nanopox and 3M exhibit similar characteristics, indicating that hydroxyl groups on the nanosilica in the 3M could also catalyse the homopolymerisation and lead to a chemical imbalance in the reacting systems, so reducing T_g in the same manner as described above. However, the increase in filler size implies a decrease in the interfacial area; consider a spherical nanoparticle having a diameter *d* and an interfacial thickness *t*, as shown in Figure 5-13.

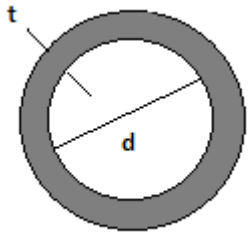

Figure 5-13 Schematic diagram of a nanoparticle and interface

Assuming no interphase overlap, the volume fraction of interphase regions can be estimated roughly based on an "effective volume fraction" approach that has recently been applied to nanocomposites [282-285]:

$$V_i = (1 + \frac{t}{r})^3 V_P - V_P \qquad Equation\ 5-1$$

where r is the mean radius of spherical nanoparticles; V_i and V_P are volume fractions of interphase regions and nanoparticles respectively. In this approach, t is the thickness of the immobilised layer surrounding a nanoparticle.

For a loading level of 12.5 wt%, the theoretical volume fraction of nanoparticles, V_P, is ~ 7.22 vol%, taking the density of silica to be 2.2 g/cm^3. The Nanopox system contains nanosilica particles of average diameter of 20 nm. Zhang et al. [285] estimated the average interfacial thickness of silica/epoxy nanocomposites, which were filled with the Nanopox XP 22/0314 master batch containing 25 nm diameter silica particles, and found that this parameter, t, ranges from ~ 3-11 nm. Petrovicova et al. [282] found that this parameter ranges ~ 3.6-22.4 nm for nylon 11/silica (7-12 nm) nanocomposites. Chen et al. [267] reported an interfacial immobilised layer of ~ 5-10 nm, depending on composition, in poly(vinyl alcohol)(PVA)/silica nanocomposites. So, setting the

thickness *t = 4-10 nm*, then V_i = 12.6-50.4 vol%. This approach results in similar estimations to calculations based on the volume fraction *f* of interface for a nanoparticle provided by Tanaka et al. [253], which can be expressed by the equation 5-2, assuming no interphase opverlap:

$$f = 3\frac{2t}{2t+d}\left[1 - \left(\frac{2t}{2t+d}\right) + \frac{1}{3}\left(\frac{2t}{2t+d}\right)^2\right] \qquad Equation\ 5-2$$

Under these assumptions, for a volume fraction of nanofiller at 7.2 vol%, the volume fraction of interphase regions would be ~ 2-7 times greater than that of nanofiller. Therefore, the characteristics of the interphase regions should dominate those of the nano-particles. However, when the average diameter of nanosilica is ~ 100 nm, as in the case of the 3M system, the volume fraction of the interphase regions, V_i, will be reduced to ~ 1.9-5.2 vol%, under the same assumptions; that is, only one tenth to one sixth of that of the Nanopox system - a significant reduction. As a consequence, the effect of interphase regions is less significant in the case of the 3M system than in the case of the Nanopox. In addition, it is well-known that the surface chemistry of fillers determines interfacial characteristics. If interfaces are characterised by weak filler-matrix interactions, the molecular mobility will be enhanced in interphase regions due to increased free volume, so leading to a reduction in T_g. This seems likely to be the case for the Nanopox-based nanocomposites. Conversely, in the case of the 3M-based systems, stronger filler-matrix interactions at interfaces may restrict chain dynamics, and hence, increase T_g. For example, Wu et al. [271] reported pronounced increases in T_g for both silica and titania-based nanocomposites. In addition, considering an inter-filler distance (surface to surface distance) *D*, using equation 5-3 [285-287]:

$$D = \left[\left(\frac{\pi}{6V_p}\right)^{\frac{1}{3}} - 1\right]d \qquad Equation\ 5-3$$

At V_p = 7.2 vol%, i.e. 12.5 wt%, nanosilica, the inter-filler distance in the Pox80-12.5 is ~ 18.7 nm. Therefore, in the case of an interphase thickness being ~ 5 nm, it is unlikely that an overlap occurs ($2t \ll D$), while an interphase thickness of ~ 9 nm will lead to an overlap of nano-partices ($2t \approx D$). The SEM images of the Pox80-12.5 show a possibility of agglomeration of nanosilica; aggregates are less than micrometer scale in

size. This suggests that the interphase thickness in the case of Nanopox-based systems may fall close to 9 nm. Overlapping of interphase regions will reduce the overall interfacial volume fraction in the sample and, lead to a decreased extra free volume. Conversely, at the same V_p = 7.2 vol%, the inter-filler distance is ~ 93.7 nm in the 3M-12.5, which is much greater than $2t$. Therefore, an overlap of interphase regions is unlikely to occur. This is supported by the SEM images shown above.

A hypothesis that may account for the observed behaviour is that the amount of catalytic impurities present in the 3M system may be smaller than that in the Nanopox. As a result, the catalytic effect also becomes more limited than in the case of the Nanopox. As a result of competition between stoichiometric and interfacial interaction effects, only a slight decrease in T_g can be observed in the case of 3M-based nanocomposites. As the size of the filler particles increases into the microsopic range, the role of the interphase regions becomes insignificant, such that the introduction of micro-silica produces no significant change in T_g compared with the corresponding unfilled epoxy, as shown in Table 5-2.

In general, the T_g behaviour can be explained by factors relating to the size of the nanofiller and surface chemistry effects involving moieties on the surface of the nano-fillers, such as hydroxyl groups or organic molecules that can directly react with species in the curing systems.

5.6 Space charge behaviour

Figures 5-14 to 5-16 show space charge profiles obtained from nanocomposites containing the Nanopox and 3M systems at various loading levels up to a poling time of 1h and at an intermediate electric field of 30 kV/mm, followed by 1h short-circuiting. It is evident again that there is only a small amount of homocharge injected from the cathode during the 1 hour charging period for all the cases under investigation. The injected charges are trapped and only stay in the vicinity of the electrode; no internal space charge is observed at other locations within the bulk of the samples. The presence of homocharge near the electrode reduces the local field at the cathode and, hence, suppresses the injection of electrons. Moreover, the quick dissipation of injected charges upon short-circuiting indicates a distribution of only shallow traps near the surface of the samples. The space charge behaviour appears comparable in all the

samples under investigation, including both the Nanopox and 3M systems. This can be explained by the following reasons. First, the FTIR spectra indicate that structures with similar chemical bonds formed in these samples. It is well-known that charge injection depends on the potential barrier between the electrode materials and the specimen, and samples of similar chemical structure can be considered to be characterised by similar potential barrier heights. The well-dispersed nanosilica fillers of both the Nanopox- and the 3M-based nanocomposites do not lead to significant changes in the general chemical molecular architecture. Many studies on space charge behaviours in an unfilled epoxy resin have reported a small amount of homocharge near the cathode [251, 288-290]. Similar behaviours are also observed in this study. Second, although the incorporation of the Nanopox and 3M systems can introduce more impurities, due to the synthesis and surface treatment processes, and/or an effective excess of hardener, as a consequence of the stoichiometric effects discussed in the previous chapter, it does not imply increased conductivity of charge carriers. Impurities can modify the trap distribution; more trap states are present in the energy gap. However, to enable charge carriers to hop or tunnel through potential barriers, the inter-state distance is critical, which should fall into the nanometer scale, especially at low fields and low temperatures. The SEM images show a relatively good dispersion of nanofillers in all samples. Therefore, the probability of the existence of such small distances is low. Moreover, all the samples are deep in their glassy state under the experimental conditions used here and, therefore, the molecular mobility is severely restricted. As a consequence, the dc conductivity is extremely low. Therefore, once injected, it becomes difficult for charge carriers to drift to the other electrode. Instead, charge carriers are trapped in the vicinity of the injecting electrode until further charge injection is suppressed due to reduced effective electric field near the electrode. An injection of homocharge close to the electrodes has been reported elsewhere [288-289]. Hajiyiannis et al. [290] found that, as the percentage loading of nanoalumina increased, the quantity of homocharge formed in the nanocomposties was considerably higher than in the unfilled resin. However, this work did not consider the dispersion of the nanofillers in the host resin, especially at high loading percentages such as 15 wt% nanoalumina. Here, the sample filled with 12.5 wt% micro silica reveals a greater accumulation of homocharge near the cathode, as shown in Figure 5-17. The presence of micro-sized silica at the surface of the sample could lower the potential barrier between the electrode and the composite, and hence, more electrons are injected

into the sample. However, SEM images showed that the microsilica fillers are largely deposited at the bottom of the specimen. Because only a small amount of filler was added, the main structural architecture was the resin matrix, which is comparable to the highly crosslinked network of the unfilled epoxy. Consequently, after being injected, electrons cannot move to the opposite electrode, and therefore, stay in the vicinity of the cathode such that further injection then becomes limited.

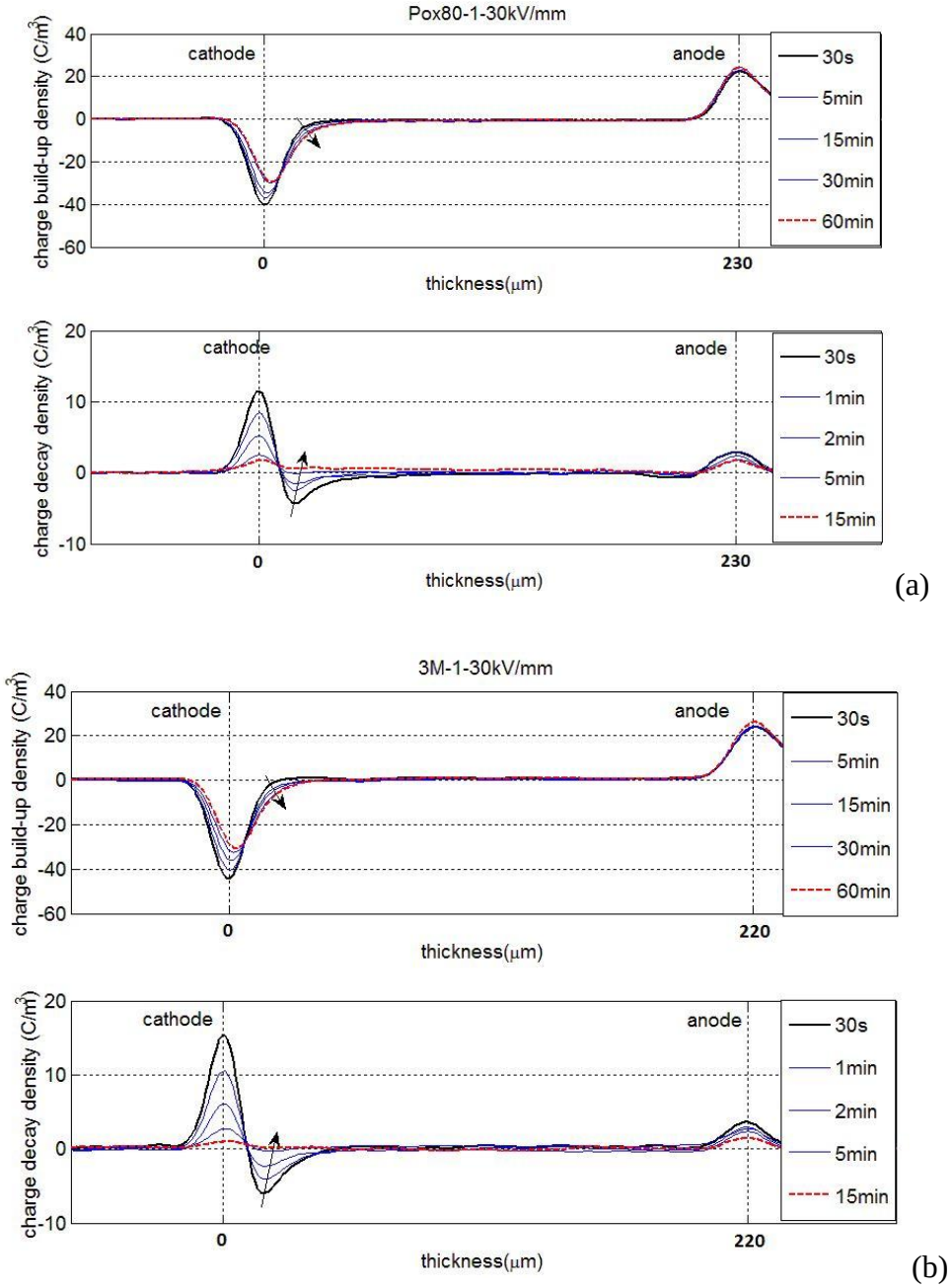

Figure 5-14 Space charge profiles obtained for nanocomposites containing 1 wt% nanosilica

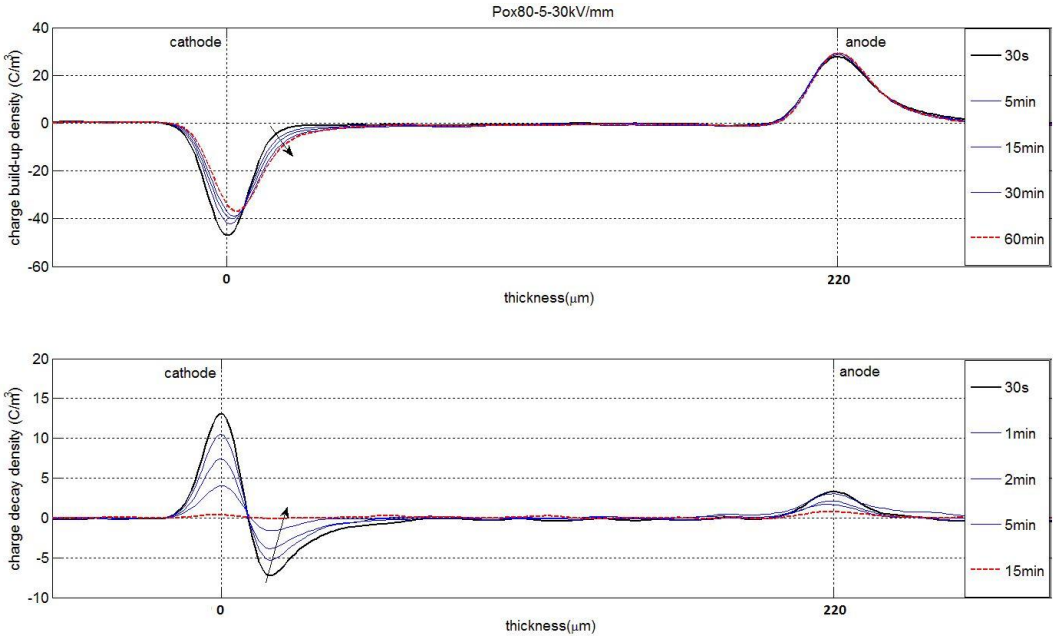

(a)

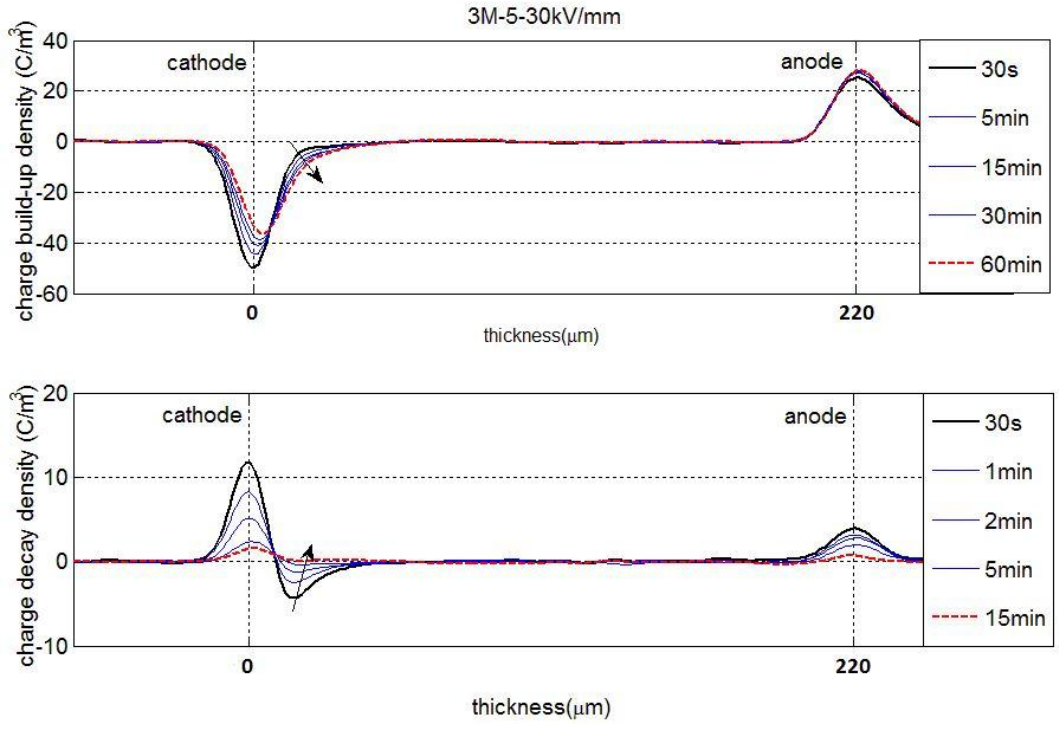

(b)

Figure 5-15 Space charge profiles obtained for nanocomposites containing 5 wt% nanosilica

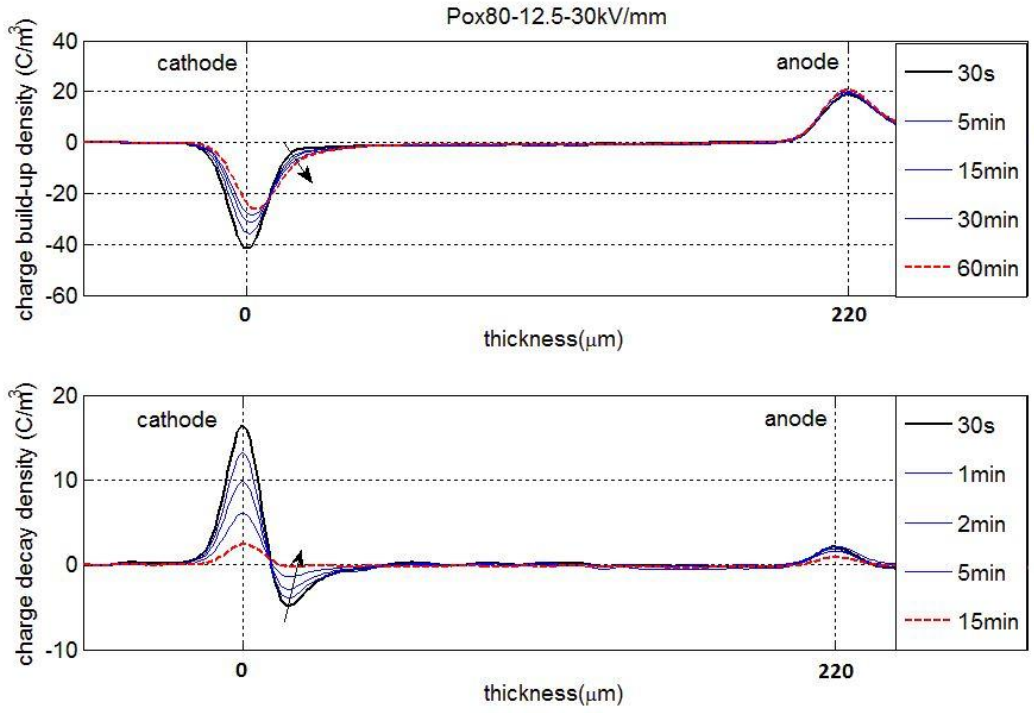

(a)

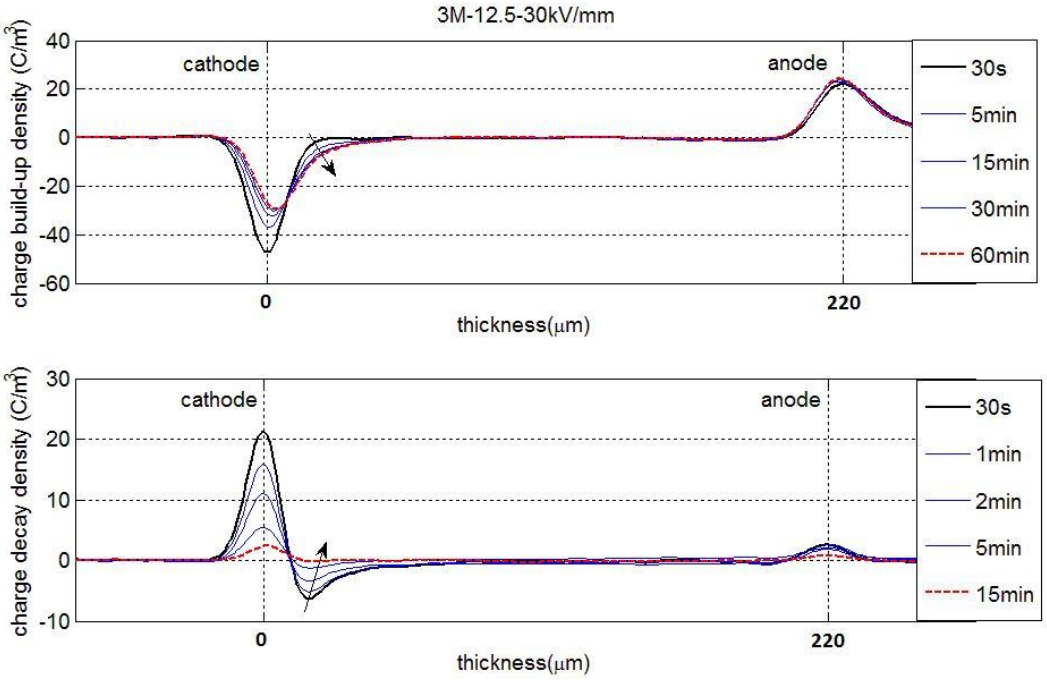

(b)

Figure 5-16 Space charge profiles obtained for nanocomposites containing 12.5 wt% nanosilica

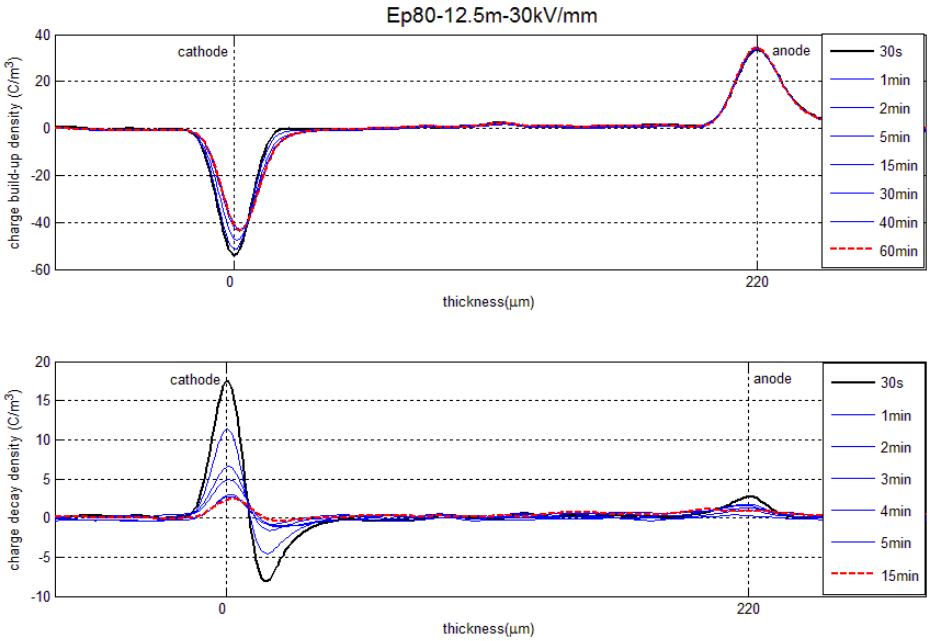

Figure 5-17 Space charge profile obtained for the system containing 12.5 wt% micro silica

5.7 AC Electrical Breakdown

Figures 5-18 to 5-19 respectively show Weibull breakdown data obtained from nanocomposites filled with the Nanopox and 3M systems at various loading levels. Evidently, the introduction of the Nanopox into the epoxy matrix at high filler loadings (i.e. > 5 %wt nanosilica) reduces the electric breakdown strength. At low filler loading, it is likely that the effect of the nanosilica is not significant. There are some possible explanations. First, breakdown phenomenon can be considered to initiate at "weak" regions within materials. The T_g results showed a reduction in this parameter due to extra free volume introduced by the presence of nanosilica, as suggested by the "multi-core" model [253]. As the loose interphase layers dominate, they could be considered as "weak" regions. This mechanism is related to the quality of surface treatment of the nanosilica. Secondly, as discussed in chapter 4, the introduction of the Nanopox at a certain level could change the stoichiometry and lead to a chemical imbalance that equates to an excess of hardener. The excess hardener could be oxidised at 160 ^{o}C during the post-curing process. The oxidation induces additional impurities into the structure and consequently leads to a reduction in the breakdown strength. In addition, the synthesis and surface treatment of nanoparticles may introduce impurities/additives

and a size distribution of nano-fillers. This may be the reason for the observed reduction in the electric breakdown strength. Finally, at high filler loading, the probability of silica aggregation increases as shown by the SEM images in Figure 5-6 in the case of Pox80-12.5. The nanoparticles may aggregate and, effectively, increase in size. When the aggregates become large enough, they may play the role of defects, leading to a reduction in breakdown strength.

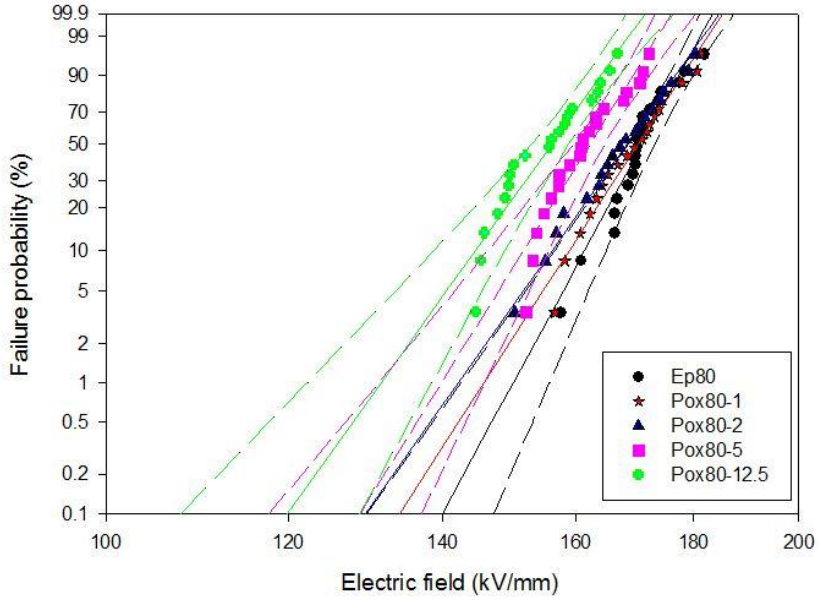

Figure 5-18 Weibull distribution of Nanopox systems

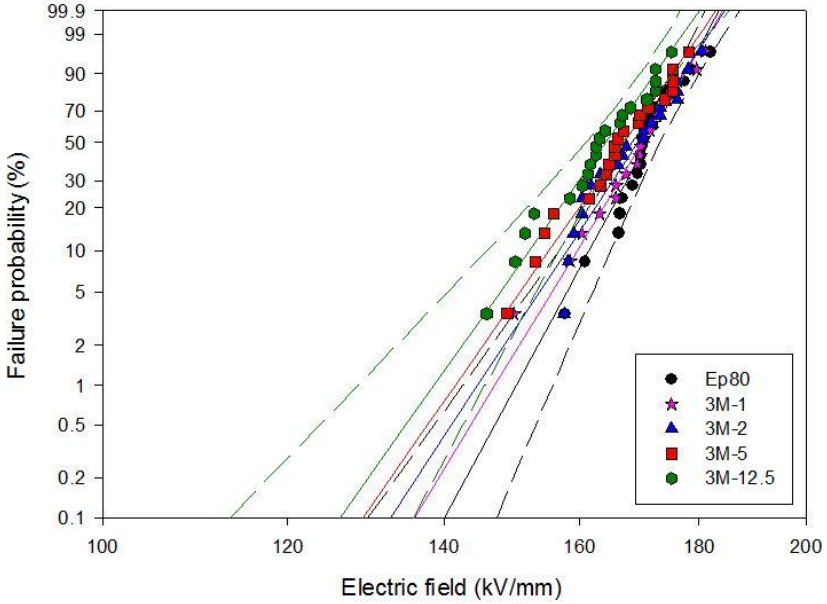

Figure 5-19 Weibull distribution of 3M systems

Table 5-3 Weibull parameters obtained for samples under interfacial study

Sample code	α (kV/mm)	β
Ep80	173 ± 1.8	32.7
Pox80-1	172.6 ± 2.6	27.4
Pox80-2	171 ± 2.9	25
Pox80-5	164.1 ± 2.5	27.6
Pox80-12.5	158.3 ± 3.0	22.9
3M-1	172.5 ± 2.5	29.1
3M-2	171.8 ± 2.7	26.9
3M-5	169.6 ± 2.8	25.4
3M-12.5	164.3 ± 2.8	23.7
Ep80-5m	160.7 ± 3.7	17.8
Ep80-12.5m	157.9 ± 4.7	13.7

In general, the 3M systems exhibit similar breakdown behaviour to that shown in Figure 5-18. However, it is evident from Table 5-3 and Figure 5-20 that the introduction of Nanopox produces more dramatic effects on the breakdown strength than the 3M system. At a 12.5 wt% nanosilica loading level, only a slight decrease in E_b can be observed for the 3M-12.5, whereas a noticeable reduction in E_b is found in the Pox80-12.5. The difference in this behaviour could be related to the filler size, the different surface functionalization of the two different nanofillers and/or different types and quantities of impurities/additives which are associated with the synthesis process. The 3M systems may contain the stronger interactions between the organic moieties attached to the filler surface and the host resin. The interphase region could therefore be more robust than does in the Nanopox systems, so improving the breakdown strength. Comparing the results presented above with those described in the literature reveals significant differences. For example, Ma et al. [291] explained the higher breakdown strength observed in nanocomposites by the modification of titanium dioxide with a polar silane coupling agent in terms of a decrease in the charge carrier mobility. In another study, Roy et al. [232] found at least a 15% increase in breakdown strength in

nanocomposites filled with nanosilica, compared to an unfilled crosslinked polyethylene at room temperature. These workers attributed this increase to the reduction in chain movement of the polymer chains through physical bonding or confinement, hence reducing the Maxwell-Wagner-Sillars interfacial polarisation at the interface of the filler-polymer. In contrast, Kim et al. [292] modified the particle surface with phosphonic acid groups. This work revealed a reduction in the breakdown strength and an increase in dielectric constant of the nanocomposites compared to the unfilled polymer, although the aggregation state of the $BaTiO_3$ nanoparticles was improved. Similar observations were reported by Li et al. [293]. They claimed that the observed decrease in the breakdown strength of poly(vinylidene fluoride) nano-$BaTiO_3$ composites was due to enhanced charge transport. Obviously, the choice of functional groups for the surface modification will affect the interfacial structure and hence, influence dielectric properties of nanocomposites.

The introduction of microscopic silica particles leads to a dramatic decrease in the electric breakdown strength and an increase in the scatter of data, as shown in Figure 5-21 and Table 5-3. The larger particle size leads to a greater field distortion and local field enhancement due to the difference in the dielectric permittivity of the silica micro-fillers in a form of quartz (~ 3.8-5.4 [141]) and the polymer matrix (~ 3.5) [294]. Furthermore, these micro-silica fillers are prone to moisture absorption due to poor surface treatment. The presence of water can increase the hydrogen bonding of water molecules onto the filler particle surfaces, as well as enhancing charge transport in the sample. In addition, the aggregation of such micro silica can be considered to introduce defect centers into the epoxy matrix. The decrease in the Weibull β parameter, as shown in Figure 5-22 upon adding micro-silica, can be attributed to the aggregation of fillers. Therefore, the breakdown strength reduces quite significantly. The addition of micron-sized fillers has been reported to produce a negative impact on breakdown strength [295]. The differences in the breakdown behaviours of different nanocomposites and micro-composites are due to their interfacial effects and the filler surface chemistry. In microcomposites, the composite properties are typically a weighted average of the constituent material component properties, whereas in the nanocomposite, the interface plays a dominant role. Therefore, at 12.5 wt% loading level, the contribution of micro-silica fillers to the microcomposite is ~ 14%, while due to the small size of nanosilica, the volume fraction of interphase regions can go up to more than 50 vol%. As a

consequence, at the same loading level, the nanocomposites show effects of fillers more significantly than the microcomposites. However, the higher the percentage of micro-filler, the larger the distribution of defect centers. Therefore, when the loading level of micro-silica becomes predominant to the host resin matrix, the properties of the composites will change in such a manner that the micro-filler is the main component of the system. More details about such micro-filled composites will be discussed in the following chapter.

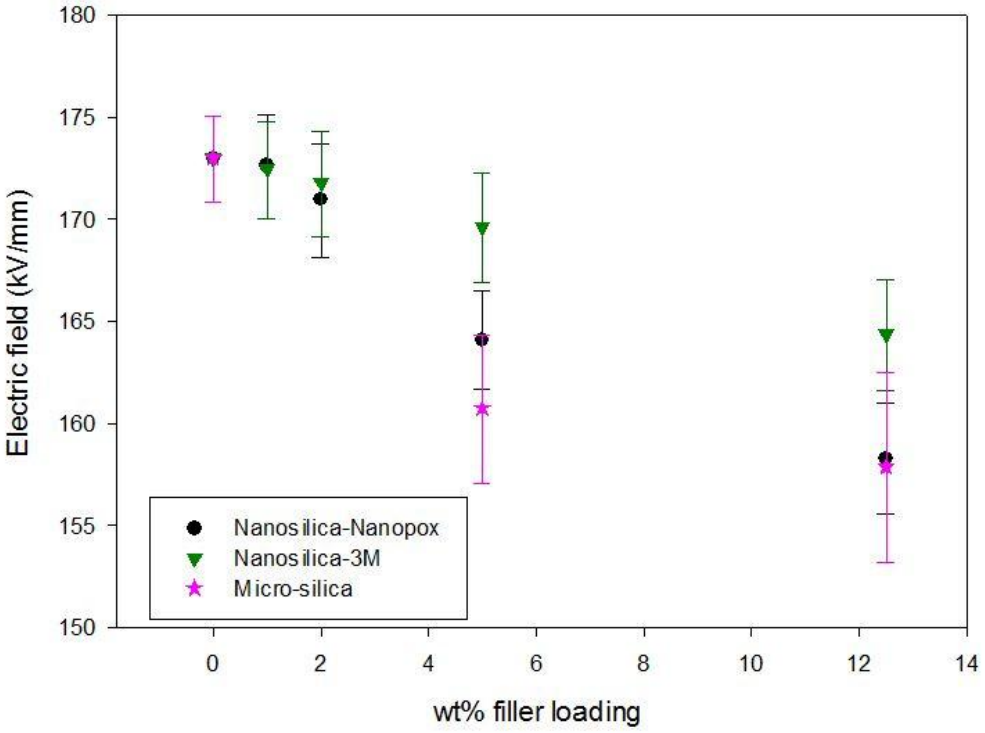

Figure 5-20 The breakdown strength of the systems containing various percentages of fillers (error bars correspond to 90% CI)

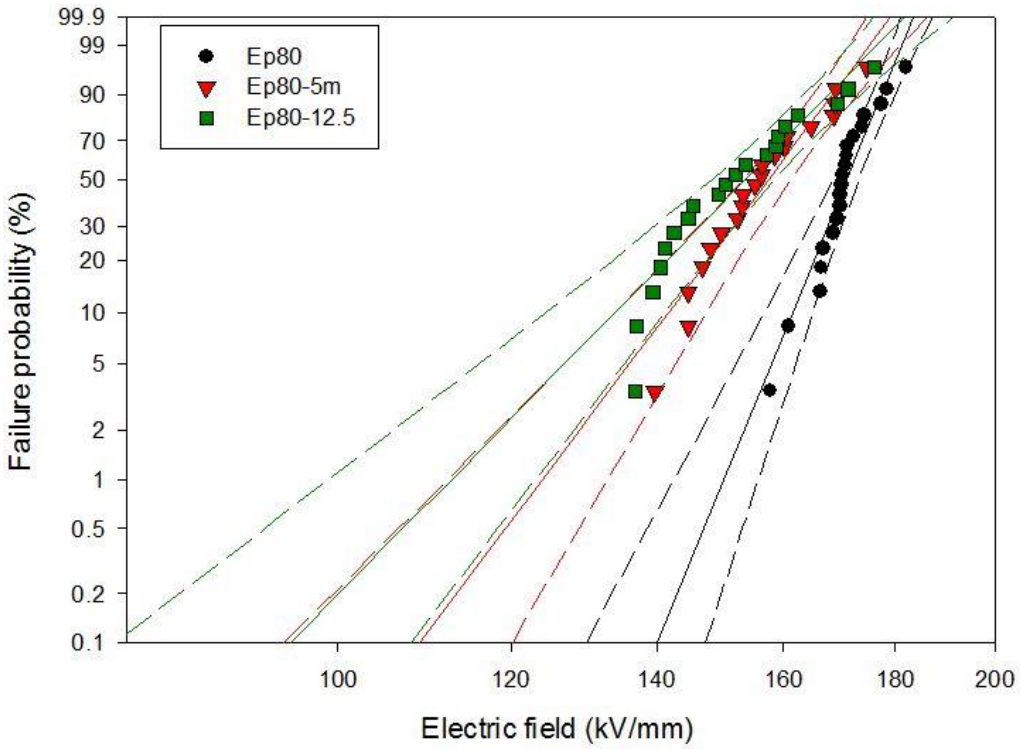

Figure 5-21 Weibull distribution of micro-silica filled composites

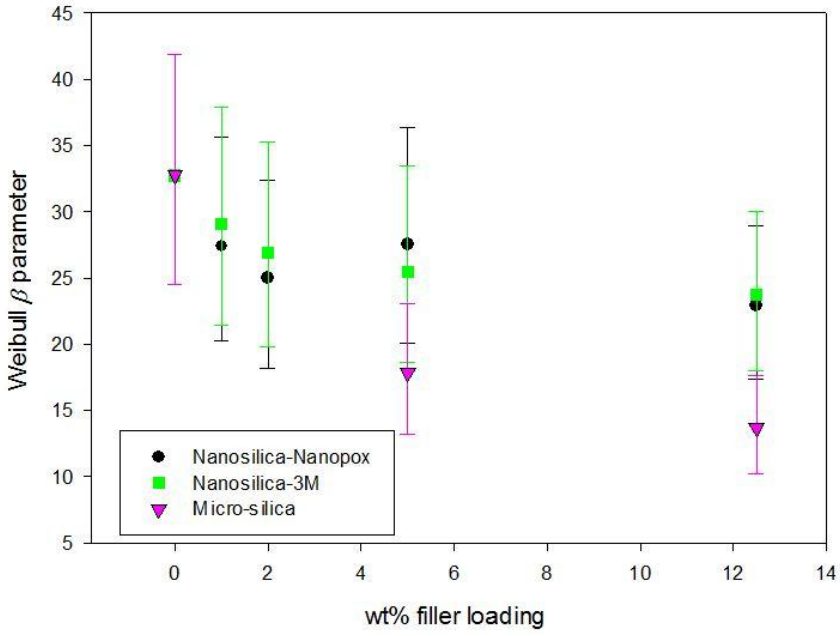

Figure 5-22 The β Weibull parameter of the systems containing various percentages of fillers (error bars correspond to 90% CI)

5.8 Dielectric response

As mentioned in Chapter 4, the incorporation of Nanopox into the unfilled system may both modify the stoichiometric balance of the curing systems, and introduce more free volume due to interfacial effects. For epoxy/silica composites, the heterogeneity introduces an extra complexity to the dielectric properties as a result of interfacial relaxations, such as the Maxwell-Wagner-Sillars effect [95]. As a consequence, the effective dielectric constant of the composites depends not only on the dielectric constant ratio of the fillers and epoxy, but also the interaction between them. Tanaka et al. [253] proposed a multi-core model to analyse the dielectric properties of polymer nanocomposites. The model suggested that the dielectric properties of composites would be most influenced by the bound and loose layers. Obviously, these two layers produce effects that are opposite in sense. Therefore, the effective dielectric properties depend on the contribution from each layer. Sun et al. [296] found that the dielectric constant and the loss factor of nanocomposites filled with silica particles were both higher than for unfilled and microsilica-filled epoxy systems, due to the enhanced dc conductivity of contaminants caused by the sol-gel synthesis of the nanosilica. Conversely, Fothergill et al. [297] observed a decrease in both dielectric constant and dielectric loss of nanocomposites compared to corresponding microcomposites and the unfilled epoxy. They also found that the dielectric spectroscopy results did not depend greatly on the filler material; only the size appeared to be important. Conversely, Zhang et al. [156] reported that, under dry conditions, the unfilled resin and nanoalumina filled composites showed no significant interfacial polarisation at the filler-resin interfaces. This work also revealed a strong dependence of dielectric properties on absorbed water. These conflicting observations are believed to depend on the properties of the interface regions. For example, Tagami et al. [298] investigated the dielectric properties of epoxy/clay and epoxy/silica nanocomposites. This work suggested that weak interactions between the clay and the epoxy matrix activated a relaxation above T_g, whereas strong bonding between the silica fillers and the resin matrix restricted molecular motion. Therefore, it is evident that surface treatment of fillers modifies composite properties. In addition, the characteristics of surface organic groups such as polarity, mobility, and size could exert a major impact on the dielectric properties of nanocomposites [299].

At low temperatures, where these epoxy-based systems are in the glassy state, the molecular motions as well as the migration of charge carriers are severely hindered. Therefore, the contributions from the different dielectric relaxation and polarisation processes are limited. In order to enable the observation of various dielectric responses and for the sake of brevity, only dielectric behaviours at high temperatures, i.e. 120 ^{o}C, 140 ^{o}C and 160 ^{o}C, are presented and analysed. Figures 5-23 to 5-25 show the complex permittivity curves of the Nanopox systems at different temperatures. It is evident that increasing temperature leads to an increase in both dielectric constant and loss factor due to the increased mobility of molecular chains and increased conduction due to impurities.

The dielectric constant of the epoxy matrix, ε_m, is ~ 3.5, whereas this value of silica nano-particles, ε_p, is ~ 3.8-4.0. Let V_p=7.2 vol%, which is equivalent to 12.5 wt%, then applying the mixing rules, such as the Lichtenecker (equation 2-16) or the Maxwell-Garnett (equation 2-17), the effective macroscopic permittivity of the heterogeneous system, ε_{eff}, is ~3.53. This indicates that from theory, the addition of nanosilica at the loading levels studied here should not result in a significant increase in the macroscopic permittivity. The observed increase in dielectric constant and loss factor upon the addition of Nanopox can therefore be attributed to the following factors. First, it is well-known that the α-relaxation is related to molecular mobility. The introduction of the Nanopox exhibited a monotonically reduced T_g with increasing filler loading level, due to a combination of stoichiometric and interfacial effects, as described in the previous sections, which implies increased chain mobility. This suggests that the relaxation time of the α-polarisation process is reduced monotonically, i.e. the α-relaxation occurs faster, upon adding Nanopox-type nanosilica. The resulting increase in the chain mobility leads to an increase in both the real and imaginary parts of the relative permittivity, as shown in Figure 5-26. The variations in temperature could move the curves along the frequency scale; this is referred to as time/temperature superposition. A monotonic increase in permittivity upon adding nano-fillers was reported by Singha and Thomas [280, 300] who investigated systems based on the epoxy resin and filled with 0.1, 0.5 and 1 % of TiO_2, ZnO and Al_2O_3. They found that the higher the filler loading level, the higher the observed relative permittivity value. Conversely, Kochetov et al. [237] reported a decrease in real permittivity of nanocomposites filled with Al_2O_3, or MgO up to 2 wt%, followed by an increase in real permittivity with further addition of

nanofiller. The decrease in real permittivity was explained by immobilised dipolar groups in the proximity of nanoparticles. Such differences highlight the importance of surface modification and interfacial volume fraction effects. Previous calculations showed that a Nanopox-based system containing 12.5 wt% nanosilica can introduce an interfacial volume fraction up to 50 vol%, assuming no interphase overlapping and an interphase thickness of 10 nm. Although SEM images of the Pox80-12.5 system show a possibility of agglomeration of nanosilica, which can reduce the overall interfacial volume fraction in the sample, the theoretical inter-filler distance in this case was estimated to be ~ 19 nm, i.e. ~ 2*t*. Therefore, interphase overlapping or agglomeration of nanoparticles can only occur up to a certain limit, assuming good sample preparation obtained. If organic groups in the interphase region can only interact weakly with the epoxy matrix, then the effective permittivity will be increased significantly. This can be the case for the Nanopox-based systems studied here. In addition, as discussed in the previous chapter, the introduction of Nanopox can change the chemical balance of the reacting systems and lead effectively to an excess of hardener. The unreacted hardener molecules could contribute to an increase in permittivity in a manner described previously, in terms of impurities such as oxidation products, mobile molecules and, small dipole moments of side branches.

At 120 ^{o}C, i.e. below the T_g of the systems under investigation (T_g ~140 ^{o}C), the real component of the relative permittivity is almost "flat" on the log-log plot, while it is likely that a dispersion process starts occurring at low frequencies below 1 Hz. Increasing the temperature reveals the power law behaviours in the low frequency range, especially for the systems containing a high content of nanosilica. A slope that is smaller than -1 indicates a non-uniform charge transport in the heterogeneous systems via clusters. Such inter-cluster approach has been proposed as the low frequency dispersion (LFD) process [238-239]. The LFD behaviour manifests itself as an increase in both the real and imaginary parts of the relative permittivity with decreasing frequency, in which $\varepsilon''_r \sim \omega^{-s}$ $(0 < s < 1)$ [238]. This process is thermally activated and becomes more pronounced at an elevated temperature, i.e. at 160 ^{o}C. The presence of nanosilica may lead to the increased amount of clusters and/or the bigger cluster sizes and hence, enhance the charge transport. As a consequence, at a high loading level of nanosilica, the power law behaviour exhibits a greater slope than that observed in the other materials. As mentioned in the previous chapter, the LFD can only occur when the

segmental motions become significant, at least in the frequency range studied here. For example, the systems Ep60 and Pox60-5, which were examined in the previous chapter, only revealed two distinct response processes, including the LFD and the dispersion D, at 140 °C and above, i.e. at least 40 °C above their T_g. However, due to the highly crosslinked nature of epoxy networks, the samples investigated here possess high T_g (~ 140 °C). As a result, neither clear LFD process nor the dispersion D can be observed, even at 160 °C.

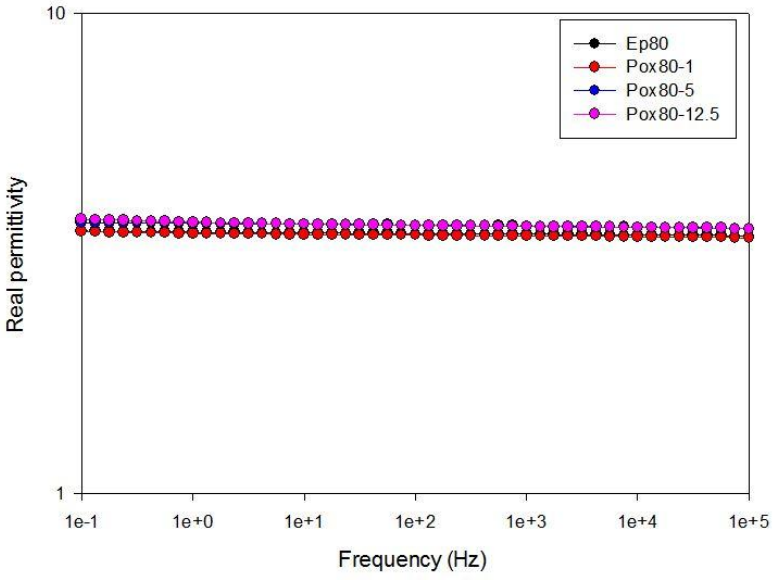

(a)

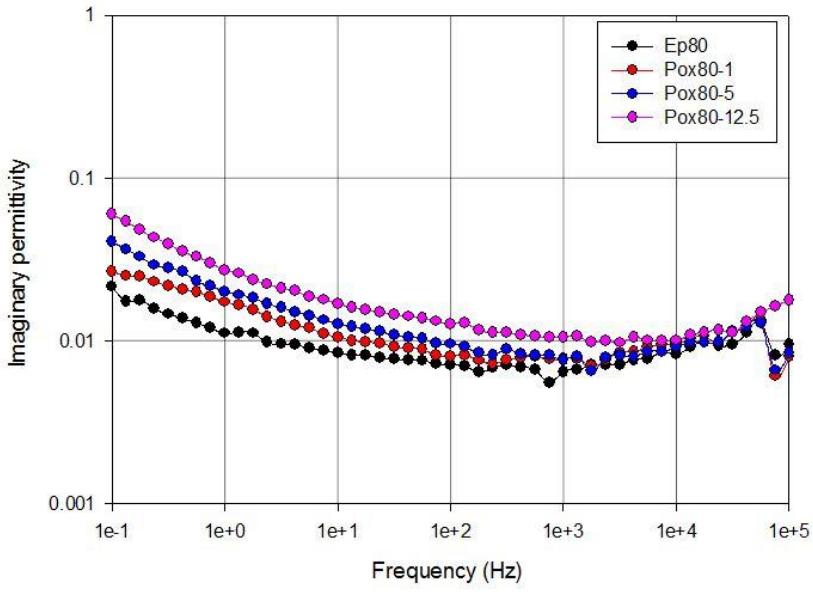

(b)

Figure 5-23 Complex permittivity of Nanopox systems at 120 °C (a) real and (b) imaginary

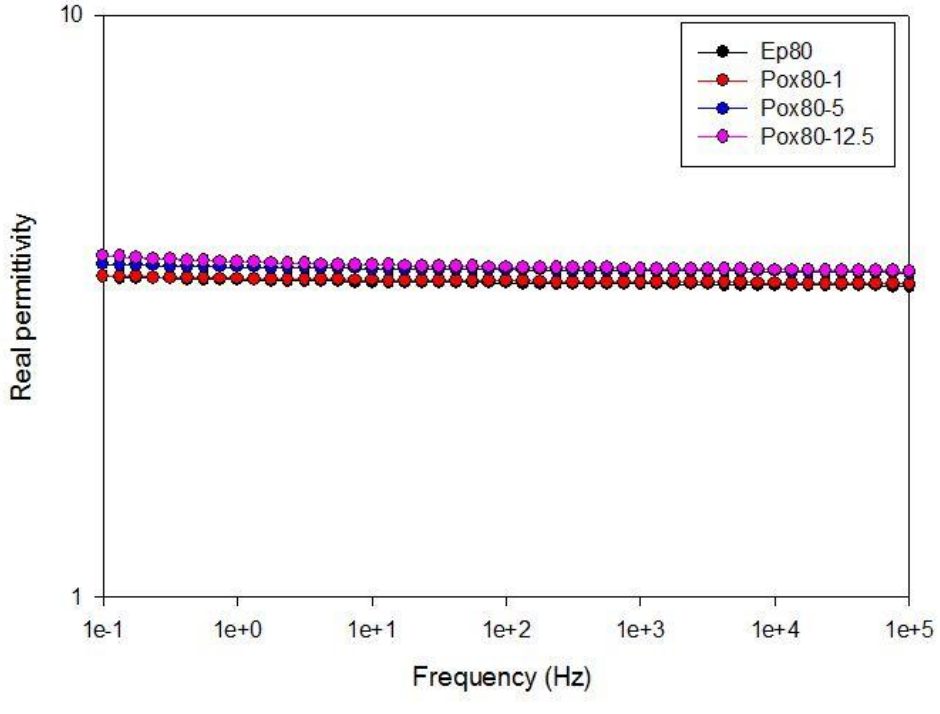

(a)

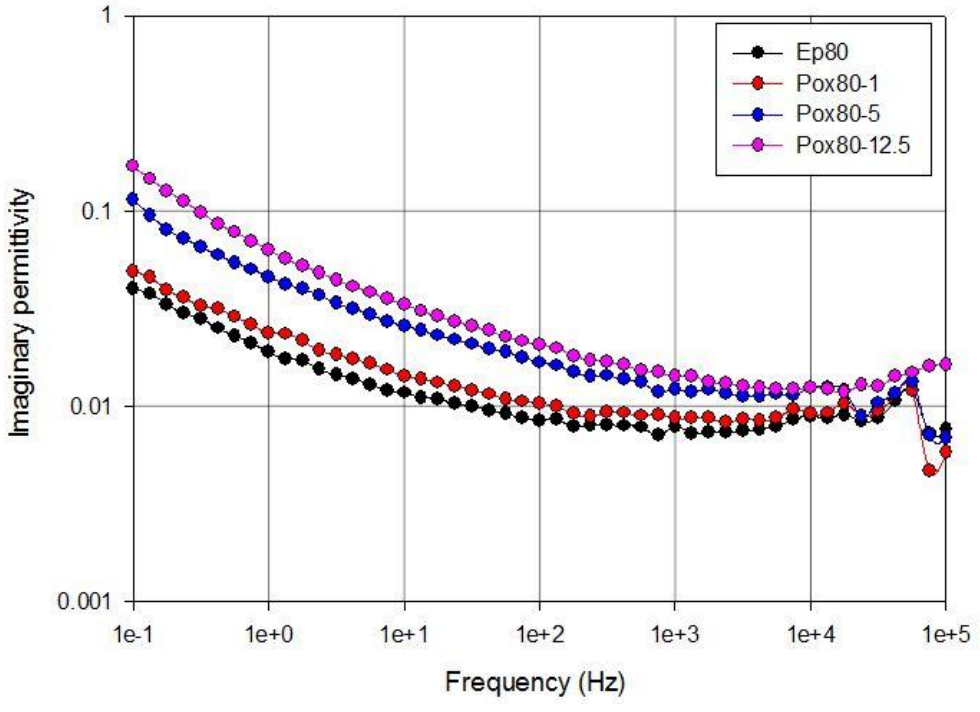

(b)

Figure 5-24 Complex permittivity of Nanopox systems at 140 ^{o}C (a) real and (b) imaginary

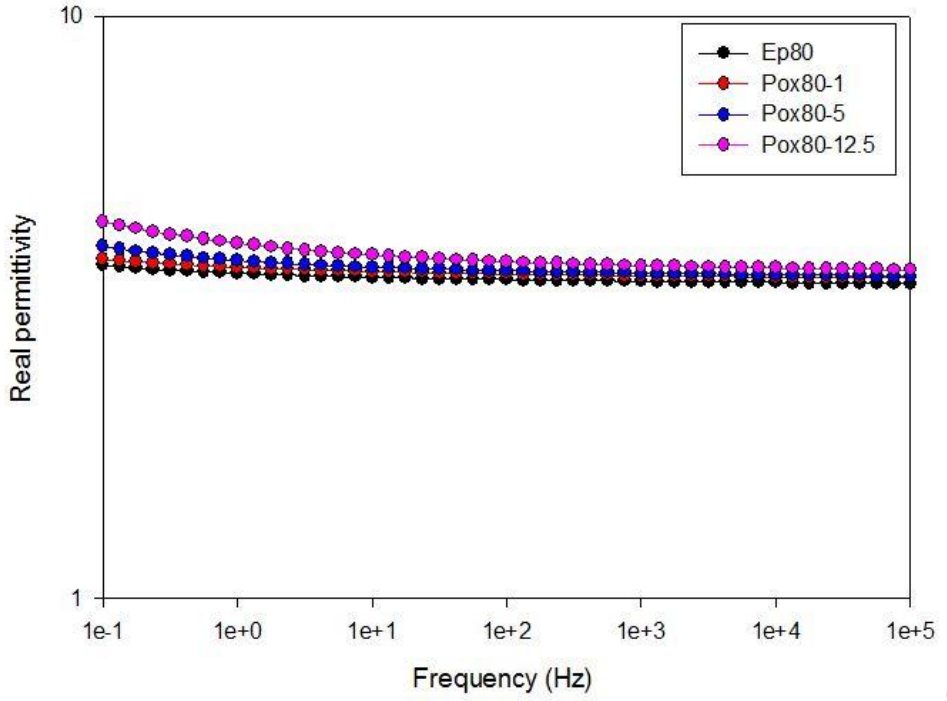

(a)

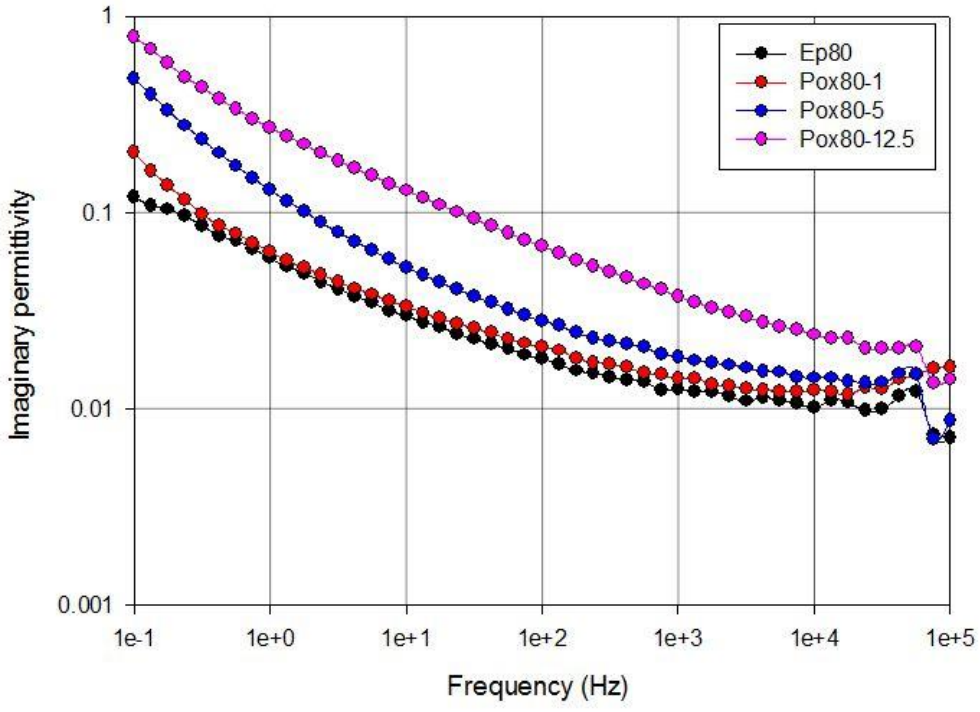

(b)

Figure 5-25 Complex permittivity of Nanopox systems at 160 °C (a) real and (b) imaginary

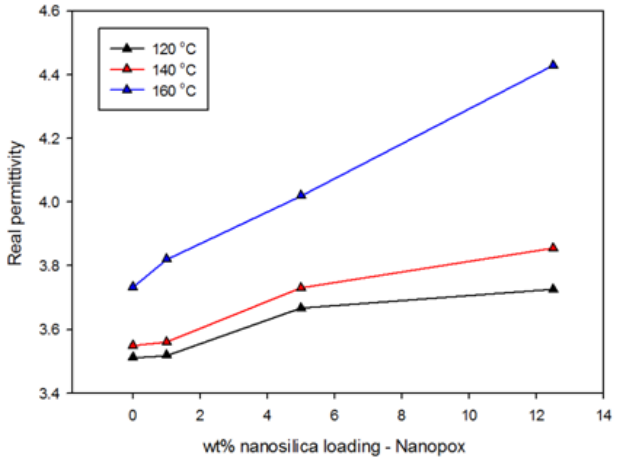

Figure 5-26 Real permittivity of Nanopox systems increases monotonically with filler loading level at different temperatures, obtained at 0.1 Hz

To explore interfacial effects further, systems based upon the 3M masterbatch (100 nm diameter nanosilica) were examined. Figures 5-27 to 5-29 present the relative permittivity data obtained from the 3M systems at 120 ^{o}C, 140 ^{o}C and 160 ^{o}C respectively. In general, the 3M systems exhibit similar behaviour to that of the Nanopox systems, i.e. the power law behaviour that indicates a non-uniform charge transport via large scale clusters in the systems. The increase in permittivity upon introducing the nanofiller can be explained by the stoichiometric and interfacial effects, as in the Nanopox systems. However, the addition of 3M exerts a less pronounced impact on the dielectric permittivity than does the incorporation of Nanopox. This behaviour can be attributed to the reduced interfacial areas due to the increased particle size, as shown in the previous theoretical calculations. Moreover, the level of impurities and additives present in the 3M system may be less than that of the Nanopox, depending on the synthesis and surface modification processes. An interesting point is that, at low concentrations of nanosilica, i.e. ~ 1 wt%, it is likely that the introduction of 3M leads to a lower dielectric constant and loss factor compared to the unfilled epoxy, as shown in Figure 5-30. This behaviour is contrary to that seen in the Nanopox system. To explain this observation, first, a comparison of interfacial volume fraction between the Nanopox and the 3M systems is estimated using Equation 5-1, as shown in Table 5-4.

Table 5-4 Interfacial volume fraction of Nanopox and 3M systems

Filler loading level		Nanopox (Assuming t = 10 nm)		3M (Assuming t = 20 nm)	
Wt%	**Vol%**	**Interphase (vol%)**	**Interphase:resin (vol%)**	**Interphase (vol%)**	**Interphase:resin (vol%)**
1	0.6	4.2	1:23	1	1:98
5	2.9	20.3	1:4	5.1	1:18
12.5	7.2	50	1:0.86	12.6	1:6

It is evident from Table 5-4 that, even at a doubled thickness, the interfacial volume fraction of interphase regions in the case of 3M systems is much smaller than in the Nanopox. At 1 wt% loading level, the contribution of interphase regions to the 3M-1 is negligible. In this case, moieties on the particle surface, such as hydroxyl groups, may react with epoxide groups remaining in the unfilled Ep80. Due to an extremely low concentration of fillers, no excess hardener may be present in this system. As a result, the crosslinking degree of the network is slightly improved, so leading to a slight reduction in real permittivity. FTIR spectra of the Nanopox (40 wt% nanosilica) and 3M (49.8 wt% nanosilica) master batches show similar characteristics. Therefore, in the case of Pox80-1, similar stoichiometric effects are expected. However, due to the increased interfacial volume fraction, interphase regions containing weak interactions at interfaces between the fillers and the resin matrix can cause an increase in permittivity. As a result of a combination of the stoichiometric and interfacial effects, a nearly unchanged permittivity is observed in the Pox80-1. At higher loading levels, the effective permittivity will result from a combination of both effects. Evidently, the contribution of interfacial effects to an increase in permittivity is significantly reduced in the 3M systems compared to that of the Nanopox. Furthermore, organic groups on the nanosilica particle in the 3M master-batch may interact with the host resin matrix more strongly than does in the Nanopox. As a result of more robust interfaces, interfacial effects could only contribute a slight increase in permittivity. Again, the increase in the loss factor at 160 ^{o}C, which is above the T_g, could also be attributable to the increased contribution of the LFD process.

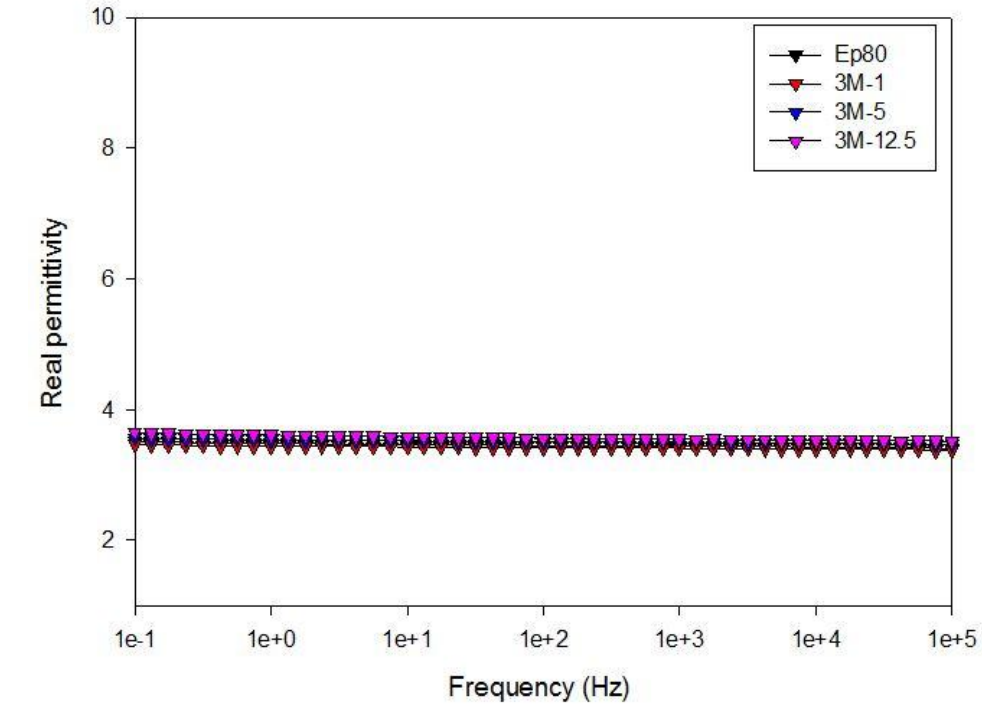

(a)

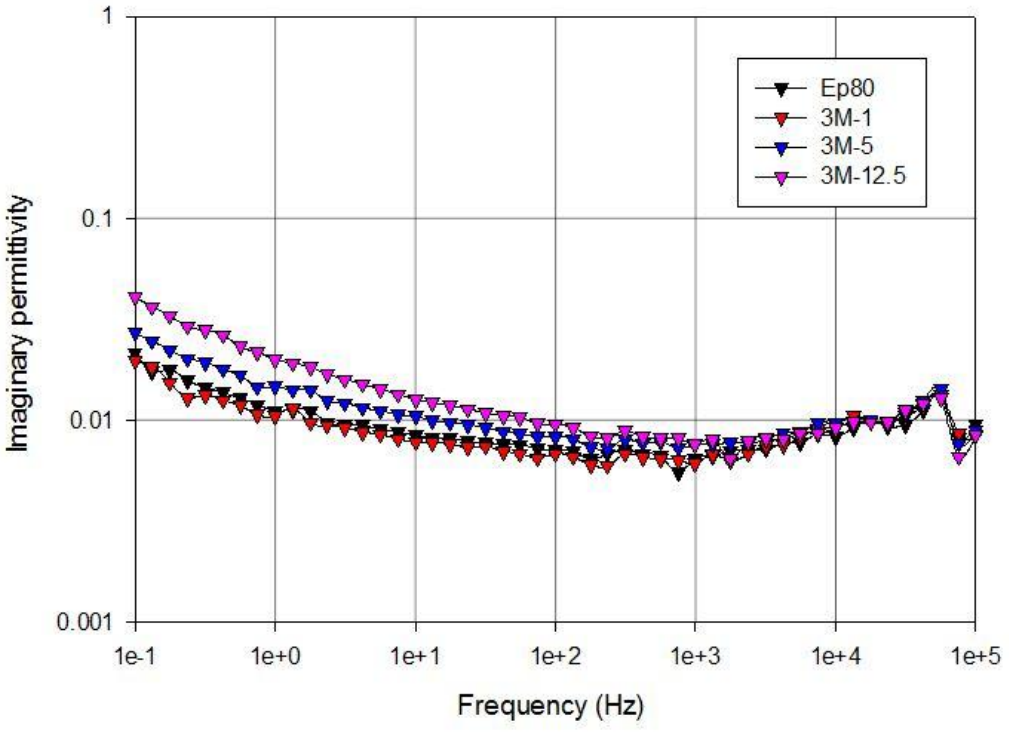

(b)

Figure 5-27 Complex permittivity of 3M systems at 120 ^{o}C (a) real (b) imaginary

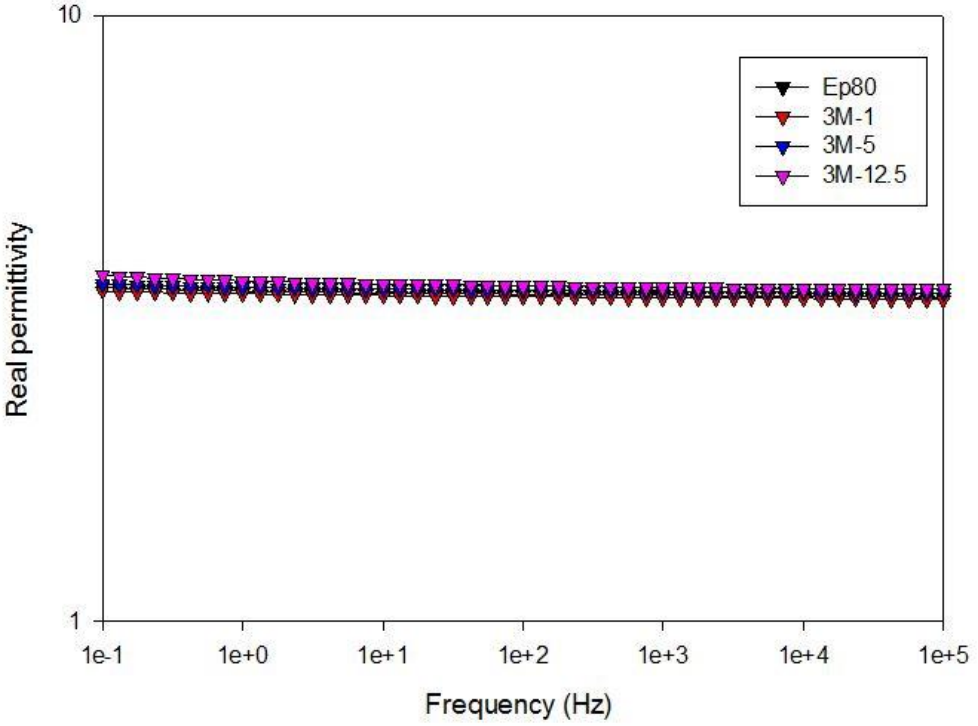

(a)

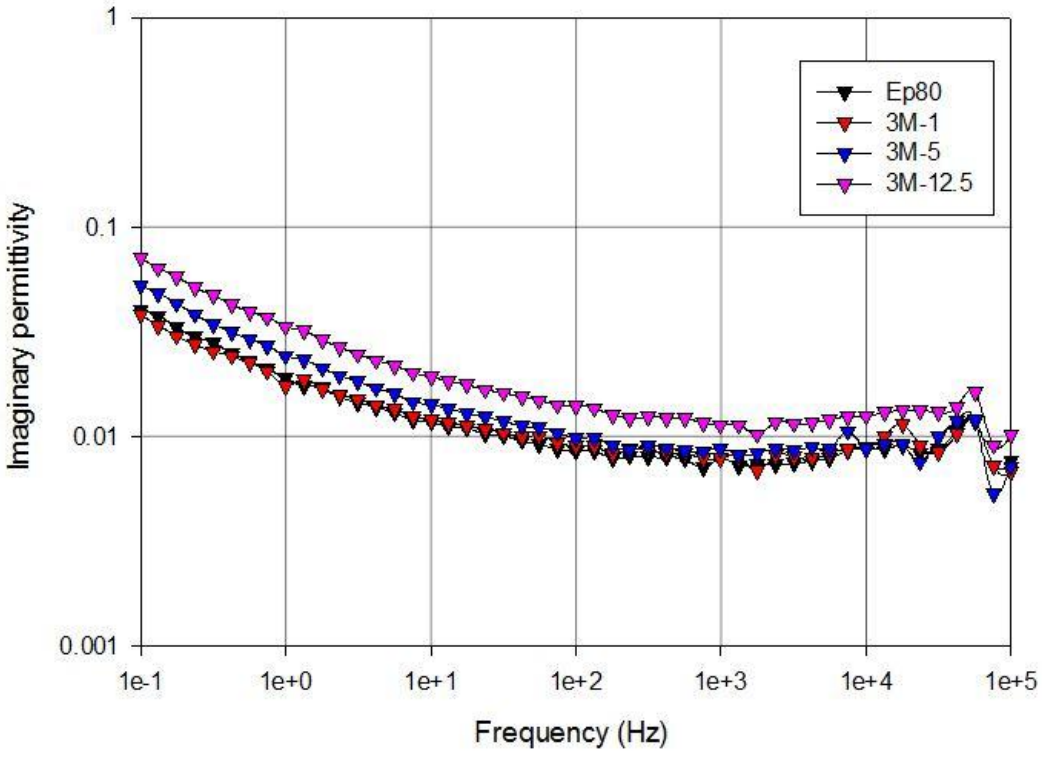

(b)

Figure 5-28 Complex permittivity of 3M systems at 140 ^{o}C (a) real (b) imaginary

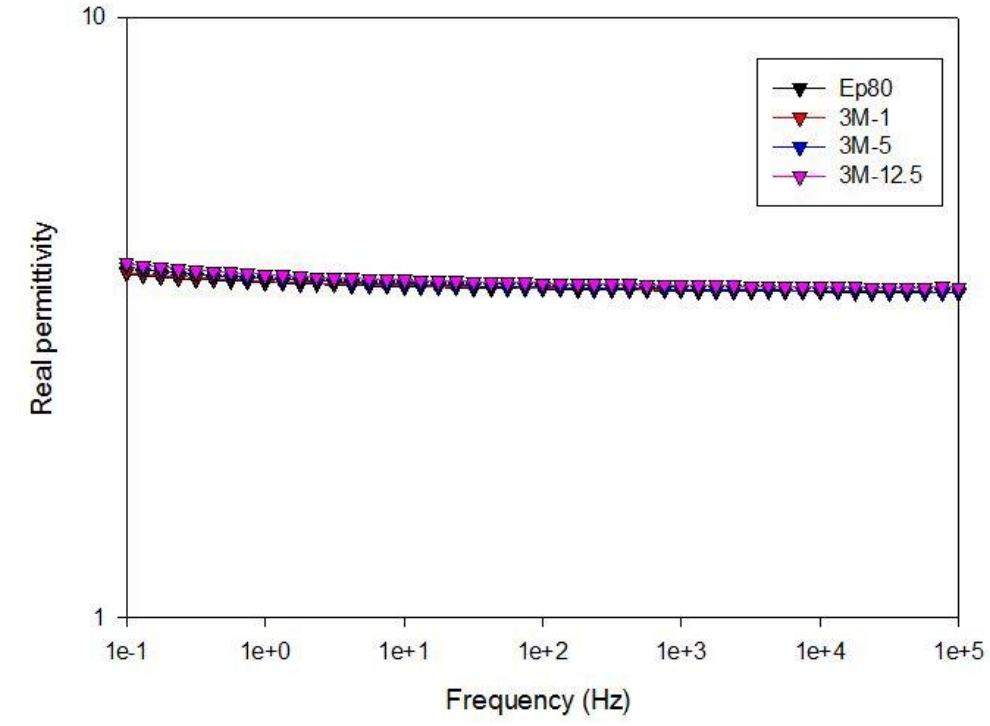

(a)

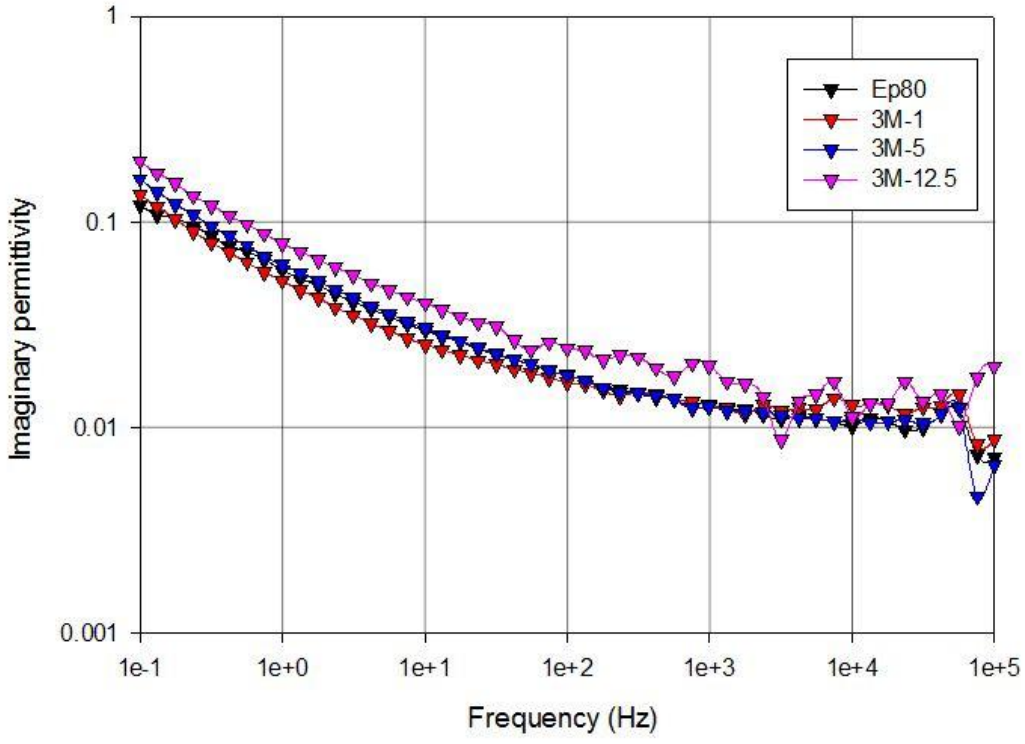

(b)

Figure 5-29 Complex permittivity of 3M systems at 160 ^{o}C (a) real (b) imaginary

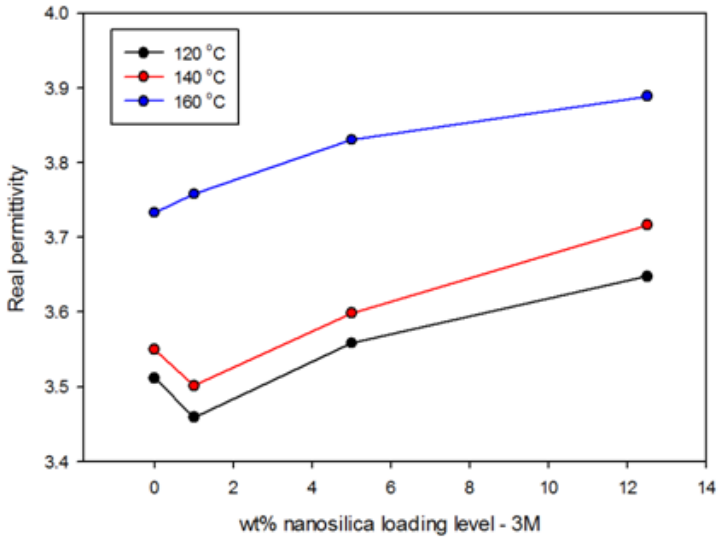

Figure 5-30 Real permittivity of 3M systems against filler loading level at different temperatures, obtained at 0.1 Hz

In order to examine size effects, micro-silica was incorporated into the unfilled epoxy. SEM images show the aggregation of micro-silica within the resin matrix. The poor dispersion of fillers could reduce the electrical properties of the microcomposite as discussed above. However, when the size of the filler is increased into the microscopic range, interfacial effects can be ignored. In microcomposites, properties are typically a weighted average of the constituent material component properties. At 12.5 wt% loading level, the microcomposite could have about 14% contribution from the silica. In practice, the microsilica particles in quartz have a permittivity of about 3.8-5.4 [141], whereas the unfilled resin permittivity is about 3.5. Therefore, the increase in dielectric constant is not significant. However, due to poor compatibility between the silica particles and the matrix, extra free volume could exist around the micro-particles or their aggregates, so providing clusters for charge transport and contribute to the LFD process at low frequencies and high temperatures. Conversely, the same loading level of nanosilica will be characterised by extremely large interfacial areas, and hence, the interfacial effect could become significant as shown in Figures 5-31 to 5-33.

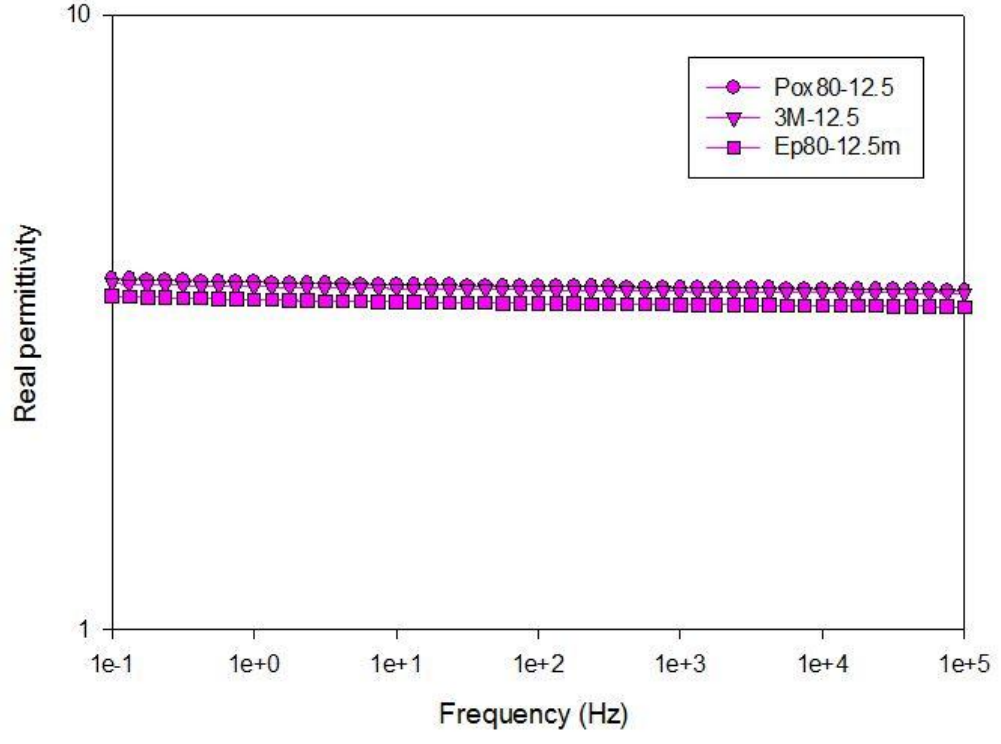

(a)

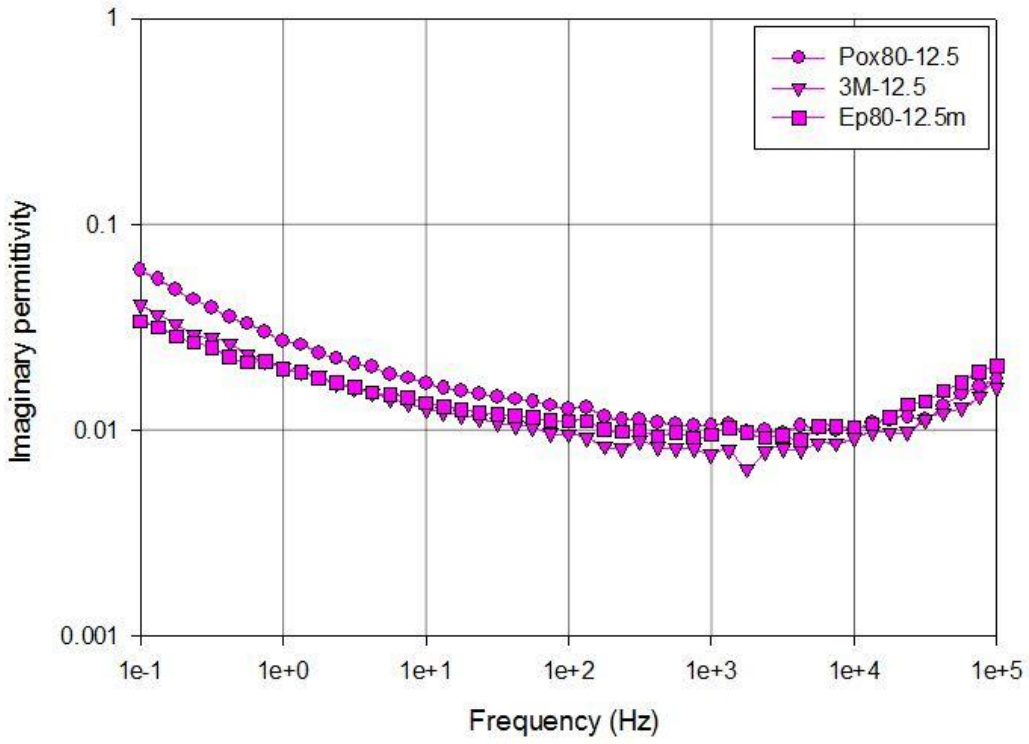

(b)

Figure 5-31 Comparison on complex permittivity at 120 ^{o}C (a) real (b) imaginary

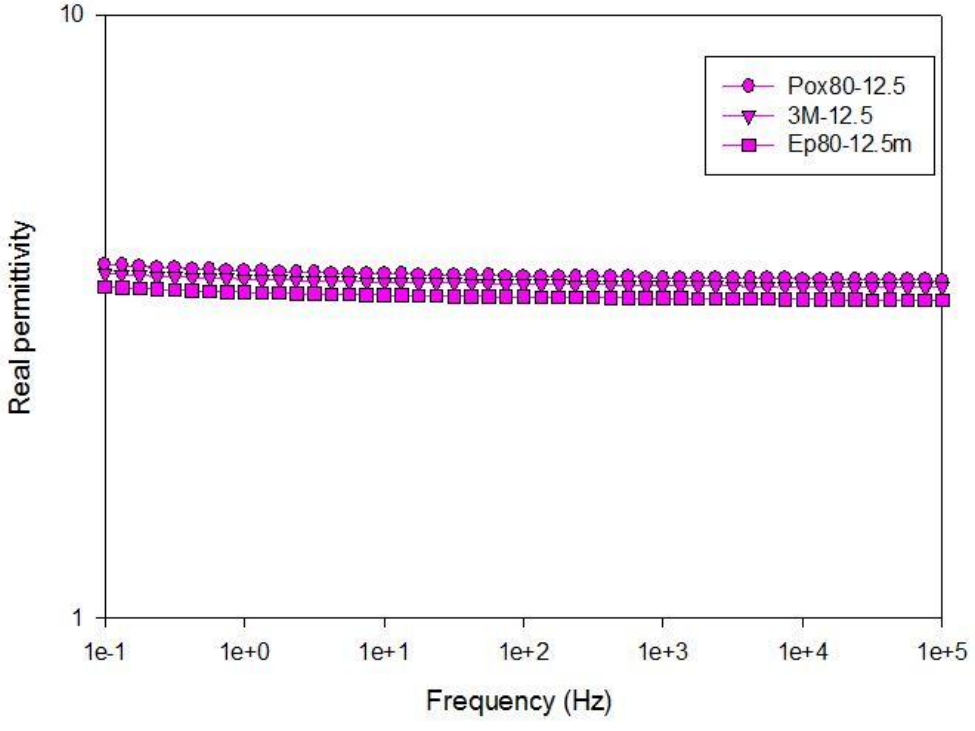

(a)

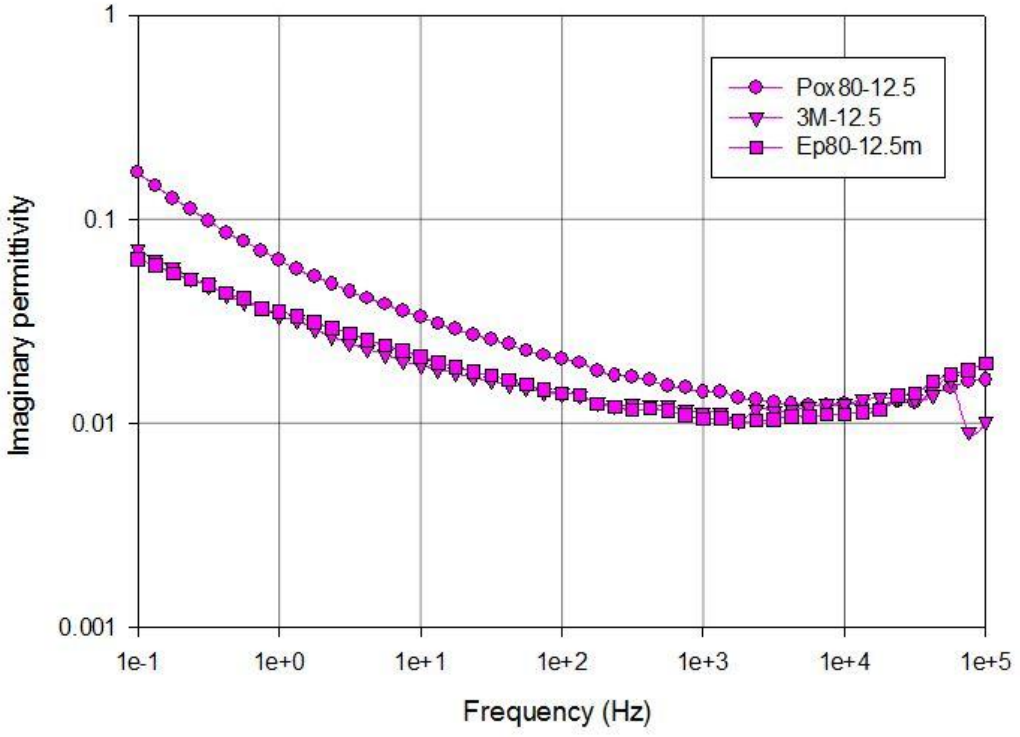

(b)

Figure 5-32 Comparison on complex permittivity at 140 ^{o}C (a) real (b) imaginary

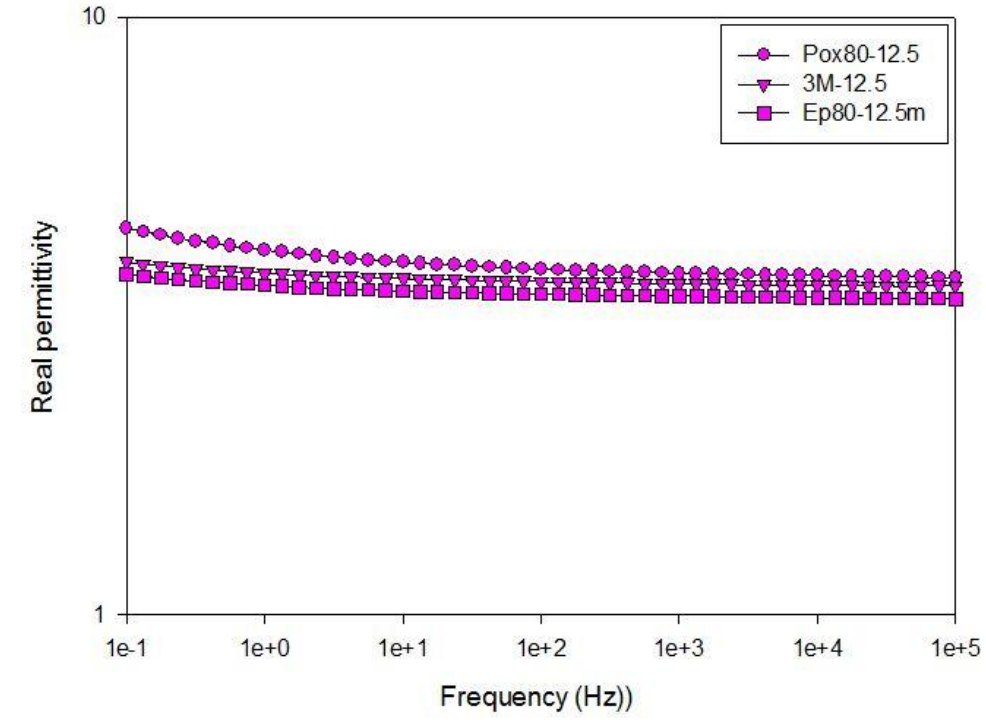

(a)

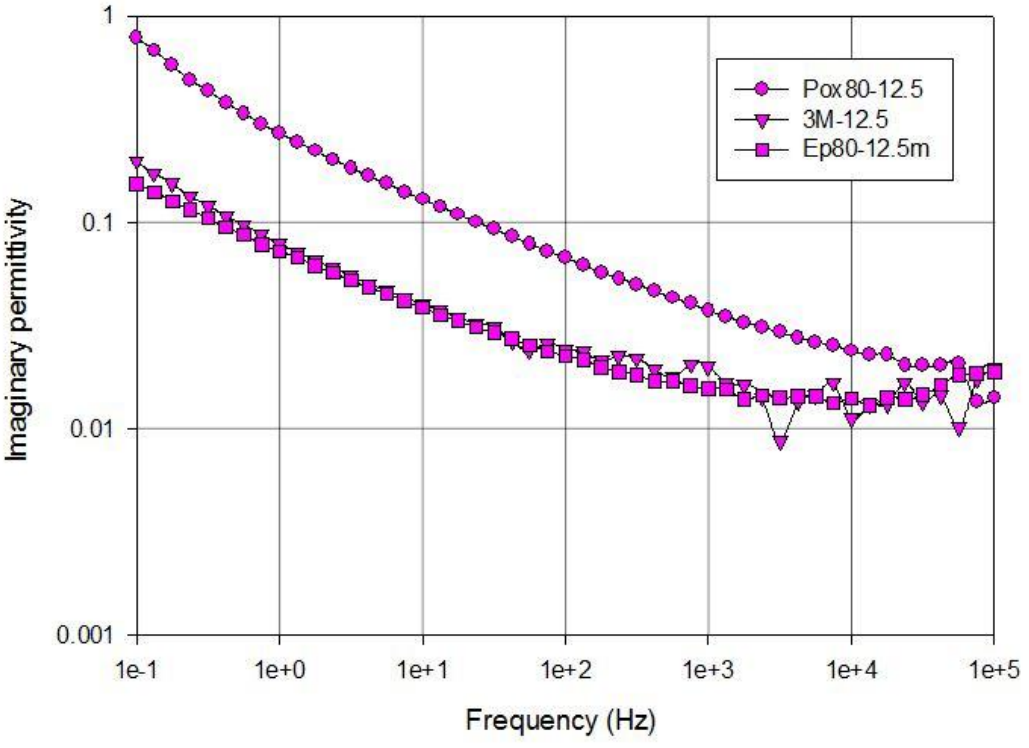

(b)

Figure 5-33 Comparison on complex permittivity at 160 ^{o}C (a) real (b) imaginary

In summary, the addition of fillers leads to an increase in dielectric constant and loss factor due to the stoichiometric and interfacial effects. Both the effects depend on the characteristics of any organic surface groups and the interfacial volume fraction. In

other words, they depend on the surface treatment and the filler size. When the filler size is in the microscopic range, interfacial effects become negligible. In this case, the properties of microcomposites are typically a weighted average of the constituent material component properties and depend on the dispersion state of fillers within the resin matrix.

5.9 Chapter summary

The incorporation of fillers markedly influences the properties of the resulting composites. In general, the addition of fillers leads to a reduction in T_g, E_b and an increase in dielectric constant and loss factor. Apart from the stoichiometric effect, interfacial effects can also be observed in the nanocomposites. The multi-core model proposed by Tanaka [253] can be applied to explain the behaviour of the nanocomposites. This model suggests the presence of three distinct phase regions at the interfaces, including the tightly bonded layer (layer 1), the bound layer (layer 2) and the loose layer (layer 3). The second and third layers are believed to exert the most worked effects on material properties. However, the effects of these two layers act in the opposite sense. Therefore, the effective properties depend on the dominant contribution from each layer. The surface treatment shows the effects on the loose layer through the interaction between the organic surface groups and the host resin matrix. Depending on the characteristic of any organic surface groups, robust or weak interfaces could be formed, hence, resulting in different dielectric behaviours, as shown in the cases of the 3M and Nanopox systems. When the filler size is in the microscopic range, interfacial effects become negligible, due to the consequent large reduction in the interfacial area. The properties of microcomposites are typically a weighted average of the constituent material component properties. Micro-fillers can be considered to be defect centers, which enhance the local field at the interfaces due to the difference in the dielectric permittivity between the filler (about 5.4) and the host resin (about 3.5). The larger the filler is, the higher the local field. Therefore, the aggregation of fillers leads to the deterioration of the material. Meanwhile, the incorporation of fillers does not result in a significant modification to the space charge behaviour of the samples. Only a small amount of homocharge can be observed near the cathode in all the cases, whereupon injection of further charge is likely to be suppressed. No internal space charge can be observed at other locations within the bulk of the samples. Moreover, the quick decay of

such injected charges suggests a distribution of only shallow traps near sample surfaces. The nanocomposites under study, in principle, possess similar structural networks with well-dispersed nanosilica. Although the concentration of defects may be different, the inter-trap distance is likely to be too large for conduction by hopping between localised states in the band gap to occur. At room temperature, all motions within the matrix are severely hindered, so ionic conduction will also be slow. Also, any polarisation process is limited at this temperature. Therefore, after being injected from the cathode, the electrons cannot move to the anode and stay in the vicinity of the electrode. For the microcomposite, poor dispersion was observed in which the bulk of the filler becomes deposited at one side of the sample; the remaining material was comparable to the unfilled epoxy. Therefore, once electrons are injected, it is difficult for them to move. Moreover, the presence of fillers may limit the injection of charges into the sample. In conclusion, to explore more about the space charge behaviours, the temperature dependence is necessary.

Chapter 6 Effects of adding nano-silica and micro-silica to epoxy-based systems

6.1 Introduction

Epoxy resins have been widely used in electrical insulation systems, including in indoor, outdoor and enclosed equipment. However, they are relatively costly compared to some other insulating materials. Therefore, composites are often employed in engineering applications and were introduced for the first time in the 1940's, mainly in the form of plastics reinforced with glass-fibres. The incorporation of inorganic fillers, such as silica, alumina, etc, into the polymer formulation helps not only to reduce cost, but also to enhance mechanical properties such as tensile modulus, fracture toughness [157], or the resistance to dry band arcing and surface discharge [20-21]. For conventional composites, the filler size is usually in the range of 15-100 μm. Many studies have been conducted to investigate the effect of microscopic fillers on the performance of epoxy-based composites employed in HV equipment [301-302]. Recently, with advances in nano-technolgy, electrical insulation systems employing nano-fillers have often proved to provide better performance than conventional micro-filled composites, including lower dielectric loss, improved dielectric strength, or enhanced resistance to erosion and tracking [20-22]. However, contradictory results have also been reported for nanocomposites [26-30]. Obviously, the difference in the size of micro and nano particles implies differences in particle mass, interfacial area, and inter-particle distance, and hence, new effects are expected upon the introduction of nano-fillers. In an attempt to produce electrical insulation materials with effective cost and good dielectric performance, the combination of nano-sized and micro-sized fillers is expected to incorporate the good properties of each type of filler into the resulting composites. This chapter is set out to investigate the effects of adding a small amount of nano-silica into epoxy-based composites filled with a larger amount of micro-silica.

Such conventional micro-composites have been widely used in engineering applications.

Table 6-1 lists the samples prepared for this investigation, along with their sample codes.

Table 6-1 List of microcomposite samples under study

Sample code	Resin ratio	%wt nano-fillers	%wt micro-fillers	Type of nano-fillers
Ep80	100:80:1	0	0	N/A
Pox80-5	100:80:1	5	0	Nanopox
3M-5	100:80:1	5	0	3M
65M	100:80:1	0	65	N/A
60M5N-Pox	100:80:1	5	60	Nanopox
60M5N-3M	100:80:1	5	60	3M

6.2 FTIR

Figure 6-1 shows the FTIR spectrum of the micro silica powder that was employed to prepare the samples. The presence of silica is demonstrated by the peaks at 1000 and 460 cm^{-1}, which are due to the stretching mode and bending mode of the Si-O-Si bonds.

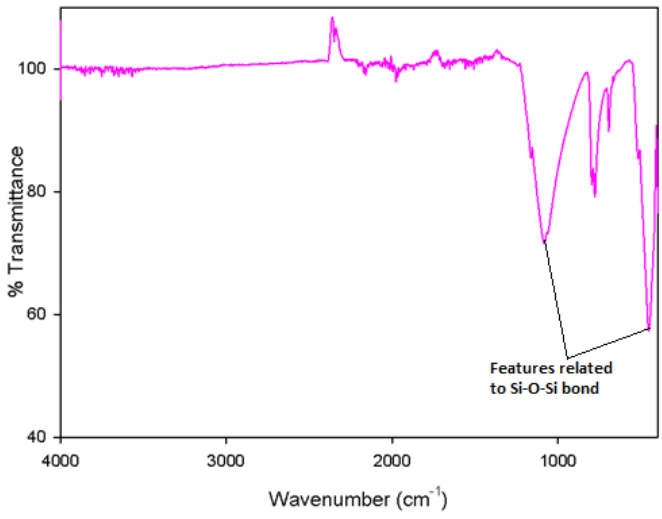

Figure 6-1 FTIR spectrum of micro silica powder

Figure 6-2 compares FTIR spectra obtained from a number of cured micro-composites. It is clear that the presence of silica particles is revealed by the peaks at 1000-1100 cm^{-1} and 460 cm^{-1}. The existence of ester groups due to the reaction of epoxy resin and hardener is evinced by the peaks at about 1735 cm^{-1}, as discussed in the previous chapters. In general, the curing mechanism is found to be the same in all three micro-composites. In addition, the basic chemical bonds present in the composites are similar to those in the unfilled epoxy and nanocomposites that were studied in the previous chapters, as shown in Figure 6-3. This suggests that the incorporation of microscopic silica produces no new curing reactions. However, it is evident from Figures 6-2 and 6-3 that the presence of Nanopox and 3M is likely to introduce hydroxyl groups, which are revealed by the broad flat peak at 3000-3500 cm^{-1}. FTIR spectra of the Nanopox E470 and the 3M masterbatches also exhibit this broad peak, as demonstrated in the previous chapters. However, this feature was not observed in FTIR spectra of cured nanocomposites studied in the previous chapter, as shown in Figure 6-3. As discussed in chapter 4, OH groups may react with epoxy groups and catalyse etherification mechanism. As a result, the presence of OH groups was not evident in the FTIR spectra of cured nanocomposites. Conversely, the existence of OH groups in cured micro-nano composites may suggest that micro-silica fillers inhibit reactions of OH groups with epoxy to a certain limit, possibly leading to hydrogen bonding between OH groups on nanoparticle surfaces to form agglomerations.

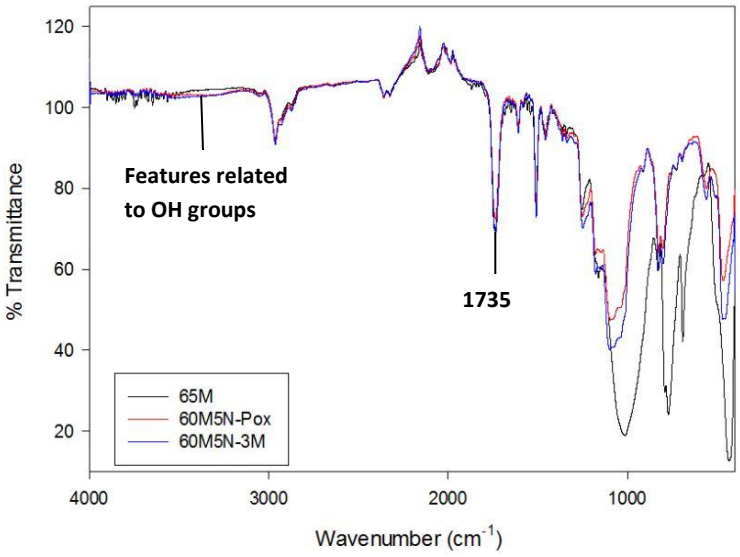

Figure 6-2 Comparison of FTIR spectra of micro composites

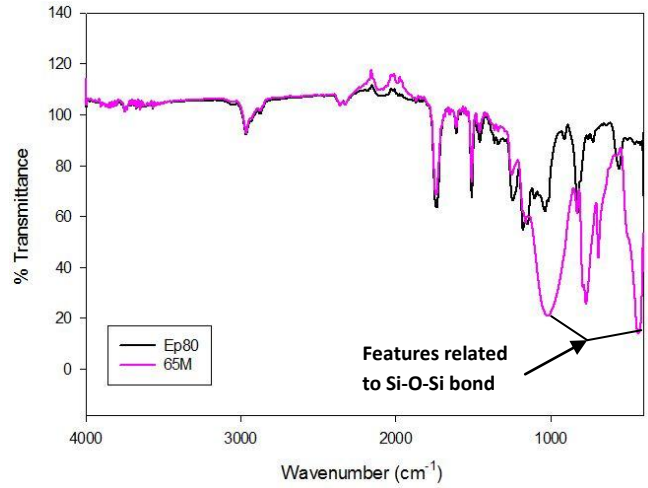

(a)

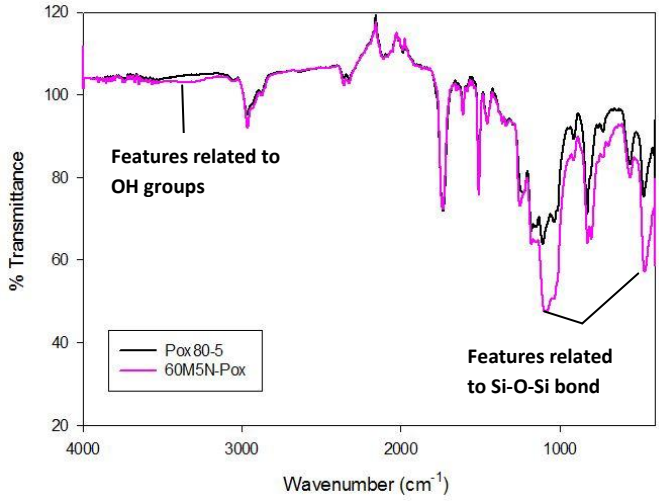

(b)

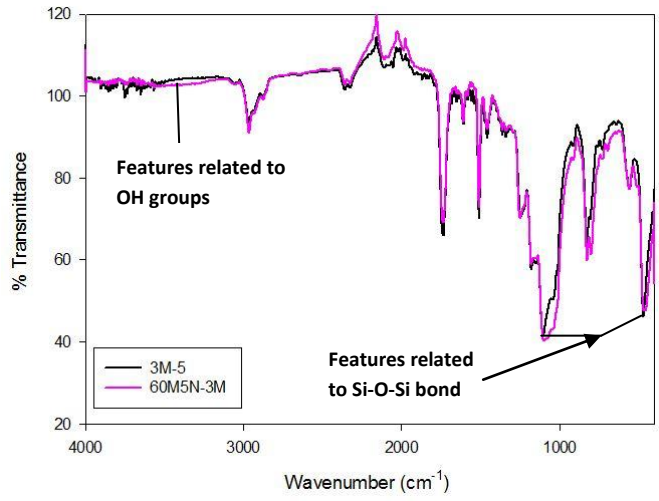

(c)

Figure 6-3 Comparison of the FTIR spectra of micro composites with spectra obtained from the corresponding resin matrix (a) 65M & Ep80, (b) 60M5N-Pox & Pox80-5, (c) 60M5N-3M & 3M-5

6.3 SEM

The addition of micro-fillers results in a fracture propagation process that is completely different from the one that occurs in unfilled epoxies and nanocomposites discussed previously. The resulting surfaces are found to be extremely rough, on the 50 μm scale, irrespective of whether or not nanofillers are present. This fact suggests that the origin of the roughness is the micro-fillers incorporated into the resin matrix. This is illustrated in Figure 6-4. The examination of low magnification images reveals two distinct structural units, namely, the micro particles, which appear as the bright objects, and the matrix texture, which appears to be darker, as shown in Figure 6-5. The red arrows in Figure 6-5 show some representative regions which contain de-bonding between the resin matrix and micro-silica. As a consequence, under fracture processes, cracks propagate through such regions. This implies that organic groups on micro-filler surfaces can only interact weakly with the resin matrix and consequently, poor dispersion of micro-silica in samples results. In addition, some variations in the structure of the 60M5N-Pox and 60M5N-3M samples are also evident in Figure 6-5 b&c. Those regions (indicated by blue arrows) that are devoid of structure and appear similar to Figure 6-5(a) and 6-6 suggest that these regions contain no nano-fillers. This observation suggests that uniform mixing and dispersion of nanoparticles in these systems is more difficult to achieve. As a consequence, the samples studied here are typical because the micro-silica has completely settled, as seen in Figure 6-4. However, the primary interest in these materials is the structure of the resin matrix and, particularly, its variability from place to place. Figures 6-6 to 6-8 contain SEM images of these samples obtained at higher magnification. It is evident that all of these systems exhibit matrix textures that are similar to those seen in the corresponding unfilled epoxy and the nanocomposites discussed in the previous chapters, as shown in Figures 6-6(d), 6-7(d), and 6-8(d). This reinforces the notion that the change in matrix texture observed in the previous chapters upon the incorporation of nano-silica is not an artefact, but is rather associated with the presence of the nano-filler. However, it is necessary to bear in mind that the images of fracture surfaces result from the combination of microstructure and the fracture propagation process. Therefore, artefacts could affect the resultant topography. However, the consistent appearance of SEM images should be considered to provide reliable information about the effects of nano-fillers and micro-fillers.

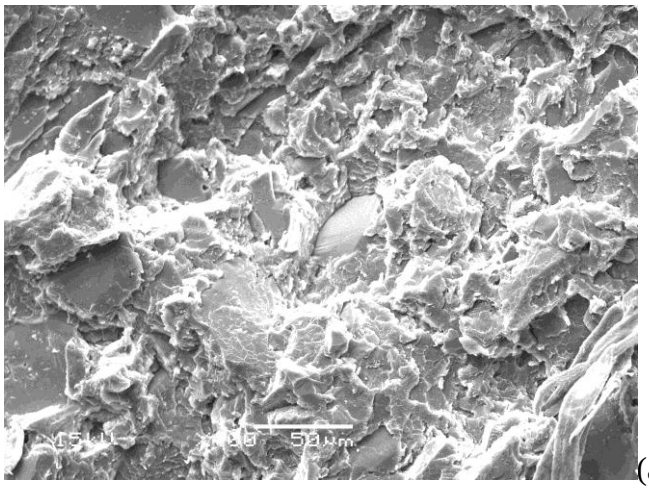

(a)

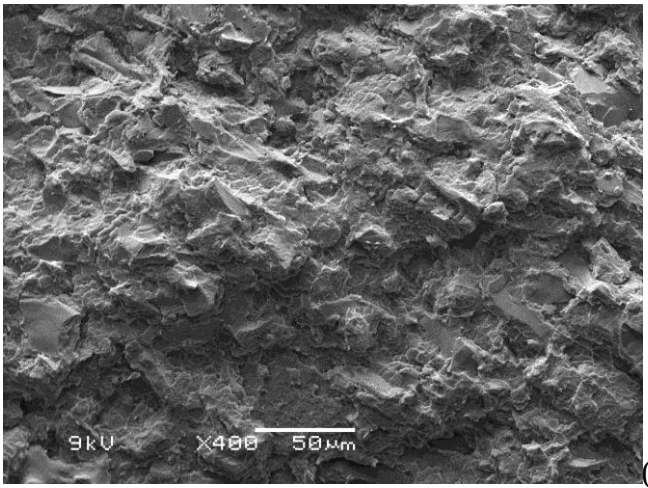

(b)

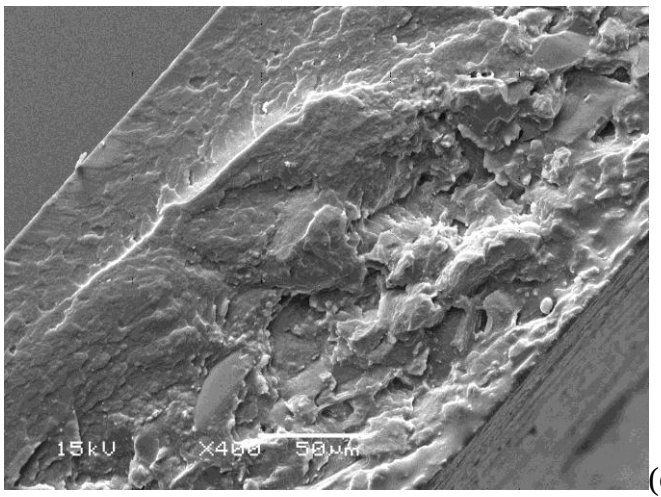

(c)

Figure 6-4 Very low magnification images of micro composites (a) 65M; (b) 60M5N-Pox; (c) 60M5N-3M

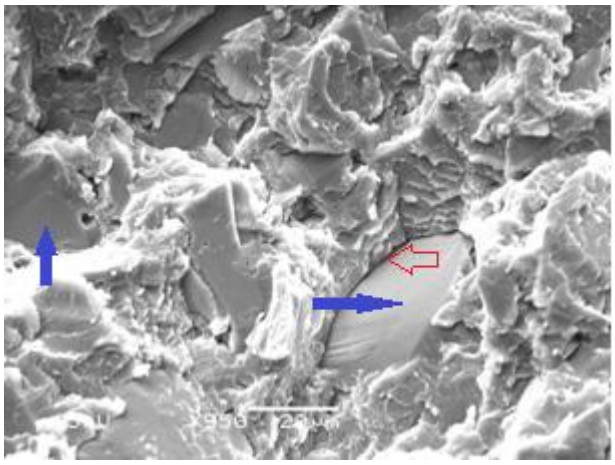
(a)

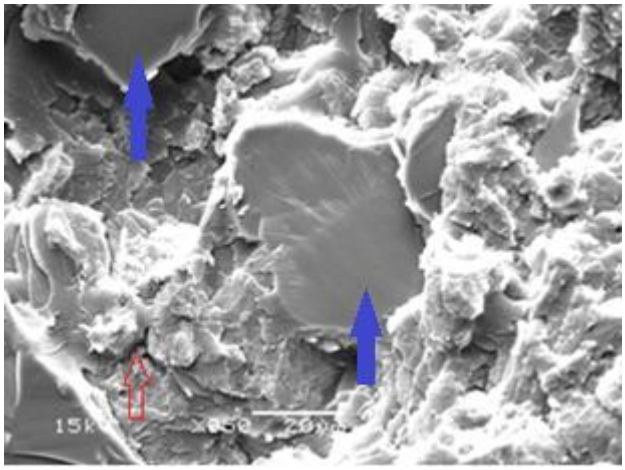
(b)

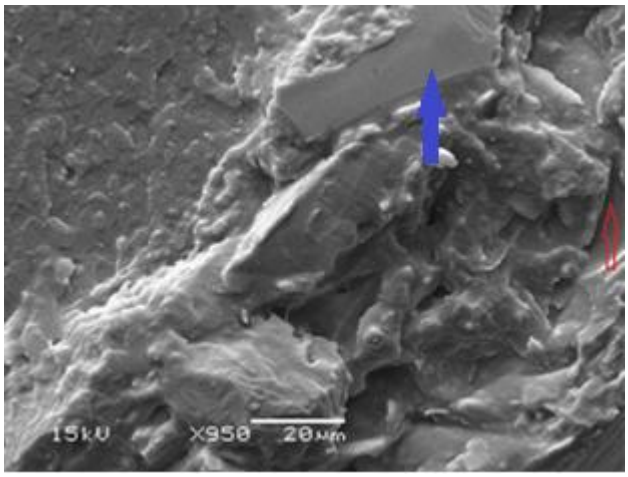

(c)

Figure 6-5 Low magnification images of micro composites (a) 65M; (b) 60M5N-Pox; (c) 60M5N-3M

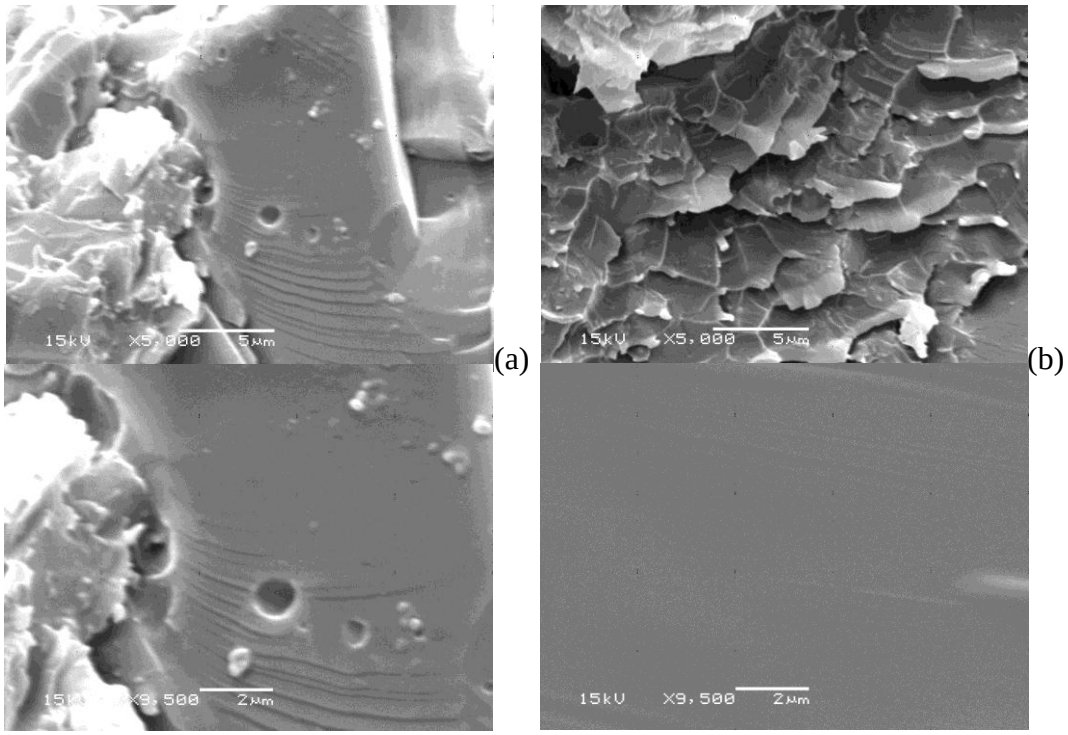

Figure 6-6 Representative matrix texture in samples (a)-(c) 65M; (d) Ep80

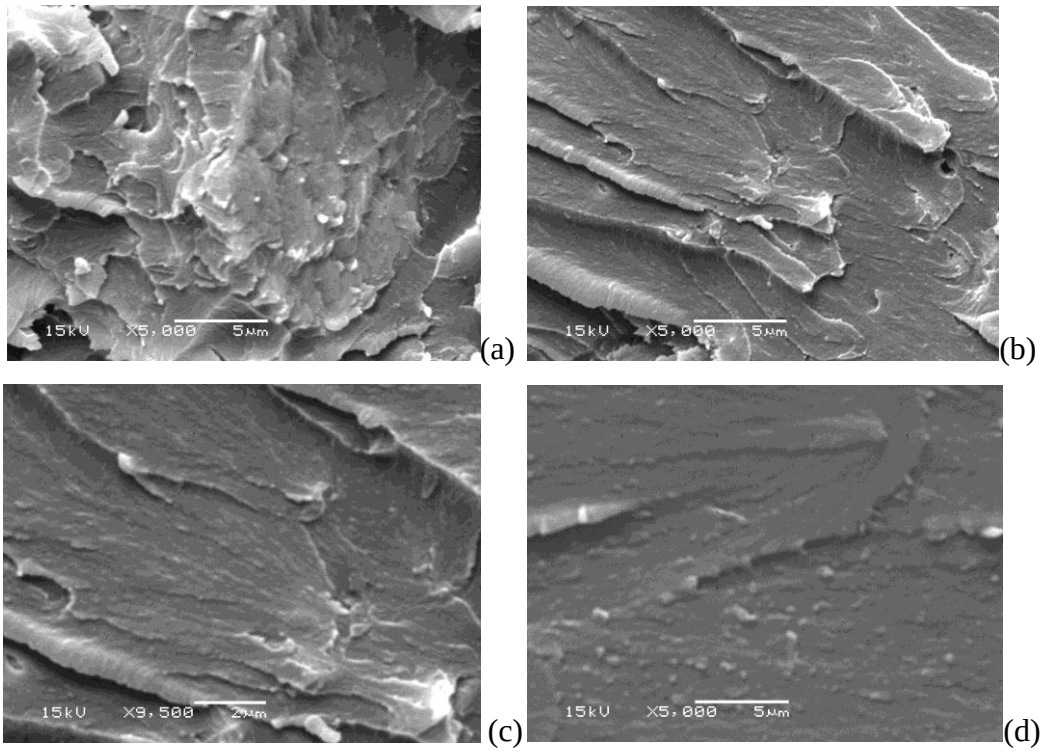

Figure 6-7 Representative matrix texture in (a)-(c) 60M5N-Pox; (d) Pox80-12.5

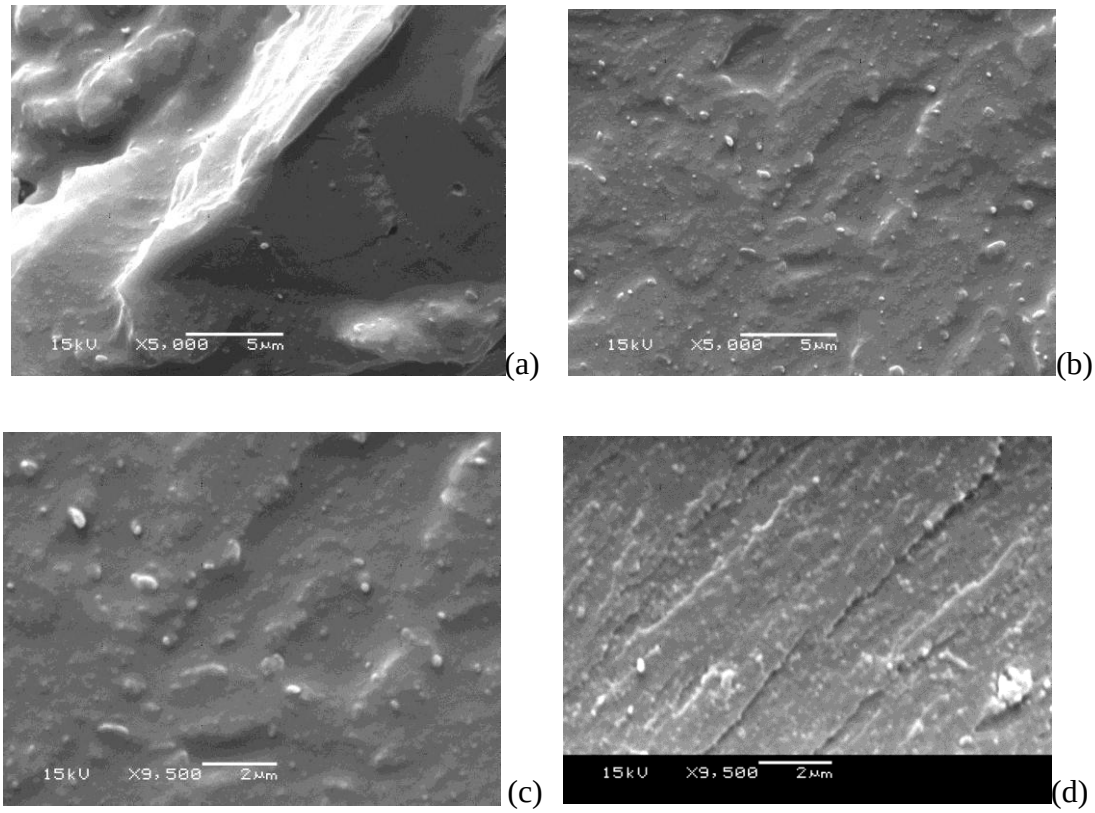

Figure 6-8 Representative matrix texture in (a)-(c) 60M5N-3M; (d) 3M-12.5

6.4 Thermal characterisation

Figure 6-9 shows the DSC thermograms obtained from the micro-composites under investigation, while Table 6-2 summarises the important information extracted from such DSC plots together with relevant data obtained in the previous chapters for comparison. It is clear that, except for the 60M5N-Pox sample, there is no significant difference in T_g of the 65M and 60M5N-3M microcomposites compared to those of the unfilled Ep80 and the 3M-12.5 nanocomposite. This implies that, in these two samples, the addition of micro silica does not exert a significant effect on the free volume in the surrounding matrix. Sun [141] also found a similar effect of micro silica on the unfilled epoxy, while the presence of nanosilica led to a significant reduction in T_g. Rouyre et al. [157] also observed comparable effects of nanosilica on T_g, but a slight decrease in T_g was revealed upon adding micro-silica. Conversely, Hyuga et al. [11] observed a decrease in T_g upon adding a small amount of nanofiller, while an increase in T_g was obtained on adding a large amount of microfiller to systems with and without co-addition of a small amount of nanofiller. However, Ma et al. [303] reported an increase

in T_g of 10 ^{o}C when 5 wt% micro silica was replaced by 5 wt% nano silica. Such discrepancies can be explained by the following factors. First, microfillers do not exert a significant interfacial effect due to their large size. However, the addition of a large amount of microfiller dominates sample properties. Obviously, the surface chemistry of micro-fillers exerts a certain influence on T_g. The presence of microfiller that strongly interacts with the resin matrix may disturb the molecular mobility of the epoxy chains so, increase T_g. However, due to the small interfacial areas of microfillers, such effects are limited. FTIR spectra of micro silica powder and the 65M sample did not reveal the existence of OH groups so, effects due to hydrogen bonding can be considered negligible. In addition, SEM images showed regions that may contain weak bonds between micro-fillers and resin matrix. Therefore, adding microsilica is likely to cause a slight reduction in T_g. Meanwhile, it is likely to appear two glass transitions in the 60M5N-Pox sample, as arrowed in Figure 6-9(b). As mentioned above, the incorporation of a large amount of micro-filler is likely to make the uniform mixing and dispersion of nanoparticles more difficult to achieve. SEM images show regions containing no fillers, with the implication that there are other regions containing higher nanofiller concentrations than would be anticipated based on the material formulation. Replacing 5 wt% of microsilica by 5 wt% nanosilica means that the ratio of nanofiller to resin matrix is about 14%, which is comparable to nanocomposites containing 12.5 wt% nanofillers. For nanocomposites, it is evident that the variation in T_g will depend on a number of factors, including the dispersion of the nanofiller, the nano-particle chemistry, the characteristics and thickness of interphase regions, etc. Adding nanosilica in the form of the 3M system resulted in no significant changes in T_g compared to the unfilled Ep80, as discussed in Chapter 5. Therefore, even though the dispersion of nanosilica is not uniform in the 60M5N-3M, there are no significant differences between the T_g values of various regions within this microcomposite. As a result, overlapping of glass transition temperatures from 140 ^{o}C to 147 ^{o}C can be seen, so the effective glass transition is likely to be 145 ^{o}C, which is slightly higher than that of the 3M-12.5. However, due to measurement uncertainties, this increase cannot be concluded. Conversely, adding Nanopox nanosilica produced a reduction in T_g of 12 ^{o}C compared to the unfilled Ep80. Therefore, two glass transitions are observed in the 60M5N-Pox, including one corresponding to the unfilled matrix and another to the filled matrices. Moreover, as mentioned above, there should be some regions containing

more than 12.5 wt% nanosilica, so the T_g of such regions should be smaller than that of the corresponding Pox80-12.5. As a consequence, the first T_g observed is about 130 ^{o}C, while the second one is about 150 ^{o}C, which is approximately equal to that of the unfilled Ep80.

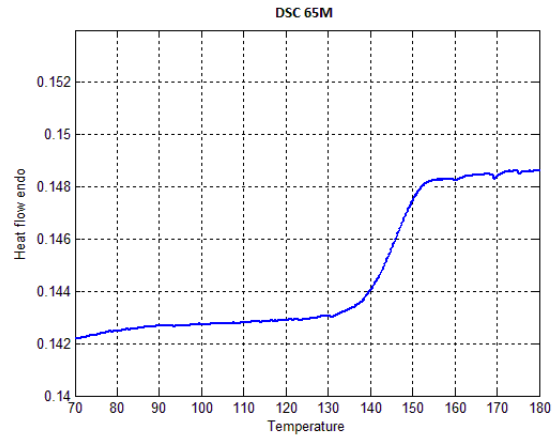

(a)

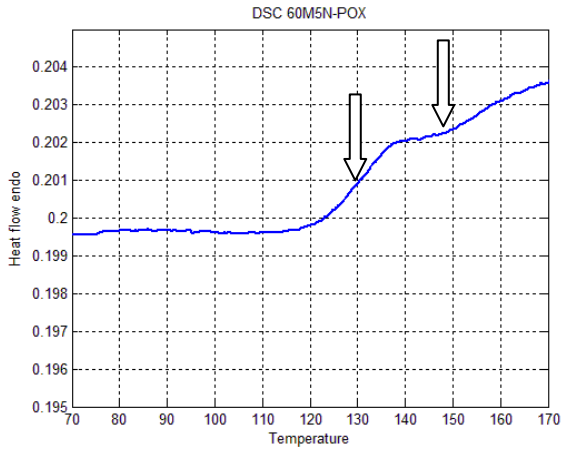

(b)

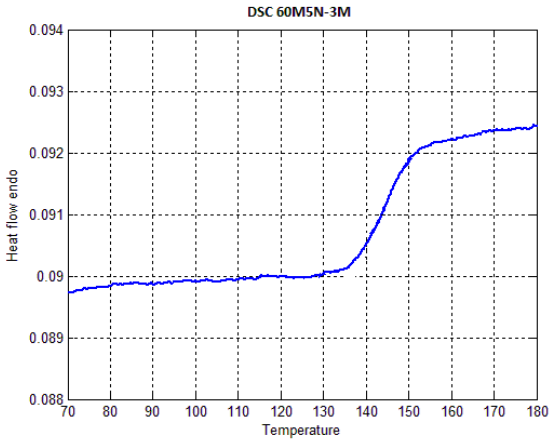

(c)

Figure 6-9 DSC obtained for (a) 65M, (b) 60M5N-Pox, (c) 60M5N-3M

Table 6-2 Thermal characteristics of microcomposite samples

Sample codes	T_g (°C) ±2 °C	ΔT (°C) ±2 °C	ΔC_p^* x10^{-1}(J/g°C) ±0.05
Ep80	147	20	5.5
65M	144	23	5.7
Pox80-12.5	135	28	7.1
60M5N-Pox	**130 & 150**	**38**	7.4
3M-12.5	143	23	5.7
60M5N-3M	145	20	5.9

6.5 Space charge behaviour

The previous chapters described how only a small amount of homocharges accumulated near the cathode in the unfilled epoxies, and epoxy-based systems containing nano-silica or a small amount of micro-silica. This fact suggests that the incorporation of nano-silica seems not significantly to influence the space charge behaviour of these systems. However, the addition of an abundant amount of micro-silica induces dramatic effects on the space charge properties. Figures 6-10 to 6-12 contain space charge profiles obtained from various formulations of the micro-composites under investigation, including 65M, 60M5N-Pox, and 60M5N-3M. These space charge data were obtained during 1h poling at different electric fields, namely 30 and 50 kV/mm, followed by 1h discharging. For all three systems, complicated patterns of space charge can be observed. First, due to gravity, microsilica fillers were deposited at the bottom of samples during a long curing cycle. This side of each sample was connected to the cathode, while the other that contains much less microsilica was connected to the anode of the space charge equipment. The presence of a high density layer of micro-silica could modify the potential barrier between the sample and the electrode, such that its height is reduced and, hence, more electrons are injected into the samples near the cathode. Moreover, the settling of microsilica particles led to a multi-layered structure in the samples. In such cases, the effects involving the interfaces can account for the space charge behaviours. A number of studies have investigated the interfacial characteristics of space charge in multi-layered materials and found that charges were

blocked at interfaces [304-306]. In this study, the injected electrons could move to the anode under the applied field and become blocked at the interfaces. These trapped electrons may induce positive charges in the next layer. As a consequence, negative charges accumulate near the anode and hence, induce positive charges on the anode. Besides, a fraction of trapped electrons may be de-trapped under the applied field and across the interface and move to the anode. Obviously, the probability of this mechanism depends on the trap levels and the potential height between the two adjacent layers. Second, micro fillers, which can be considered as defects/impurities, contribute a high density distribution of trap states in the energy gap such that the inter-state distance can become very small. Under such circumstances, injected electrons could tunnel or hop between trap sites and, drift to the anode. Electrons can be considered to move along the microsilica aggregates. Third, at the anode, the density of micro fillers reduces significantly such that the inter-state distance becomes larger, so hopping conduction is limited. Moreover, at the anode, a layer containing a majority of resin matrix is in contact with the electrode. Therefore, the potential height between the sample and the anode may increase significantly. Consequently, the exchange of electrons is limited at the anode, and hence, the electrons are accumulated here. It is possible that a fraction of these electrons is neutralised by holes injected from the anode. The accumulation of homocharge reduces the electric field near the electrode and, hence, suppresses charge injection, while the opposite behaviour can be obtained for heterocharge accumulation. In this study, the samples of ~ 220 μm were used, whereas the average diameter of microsilica is ~ 16 μm with the upper grain of 50 μm. In addition, a high content of microsilica that can be up to 65 wt% was incorporated into the samples. Therefore, the silica layer could account for an observable thickness in the samples. Furthermore, the non-uniform mixing made the multi-layer structure become more complex and different from sample to sample, place to place. Increasing the electric field will increase the amount of injected electrons and the probability of trapped electrons that can across the interfaces and move along the microsilica aggregates to the anode.

Replacing 5 wt% micro-silica by 5 wt% of the 3M nano-silica leads to only a slight increase in the amount of heterocharge accumulated at the anode, whereas a dramatic increase can be seen in the 60M5N-Pox. Such differences were not observed in the corresponding nanocomposites. Many different mechanisms may contribute to the effects shown in Figures 6-11 and 6-12. For example, one possibility is ionic

conduction. FTIR spectra showed the presence of OH groups in the Nanopox and 3M masterbatches. As discussed in chapter 4, these OH groups can react with epoxy groups in the nanocomposites. Therefore, no evidence of OH groups can be observed in cured nanocomposites. However, the presence of microsilica may inhibit reactions of OH groups on the nano-particle surfaces with epoxy, as evinced by FTIR spectra, and make uniform mixing and dispersion of nanosilica difficult to achieve, as shown in SEM images. Consequently, nanosilica can agglomerate via hydrogen bonding between OH groups on filler surfaces. A possible mechanism for intrinsic ionic conduction may occur by electron and proton transfer through weakly-bonded hydroxyl groups [118]. However, for this type of conduction to occur, the groups must be in energetically favourable positions for charge transfer to take place [118]. That is, flexible side chains/groups are required. As discussed previously, the 3M masterbatch may produce stronger interactions between the nano-silica and the resin matrix than the Nanopox, i.e. more robust interfaces resulted. In addition, due to the larger size of nano-particles, the probability of OH groups that come into close proximity to form hydrogen bonding is lower in the 3M-based systems than in the Nanopox ones. As a result, greater accumulations of heterocharge near the anode are observed in the 60M5N-Pox than in the 60M5N-3M. In ionic conduction, electrons and positive charges move to the anode and cathode respectively and, contribute to the effective space charge profiles. Positive charges may be neutralised by the injected electrons at the cathode while the electrons could increase the amount of heterocharge at the anode. The amount of space charge is the sum of the negative and positive charges at each location across the samples. However, unambiguous interpretation of these data in isolation is not possible.

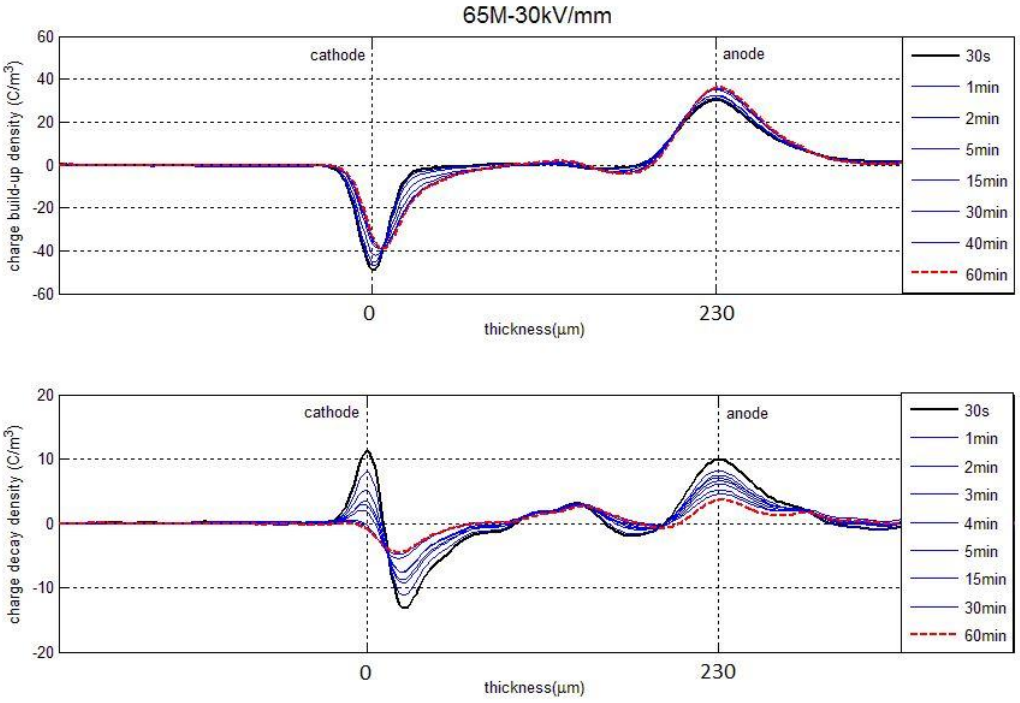

(a)

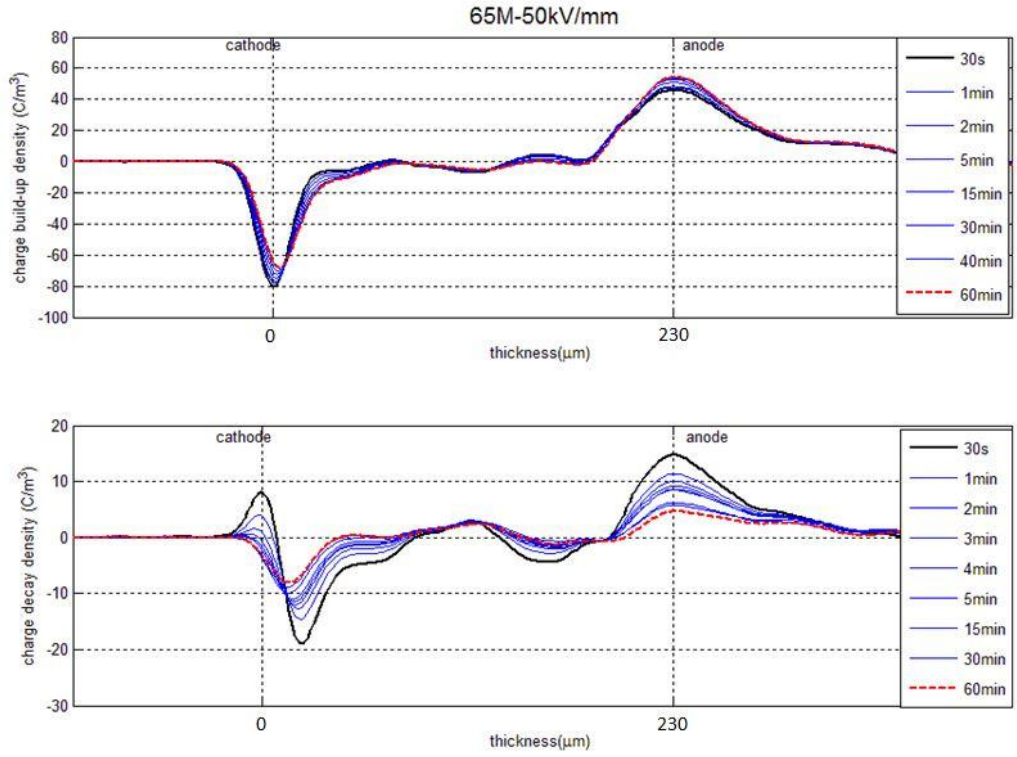

(b)

Figure 6-10 Space charge profiles of 65M at (a) 30 kV/mm, (b) 50 kV/mm

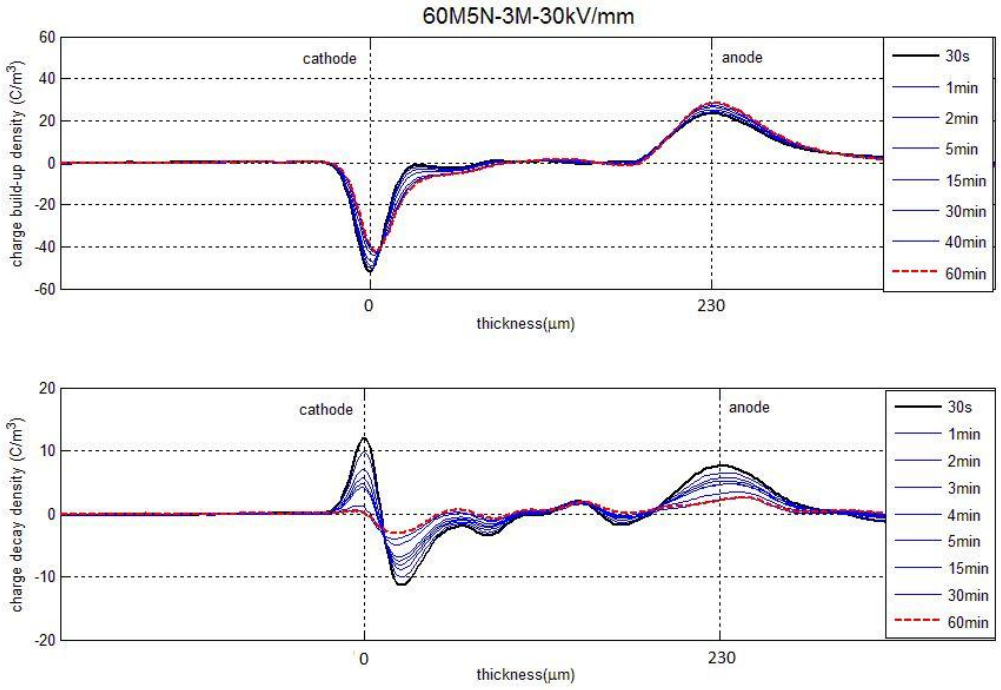

(a)

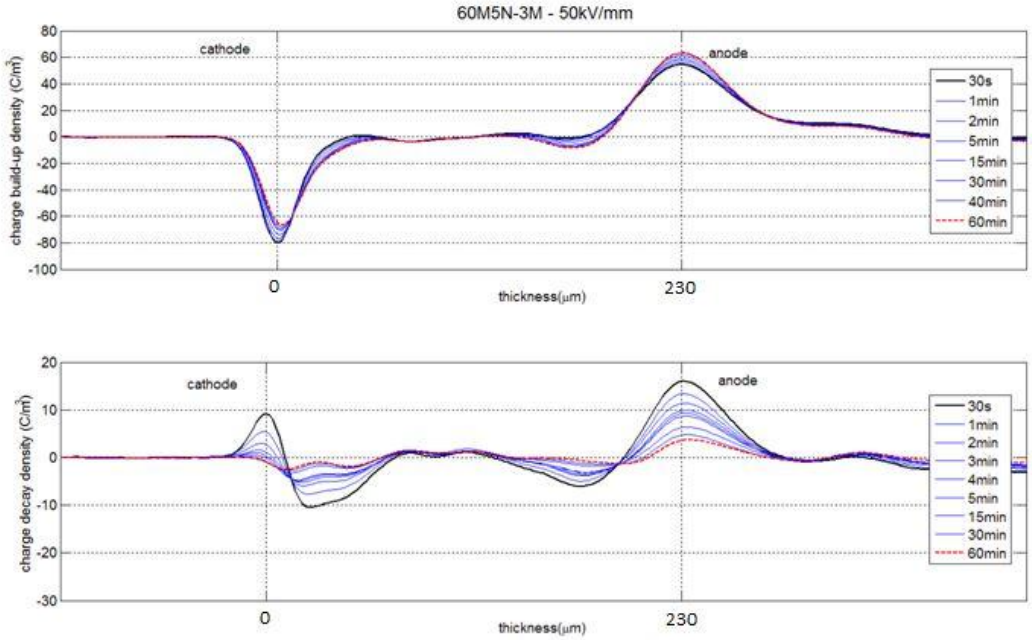

(b)

Figure 6-11 Space charge profiles of 60M5N-3M at (a) 30 kV/mm (b) 50 kV/mm

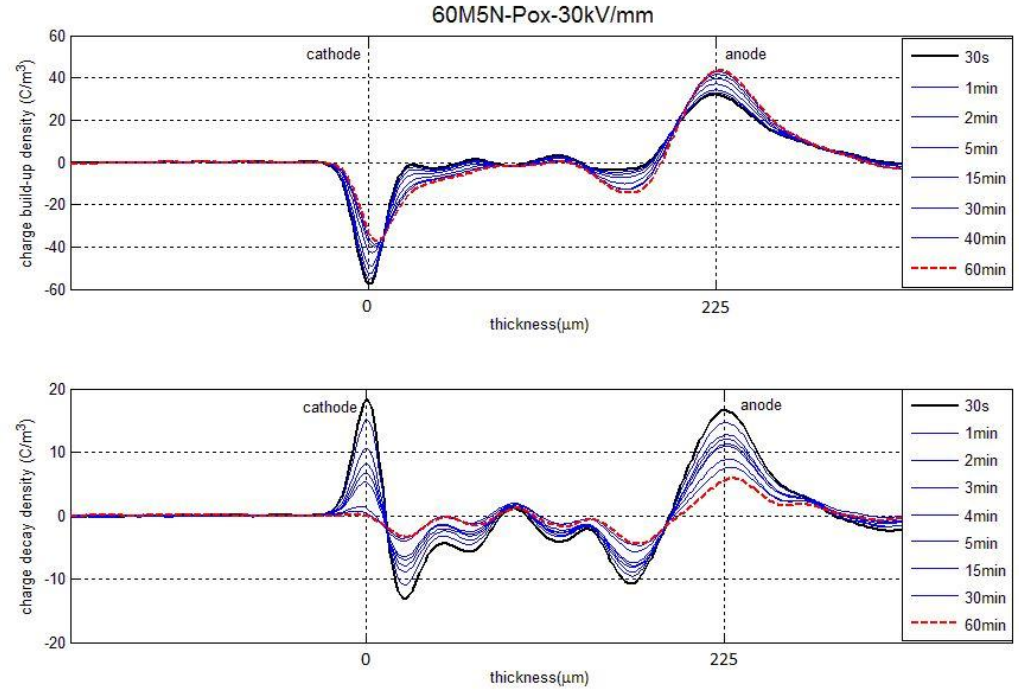

(a)

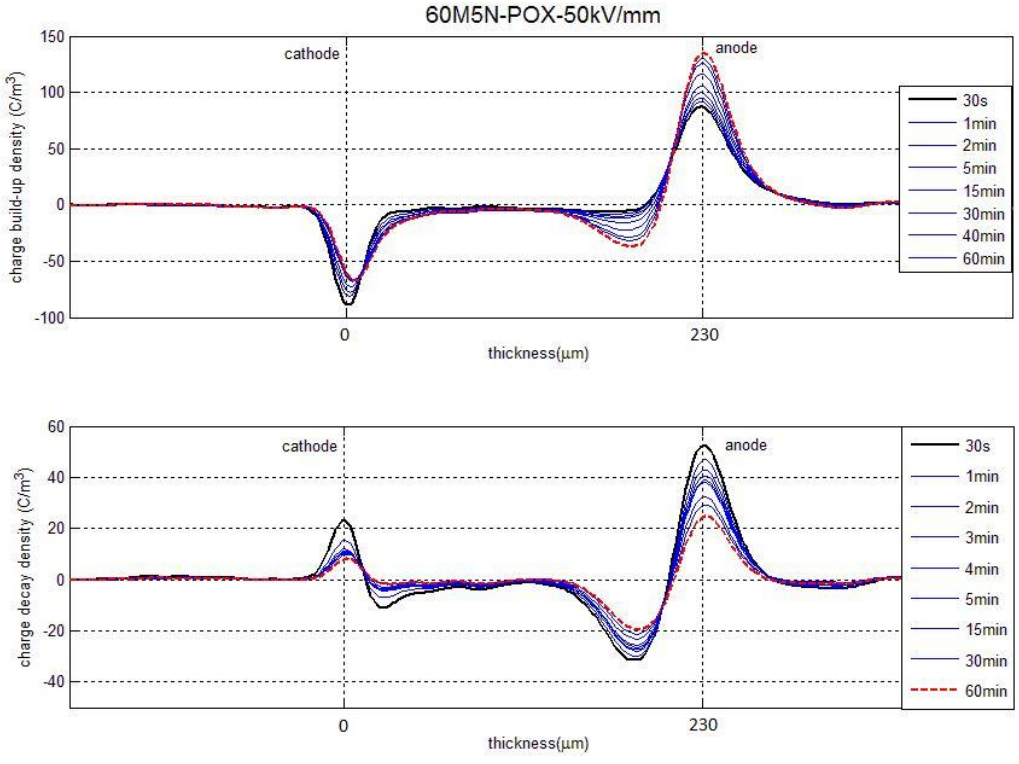

(b)

Figure 6-12 Space charge profiles of 60M5N-Pox at (a) 30 kV/mm, (b) 50 kV/mm

6.6 AC Electrical breakdown

The following breakdown measurements were performed using 500 µm thick samples. Figure 6-13 shows Weibull distribution plots of the data obtained for all the samples under study, while Figure 6-14 presents the scale and shape parameters obtained from these. Incorporating nano-fillers of either type leads to a decrease in E_b. However, for the same loading level, the reduction in E_b is smaller for the 3M-based systems than for those containing Nanopox. This observation is consistent with the data reported in Chapter 5, where it was ascribed to differences in the surface chemistry of the nano-particles, the size of the fillers and related stoichiometric effects, and the amount of residual impurities associated with the synthesis and surface treatment processes. Rouyre et al. [157] performed fracture tests using epoxy nanocomposites containing nanosilica particles from the Nanopox masterbatch supplied by Nanoresins and others produced using dry nano-silica powder distributed by Sigma Aldrich. This work revealed the lower roughness in the premixed nano-silica compounds than in those produced using the dry nanosilica. It was suggested that the premixed particles are likely not to interact with the polymer chains as strongly as the dry nano-silica due to poor bonding of "the surfactant" to polymer chains.

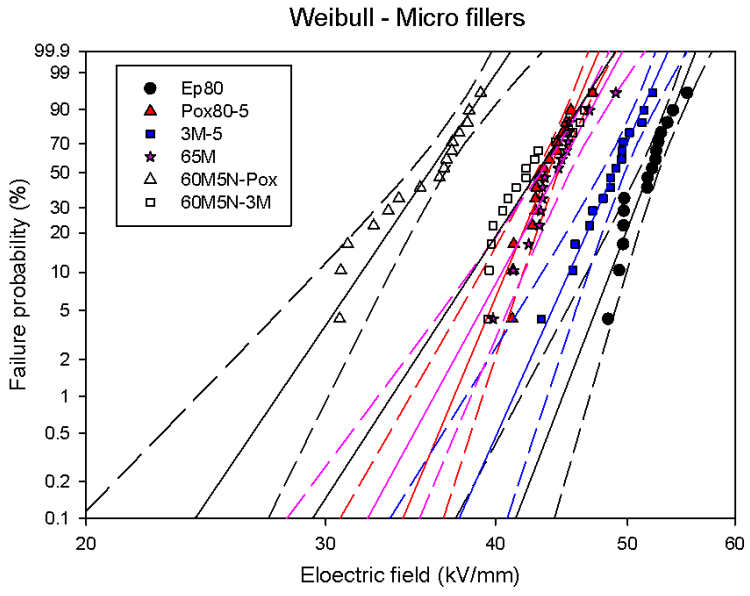

Figure 6-13 Weibull distribution plots (90 % confidence interval)

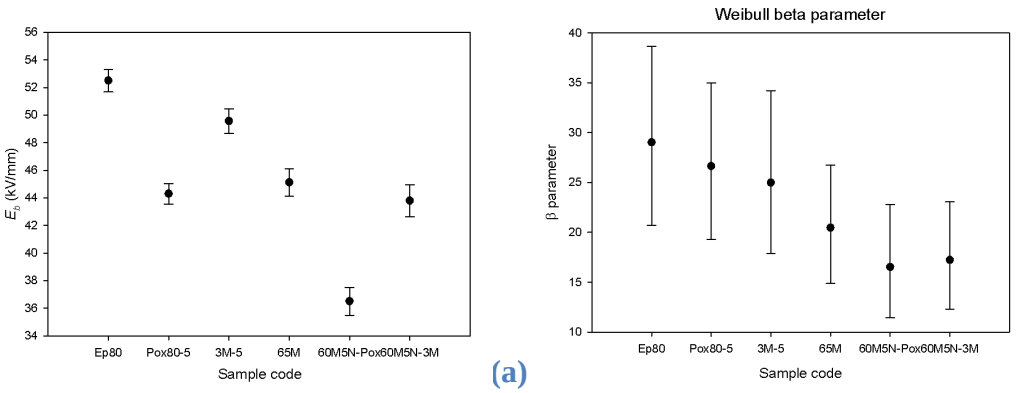

Figure 6-14 Plots of Weibull parameters (a) α and (b) β obtained from various samples under study showing decreased Eb and increased scattering upon adding micro silica

It is evident from Figures 6-13 and 6-14 that the addition of a large amount of micro-silica reduces E_b significantly and increases the scattering in the breakdown data. The decrease in Weibull shape parameter β, as shown in Figure 6-14(b), also signifies a decrease in the uniformity of the sample due to the presence of the micro-filler. As discussed previously, the presence of micro-fillers makes uniform mixing and dispersion of nanoparticles difficult to achieve. The above results are, however, markedly different from those reported by Rouyre et al. [157], who reported an increase in the electrical breakdown strength on incorporating micro-fillers. Similar results were reported by Park [307], who observed an increase in E_b upon adding either micro silica or both micro silica and a small amount of nano-silicate. In this work, the improvement in E_b was suggested to be ascribed to the electron blocking by the sphere-like silica particles and sheet-like silicates such that the breakdown rate was retarded. Conversely, Iyer et al. [308] observed a slight decrease in E_b upon adding 65 wt% micro-silica. However, they found that replacing 5 wt% micro-silica by 5 wt% nano-silica was likely to improve E_b of the micro-composite, although the differences in the shape and scale parameters were not statistically significant. In this work, it was suggested that the presence of nanofillers mitigated space charge build-up in the samples, such that an improvement in E_b was obtained upon adding nano silica. However, it is necessary to note that these studies did not investigate the dispersion of micro-fillers in samples, whereas a complete settling of the micro-silica can be observed in the microcomposites under this study. As a consequence of settling of the filler particles, a layered structure is considered to be formed in the microcomposites and hence, reducing the effective

thickness of the samples. In other words, the effective breakdown electric field is reduced. Therefore, discrepancies could be resulted from poor dispersion of micro-fillers in samples.

In this study, the incorporation of nano-silica or micro-silica on its own produces an observable reduction in E_b. For microcomposites, in addition to settling of the micro-silica, a number of explanations can be proposed for the negative consequences of adding the filler. First, as shown in the previous section, the presence of the micro-silica results in the accumulation of heterocharge near the anode, and of homocharge near the cathode. This heterocharge will increase the local electric field near the anode, leading to the breakdown process being initiated at these regions, close to the electrode. The increase in the heterocharge could therefore lead to a decrease in E_b. Second, the presence of any impurities associated with the incorporation of micro-fillers could also be a factor in reducing E_b. The larger the amount of impurities, the lower E_b is obtained.

Replacing 5 wt% micro-silica by 5 wt% nano-silica can introduce more residual impurities into the samples due to the synthesis method and surface treatment, so lowering E_b, as in the cases of 60M5N-Pox and 60M5N-3M. Finally, breakdown can be considered to be initiated at 'weak' regions. SEM images show that cracks are likely to propagate along interfaces between the resin matrix and micro fillers. This suggests that these interphase regions could contain weaker bonding than other regions in the resin matrix. The breakdown process could be initiated at these interfaces. As a consequence, the breakdown strength in the micro-composites is reduced. Relative to 65M, the samples 60M5N-Pox and 60M5N-3M contain larger interfacial areas due to the presence of the nanoparticle. As discussed previously, interfacial effects in the Nanopox-based systems led to a reduction in E_b, whereas these effects were not significant in the 3M-based system due to the chemical characteristics of particle surfaces and size effects. As a result of a smaller amount of hetero space charge, stronger interactions at the interfaces between the nano-silica and the resin, and the larger size of the nano-filler, the increased breakdown is obtained in 60M5N-3M, compared with 60M5N-Pox. This suggests that the properties of the samples are the combined results of effects produced by all structural components, including resin mixture, micro-filler and nano-filler.

6.7 Dielectric response

Figures 6-15 to 6-18 show the real and imaginary parts of the relative permittivity obtained at various temperatures, namely room temperature, 120 ^{o}C, 140 ^{o}C and 160 ^{o}C respectively. It is clear that there exists a dramatic increase in the permittivity values of the micro-filled systems compared to the unfilled and nanocomposite samples. Such an increase can be explained by a number of factors. First, the micro-filled samples contain a large amount of micro-silica of high permittivity (up to 5.4 for quartz) and a smaller amount of base resin of lower permittivity (about 3.5). The dominance of micro-silica in the formulation leads to an increase in the effective permittivity of the samples. For example, let ε of micro-silica is 4-5.4, the effective permittivity of 65M will be ~ 3.7-4.3, using either Lichtenecker or Maxwell-Garnett mixing rule (Equation 2-16 and 2-17). The measured value at room temperature is about 4.43 at 0.1 Hz. The difference between the theoretical and measured values can also be attributable to the shape and size of the filler. In addition, the presence of a high content of the microsilica, together with the settling of the filler particles and the non-uniform mixing can lead to a significant increase in the amount of clusters and to a broad distribution of cluster size. As a consequence, the charge transport between clusters can be enhanced; this is termed a LFD process [238-241]. This process is evinced by the power law behaviour observed in the imaginary component of the relative permittivity in a log-log plot, especially in the low frequency region due to the low mobility of charge carriers. The LFD leads to an increase in the real and imaginary parts of relative permittivity in the micro-composites [238-239]. At room temperature, the peaks observed in the systems Ep80, Pox80-5 and 3M-5 are attributed to the instrument response. Differences in the real and imaginary permittivity of the systems 65M, 60M5N-Pox and 60M5N-3M could be attributed to following factors. First, there exist OH groups and/or hydrogen bonding in the samples 60M5N-Pox and 60M5N-3M, as revealed in the FTIR spectra. Under the influence of the applied field, these hydroxyl groups can orient and contribute to an increase in permittivity. Also, the hydrogen bonding of the OH groups onto the filler surfaces can lead to an increased amount and a broader distribution of clusters and hence, enhance the inter-cluster charge transport further. Second, the dielectric behaviour depends on characteristics of interfaces and interphase regions. The free volume existing at interfaces between fillers and the resin matrix will facilitate segmental motions of groups or side chains in these regions. From previous discussions,

it is likely that the Nanopox system introduce more free volume at interfaces than the 3M masterbatch due to poorer surface treatment and its smaller particle size. Therefore, the permittivity of the 60M5N-Pox is higher than the 60M5N-3M. Again, increasing the temperature leads to an increase in both the real and imaginary parts of the relative permittivity due to the increased mobility of molecular segments and enhanced transport of charge carriers and impurity ions. At high temperatures, the LFD becomes more pronounced. Also, a fraction of dc conduction can contribute to an increase in the relative permittivity. An increase in the real part and a slope less than -1 in the imaginary part indicate a non-uniform charge transport occurring inside the materials due to a broad distribution of clusters. This fact suggests that in the micro-filled composites, with and without nanofillers, the power law behaviour dominates the dielectric behaviour due to inhomogeneity in sample structure.

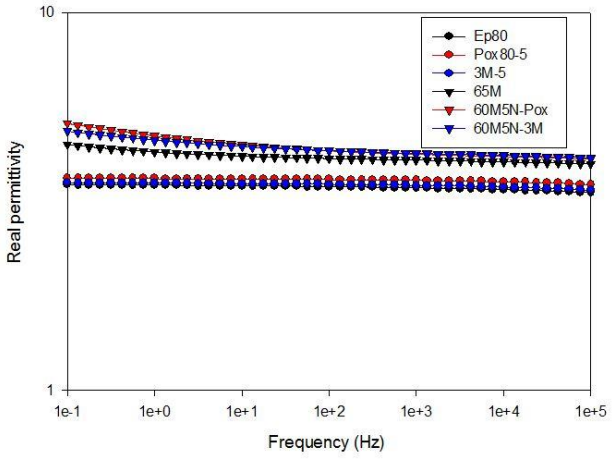

(a)

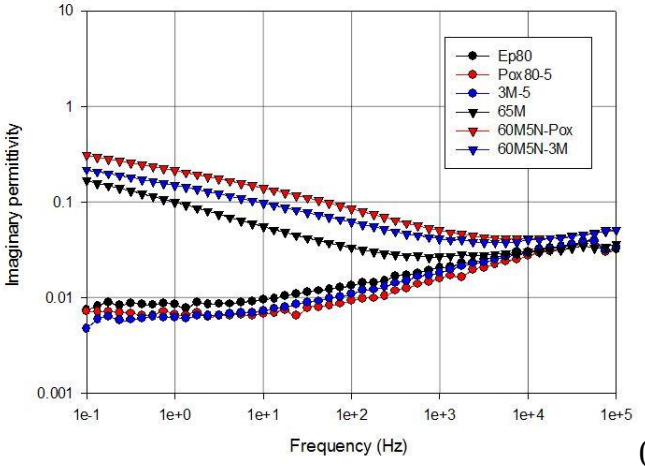

(b)

Figure 6-15 Complex permittivity of various samples at room temperature: (a) real, (b) imaginary

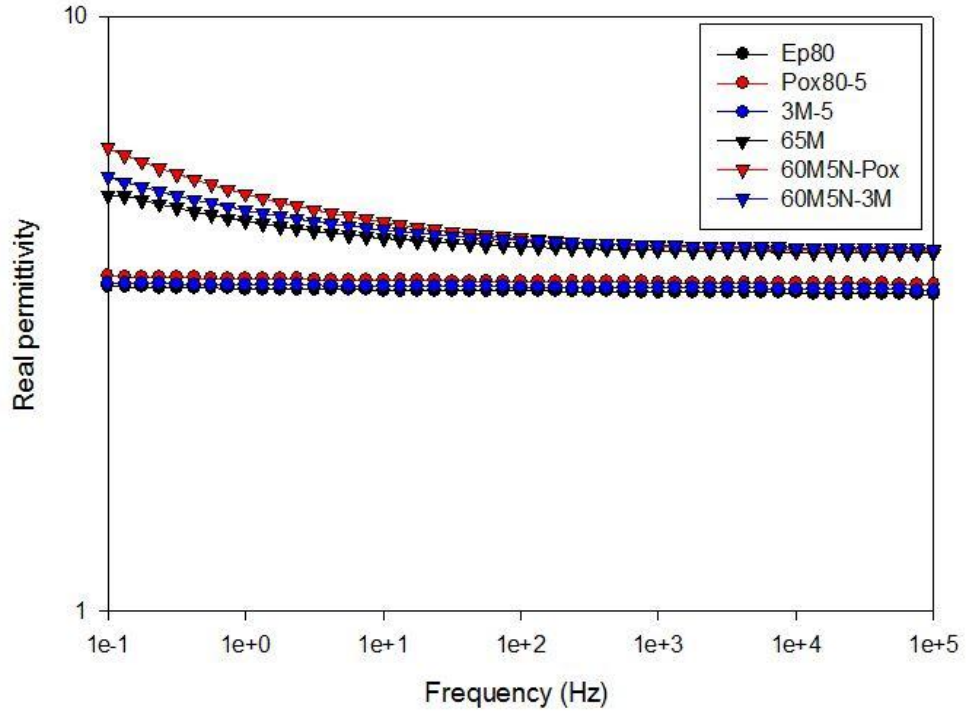

(a)

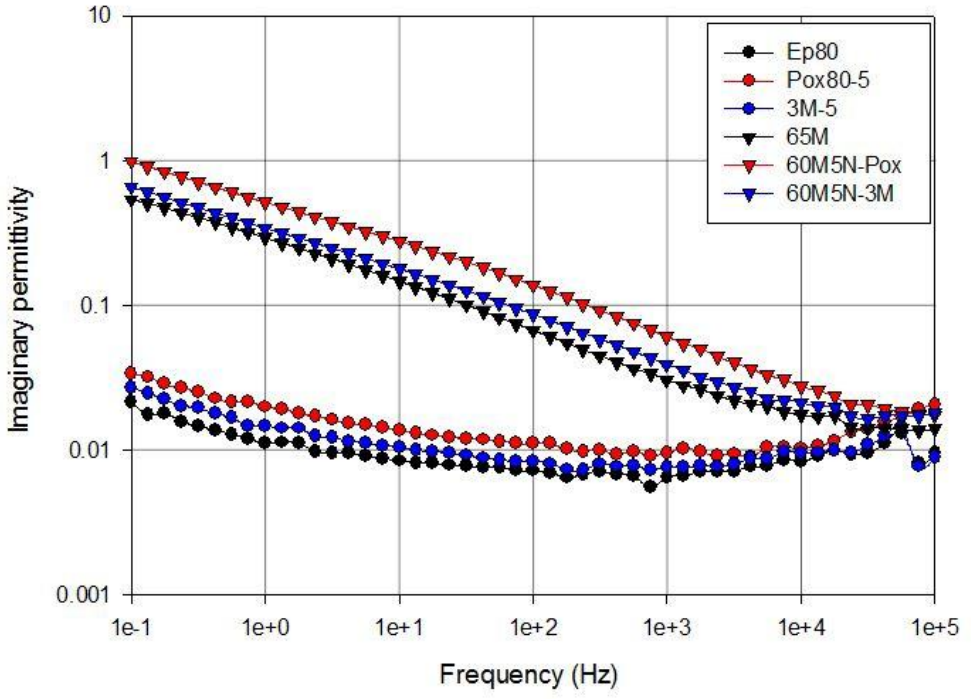

(b)

Figure 6-16 Complex permittivity of various samples at 120 °C: (a) real, (b) imaginary

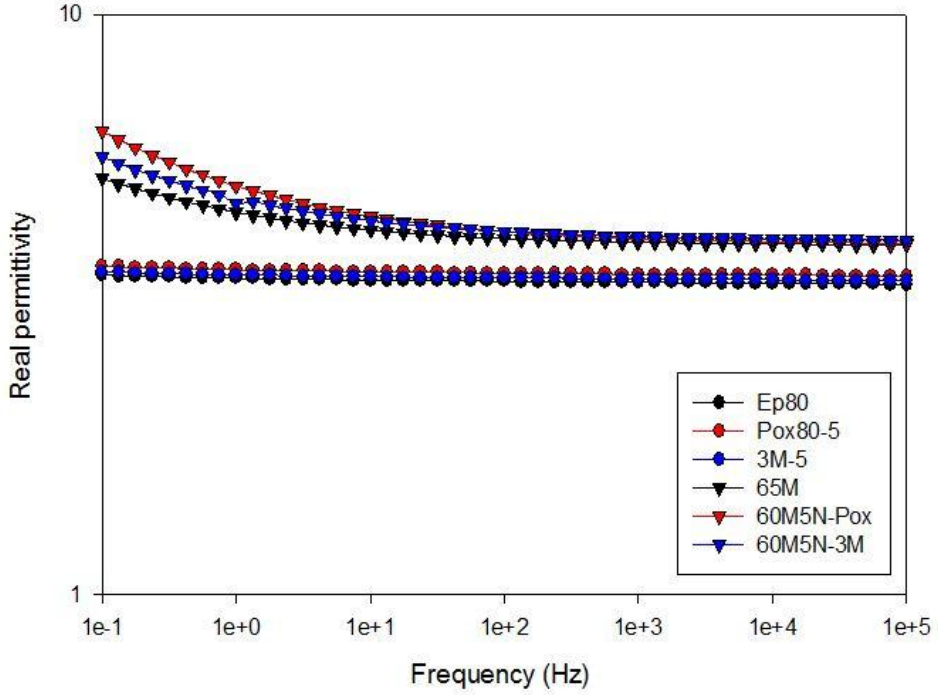

(a)

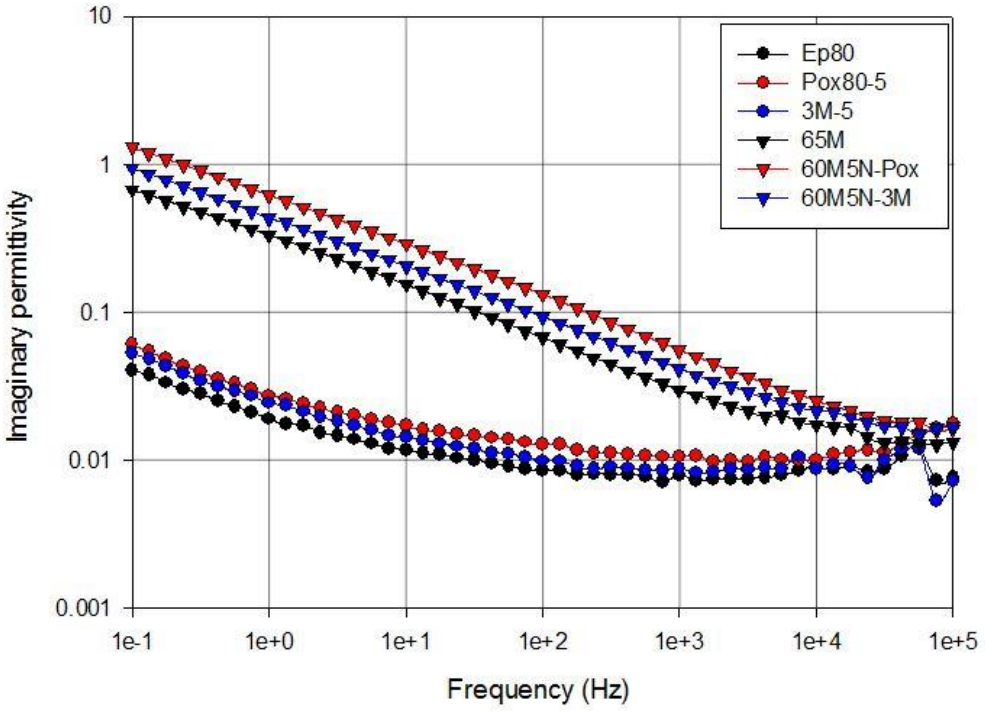

(b)

Figure 6-17 Complex permittivity of various samples at 140 ^{o}C: (a) real, (b) imaginary

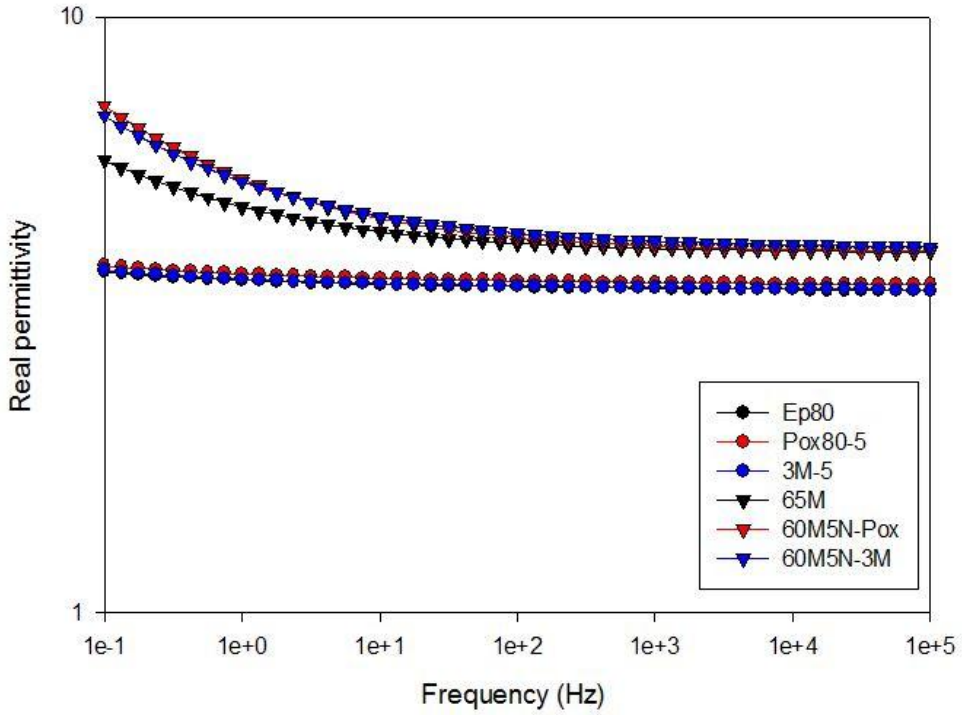

(a)

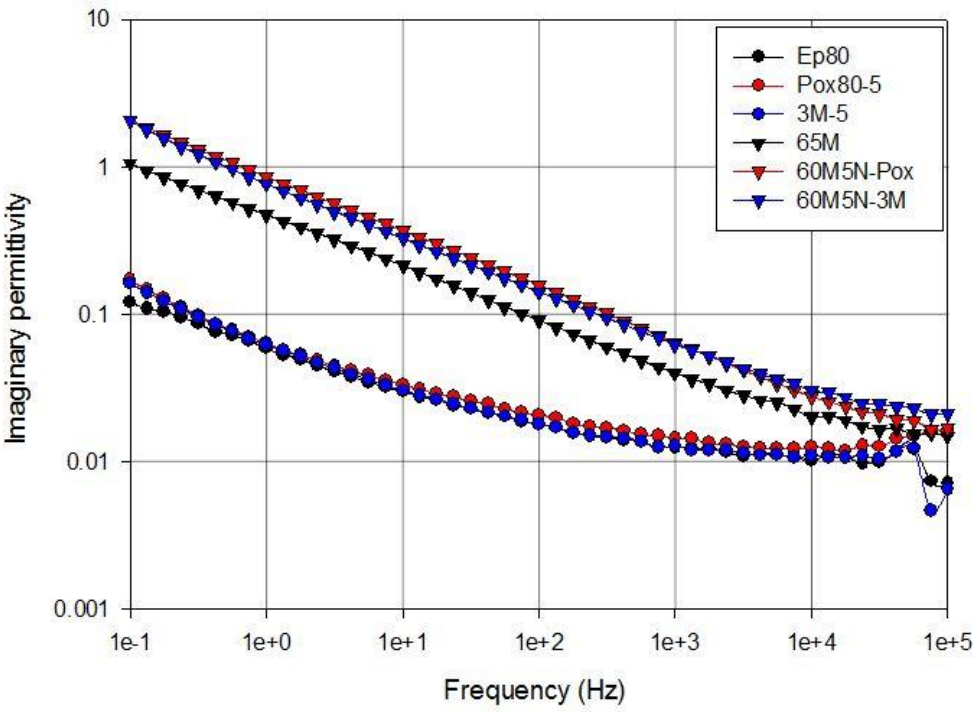

(b)

Figure 6-18 Complex permittivity of various samples at 160 ^{o}C: (a) real, (b) imaginary

6.8 Chapter summary

The incorporation of a large quantity of micro-silica produces significant changes compared to both the unfilled epoxy and related nanocomposites. First, the microfillers can be considered to be the origin of the roughness of fracture surfaces. The presence of microfillers also makes uniform mixing and dispersion of nanofillers difficult to achieve, as shown in the SEM images. Furthermore, it is likely that microfillers inhibit reactions of OH groups on nanoparticle surfaces with epoxy groups, so enabling hydrogen bonding between hydroxyl groups to occur. The settling of microfillers and the non-uniform mixing introduces a multi-layered structure and a broad distribution of clusters inside the materials and hence, lead to the complicated patterns of space charge formation and cause the power law behaviour or the LFD of the relative permittivity. In addition of the higher permittivity of quartz micro-silica, the LFD causes an increase in the dielectric constant and dielectric loss. The layered structure with the enhanced charge transport between clusters and trap, as well as the existence of impurities, lead to a reduction in electrical breakdown strength of micro-filled composites compared to the unfilled and nanocomposite samples. The addition of nanofillers into the microcomposites introduces further effects due to their large interfacial areas and the surface chemistry of nanoparticles. Therefore, the effects imposed on these systems are similar to the ones discussed in Chapter 5. Consequently, at the same loading level, the microcomposites containing 3M type nanofillers exhibit better performances than the ones containing Nanopox. In addition, a key fact that needs to be acknowledged here is that these samples are typical because the micro-silica has completely settled. Consequently, conclusions about material properties are likely to be limited to these samples.

Chapter 7 Electrical treeing

7.1 Introduction

Electrical treeing is a technologically important phenomenon that involves the long-term degradation of insulation materials and ultimately can lead to catastrophic electrical failure. The formation of electrical trees involves three stages [118]. First, the formation of a micro void is initiated in a region of high electric field; this stage is termed inception. Second, a branched fractal structure composed of elongated fine erosion channels develops from such micro voids through subsequent partial discharge (PD) activity; this is the propagation stage of electrical trees. Finally, when the growing tree channels create a conducting path that completely bridges the insulation, dielectric breakdown occurs. Due to its importance, especially for high voltage engineering, many studies of electrical treeing in polymeric materials have been conducted for a wide range of insulating materials, including polyethylene and epoxy resin [309-312], polypropylene [313-314], etc. A number of models have been proposed to describe the processes involved in electrical treeing [315-317]. PD activity within the tree has been suggested to be the main cause of localised material damage through the progressive accumulation of chemical damage caused by molecular excitation/ionisation [318-319] or as a result of enhanced local fields at the channel tips that exceed the breakdown strength of the material [320-322]. It is well-known that discharge activity, dynamic space charge, and the local physical and chemical properties of electrical trees are closely interrelated. Due to the local field distribution, which is determined by a number of factors including morphology, chemical composition, temperature, etc [313, 323-324], PD activity occurs in a certain subset of available branches within the tree, so different forms of tree, namely conducting and non-conducting structures, have been observed [315, 325]. In one form, discharge activity is confined to growth tips, which implies that tree channels are sufficiently conducting to prevent PD activity. Those conducting channels ultimately create an open branched tree structure. Conversely, a

bush-like tree structure is sufficiently insulating for PD discharge to occur throughout the body of trees, even within mature tubules.

In order to understand the formation of electrical trees, it is necessary to understand how voids are produced in polymeric materials upon the application of electric fields. Electrical treeing involves chemical conversion of polymer macromolecules into volatile fragments through the transfer of energy from the electric field [326]. Therefore, chemical change is an important factor in understating electrical trees. Many studies have concentrated on a number of factors affecting the tree initiation [327] and propagation characteristics of electrical trees [313], mainly based on PD measurements and optical observations. However, relatively few studies have included the chemical analysis of electrical trees. FTIR was first used to characterise trees grown in epoxy resin [328-329]. Recently, Vaughan et al. [173-174] reported on the application of confocal Raman microprobe spectroscopy (CRMS) to analyse chemical changes within electrical trees grown in polyethylene (PE). These studies revealed that CRMS appears to be an effective tool in the analysis of electrical trees, albeit that caution must be taken during acquisition of Raman spectra and interpretation of data. The studies also revealed the presence of three separate components, which were observed at different spatial locations within a conducting tree; the common spectrum of PE was seen at the tips of tree channels and in the bulk material surrounding the trees, the fluorescence was detected in the main body of the tree and the existence of the D and G bands of sp^2 hybridised carbon was shown in mature tree channels. Also, these studies revealed the presence of PE and increased fluorescence, but no evidence of carbon in the spectra of the non-conducting tree. Similar observations concerning the appearance of these three separate features of a conducting tree were reported later for silicone rubber [175].

This chapter set out to extend the work of Vaughan et al. [173-174] further by performing chemical analysis of electrical trees grown in an anhydride cured epoxy resin and its nanocomposites. This study investigates the chemical characteristics of breakdown channels and tree branches in samples using CRMS and SEM and compares the results obtained to those reported previously. In addition, the propagation of electrical trees grown in samples is monitored in-situ in order to obtain better understanding of the effect of adding nano-silica fillers on the morphology of electrical trees.

7.2 Raman Microprobe Spectroscopy

Although the Raman effect was discovered in the 1920's [330], it has been only used as a spectroscopic technique relatively recently, thanks to the development of lasers and advances in computing technology. The Raman effect can be described using both a quantum mechanical model and a classical one. According to quantum mechanics, when monochromatic visible light interacts with a material, molecules will be excited to a higher real or virtual state. When these excited molecules relax back into the same original states, there is no shift in photon energy/frequency. This is called Rayleigh scattering. However, when the molecules relax back into a vibrational state that is higher in energy than the original state, there will be a shift of photon to lower frequencies. This is termed Stokes Raman scattering. Conversely, a shift to higher frequencies occurs when the excited molecule relaxes into a vibrational state that is lower in energy than the original state; this is termed anti-Stokes Raman scattering [331]. At thermal equilibrium, the number of photons involved in Stokes radiation is greater than those associated with anti-Stokes scattering and, hence, a higher intensity of the spectral peaks results. As a consequence, Raman spectroscopy generally uses the Stokes region of the spectrum. Each bond in the molecules of a material is associated with a characteristic frequency/energy shift so, by detecting these shifts, chemical composition can be determined. A Raman microscope can achieve a potential lateral resolution of ~ 1 μm [332] and, therefore, it is well suited to the study of electrical treeing in solid dielectrics [333-334].

In 1957, Minsky [335] improved conventional Raman microprobe spectroscopy by excluding out of focus light, so enabling images of a specific location to be acquired. This is known as confocal Raman microprobe spectroscopy. The CRMS technique places a small aperture or 'pin hole' at the back focal plane of the objective lens. Under these conditions, only light from the plane of focus passes through the aperture and contributes to the final signal, whereas light from out of focus planes is rejected. CRMS is a non-destructive method with high spatial resolution. In addition, it can be used in situ and requires no sample preparation. Therefore, CRMS has been widely applied to study transparent and translucent materials [173-175]. However, the Raman spectrum may be masked by a fluorescent background. In fluorescence, molecules absorb electromagnetic radiation at specific wavelengths and are excited. Fluorescence is

related to the transition energy between two electronic states whereas virtual states have to be considered in the Raman scattering. As a consequence, the fluorescence spectrum is much stronger and broader and obscures the Raman peaks. One way to reduce the fluorescence effect is to use a laser with a longer excitation wavelength [336]. However, this method is relatively costly.

7.3 Results and discussion

7.3.1 Morphology and growth dynamics of electrical trees

Figures 7-1 to 7-3 show a series of images of electrical trees grown at 18 kV in the unfilled epoxy and the nanocomposites studied here. The images were obtained at various durations after an observable tree was formed at the needle tip, i.e. tree A in all figures. It is evident that there exist a number of differences in morphology of these electrical trees. In the Ep80, the tree grew to approximately 1300 µm in length and it appeared to stagnate and cease growing. The tree was comprised of two main branches with a number of short, extremely fine side branches. It appears that the occurrence of PD activity is confined to the needle tip. It is likely that the stagnation of the tree is due to an insufficiently high electric field at the branch tips to sustain tree growth. PD activity only occurs in the existing tree channels and, gradually, a heavily branched tree that is more bush-like is formed near the needle tip, as shown in Figure 7-4. Besides, the formation of this bush-like tree can be also due to the water ingress into the sample, as reported by Champion and Dodd [337].

On the other hand, the addition of nano-silica fillers seems to increase the length, the growth rate and the degree of branching of electrical trees approaching the earth electrode. According to Tanaka [338], treeing occurs in nanocomposites through the formation of breakdown paths that propagate between nano particles. The PD activity then occurs in the existing tree channels. When tree channels approach the interfaces, they cannot continue growing in the same direction. Instead, tree channels will propagate along these interfaces, so increasing the degree of branching. The higher the filler loading level, the higher the degree of branching. Also, as discussed in previous chapters, the Nanopox contains nano-silica particles with weak interactions at interfaces. As a consequence, electrical trees grow faster at such weakly bonded

interfaces. The presence of nanosilica may also prevent the water ingress into the nanocomposite samples.

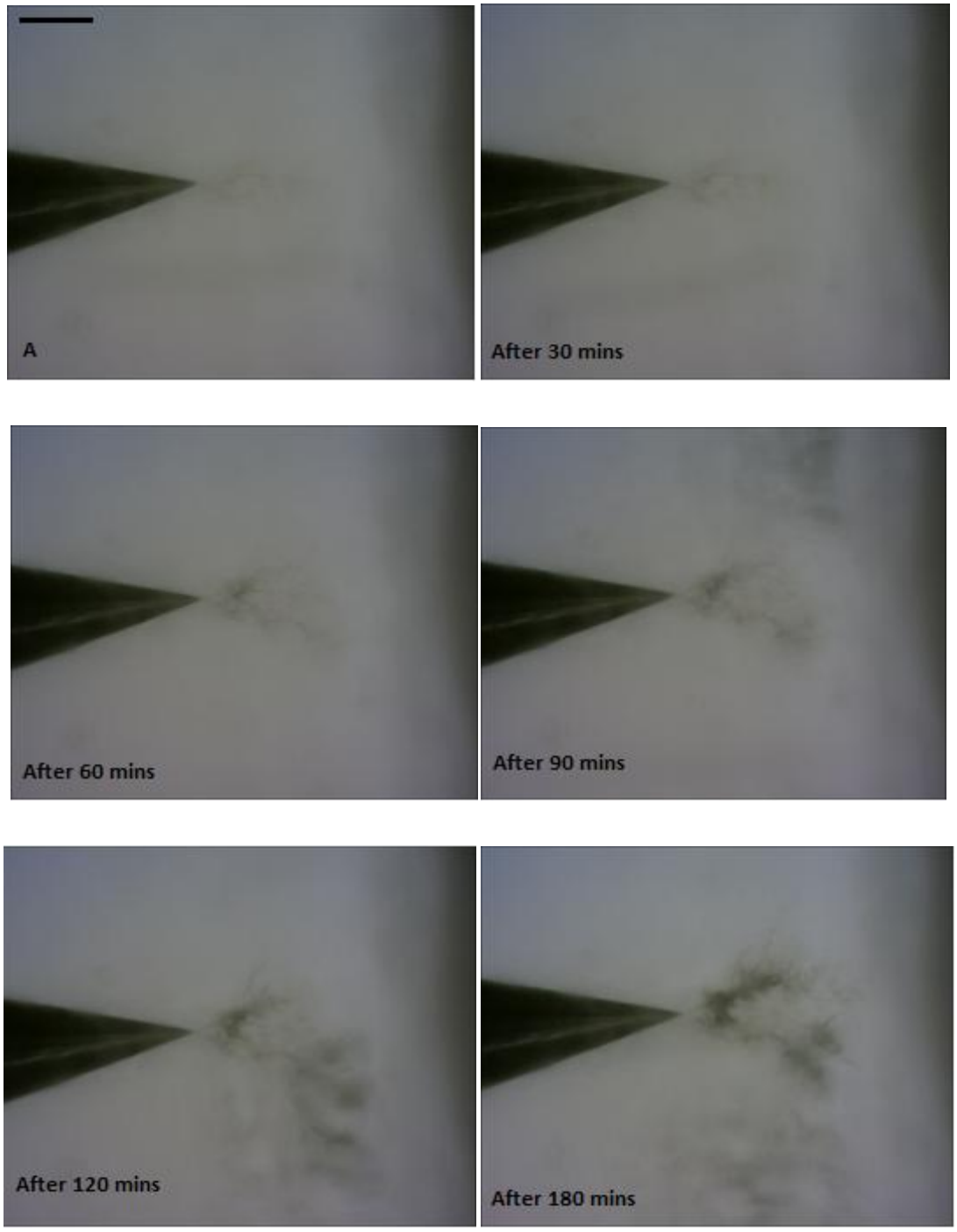

Figure 7-1 Optical images showing tree growth in Ep80 taken in situ at various durations after tree initiation (note: scale bar is ~ 500 µm and applies to all images)

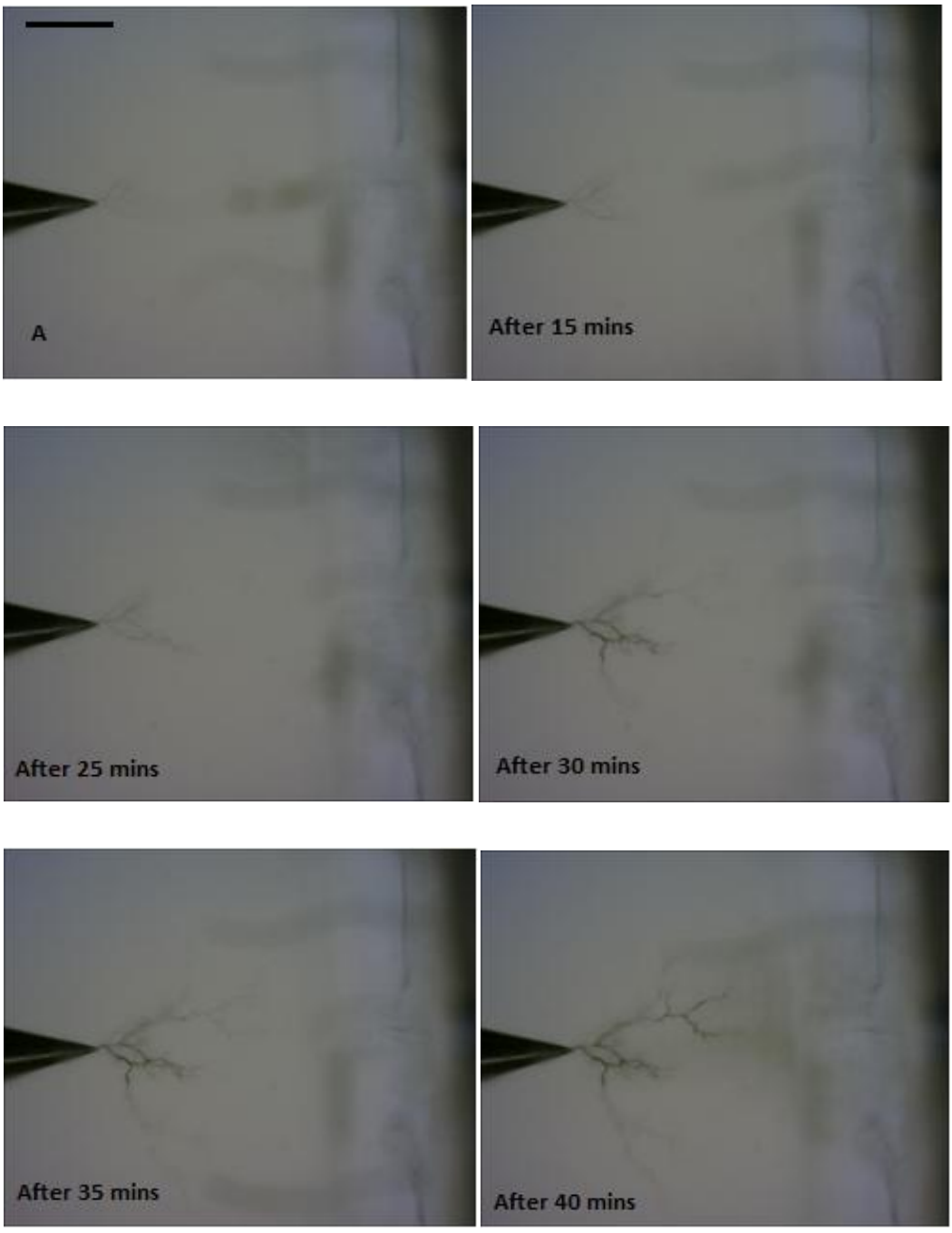

Figure 7-2 Optical images showing tree growth in Pox80-5 taken in situ at various durations after tree initiation (note: scale bar applies to all images and is ~ 500 μm)

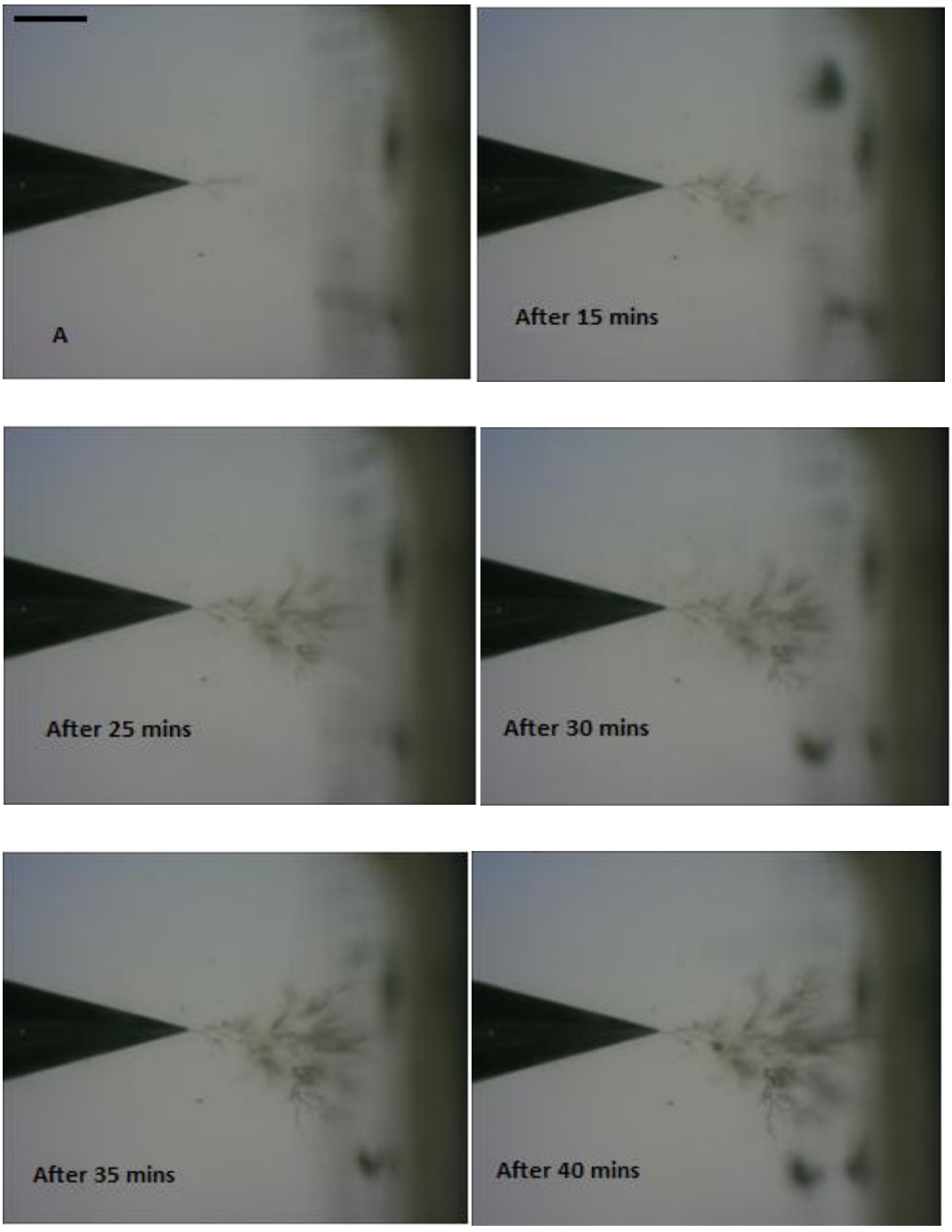

Figure 7-3 Optical images showing tree growth in Pox80-12.5 taken in situ after tree initiation (note: scale bar applies to all images and ~ 500 µm)

Figure 7-4 Optical image showing a heavily branched tree, which is more bush-like, grown in Ep80 at 18 kV after 300 mins

Many studies on material life-time have suggested that the addition of nano-fillers can increase the PD erosion resistance and, hence, increase the life-time of materials [15, 244, 249]. In such cases, PD activity can be considered to be a predominant mechanism that leads to material degradation, as shown in Figure 7-5. However, in this study, the addition of nano-silica increases not only the degree of branching, but also the tree growth rate. In addition to the interfacial characteristics mentioned above, this feature can also be explained by the crossover phenomenon that has been proposed by Tanaka [338]. According to this proposal, under high electric fields, treeing breakdown is related to short-time breakdown mechanisms rather than PD degradation. Under high electric fields, electrons will be accelerated if nano particles are positively charged as shown in Figure 7-6, such that electrical trees grow faster in nanocomposites than in unfilled epoxies. Although this proposal requires further analysis, the results in the study are consistent with the breakdown data obtained in the previous chapters. This suggests that, at this electric field, short-time breakdown mechanism exerts certain effects on treeing behaviours. The crossover phenomenon has been observed in other studies [339].

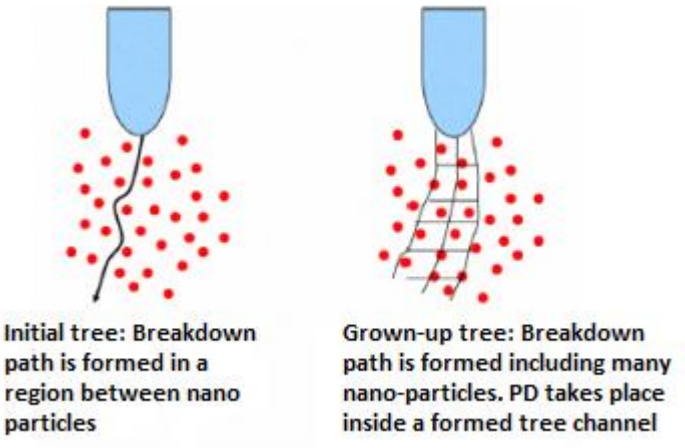

Figure 7-5 Initiation and propagation of trees in material degradation [338]

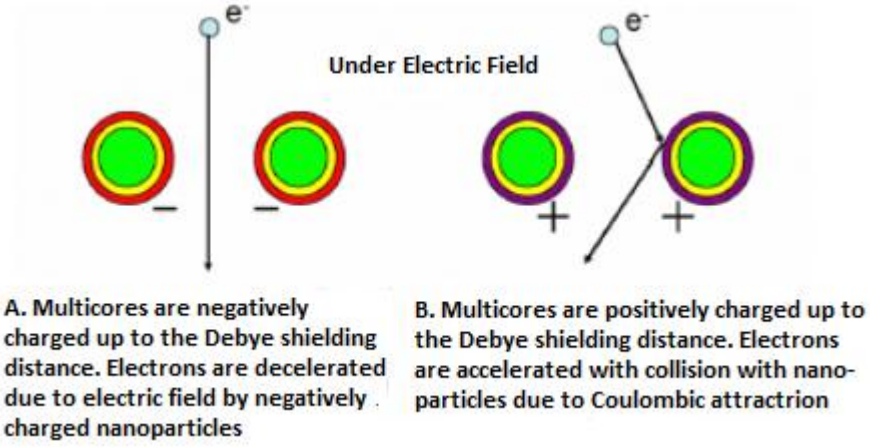

Figure 7-6 Proposed mechanism for interactions between electrons and nano particles under high electric fields by Tanaka

7.3.2 Chemical analysis of electrical trees

7.3.2.1 Raman spectroscopy of breakdown channels

In this study, electrical trees grown at an applied voltage of 18 kV in the Ep80 and Pox80-5 were allowed to progress until final failure occurred. The samples were then cut open such that the internal walls of the breakdown channels were exposed, which were analysed chemically using CRMS at various positions along their length. Figure 7-7(a) shows part of an exposed breakdown path in Ep80, while Figure 7-7(b) contains four Raman spectra, A, B, C and D, which were obtained from the points marked A, B, C and D respectively. Trace D is likely to show peaks similar to those we would expect in the epoxy resin [340]. However, traces A, B and C show a pronounced fluorescent

background. This indicates the degradation process in these channels. However, in contrast to results reported elsewhere [173-175], it is difficult to determine the presence of the G and D bands of carbon, although it is likely that the G band appears at about 1580 cm^{-1}. Nevertheless, it is difficult to draw an unambiguous conclusion because the host resin contains spectral peaks in this region. In addition, as discussed above, the Ep80 contains a heavily branched tree, as shown in Figure 7-4. Vaughan et al. [174] found that in a non-conducting tree formed in PE, the conversion from degraded material to carbonised residues did not occur. This suggests that in the Ep80, the PD activity can occur throughout the body of the tree, and may lead to a form of non-conducting tree. Therefore, more experiments are required to explore the nature of electrical trees in this resin, such as the chemical analysis as a function of distance from the central axis of the breakdown channel.

Figure 7-8 shows the exposed path of the breakdown channel in a sample of Pox80-5, together with the corresponding Raman spectra acquired at various points marked as A, B, C and D. In general, similar characteristics to those of the Ep80 are observed; a highly fluorescent background is superimposed upon and masks the spectral peaks of the host resin. However, the presence of the G band of carbon appears to be more evident, as shown in traces A and B. It suggests that the electrical tree grown in the Pox80-5 can be a conducting one. Nevertheless, the D band of disordered carbon, which has been observed elsewhere [173-175], is not evident in these Raman spectra, possibly due to the weak intensity of the D band and the dominance of resin peaks. Also, in this specimen, the presence of the nano-silica would be expected to lead to a large peak located at 465 cm^{-1} [341]. However, the results show little or no evidence of this, as previously observed by Freebody [340].

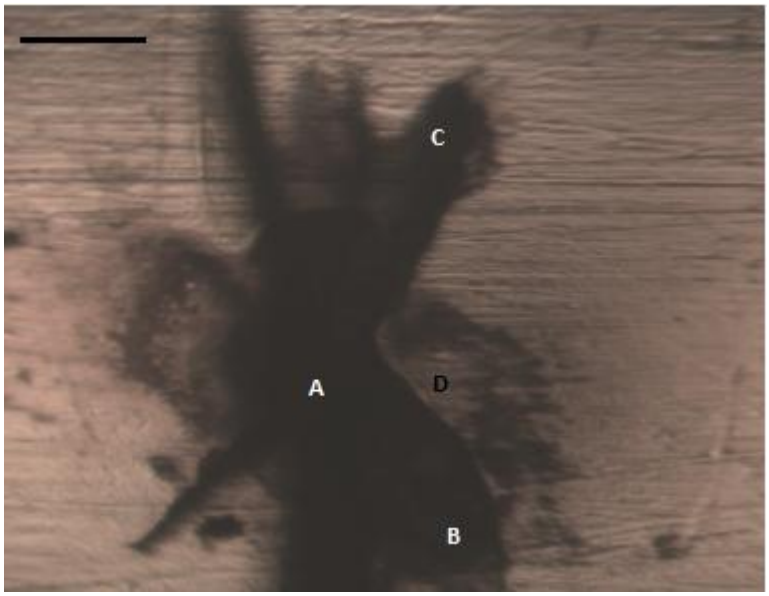

(a)

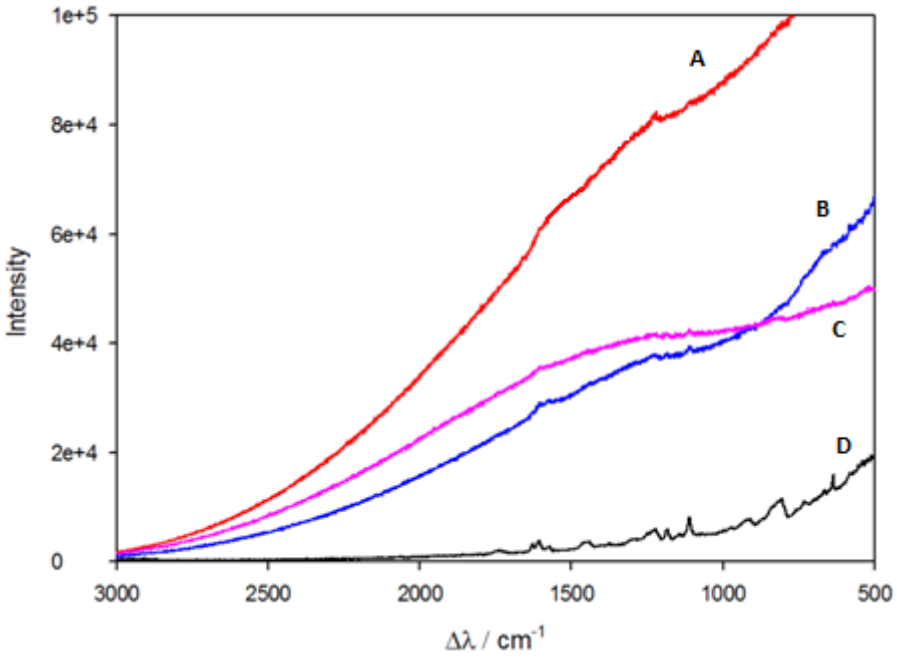

(b)

Figure 7-7 Exposed breakdown channel in Ep80 of (a) micrograph, (b) Raman spectra at various points (note: scale bar is equivalent to 100 µm)

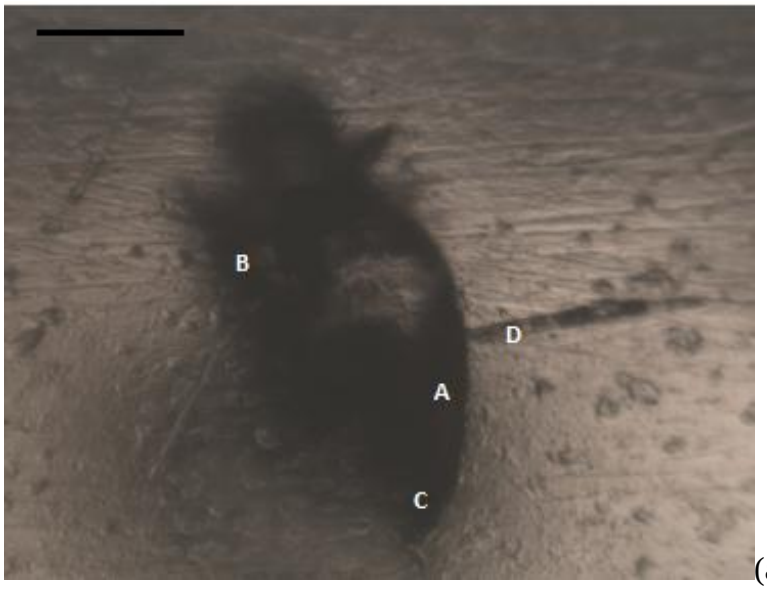

(a)

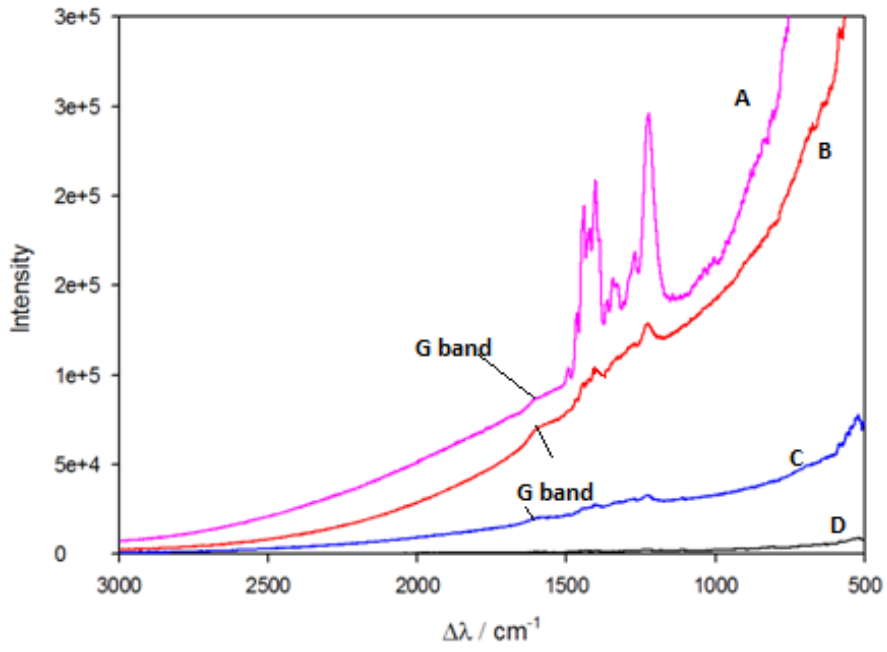

(b)

Figure 7-8 Exposed breakdown channel in Pox80-5 of (a) micrograph, (b) Raman spectra at various points (note: scale bar is equivalent to 100 µm)

7.3.2.2 Raman spectroscopy of a tree channel

The chemical nature of a conducting tree in the Pox80-5 was examined using the specimen shown in Figure 7-9(a), which was grown at 18 kV. Figure 7-9(b) contains Raman spectra obtained at the various points marked as A, B, C and D. The presence of the G band of carbon is evident in trace A, albeit that again, the D band of carbon is not seen, similar to results obtained from the breakdown channel. In addition, a degree of fluorescence is evident in all the obtained spectra. This indicates that although the material degradation occurs via physical processes during tree growth, evidence of chemical changes is retained until a mature channel is formed.

The Raman spectra in this study show similar features to those reported previously by Vaughan et al. [173-174]. First, the Raman spectrum of the host resin is observed in both the tree channel and the surrounding bulk material. Second, a fluorescent background is found to be superimposed onto the resin spectrum. Their relative intensities vary from place to place within the samples. This indicates degradation of the material. Third, for a conducting tree, in the core of mature channels, in addition to pronounced fluorescence, the G band of sp^2 hybridised carbon are observed. However, in this study, the presence of the D band of carbon in these Raman spectra is not evident. The tree channels can be considered as hollow tubules surrounded by a carbonaceous shell that is sufficiently conducting to prevent PD activity. Other tree channels are characterised by only the Raman spectrum of the host resin superimposed on a reduced fluorescent background. In this case, the tree channels can be considered as non-conducting hollow tubules. PD activity can occur inside these channels. For a non-conducting tree, it is difficult to observe the G and D bands of carbon, which suggests that PD activity can occur throughout the whole tree body. Chemical characteristics of breakdown and tree channels grown in the Ep80 and Pox80-5 are found to be in line with their morphology analysis.

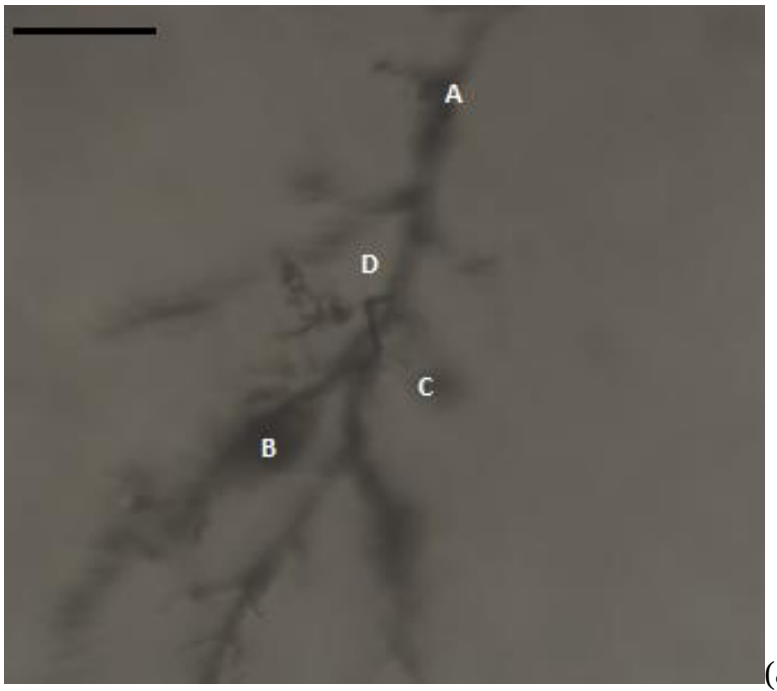

(a)

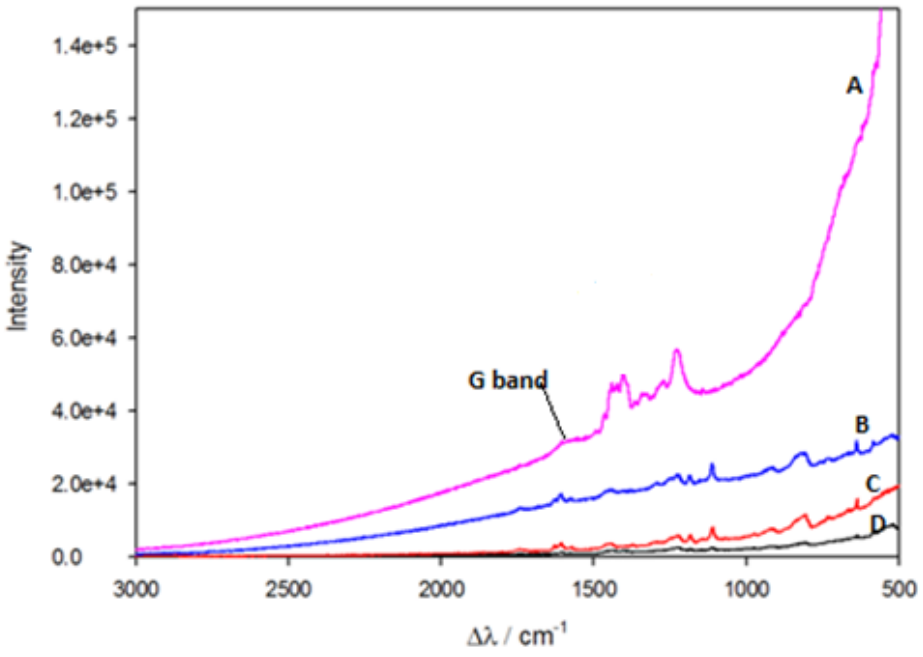

b)

Figure 7-9 Exposed treeing channel in Pox80-5 of (a) micrograph, (b) Raman spectra at various points (note: scale bar is equivalent to 30 µm)

7.3.3 SEM analysis

Figures 7-10 to 7-12 show a selection of typical SEM images revealing the internal structure of main breakdown channels and a tree channel grown in Ep80 and Pox80-5, together with the corresponding SEM micrographs obtained for the bulk materials for comparison. It is clear from Figure 7-10 that, in the Ep80, the morphology of the breakdown channel is similar to that of the bulk resin matrix. Although the channel surfaces are rougher, which may relate to material degradation, there is no evidence to suggest the existence of graphitic material deposited at the interior walls. This observation supports the Raman spectra obtained for the non-conducting tree grown in the Ep80. Vaughan et al. [174] reported similar results for an etched non-conducting tree grown in PE. In this study, the texture of PE was apparent within tree channels without evidence of graphitic material. Conversely, Figure 7-11 shows a coated nodular texture on the channel surface, which is different from the corresponding bulk resin matrix. Although the addition of nano-silica also leads to a nodular texture in the Pox80-5, this feature can only be observed at much higher magnifications, as discussed in the previous chapters. Therefore, at this intermediate magnification, the nodular feature in the morphology of the channel wall must be related to other mechanisms and is not associated with nano-silica particles alone. The Raman spectra obtained from the breakdown channel in the Pox80-5 suggested the presence of a carbonaceous shell on the interior walls. Similar observations have been reported by Vaughan et al. [174] and Freebody [340], who suggested that carbonaceous residues make up the nodular structures with sizes up to approximately 10 μm. Besides, during PD activity, nanosilica particles will be left in the tree channels, which will agglomerate and also contribute to a nodular structure.

To explore this further, a section of a tree channel in the Pox80-5 was examined using SEM. Again, a nodular texture is observed at an intermediate magnification. This reinforces the idea that the formation of a carbonaceous shell on interior walls occurs during propagation of tree channels, as discussed above. In addition, it would appear from Figure 7-12(b) that the matrix texture surrounding the tree channel (as indicated by the arrow) is different from that of the bulk. In this region, which may extend as far as 10 μm, it is likely that the resin matrix is damaged, probably due to electrical activity

such as PD and Joule heating. Similar observations have previously been reported by Vaughan et al. [174].

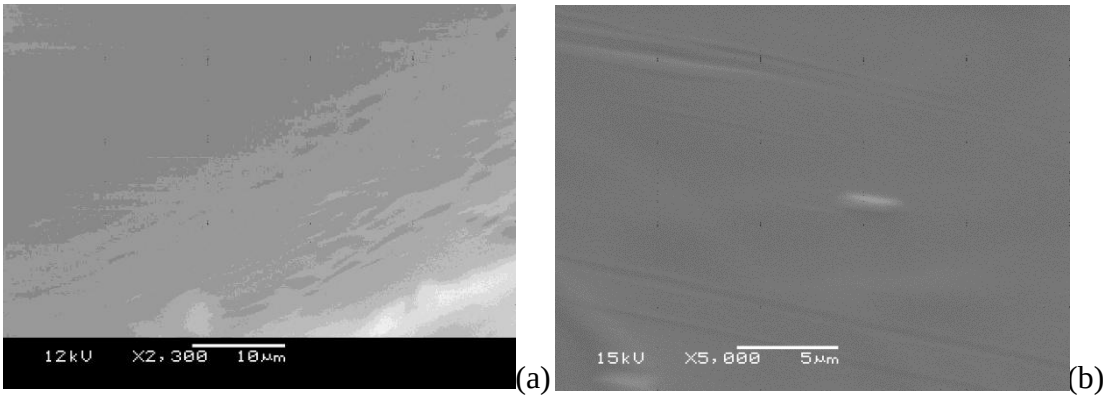

(a) (b)

Figure 7-10 SEM images revealing granular textures in (a) the internal wall of a breakdown channel and (b) the bulk resin in the Ep80

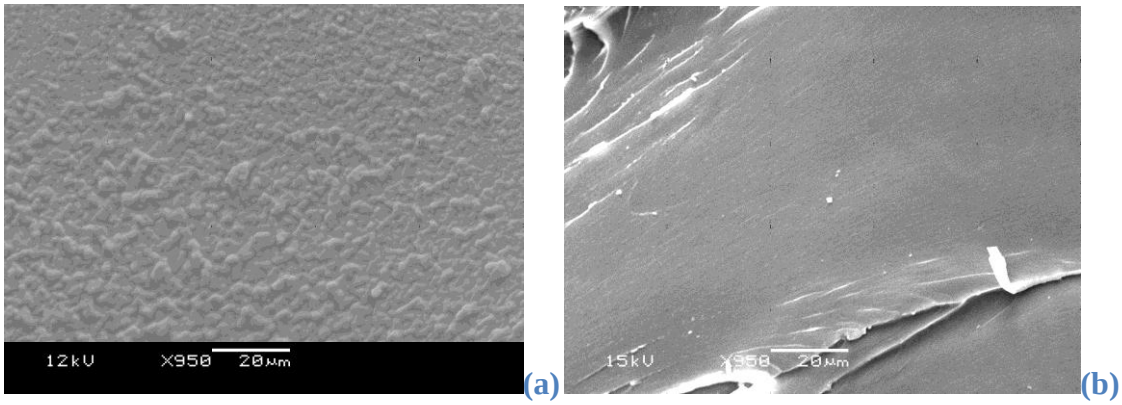

(a) (b)

Figure 7-11 SEM images of (a) the nodular texture of the internal wall of a breakdown channel and (b) the bulk material in the Pox80-5

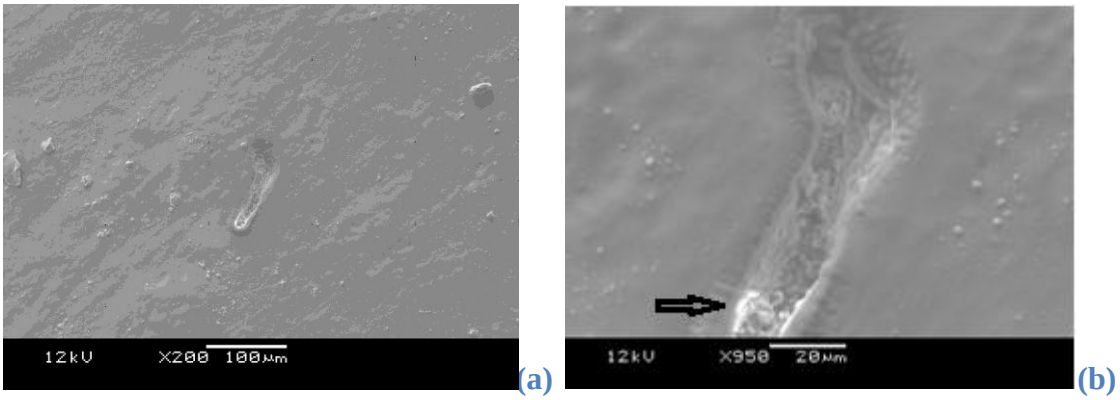

(a) (b)

Figure 7-12 SEM images revealing (a) a section of tree channel, and (b) nodular texture of this section in the Pox80-5

7.4 Conclusions

This chapter describes an optical and chemical study of electrical trees grown in the unfilled epoxy and its nanocomposites. From the results obtained, the following conclusions can be drawn:

- A heavily branched tree that is more bush-like is grown in the unfilled epoxy, while the addition of nanosilica increases not only the degree of branching, but also the growth rate and length of electrical trees. The increase in the growth rate may be due to the crossover phenomenon. At high electric fields, treeing breakdown seems to be dominated by short-time breakdown mechanisms rather than PD activity. The processes are influenced by the interfacial characteristics of the nano particles, including interactions between organic surface groups and the resin matrix, and charges on the nano-particles.
- As reported previously by Vaughan et al. [173-174], in a conducting breakdown/tree channel, there exist three components; the common Raman spectrum of the host resin superimposed on a pronounced fluorescent background, which indicates material degradation, plus the G band of sp^2 hybridised carbon. It is this carbonaceous shell that is sufficiently conducting to prevent PD activity. However, the presence of the D band of carbon is not evident in these samples. On the other hand, in a more bush-like tree, the degradation of material is still evinced by a highly fluorescent background. However, it is difficult to observe the existence of the G and D bands of carbon, which indicates the non-conducting nature of the breakdown channel. As a consequence, PD activity can occur throughout the tree body, leading to a more bush-like shape. The Raman spectra indicating the presence of carbonaceous material are supported by SEM images.

Chapter 8 General Discussion

This chapter sets out to generalise the common factors that affect the system performance.

8.1 Effects of stoichiometry

For non-stoichiometric formulations, excess hardener and/or excess epoxy molecules can exist in terms of dangling ends, loops or sols in the epoxy network. Consequently, extra free volume can be introduced into the network and hence, reduce the T_g. In the case of an excess of hardener, the entanglement of long chains, probably via hydrogen bonding of terminal carboxyl groups, can produce the effects similar to the crosslinking and therefore, the reduction in T_g is not significant. Conversely, for an excess of epoxy, the decreased quantity of hardener used for curing an epoxy leads to a reduced crosslinking degree and hence, a dramatically reduced T_g. However, the effects of stoichiometry on the E_b are in marked contrast to those on the T_g. The unreacted hardener molecules may be oxidised during post-curing and consequently, introduce more impurities in the materials. Oxidation can lead to the material degradation and reduce the E_b. In addition, the materials with an excess of hardener are hard and brittle. The electromechanical breakdown mechanism can occur in these materials. On the other hand, the materials with an excess of epoxy are softer due to a decrease in the crosslinking degree and lead to an increase in the toughness. An increase in toughness allows an increase in the plastic deformation, so reducing the stress concentration around any crack tips, and increasing the breakdown strength. The effects of stoichiometry on the T_g and E_b behaviours of unfilled epoxy can be summarised in Figure 8-1. However, the chemical morphology of unfilled epoxy systems is similar, including ester and ether linkages. Therefore, no significant difference in space charge formation can be observed at room temperature. An amount of homocharge can be observed at the cathode and no internal space charge in the bulk of materials. Epoxy resins are usually associated with a heterogeneous structure that contains different domains. Therefore, the power law behaviour with a slope less than -1 can be observed

in the relative permittivity due to the non-uniform charge transport. At temperatures much higher than the T_g, two distinct processes can be observed, including the LFD and the dispersion D. The LFD is ascribed to the charge transport between clusters, while the dispersion D describes the process where the inter-cluster charge transport is not possible.

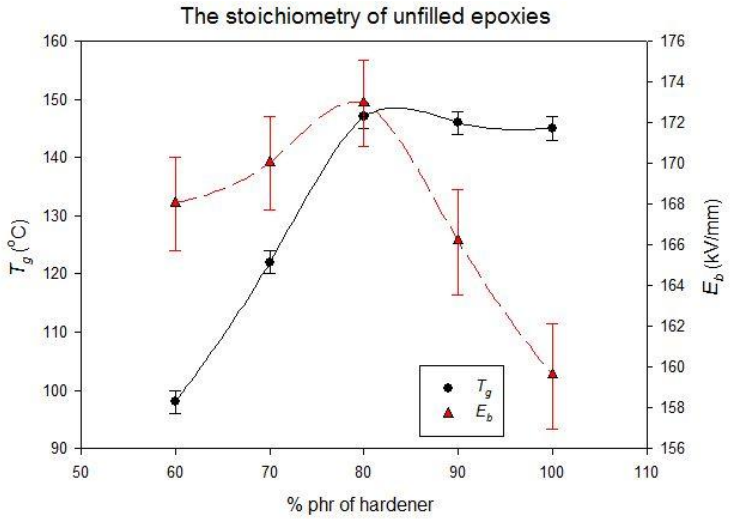

Figure 8-1 Stoichiometry effects on T_g and E_b of unfilled epoxy systems

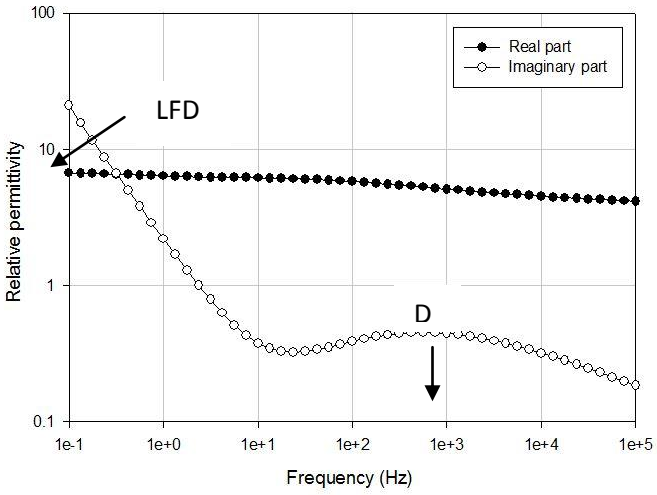

Figure 8-2 Relative permittivity of an unfilled epoxy (resin ratio 100:60:1) at 60 °C above its T_g

8.2 Effects of adding nanosilica

The incorporation of nanosilica of either Nanopox or 3M master-batch induces changes in the system performance. First, the Nanopox and 3M can contain different quantities of impurities and additives that are associated with the synthesis and surface treatment processes. Such impurities and additives will put certain impacts on the material properties, such as a reduction in E_b and an increase in the relative permittivity. Second, the hydroxyl groups on the nanosilica surfaces and/or residual catalytic impurities can catalyse the homopolymerisation of epoxy groups and/or react with epoxy groups via the etherification reactions. Consequently, an effective excess of hardener can be resulted in some formulations, which can deteriorate the material properties. Conversely, for the systems containing an excess of epoxy, this effect can reduce the amount of unreacted epoxy molecules and increase the crosslinking degree; so, improve the material performance, as shown in Figure 8-3.

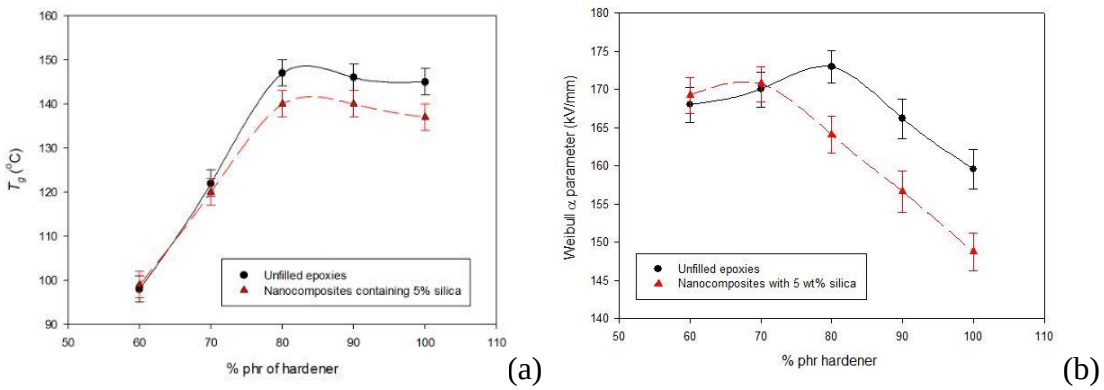

Figure 8-3 The hydroxyl groups on nano-particle surfaces induces different catalytic effects on (a) T_g, (b) E_b, depending on the resin ratio

Finally, for nanocomposites, due to the small size, the interfacial area becomes very large. In such cases, the volume fraction of interphase regions can become comparable to that of the fillers and resin. If organic surface groups on the nano-particles can only react weakly with the resin matrix, the T_g and E_b will be reduced. Conversely, a strong interaction between the nano-particles and the resin matrix will improve the system performance. As long as the fillers are in the nanoscopic scale and well-dispersed in the samples, the characteristics of interphase regions will play a key role in determining the material properties, rather than the filler size, as shown in Figures 8-4 and 8-5. Concepts about the characteristics of interphase regions are related to the so-called "multi-core model" proposed by Tanaka [253], which suggests that the introduction of nano-fillers

into a polymer matrix can create a number of distinct interphase regions, each with nanometric dimensions. First, chemical interactions between the matrix and the nanoparticle might lead to tightly bound regions, in which molecular mobility is dramatically reduced. Surrounding this, it is suggested that regions of increased free volume may exist. Evidently, from the perspective of T_g, these two factors would act in opposite senses. On the other hand, the presence of nanosilica can increase the amount and the size of clusters, so enhancing the charge transport between clusters in the samples. Therefore, the power law behaviour that indicates a non-uniform charge transport can be observed in the relative permittivity, especially for the systems containing a high loading level of nanosilica at high temperatures, as shown in Figure 8-6. In addition, due to a good dispersion of nano-fillers, no significant difference in space charge behaviours can be observed at room temperature.

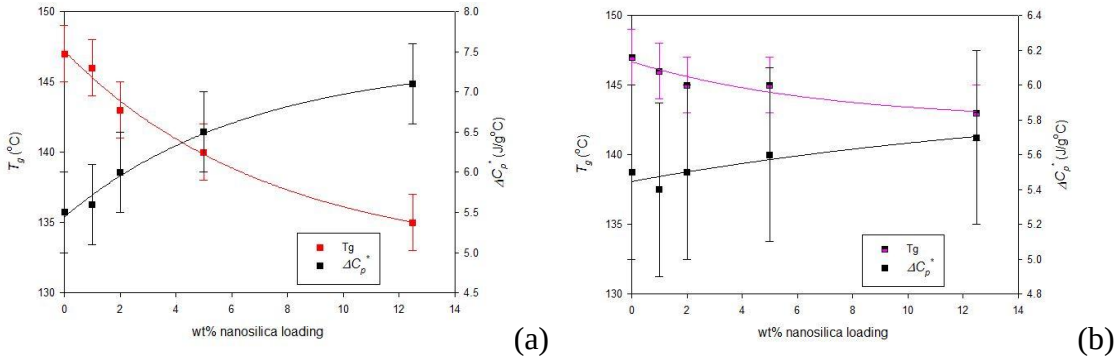

(a) (b)

Figure 8-4 Effects of organic surface groups and characteristics of interphase regions on T_g: (a) using Nanopox (d=20 nm), (b) using 3M (d=100 nm)

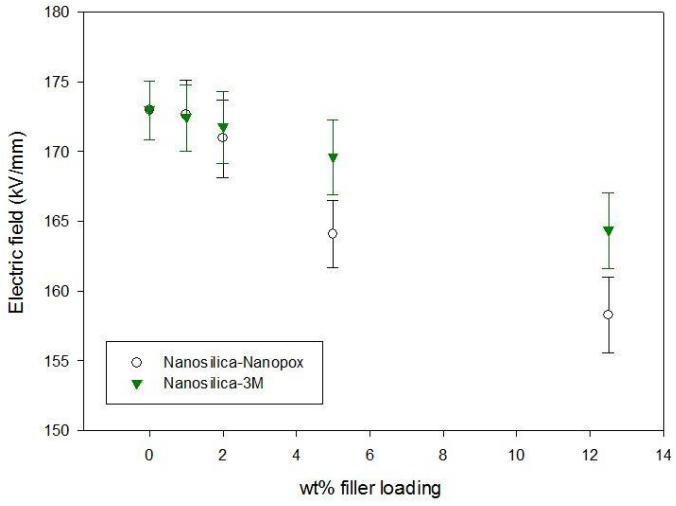

Figure 8-5 Effects of organic surface groups and characteristics of interphase regions on E_b: (a) using Nanopox (d=20 nm), (b) using 3M (d=100 nm)

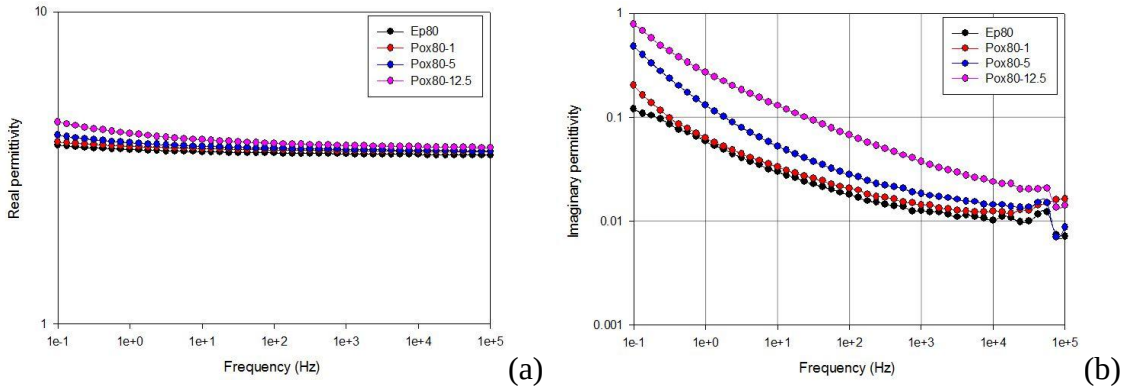

Figure 8-6 The power law behaviour and LFD indicating a non-uniform charge transport between clusters at 160 ^{o}C: (a) real part, (b) imaginary part

8.3 Effects of adding a large amount of microsilica

When the filler size is in the microscopic range, interfacial effects become negligible, due to the consequent large reduction in the interfacial area. The properties of microcomposites are typically a weighted average of the constituent material component properties. The incorporation of a large quantity of micro-silica produces significant changes compared to both the unfilled epoxy and related nanocomposites. First, the microfillers can be considered to be the origin of the roughness of fracture surfaces. The presence of microfillers also makes uniform mixing and dispersion of nanofillers difficult to achieve, as shown in Figure 8-7. Furthermore, it is likely that microfillers inhibit reactions of OH groups on nanoparticle surfaces with epoxy groups, so enabling hydrogen bonding between hydroxyl groups to occur, as seen in Figure 8-8. The settling of microfillers and the non-uniform mixing introduces a multi-layered structure and a broad distribution of clusters inside the materials and hence, lead to the complicated patterns of space charge formation and cause the power law behaviour or the LFD of the relative permittivity. In addition of the higher permittivity of quartz micro-silica, the LFD causes an increase in the dielectric constant and dielectric loss. In addition, the presence of a large quantity of microsilica, together with the poor dispersion of fillers, can reduce the inter-trap distance in the band gap such that electrons can hop or tunnel through the potential heights; so, facilitate the charge transport inside the materials. The enhanced charge transport via clusters and traps, as well as impurities, lead to a reduction in electrical breakdown strength of micro-filled composites compared to the unfilled and nanocomposite samples. Also, a layered structure will reduce the effective thickness of the samples and hence, reduce the E_b. The addition of nanofillers into the

conventional microcomposites introduces further effects due to their large interfacial areas and the surface chemistry of nanoparticles, as well as the possible synergy between the micro- and nano-silica fillers.

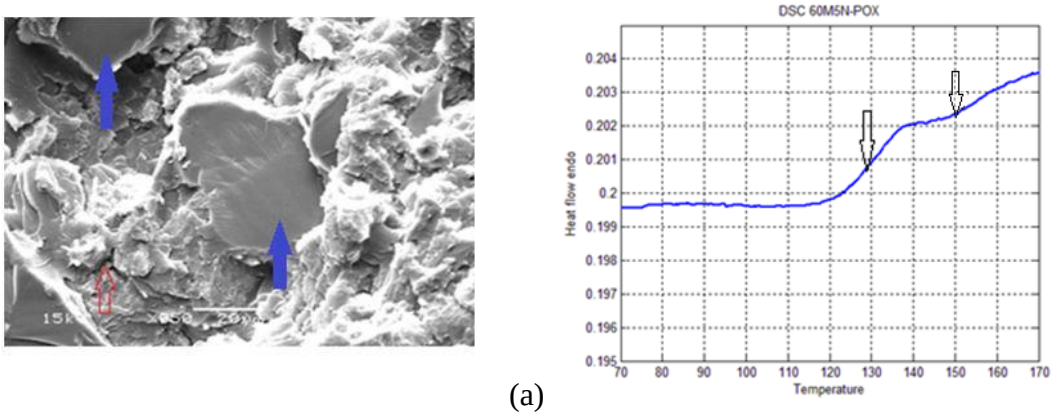

Figure 8-7 Non-uniform mixing: (a) SEM image, (b) two glass transition in DSC diagram

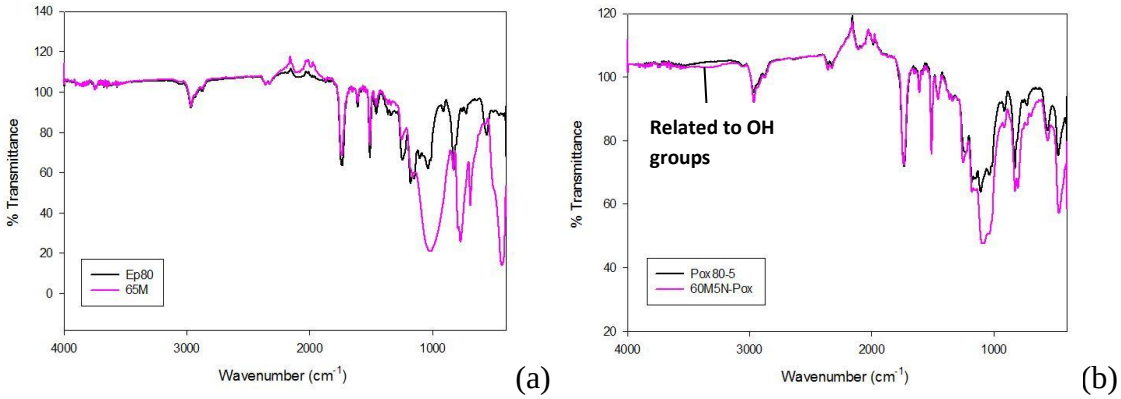

Figure 8-8 FTIR spectra of micro-filled composites: (a) no OH groups, (b) presence of OH groups due to the presence of nanosilica

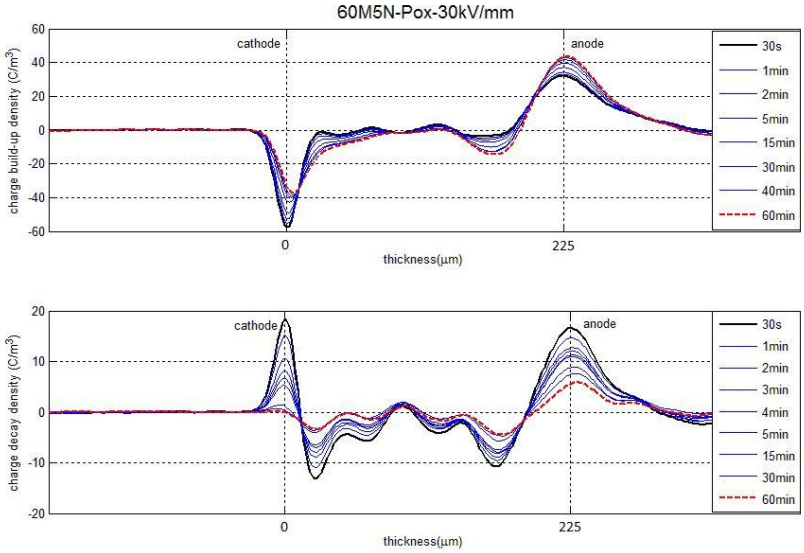

Figure 8-9 Complicated patterns of space charge due to the settling of microsilica and non-uniform mixing

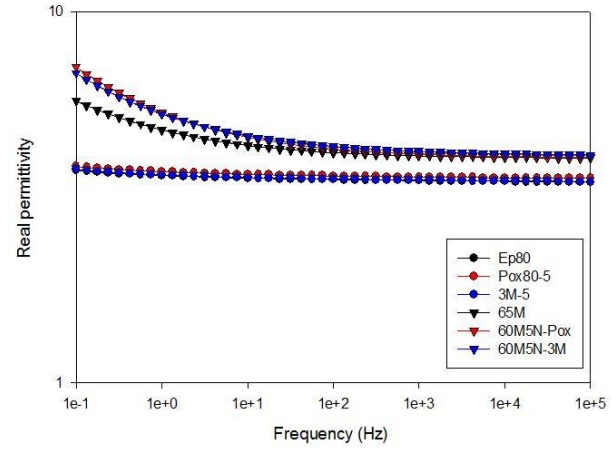

(a)

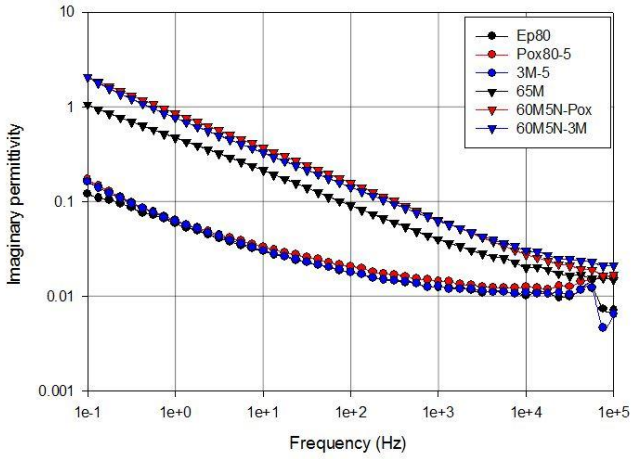

(b)

Figure 8-10 Relative permittivity showing a LFD with the slope less than -1 due to non-uniform charge transport between large scale clusters

Chapter 9 Conclusions and Future Works

This chapter sets out to summarise the main conclusions drawn from this project and suggest potential work in order to expand the research further.

9.1 Conclusions

The aim of the thesis is to investigate effects involving the addition of nano-silica particles of different size on properties of anhydride cured epoxy-based systems, including unfilled epoxy and conventional microcomposites. These nano-silica particles are premixed in the commercial masterbatches, namely the Nanopox and 3M systems. From SEM images, the use of the above masterbatches has been proven to lead to samples containing a reasonable dispersion of nano-particles, so limiting the effect of filler agglomeration on material properties. However, the study has revealed that the addition of nano-silica particles exerts a significant impact on material properties through changes in the resin stoichiometry and as a result of the interfacial interactions between the polymer matrices and the fillers. The stoichiometry of the unfilled epoxy systems markedly influences T_g and E_b. The T_g value peaks at the optimum proportion, and decreases at different rates away from the optimum. While an excess of hardener exerts no marked effect on T_g, it leads to a dramatic decrease in E_b, probably due to oxidation of unreacted hardener molecules during thermal processing. Conversely, systems containing an excess of epoxy show less pronounced effects on E_b, whereas a significant reduction in T_g can be observed when compared to the optimum system. Based on these fundamental behaviours, the introduction of Nanopox into the host resin has been shown to induce changes in the stoichiometry of the reacting systems, and hence, the curing mechanisms. At a 5 wt% loading level of nanosilica, systems containing an excess of epoxy exhibited unchanged T_g and E_b. Conversely, materials based upon the epoxy plus 80 phr hardener and more have shown reduced T_g's and a significant decrease in E_b. It has been suggested that impurities and/or hydroxyl groups located on the nanoparticle surface, which depend on the synthesis and surface treatment processes of nano-fillers, have modified the curing mechanisms through catalytic effects on homopolymerisation reactions, so leading to an effective excess of

hardener. The existence of excess hardener can be observed in the FTIR spectra. The dielectric permittivity values have also been affected by the stoichiometry and the presence of nanosilica. The excess hardener/epoxy systems show increased real and imaginary permittivity values. Due to the stoichiometric effect, upon the addition of nano-silica, the systems containing an excess hardener attain a lower crosslinking degree, and hence, a reduced T_g and a higher permittivity. The changes in the loss factor upon the introduction of the Nanopox also support this explanation about changes in stoichiometry and its impact on E_b. The higher loss factor, the lower E_b.

Apart from the above stoichiometric effect, interfacial effects have also been observed in the nanocomposites. The incorporation of fillers has significantly influenced the properties of the resulting composites. In general, the addition of fillers leads to a reduction in T_g, E_b and an increase in dielectric constant and loss factor. The surface treatment shows the effects on the loose layer through the interaction between the organic surface groups and the host resin matrix. Depending on the characteristic of any organic surface groups, robust or weak interfaces could be formed, hence, resulting in different dielectric behaviours. In this study, the 3M-based samples have exhibited better performance than the Nanopox-based ones. The superior properties of the 3M-based nanocomposites have been explained by a reduction in the interphase volume due to the increased particle size, and more robust interfaces as a result of stronger interactions between the organic surface groups and the host resin matrix, whereas loosely bound interfacial layers have been supposed to exist in the Nanopox-based samples. The average diameter of nano-silica particles in the Nanopox system is 20 nm, while that of the 3M masterbatch is 100 nm. Therefore, the study has suggested that as long as a good dispersion of nano-fillers is achieved and the size of nano-fillers is in the nanometric range, the interfacial characteristics exert a more marked influence on material properties than the filler size.

Meanwhile, neither changes in stoichiometry nor addition of nanosilica have produced a significant effect on the space charge behaviour of the samples. Only a small amount of homocharge was observed near the cathode in all the systems, and then the injection is likely to be suppressed. No internal space charge can be observed at other locations within the bulk of the samples. Moreover, the quick decay of such injected charges suggests a distribution of only shallow traps near the sample surfaces. The

nanocomposites under study, in principle, possess similar structural networks with well-dispersed nanosilica. Although the concentration of defects may be different, inter-trap distances are likely to be too large for conduction in the band gap to occur. At room temperature, all molecular motion within the matrix is severely hindered, so ionic conduction is also likely to be slow and any polarisation process is limited at this temperature. After being injected from the cathode, electrons cannot move to the anode and remain in the vicinity of the electrode. Therefore, one can conclude that, in these well-dispersed samples, space charge will not be a major factor in influencing electrical properties, at least at room temperature, which is far below T_g.

When the filler size is in the microscopic range, interfacial effects become negligible, due to the consequent large reduction in the interfacial area. The properties of microcomposites are typically a weighted average of the constituent material component properties. Micro-fillers can be considered to be defect centers, which reduce E_b. Therefore, the aggregation of fillers leads to the deterioration in material performance. The incorporation of a large quantity of micro-silica filler has led to significant changes compared to both the unfilled epoxy and the nanocomposites. The fracture surfaces have been found to be extremely rough. The micro-fillers have been considered to be the cause of this roughness. The presence of microfillers also makes uniform mixing and dispersion of nanofillers difficult to achieve, as shown in the SEM images. As a consequence, the microsilica particles were completely settled in the microcomposite samples studied here. In addition, the FTIR spectra of samples containing both nano and micro silica have suggested that the micro-fillers may inhibit reactions of OH groups on nanoparticle surfaces with epoxy groups; so hydrogen bonds between hydroxyl groups can be formed. The presence of micro-fillers, which act as charge defects, can contribute to a type of conduction in the band gap and the formation of homocharge near the cathode and heterocharge near the anode. Furthermore, the higher permittivity of quartz micro-silica (5.4) slightly increases the dielectric constant and dielectric loss, according to the Lichtenecker and Maxwell-Garnett mixing rules. The settling of microfillers and the non-uniform mixing introduces a multi-layered structure and a broad distribution of clusters inside the materials and hence, lead to the complicated patterns of space charge formation and cause the power law behaviour or the LFD of the relative permittivity. In addition of the higher permittivity of quartz micro-silica, the LFD causes an increase in the dielectric constant and dielectric loss. All these factors,

including space charge formation, enhanced inter-cluster charge transport and impurities, lead to a reduction in electrical breakdown strength of micro-filled composites compared to the unfilled and nanocomposite samples. The addition of nanofillers into the microcomposites introduces further effects due to the large interfacial areas that result, the surface chemistry of the nanoparticles, and other possible effects due to the synergy between nano and micro fillers. Consequently, at the same loading level, microcomposites containing 3M type nanofillers exhibit better performance than those containing Nanopox.

The addition of nanosilica particles also exerts certain effects on electrical treeing in epoxy resin and its nanocomposites. It is likely that the addition of nanosilica particles leads to an increase in the extent of the tree. The interfacial characteristics of nano-particles, i.e. interactions between organic surface groups and resin matrix, and charges on nano-particles, can influence the growth rate of electrical trees, according to the crossover phenomenon proposed by Tanaka [338]. The crossover phenomenon suggests that at high electric fields, treeing breakdown is dominated by short-time breakdown mechanisms rather than PD activity.

Raman spectroscopy has been proven to be an effective tool in analysing electrical trees chemically. In general, in a conducting breakdown/tree channel, three components are observed in the spectrum; the common Raman spectrum of the host resin superimposed on a pronounced fluorescent background that is indicative of material degradation, plus the G band of sp^2 hybridised carbons. Their relative intensities vary from place to place. The carbonaceous shell is conducting in nature and is thought to prevent PD activity. On the other hand, in a more bush-like tree, the degradation of material is still evinced by a highly fluorescent background. However, the presence of the G and D bands of carbon is not apparent. Such trees are thought to be non-conducting, thereby allowing PD activity to occur throughout the tree body. The Raman spectra indicating the presence of carbonaceous material are supported by SEM images.

9.2 Future works

Several areas of this project present potential for further study, some of them are detailed as follows:

- Functionalisation of nano-silica particles should be conducted. The surface of functionalised nano-particles can be then analysed chemically prior to preparing nanocomposites. This allows more precise investigation of the influence of interfacial characteristics on material properties, including the stoichiometric effect;
- Samples filled with nano-silica particles of different sizes should be characterised to evaluate the size effect on material performances. From this study, the upper limit in nanoscale size of particles can be determined, i.e. the size range in which nano-particles provide nanoscale properties;
- Experiments such as AC breakdown, DC breakdown and space charge should be conducted as a function of environmental factors such as moisture and temperature to approach the performance in service conditions;
- A more wide ranging tree study should be conducted involving more detailed structural and chemical analysis, including different types of electrical tree and effects of temperature and moisture;
- PD activity should be monitored during propagation of different types of electrical tree to obtain the relationship between type of tree, PD activity and possible associated chemical changes in the material;
- The crossover phenomenon should be clarified. To do this, electrical trees should be grown at various voltages ranging from low to high magnitude.

References

1. R R Bauer, *Epoxy Resin Chemistry*. Washington DC: American Chamical Society, 1979.
2. J A Nielsen, S J Chen and D C Tim, *Intermolecular reaction kinetics for the PGE/NMA/BDMA anhydride-cured epoxy*. Macromolecules, 1993. **26**(6): p.1369.
3. T W Dakin, *Application of Epoxy Resins in Electrical Apparatus.* IEEE Transactions on Electrical Insulation, 1974. **EI-9**(4): p.121.
4. J Sato, *New technology for medium voltage solid insulated switchgear*. Transmission and Distribution Conference and Exhibition, 2002: Asia Pacific. IEEE/PES.
5. T Shimizu, *Material and simulation technology for solid insulated switchgear.* Proceedings of the IEEE 7th International Conference on Properties and Applications of Dielectric Material, 2003.
6. D A Bolon, *Epoxy chemistry for electrical insulation*. IEEE Electrical Insulation Magazine, 1995. **11**(4): p.10.
7. R S Gorur, E A Cherney, and J T Burnham, *Outdoor Insulators*. Ravi S Gorur Inc., Phoenix, USA, 1999.
8. Market Report: *World Epoxy Resin Market*. Code C0530, 2010.
9. T Tanaka, Y Ohki, M Ochi, M Harada, and T Imai, *Enhanced partial discharge resistance of epoxy/clay nanocomposite prepared by newly developed organic modification and solubilization methods.* IEEE Transactions on Dielectrics and Electrical Insulation, 2008. **15**(1): p.81.
10. Z Li, K Okamoto, Y Ohki, T Tanak, *Effects of nano-filler addition on partial discharge resistance and dielectric breakdown strength of Micro-Alumina Epoxy composite*. IEEE Transactions on Dielectrics and Electrical Insulation, 2010. **17**(3): p.653.
11. M Hyuga, N Tagam, T Tanaka, Y Ohki, T Imai, M Harada, and M Ochi, *Improvement in High-temperature Dielectric Properties of Epoxy Resin by Abundant Addition of Micro-silica.* Annual Report Conference on Electrical Insulation and Dielectric Phenomena, 2009.

12. T Imai, *Improving Epoxy-based Insulating Materials with Nano-fillers toward Practical Application*. Conference Record of the IEEE International Symposium on Electrical Insulation, 2008.
13. N Fuse, *Possible mechanism of superior partial-discharge resistance of polyamide nanocomposites*. Annual Report Conference on Electrical Insulation and Dielectric Phenomena, 2004.
14. T Imai, *Insulation properties of nano- and micro-filler mixture composite*. Annual Report Conference on Electrical Insulation and Dielectric Phenomena CEIDP, 2005.
15. M Kozako, *Surface erosion due to partial discharges on several kinds of epoxy nanocomposites*. Annual Report Conference on Electrical Insulation and Dielectric Phenomena, 2005.
16. A Haque, M Shamsuzzoha, F Hussain, D Dean, *S2-glass/epoxy polymer nanocomposites: manufacturing, structures, thermal and mechanical properties*. Journal of composite materials, 2003. **37**(10): p.1821.
17. C L Chiang, C C M Ma, F Y Wang, and H C Kwan, *Thermo-oxidative degradation of novel epoxy containing silicon and phosporous nanocomposite*. European Polymer Journal, 2003. **39**(4): pp.825.
18. T J Lewis, *Nanometric Dielectrics*. IEEE Transactions on Dielectrics and Electrical Insulation, 1994. **1**(5): p.812.
19. C Green and A S Vaughan, *Nanodielectrics-How much do we really understand?*. IEEE Electrical Insulation Magazine, 2008. **24**(4): p.6.
20. B Venkatasulu, and M J Thomas, *Erosion resistance of silicone rubber nanocomposites at lower filler loadings*. International Symposium on High Voltage Engineeing, 2009.
21. B Venkatasulu, and M J Thomas, *Studies on the tracking and erosion resistance of RTV silicone rubber nanocomposites*. IEEE Conference on Electrical Insulation and Dielectric Phenomena, 2008.
22. I Ramirez, E A Cherney, S Jayaram, and M Gauthier, *Silicone rubber nanocomposites for outdoor insulation applications*. IEEE Conference on Electrical Insulation and Dielectric Phenomena, 2007.

23. M Kurimoto, *Dielectric properties of epoxy/alumina nanocomposite influenced by control of micrometric agglomerates*. IEEE Transactions on Dielectrics and Electrical Insulation, 2010. **17**(3): p.662.
24. T.J. Lewis, *Interfaces are the dominant feature of dielectrics at the Nanometric level.* IEEE Transactions on Dielectrics and Electrical Insulation, 2004. **11**(5): p.739.
25. Y. Li, B Zhang, X Pan, *Preparation and characterization of PMMA–kaolinite intercalation composites*. Composites Science and Technology, 2008. **68**(9): p.1954.
26. T Imai, F Sawa, T Ozaki, Y Inoue, T Shimizu, and T Tanaka, *Comparision of insulation breakdown properties of epoxy nanocomposites under homogeneous and divergent electric fields*. IEEE Conference on Electrical Insulation and Dielectric Phenomena CEIDP, 2006.
27. Y Hu, R C Smith, J K Nelson, and L S Schadler, *Some mechanistic understanding of the impulse strength of nanocomposites*. IEEE Conference on Electrical Insulation and Dielectric Phenomena, 2006.
28. R Sarathi, R K Sahu, and P Rajeshkumar, *Understanding the thermal, mechanical and electrical properties of epoxy nanocomposites*. Meterials Science Engineering, 2007. **A 445-44)**: p.567.
29. M Roy, C W Reed, R K MacCrone, L S Schadler, J K Nelson, R Keefe, and W Zenger, *Evidence for the role of interface in polyolefin nanocomposites*. International Symposium on Electrical Insulating Materials ISEIM, 2005.
30. T Imai, F Sawa, T Ozaki, T Shimizu, R Kido, M Kazako, T Tanaka, *Evaluation of insulation properties of epoxy resin with nano-scale silica particles*. International Symposium on Electrical Insulating Materials ISEIM, 2005.
31. P Maity, P K Poovamma, S Basu, V Parameswaran, N Gupta, *Dielectric Spectroscopy of Epoxy Resin with and without Nanometric Alumina Fillers*. IEEE Transactions on Dielectrics and Electrical Insulation, 2009. **16**(5): p.1481.
32. P F Bruins, *Epoxy Resin Technology (Polymer Engineering & Technology)*. John Wiley & Sons Inc, 2007.
33. E M Petrie, *Epoxy Adhesive Formulations (Chemical Engineering)*. McGraw-Hill Professional, 2005.

34. L Quercia, F Loffredo and F Di Francia, *Influence of filler dispersion on thin film composites sensing properties*. Sensors and Actuators B: Chemical, 2005. **109**(1): p.153.
35. J Moczo, E Fekete, K Laszlo, and B Pukanszky, *Aggregation of particulate fillers: factors, determination, properties*. Macromolecular Symposia, 2003. **194**(1): p.111.
36. F Lianhua, Z Zhuqing, and C P Wong, *Effect of filler settling of underfill encapsulant on reliability performance*. Proceedings International Symposium on Advanced Packaging Materials: Processes, Properties and Interfaces, 2001.
37. Y H Lee, C B Park, M Sain, M Kontopoulou, and W Zheng, *Effects of clay dispersion and content on the rheological, mechanical properties and flame retardance of HDPE/clay nanocomposties.* Journal of Applied Polymer Science, 2007. **105**(4): p.1993.
38. T Ramanathan, S Stankovich, D A Dikin, H Liu, H Shen, S T Nguyen and L C Brinson, *Graphitic nanofillers in PMMA nanocomposites- An investigation of particle size and dispersion and their influence on nanocomposite properties.* Journal of Polymer Science Part B: Polymer Physics, 2007. **45**(15): p.2097.
39. A S Vaughan, S G Swingler and Y Zhang, *Polyethylene Nanodielectrics: The Influence of nanoclays on structure formation and dielectric breakdown*. IEEJ Trans. FM, 2006. **126**(11): p.1057.
40. P C Hiemenz, R Rajagopalan, *Principles of Colloid and Surface Chemistry (3rd Ed)*. New York: Marcel Dekker, 1997.
41. T Iizuka, Y Ohki, and T Tanaka, *Effects of coupling agent and filler dispersion on V-t characteristics of epoxy/silica nanocomposites*. International Symposium on Electrical Insulating Materials, 2008.
42. P Maity, *Improvement in surface degradation properties of polymer composites due to pre-processed nanometric alumina fillers*. IEEE Transactions on Dielectrics and Electrical Insulation, 2008. **15**(1): p.63.
43. H Xingyi, *Influence of nanoparticle surface treatment on the electrical properties of cycloaliphatic epoxy nanocomposites*. IEEE Transactions on Dielectrics and Electrical Insulation, 2010. **17**(2): p.635.

44. T Iizuka and T Tanaka, *Effects of nano silica filler size on treeing breakdown lifetime of epoxy nanocomposites*. IEEE 9th International Conference on the Properties and Applications of Dielectric Materials ICPADM, 2009.
45. H Miyagawa, and L T Drzal, *Thermo-physical and impact properties of epoxy nanocomposites reinforced by single-wall carbon nanotubes*. Polymer, 2004. **45**(15): p.5163.
46. Y Miwa, A R Drews, S Schlick, *Detection of the Direct Effect of Clay on Polymer Dynamics: The Case of Spin-Labeled Poly(methyl acrylate)/Clay Nanocomposites Studied by ESR, XRD, and DSC*. Macromolecules, 2006. **39**(9): p.3304.
47. C Zou, J C Fothergill, S W Rowe, *The effect of water absorption on the dielectric properties of epoxy nanocomposites*. IEEE Transactions on Dielectrics and Electrical Insulation, 2008. **15**(1): p.106.
48. J Ma, M S Mo, X S Du, P Rosso, K Friedrich, H C Kuan, *Effect of inorganic nanoparticles on mechanical property, fracture toughness and toughening mechanism of two epoxy systems*. Polymer, 2008. **49**(16): p.3510.
49. P Rosso, L Ye, K Friedrich, and S Sprenger, A Toughened Epoxy Resin by Silica Nanoparticle Reinforcement. Journal of Applied Polymer Science, 2006. **100**(3): p.1849.
50. B R K Blackman, A J Kinloch, J S Lee, A C Taylor, R Agarwal, G Schueneman, S Sprenger, *The fracture and fatigue behavior of nano-modified epoxy polymers*. Journal of Materials Science, 2007. **42**(16): p.7049.
51. T Mahrholz, J Stangle, M Sinapius, *Quantitation of the reinforcement effect of silica nanoparticles in epoxy resins used in liquid composite moulding processes*. Composites Part A: Applied Science and Manufacturing, 2009. **40**(3): p.235.
52. B Ellis, *Chemistry and Technology of Epoxy Resins*. Kluwer Academic Publishers, 1992.
53. H L Lee, K Neville, *Handbook of Epoxy Resins*. McGraw Hill Higher Education, 1967.
54. D Harran, M F Grenier-Loustalot and Ph Monge, *Avancement de la réaction chimique au point de gel d'une résine epoxyde: Systèmes (diglycidyl ether du bisphénol A-diamino diphényl méthane et diglycidyl ether du bisphénol A-diamino diphényl sulfone)*. European Polymer Journal, 1988. **24**(3): p.225.
55. P J Flory, *Principles of Polymer Chemistry*. New York: Cornell University, 1988.

56. H H Winter, *Techniques in Rheological Measurement (A.A. Ed)*. Collyer., London: Chapman & Hall, 1997.
57. D J O'Brien, P T Mather, S R White, *Viscoelastic Properties of an Epoxy Resin during Cure*. Journal of Composite Materials, 2001.**35**(10): p.883.
58. P J Halley, M E Mackay, G A George, *Determining the gel point of an epoxy resin by various theological methods*. High Performance Polymers, 1994. **6**(4): p.405.
59. R B Prime, *Thermal Charadcterization of Polymeric Materials*. San Diego: Academic Press, 1997.
60. J K Gillham, J B Enns, *On the cure and properties of thermosetting polymers using Torsional Braid Analysis*. Trends in Polymer Science, 1994. **2**(12): p.406.
61. G Wisanrakki, and J K Gillham, *The Glass Transition Temperature (Tg) as an Index of Chemical Conversion for a High-Tg Amine/Epoxy System: Chemical and Diffusion Controlled Reaction Kinetics*. Journal of Coatings Technilogy, 1990. **62**(783): pp.35.
62. M T Aronhime, and J K Gillham, *The Time-Temperature-Transformation (TTT) Cure Diagram of Thermosetting Systems*. Advances in Polymer Science, 1986. **78**: p.83.
63. H Stutz, J Mertes, and K Nuebeche, *Kinetics of thermoset cure and polymerization in the glass transition region*. Journal of Polymer Science Part A: Polymer Chemistry, 1993. **31**(7): p.1879.
64. G V Assche, A V Hemelrijck, H Rahier, B V Mele, *Modulated differential scanning calorimetry: isothermal cure and vitrification of thermosetting systems*. Thermochimica Acta, 1995. **268**: p.121.
65. A Shimazaki, *Viscoelastic changes of epoxy resin–acid anhydride system during curing*. Journal of Applied Polymer Science, 1968. **12**(9): p.2012.
66. G Kortaberria, L Solar, A Jimeno, P Arruti, C Gomez, I Mondragon, *Curing of an Epoxy Resin Modified with Nanoclay Monitored by Dielectric Spectroscopy and Rheological Measurements*. Journal of Applied Polymer Science, 2006. **102**(6): p.5927.
67. L Khoun, and P Huber, *Cure shrinkage characterization of an epoxy resin system by two in situ measurement methods*. Polymer Composites, 2010. **31**(9): p.1603.

68. H Yu, S G Mhaisalkar, E H Wong, *Observations of Gelation and Vitrification of a Thermosetting Resin during the Evolution of Polymerization Shrinkage*. Macromolecules Rapid Communication, 2005. **26**(18): p.1483.
69. R Thomas, S Durix, C Sinturel, T Omonov, S Goossens, G Groeninckx, P Moldenaers, S Thomas, *Cure kinetics, morphology and miscibility of modified DGEBA-based epoxy resin – Effects of a liquid rubber inclusion*. Polymer, 2007. **48**(6): p.1695.
70. M Opalicki, J M Kenny, L Nicolais, *Cure kinetics of neat and carbon-fiber-reinforced TGDDM/DDS epoxy systems.* Journal of Applied Polymer Science, 1996. **61**(6): p.1025.
71. G W Scherer, *Use of the Adam-Gibbs Equation in the Analysis of Structural Relaxation*. Journal of the American Ceramic Society, 1984. **67**(7): p.504.
72. D J Hourston, M Song, S U Schafer, H M Pollock, A Hammiche, *Modulated-temperature differential scanning calorimetry: 15. Crosslinking in polyurethane-poly(ethyl methacrylate) interpenetrating polymer networks*. Polymer, 1999. **40**(17): p.4769.
73. N M Alves, J L Gomez Ribelles, J F Mano, *Enthaply relaxation studies in polymethyl methacrylate networks with different crosslinking degrees*. Polymer, 2005. **46**(2): p.491.
74. S Montserrat, F Roman, P Colomer, *Vitrification and dielectric relaxation during the isothermal curing of an epoxy-amine resin*. Polymer, 2003. **44**(1): p.101.
75. L Haiying, W Lejun, and C P Wong, *Study of a controlled thermally degradable epoxy resin system for electronic packaging*. Proceeding Electronic Components and Technology Conference 51st, 2001.
76. http://www.colby.edu/chemistry/PChem/lab/DiffScanningCal.pdf
77. E R v Schweidler, *Studien über die Anomalien im Verhalten der Dielektrika*. Annalen der Physik, 1907. **329**(14): p.711.
78. R R Benedict, *Behavior of Dielectrics A Study of the Anomalous Charging Current and the Variation of Dielectric Energy Loss and Capacitance with Frequency*. Transactions of American Institute of Electrical Engineers, 1930. **49**(2): p.739.

79. L A Dissado and R M Hill, *A Cluster Approach to the Structure of Imperfect Materials and Their Relaxation Spectroscopy*. Proceedings of the Royal Society of London Series A, 1983. **390**(1798): p.131.
80. T Blythe and D Bloor, *Electrical properties of polymers*. Cambridge University Press, 2005.
81. F Kremer, A Schonhals, *Broadband Dielectric Spectroscopy*. Springer, 2002.
82. K C Kao, *Dielectric Phenomena in Solids*. Academic press, 2004.
83. L H Garden, D Hayward, and R A Pethrick, *Dielectric non-destructive testing approach to cure monitoring of adhesives and composites*. Proceedings of the Institution of Mechanical Engineers, Part G: Journal of Aerospcae Engineering, 2007. **221**(4): p.521.
84. R Casalini, A Livi, and P A Rolla, *Self-similarity of dielectric relaxation and conductivity in cross-linking systems*. Physical Review B, 1996. **53**(2): p.564.
85. K Nixdorf, G Busse, *The dielectric properties of glass-fibre-reinforced epoxy resin during polymerisation*. Composites Science and Technology, 2001. **61**(6): p.889.
86. L Nunez, S Gomez-Barreiro, C A Gracia-Fernandez, M R Nunez, *Use of the dielectric analysis to complement previous thermoanalytical studies on the system diglycidyl ether of bisphenol A/1,2 diamine cyclohexane.* Polymer, 2004. **45**(4): p.1167.
87. D Puglia, L Valentini, I Armentano, J M Kenny, *Effects of single-walled carbon nanotube incorporation on the cure reaction of epoxy resin and its detection by Raman spectroscopy*. Diamond and Related Materials, 2003. **12**(3): p.827.
88. O Becker, G P Simon, *Epoxy layered silicate nanocomposites*. Advances in Polymer Science, 2005. **29**: p.29.
89. A Allaoui, N El Bounia, *How carbon nanotube affect the cure kinetics and glass transition temperature of their epoxy composites – A review.* Express Polymer Letters, 2009. **3**(9): p.588.
90. P Pissis, D Fragiadakis, *Dielectric Studies of Segmental Dynamics in Epoxy Nanocomposites.* Journal of Macromolecular Science, Part B: Physics, 2007. **46**(1): p.119.
91. A Kyritsis, G Vikelis, P Maroulas, P Pissis, B Milosheva, R Kotsilkova, A Toplijska, C Silvestre, D Duraccio, *Polymer Dynamics in Epoxy/Alumina*

Nanocomposites Studied by Various Techniques. Journal of Applied Polymer Science, 2011. **121**(6): p.3613.

92. D H Yoon, J Zhang, B I Lee, *Dielectric constant and mixing model of barium titanate composite thick films*. Materials Research Bulletin, 2003. **38**(5): p.765.
93. Y Rao, C P Wong, *Material characterization of a high-dielectric constant polymer-ceramic composite for embedded capacitor for RF applications*. Journal of Applied Polymer Science, 2004. **92**(4): p.2228.
94. M G Todd, F G Shi, *Complex permittivity of composite systems: A comprehensive interphase approach*. . IEEE Transactions on Dielectrics and Electrical Insulation, 2005. **12**(3): p.601.
95. H T Vo, F G Shi, *Towards model-based engineering of optoelectronic packaging materials: Dielectric constant modelling*. Microelectronics, 2002. **33**(5-6): p.409.
96. D J Mackish, *Effects of interfacial polarization and loading factor in dielectric-loss measurements of composites*. Journal of Applied Physics, 1979. **50**(9): p.5923.
97. Ari H Sihvola, *Electromagnetic Mixing Formulas and Applications*. The Institution of Engineering and Technology, 2000.
98. E Kuffel, W S Zaengl, *High Voltage Engineering Fundamental*. Pergamon: New York, NY, USA, 1984.
99. I Bunget, M Popescu, *Physics of Solid Dielectrics*. Elsevier: Amsterdam, 1984.
100. F. Seitz, *On the Theory of Electron Multiplication in Crystals*. Physical Review, 1949. **76**(9): p.1376.
101. V A Zakrevski, N T Sudar, A Zappo, Y A Dubitsky, *Mechanism of electrical degradation and breakdown of insulating polymers*. Journal of Applied Physics, 2003. **93**(4): p.2135.
102. M Ieda, *Dielectric breakdown process of polymers*. IEEE Transactions on Dielectrics and Electrical Insulation, 1980. **15**(3): p.206.
103. J E Falk, R J Fleming, *Calculation of the electronic energy band structure of polyethylene*. Journal of Physic C: Solid State Physics, 1973. **6**(20): p.2954.
104. Y Okhi, N Fuse, T Arai, *Band gap energies and localized states in several insulating polymers estimated by optical maesurement*, Annual Report Conference on Electrical Insulation and Dielectric Phenomena, 2010.

105. G C Steven, E Perkins, and J V Champion, *IEE Conference: Dielectric Materials Mearurements and Applications*. 1988. **289**: p.234.
106. W Nelson, *Applied Life Data Analysis*. Wiley: New York, NY, USA, 1981.
107. J C Fothergill, *Estimating the cumulative probability of failure data points to be plotted on Weibull and other probability paper*. IEEE Transactions on Dielectrics and Electrical Insulation, 1990. **25**(5): p.489.
108. Gallot-Lavallee, V Griseri, G Teyssedre, C Laurent, *The pulsed electro-acoustic technique in research on dielectrics for electrical engineering*. RS-RIGE, 2005. **8**(5-6): p.749.
109. Patent EP 1666515 B1, *Alicyclic epoxy resin, process for producing the same, composition thereof, cured epoxy resin, and use of alicyclic epoxy resin*.
110. G Chen, T Y G Tay, A E Davies, Y Tanaka and T Takada, *Electrodes and charge injection in low-density polyethylene, using the pulsed electroacoustic technique*. IEEE Transaction on Dielectrics and Electrical insulation, 2001. **8**(6): p.867.
111. Y Zhang, J Lewiner, C Alquie, N Hampton, *E*vidence of strong correlation between space-charge buildup and breakdown in cable insulation**.** IEEE Transactions on Dielectrics and Electrical Insulation, 1996. **3**(6): p.778.
112. L A Dissado, G Mazzanti, G C Montanari, *The role of trapped space charges in the electrical ageing of insulating materials*. IEEE Transaction Dielectric and Electrical Insulation, 1997. **4**(5): p.496.
113. L S Roman, I A Hummelgen, F C Nart, L O Peres and E L de Sa, *Determination of electro affinity and ionization potential of conjugated polymers via Fowler-Nordheim tunneling measurements: theoretical formulation and application to poly(p-phenylene vinylene)*. Journal of Chemical Physics, 1998. **105**(23): p.10614.
114. K C Kao, W Hwang, *Electrical transport in solids, with particular reference to organic semiconductors (International series in the science of the solid state).* Pergamon Press, 1981.
115. N Hozumi, H Suzuki, T Okamoto, K Watanabe, A Watanabe, Direct observation of time-dependent space charge profiles in XLPE cable under high electric fields. IEEE Transactions on Dielectrics and Electrical Insulation, 1994. **1**(6): p.1068.
116. G Chen, and S H Loi, *Space Charge Modelling in Solid Dielectrics under High Electric Field Based on Double Charge Injection Model*. Proceedings of MRS Fall Meeting MRS Symposium W, Boston USA, 2005.

117. L S Roy, G Teyssedre, C Laurent, P Segur, Numerical model for studying dynamic space charge behavior in polyethylene. Proceedings of the 7th International Conference on Properties and Applications of Dielectric Materials, 2003. **3**(1-5): p.859.
118. L A Dissado, J C Fothergill, *Electrical degradation and breakdown in polymers*. Institution of Engineering and Technology, 1992.
119. P Morshuis, M Jeroense, Space charge measurements on impregnated paper: a review of the PEA method and a discussion of results. IEEE Electrical Insulation Magazine, 1997. **13**(3): p.26.
120. A Cherifi, M A Dakka, A Toureille, The validation of the thermal step method. IEEE Transactions on Dielectrics and Electrical Insulation, 1992. **27**(6): p.1152.
121. Gerhard-Multhaupt, *Analysis of Pressure-wave Methods for the Nondestructive Determination of Spatial charge or Field Distributions in Dielectrics*. Physical. Review B, 1983. **27**: p. 2494.
122. P Laurenceau, G Dreyfus and J Lewiner, *New Principle for the Determination of Potential Distributions in Dielectrics*. Physical Review Letter, 1977. **38**: p.46.
123. L Ying, M Yasuda, T Takada, Pulsed electroacoustic method for measurement of charge accumulation in solid dielectrics. IEEE Transactions on Dielectrics and Electrical Insulation, 1994. **1**(2): p.188.
124. G Chen, Y L Chong and M Fu, *Calibration of the Pulsed Electroacoustic Technique in the Presence of Trapped Charge*. Measurement Science and Technology, 2006. **17**(7): p.1974.
125. N B Colthup, L H Daly and S E Wiberley, *Introduction to Infrared and Raman Spectroscopy (3rd Ed)*. London: Academic press Ltd., 1990.
126. *http://physics.schooltool.nl/irspectroscopy/theory.php*
127. G Fischer, *Vibronic Coupling – The interaction between the Electronic and Nuclear Motions*. New York: Academic Press, 1984
128. B H Stuart, *Infrared Spectroscopy: Fundamentals and Applications*. John Wiley & Sons, Ltd., London, UK, 2004.
129. A A Bunaciu, H Y Aboul-Enein and S Fleschin, *FT-IR Spectrophotometric analysis of acetylsalicylic acid and its pharmaceutical formulations*. Canadian Journal of Analsysis Science and Spectroscopy, 2006. **51**(5): p.253.

130. R Neubert, B Colin and S Wartewig, *Quantitative analysis of drug content in semisolid formulations using step-scan FT-IR photoacoustic spectroscopy*. Vibrational Spectroscopy, 1997. **13**(2): p.241.
131. Leif Gerward at Technical University of Denmark, *http://www.canberra.edu.au/irps/Archives/vol21no1/blbalaw.html*
132. B C Smith, *Fundamentals of Fourier transform infrared spectroscopy*. CRC press, 1996.
133. C Zhu and P R Griffiths, *Extending the range of Beer's law in FT-IR Spectrometry. Part 1: Theoretical study of Norton-Beer Apodization Functions*. Applied Spectroscopy, 1998. **52**(11): p.1403.
134. Z Zhang, E Beatty, C P Wong, *Study on the Curing Process and the Gelation of Epoxy/Anhydride System for No-Flow Underfill for Flip-Chip Applications*. Macromolecular Materials and Engineering, 2003. **288**(4): p.365.
135. P Preetha, and M J Thomas, *Partial Discharge Resistant Characteristics of Epoxy Nanocomposites*. IEEE Transactions on Dielectrics and Electrical Insulation, 2011. **18**(1): p.264.
136. M. Knoll, *Aufladepotentiel und Sekundäremission elektronenbestrahlter Körper*. Zeitschrift für technische Physik, 1935. **16**: p.467.
137. I L Hosier, *Morphology and Electrical Properties of Polyethylene Blends*. PhD Thesis, University of Southampton, UK, 1996.
138. R. Hessel and B.Gross, *Escape Depth of Secondary Electrons from electron-irradiated polymers*. IEEE Transactions on Dielectrics and Electrical Insulation, 1992. **27**(4): p.831.
139. M A Corcuera, K D L Caba, N Gabilondo, C Marieta, G Kortaberria, A Eceiza, *Rheokinetic and Dynamic Mechanical Analysis of Tetrafunctional Epoxy/anhydride Mixtures. Influence of Stoichiometry and Cure Conditions*. High Performance Polymers, 2006. **18**(1): p.17.
140. E M Petrie, *Epoxy Adhesive Formulations (Chemical Engineering)*. McGraw-Hill Professional, 2005.
141. Y Sun, *STUDY ON THE NANOCOMPOSITE UNDERFILL FOR FLIP-CHIP APPLICATION*. PhD thesis, Georgia Institute of Technology, USA, 2006.
142. K Kihara, *An x-ray study of the temperature dependence of the quartz structure*. European Journal of Mineralogy, 1990. **2**: p.63.

143. F D Osterholz, E R Pohl, *Silane and Other Coupling Agents*. Utrecht, the Netherlands: VSP, 1992.
144. Harimic Malaysia (Company)**,** *www.harimic.com/images/category03_4.jpg*
145. *www.utas.edu.au/sciencelinks/chemincon/files/s1_grow/s1_soils/bonding/net*work .htlm
146. R K Iler, *The Chemistry of Silica*. New York: John Wiley & Sons, 1979.
147. H Zou, S Wu, J Shen, *Polymer/Silica Nanocomposites: Preparation, Characterization, Properites, and Application*. Chemical Reviews, 2008. **108**(9): p.3893.
148. C Gurumurthy, and C Y Hui, *Controlling interfacial interpenetration and fracture properties of polyimide/epoxy interfaces.* Journal of Adhesion, 2006. **82**: p.239.
149. W Fisch, and W Hofmann, *Über den Härtungsmechanismus der äthoxylinharze.* Journal of polymer science, 1954. **12**(1): p.497.
150. R F Fischer, *Polyesters from Epoxides and Anhydrides*. Journal of Polymer Science, 1960. **44**(143): p.155.
151. M F Sorokin, L G Shode, A B Shteinpress, *Polymerization of phenyl glycidyl ether induced by tertiary amines in the absence of proton donating compounds*. Polymer Science U.S.S.R, 1971. **13**(4): p.841.
152. F Kolar, and J Svitilova, *Kinetics and Mechanism of curing epoxy/anhydride systems*. Acta Geodyn. Geomater., 2007. **4**(3): p.85.
153. L Matejka, J Lovy, S Pokorny, K Bouchal, K Dusek, *Curing epoxy resins with anhydrides. Model reactions and reaction mechanism*. Journal of Polymer Science, Polymer Chemistry Edition, 1983. **21**(10): p.2873.
154. M Fedtke, and F Domaratius, *Curing of Epoxide Resins by Anhydrides of Dicarboxylic Acids: Model Reactions*. Polymer Bulletin, 1986. **15**: p.13.
155. Won Ho Park, *A study on Isothermal Cure Behavior of An Epoxy-Rich/Anhydride System by Differential Scanning Calorimetry.* Journal of Applied Polymer Science, 1998. **67**(6): p.1101.
156. C Zhang, G C Stevens, *The dielectric response of polar and non-polar nanodielectrics*. IEEE Transactions on Dielectrics and Electrical Insulation, 2008. **15**(2): p.606.

157. T Rouyre, A C Taylor, M Fu, F Perrot, I James, *Nano- and Micro-silica Modification of Epoxy Polymers*. International Conference on Solid Dielectrics, Potsdam, Germany, 2010.
158. S Montserrat, J L Gomez Ribelles, J M Meseguer, *The application of a new configurational entropy mode to the structural relaxation in an epoxy resin*. Polymer, 1998. **39**(16): p.3801.
159. H J Chung, S T Lim, *Physical Aging of Amorphous Starches (A review)*. Starch, 2006. **58**: p.599.
160. J M Morancho, J M Salla, *Relaxation in partially cured samples of an epoxy resin and of the same resin modified with a carboxyl-terminated rubber*. Polymer, 1999. **40**(10): p.2821.
161. J Shin, S Nazarenko, J P Phillips, C E Hoyle, *Physical and chemical modifications of thiol-ene networks to control activation anergy of enthalpy relaxation*. Polymer, 2009. **50**(26): p.6281.
162. J H Mason, *Effects of frequency on the electric strength of polymers*. IEEE Transactions on Electrical Insulation, 1992. **27**(6): p.1213.
163. D M Tu, W B Liu, G P Zhuang Z Y Liu, K C Kao, *Electrical breakdown under quasi-uniform field conditions and effect of emission shields in polyethylene*. IEEE Transactions on Electrical Insulation, 1989. **24**(4): p.581.
164. H C Miller, *Flashover of insulators in vacuum: review of the phenomena and techniques to improved holdoff voltage*. IEEE Transactions on Electrical Insulation, 1993. **28**(4): p.512.
165. J H Mason, *Effects of thickness and area on the electric strength of polymers*. IEEE Transactions on Electrical Insulation, 1991. **26**(2): p.318.
166. R Lovell, *The Effect of Specimen Size on the Electric Breakdown of Unfilled and Filled Epoxy Polymers*. IEEE Transactions on Electrical Insulation, 1976. **11**(4): p.110.
167. G Gherbaz, *Nanostructured Polymers: Morphology and Properties*. PhD Thesis in University of Southampton, 2009.
168. Confidence bounds, *www.weibull.com/LifeDataWeb*
169. R B Abernethy, *The New Weibull Handbook*. Robert B. Abernethy, 1993.
170. A S Vaughan, G Gherbaz, S G Swingler and N A Rashid, *Polar/nonpolar Polymer Blends: On structural evolution and the electrical properties of blends of*

polyethylene and ethylene – vinyl acetate. Annual Report Conference on Electrical Insulation and Dielectric Phenomena, 2006.

171. N Mann and K Fertig, *Tables for obtaining Weibull confidence bounds and tolerance bounds based on best linear invariant estimates of parameter of the extreme-value distributions*. Technometrics, 1973. **15**(1): p.87.
172. S H Carr, R F Cozzens, D K Davies, P Fischer, V Y Merritt, D A Seanor and G M Sessler, *Electrical Properties of Polymers*. Academic Press, London, UK, 1982.
173. A S Vaughan, S J Dodd, and S J Sutton, *A Raman microprobe study of electrical treeing in polyethylene.* Journal of Materials Science, 2004. **39**(1): p.181.
174. A S Vaughan, I L Hosier, S J Dodd, and S J Sutton, *On the structure and chemistry of electrical trees in polyethylene.* Journal of Physics D: Applied Physics, 2006. **39**(5): p.962.
175. I L Hosier, N A Freebody, A S Vaughan, S G Swingler and G Moss, *Electrical Treeing in Silicone Rubber.* The 17th International Symposium on High Voltage Engineering, 2011.
176. S Popineau, C Rondeau-Mouro, C Sulpice-Gaillet, M E R Shanahan, *Free/bound water absorption in an epoxy adhesive*. Polymer, 2005. **46**(24): p.10733.
177. M C Lee, N A Peppas, *Water transport in epoxy resins*. Progress in Polymer Science, 1993. **18**(5): p.947.
178. K Doukkali, Y Segui, *Effect of Moisture Sorption on ac Properties of Glass-Epoxy Composites*. Journal of Applied Polymer Science, 1990. **41**(7-8): p.1533.
179. J Wang, H J Ploehn, *Dynamic Mechanical Analysis of the Effect of Water on Glass Bead-Epoxy Composites*. Journal of Applied Polymer Science, 1996. **59**(2): p.345.
180. H Zhao, r K Y Li, *Effect of water absorption on the mechanical and dielectric properties of nano-alumina filled epoxy nanocomposites*. Key Engineering Materials, 2007. **334-335 I**: p.617.
181. Y Sun, Z Zhang, K S Moon, C P Wong, *Glass Transition and Relaxation Behaviour of Epoxy Nanocomposites.* Journal of Polymer Science Part B: Polymer Physics, 2004. **42**(21): p.3849.
182. Y Sun, Z Zhang, C P Wong, *Fundamental Research on Surface Modification of Nano-size Silica for Underfill Application*. 9th International Symposium on Advanced Packaging Materials, 2004.

183. O H Lin, H M Akil, Z A M Ishak, *Surface-activated nanosilica treated with silane coupling agents/polypropylene composites: Mechanical, morphological, and thermal studies*. Polymer Composites, 2011. **32**(10): p. 1568.
184. Martin Reading, *An Investigation into the Structure and Properties of Polyethylene Oxide Nanocomposite*. PhD thesis, University of Southampton, 2010.
185. David H Mills, *Electroluminescene and Ageing of Polyethylene*. PhD thesis, University of Southampton, 2012.
186. Z Xu, *Space Charge Measurement and Analysis in Low Density Polyethylene Film*. PhD thesis, Univeristy of Southampton, 2009.
187. T Maeno, T Futami, H Kushibe, T Takada and C M Cooke, *Measurement of spatial charge distribution in thick dielectrics using the pulsed electroacoustic method*. IEEE Transactions on Electrical Insulation, 1988. **23**(3): p.433.
188. Junwei Zhao, *Dynamics of space charge and electroluminescence modelling in polyethylene*. PhD thesis, University of Southampton, 2012.
189. Y L Chong, G Chen, H Miyaka, K Matsui, Y Tanaka, T Tanaka, *Space Charge and Charge Trapping Characteristics of Crosslinked Polyethylene Subjected to AC Electric Stresses*. Journal of Physics and Dielectric Application, 2006. **39**(8): p.1658.
190. Nuriziani Hussin, *The Effects of Crosslinking Byproducts on the Electrical Properties of Low Density Polyethylene*. PhD thesis, University of Southampton, 2011.
191. Dao Ngoc Long, *Impulse ageing of polymeric materials*. PhD thesis, University of Southampton, 2011.
192. Qi Wang, *The Effect of Nano Size Fillers on Electrical Performance of Epoxy Resin*. PhD thesis, University of Southampton, 2012.
193. K Bambery and R Fleming, *The temperature dependence of space charge accumulation in cross-linked polyethylene*. Journal of Thermal Analysis and Calorimetry, 1997. **50**(1): p.19.
194. S Delpino, D Fabiani, G C Montanari, C Laurent, G Teyssedre, P H F Morshuis, R Bodega and L A Dissado, *Polymeric HVDC cable design and space charge accumulation. Part 2: Insulation interfaces*. IEEE Electrical Insulation Magazine, 2008. **24**(1): p.14.

195. C D Wingard, and C L Beatty, *Crosslinking of an Epoxy with a Mixed Amine as a Function of Stoichimetry. I. Cure Kinetics via Dynamic Mechanical Spectroscopy*. Journal of Applied Polymer Science, 1990. **40**(1112): p.1981.
196. G R Palmese, and R L McCullough, *Effect of Epoxy-Amine Stoichiometry on Cured Resin Material Properties*. Jounal of Applied Polymer Science, 1992. **46**(10): p.1853.
197. T Adachi, K Oishi, M Higuchi, M K Umboh, *Non-Stoichiometric Curing Effect on Dynamic Mechanical Properties of Bisphenol A-Type Epoxy Resin*. International Symposium on Electric Machinery, 2012.
198. C E Pizzutto, *Study of Epoxy/CNT Nanocomposites Prepared Via Dispersion in the Hardener*. Materials Research, 2011. **14**(2): p.257.
199. A L Smith, *Applied Infrared Spectroscopy*. John Wiley New York, 1979.
200. D L Pavia, G M Lampman, G S Kriz, *Introduction to Spectroscopy* (3rd Ed). Thomson Learning, 2001.
201. M A Thomson, P J Melling, and A M Slepski, *Real time monitoring of isocyanate chemistry using a fiber-optic FTIR probe*. Polymer Preprints, 2001. **41**(1): p.310.
202. J Coates, *Interpretation of Infrared Spectra, A Practical Approach*. Encyclopaedia of Analytical Chemistry, R.A. Meyers (Ed.), 2000.
203. T Theophile, *Infrared Spectroscopy – Materials Science, Engineering and Technology*. In Tech, 2012.
204. A Beganskiene, V Sirutkaitis, M Kurtinaitiene, R Juskenas, A Kareiva, *FTIR, TEM and NMR investigation of Stober Silica Nanoparticles*. Materials Science, 2004. **10**(4): p.287.
205. N P Bansal, *Low Temperature Synthesis of CaO-SiO_2 Glasses Having Stable Liquid-Liquid Immiscibility by Sol-Gel Process*. NASA Contractor Report 185293, 1990.
206. B M V Romao, M F Diniz, M F P Azevedo, V L Lourenco, L C Pardini, R C L Dutra, *Characterization of the Curing Agents Used in Epoxy Resins with TG/FT-IR Technique*. Polimeros, 2006. **16**(2): p.94.
207. F X Llabres i Xamena, and A Zecchina, *FTIR spectroscopy of carbon dioxide adsorbed on sodium- and magnesium-exchanged ETS-10 molecular sieves*. Physical Chemistry Chemical Physics, 2002. **4**(10): p.1978.

208. V B Gupta, L T Drzal, CY-C Lee, M J Rich, *The temperature-dependence of some mechanical properties of a cured epoxy resin system*. Journal of Polymer Engineering & Science, 1985. **25**(13): p.812.

209. Y Calventus, S Montserrat, J M Hutchinson, *Enthalpy relaxation of non-stoichiometric epoxy-amine resins*. Polymer, 2001. **42**(16): p.7081.

210. P Gupta, Sharif Ahmad, Anshu Dev, *Development of Novel Bio-Based Soybean Oil Epoxy Resins as a Function of Hardener Stoichiometry*. Polymer-Plastics Technology and Engineering, 2010. **49**(7): p.657.

211. G Polizos, V Tomer, E Manias, C A Randall, *Epoxy-based nanocomposites for electrical energy storage. II: Nanocomposites with nanofillers of reactive montmorillonite covalently-bonded with barium titanate*. Journal of Applied Physics, 2010. **108**(7): p.074117.

212. A J Kovacs, J J Aklonis, J M Hutchinson, A R Ramos, *Isobaric volume and enthalpy recovery of glasses. II. A transparent multiparameter theory*. Journal of Polymer Science: Polymer Physics Edition, 1979. **17**(7): p.1097.

213. F Romero Colomer, J L Gomez Ribelles, *Structural relaxation of poly(γ-benzyl-L-glutamate)*. Polymer, 1989. **30**(5): p.849.

214. A Brunacci, J M G Cowie, R Ferguson, J L Go´mez Ribelles, A V Garayo, *Structural relaxation in Polystyrene and Some Polystyrene Derivatives*. Macromolecules, 1996. **29**(24): p.7976.

215. G C Stevens, *Cure kinetics of a low epoxide/hydroxyl group-ratio bisphenol a epoxy resin-anhydride system by infrared absorption spectroscopy*. Journal of Applied Polymer Science, 1981. **26**(12): p.4259.

216. G C Stevens, *Cure kinetics of a high epoxide/hydroxyl group-ratio bisphenol a epoxy resin-anhydride system by infrared absorption spectroscopy*. Journal of Applied Polymer Science, 1981. **26**(12): p.4279.

217. P Guerrero, De la Caba, A Valea, M A Corcuera, I Mondragon, *Influence of cure schedule and stoichiometry on the dynamic mechanical behaviour of tetrafunctional epoxy resins cured with anhydrides*. Polymer, 1996. **37**(11): p.2195.

218. Juan De Vicente, *Rheology*. InTech, 2012.

219. M A Garcia del Cid, M G Prolongo, C Salom, C Arribas, M Sanchez-Cabezudo, R M Masegosa, *The effect of stoichiometry on curing and properties of epoxy-clay nanocomposites*. Thermal Analytical Calorimetry, 2012. **108**(2): p.741.
220. M R Vanlandingham, R F Eduljee, W Gillespie, *Relationships between Stoichiometry, Microstructure, and Properties for Amine-cured Epoxies*. Journal of Applied Polymer Science, 1999. **71**(5): p.699.
221. H Xie, B Liu, Q Sun, Z Yuan, J Shen, R Cheng, *Cure kinetic study of carbon nanofibres/epoxy composites by isothermal DSC*. Journal of Applied Polymer Science, 2005. **96**(2): p.329.
222. K Tao, S Yang, J C Grunlan, Y S Kim, B Dang, Y Deng, R L Thomas, B L Wilson, X Wei, *Effects of carbon nanotube fillers on the processes of epoxy resin-based composites*. Journal of Applied Polymer Science, 2006. **102**(6): p.5248.
223. S Das, and N Gupta, *Space charge accumulation in epoxy resin and polyethylene*. 10th International Conference on the Properties and Applications of Dielectric Materials, 2012.
224. T Iizuka, and H Takai, *Measurement of Space Charge Distribution in Epoxy Resin after Water Absorption Treatment*. Annual Report Conference on Electrical Insulation and Dielectric Phenomena, 1997. **1**: p.41.
225. K Fukunaga, T Maeno, and V Griseri, *Space Charge Observation of a Filler Free Epoxy Resin*. Annual Report Conference on Electrical Insulation and Dielectric Phenomena, 2000. **1**: p.125.
226. L A Dissado, V Griseri, W Peasgood, E S Cooper, K Fukunaga, and J C Fothergill, *Decay of Space Charge in a Glassy Epoxy Resin Following Voltage Removal*. IEEE Transactions on Dielectrics and Electrical Insulation, 2006. **13**(4): p.903.
227. C Guillermin, P Rain, A Sylvestre, S Rowe, *Space charge measurements in epoxy resin under DC voltage.* Annual Report Conference on Electrical Insulation and Dielectric Phenomena, 2002.
228. IEEE 930, *Guide for statistical analysis of insulation breakdown data*. 1987.
229. J C Fothergill, *Filamentary electromechanical breakdown*. IEEE Transactions on Electrical Insulation, 1991. **26**(6): p.1124.

230. T H Hsieh, A J Kinloch, K Masania, A C Taylor, S Sprenger, *The mechanisms and mechanics of the toughening of epoxy polymers modified with silica nanoparticles*. Polymer, 2010. **51**(26): p.6284.
231. M Reading, Z Xu, A S Vaughan, P L Lewin, *The thermal and electrical properties of nano-silicon dioxide filled epoxy systems for use in high voltage insulation*. Electrical Insulation Conference, 2011.
232. M Roy, J K Nelson, R K MacCrone, L S Schadler, *Candidate mechanisms controlling the electrical characteristics of silica/XLPE nanodielectrics*. Journal of Materials Science, 2007. **42**(11): p.3789.
233. K Y Lau, A S Vaughan, G Chen, *The effect of nanofiller on polyethylene system*. Dielectrics, 2011.
234. S D Senturia, Jr. N F Sheppard, *Dielectric analysis of thermoset cure*. Advances in polymer science, 1986. **80**: p.1.
235. A F Lewis, *Dynamic mechanical behaviour during the thermosetting curing process*. Polymer Engineering & Science, 1963. **3**(3): p.201.
236. G A Pogany*, The β-relaxation in the epoxy resins; the temperature and time-Dependence of cure*. Journal of Materials Science, 1969. **4**(5): p.405.
237. R Kochetov, T Andritsch, U Lafont, P H F Morshuis, J J Smit, *Effects of inorganic nanofillers and combinations of them on the complex permittivity of epoxy-based composites*. Proceedings of Internaltional Symposium on Electrical Insulation, 2010.
238. A K Jonscher, *Dielectric Relaxation of solids*. Chelsea Press, 1983.
239. L A Dissado, and R M Hill, *A cluster approach to the structure of imperfect materials and their relaxation spectroscopy.* Proceedings of the Royal Society A, 1983. **390**(1798): p.131.
240. S J Dodd, N M Chalashkanov, J C Fothergill, L A Dissado, *Influence of the temperature on the dielectric properties of epoxy resin*. IEEE International Conference on Solid Dielectrics, 2010.
241. S J Dodd, N M Chalashkanov, L A Dissado, J C Fothergill, *Influence of absorbed moisture on the dielectric properties of epoxy resins.* IEEE Conference on Electrical Insulation and Dielectric Phenomena, 2010.

242. Y Cao, P C Irwin and K Younsi, *The Future of Nanodielectrics in the Electrical Power Industry*. IEEE Transactions on Dielectrics and Electrical Insulation, 2004. **11**(5): p.797.
243. M Kozako, *Surface degradation of polyamide nanocomposites caused by partial discharges using IEC (b) electrodes*. IEEE Transactions on Dielectrics and Electrical Insulation, 2004. **11**(5): p.833.
244. M Kozako, *Surface roughness change of epoxy/TiO_2 nanocomposites due to partial discharges*. Proceedings of International Symposium on Electrical Insulating Materials, 2005. **3**: p.661.
245. M Kawasumi, N Hasegawa, M Kato, A Usuki, A Okada, *Preparation and Mechanical properties of polypropylene-Clay Hybrids*. Macromolecules, 1997. **30**(20): p.6333.
246. Y Wang, and N Herron, *Nanometer-sized semiconductor clusters: Materials synthesis, quantum size effects, and photo physical properties*. Journal of Physical Chemistry, 1991. **95**(2): p.525.
247. A Bergeret, N Alberala, *A study of the interphase in styrene-methacrylic acid copolymer/glass bead composite*. Polymer, 1996. **37**(13): p.2759.
248. K Mai, E Mader, M Muhle, *Interphase characterization in composites with new non-destructive methods*. Composites Part A: Applied Science and Manufacturing, 1998. **29**(9-10): p.1111.
249. T Tanaka, Y Tatsuya, Y Ohki, M Ochi, H Miyuki, T Imai, *Frequency Accelerated Partial Discharge Resistance of Epoxy/Clay Nanocomposite Prepared by Newly Developed Organic Modification and Solubilization Methods*. IEEE International Conference on Solid Dielectrics, 2007.
250. J K Nelson, and Y Hu, *The impact of Nanocomposite Formulations on Electrical Voltage Endurance*. IEEE International Conference on Solid Dielectrics, 2004.
251. P O Henk, *Increasing the electric discharge endurance of acid anhydride cured DGEBA epoxy resin by dispersion of nanoparticle silica*. High Performance Polymer, 1999. **11**(3): p.281.
252. Q Wang, G Chen, A S Alghamdi, *Influence of Nanofillers on Electrical Characteristics of Epoxy Resins Insulation*. IEEE International Conference on Solid Dielectrics, 2010.
253. T Tanaka, *Proposal of a multi-core model for polymer nanocomposite dielectrics.*

IEEE Transactions on Dielectrics and Electrical Insulation, 2005. **12**(4): p.669.

254. T J Lewis, *A Model for Nano-composite Polymer Dielectrics under Electrical Stress*. IEEE International Conference on Solid Dielectrics, 2007.
255. C Zou, M Fu, J C Fothergill, S W Rowe, *Influence of absorbed water on the dielectric properties and glass-transition temperature of silica-filled epoxy nanocomposites*. IEEE Conference on Electrical Insulation and Dielectric Phenomena, 2006.
256. J Wu, D D L Chung, *Calorimetric study of the effect of carbon fillers on the curing of epoxy*. Carbon, 2004. **42**(14): p.3039.
257. G Tsagaropoulos and A Eisenberg, *Dynamic Mechanical Study of the Factors Affecting the Two Glass Transition Behaviour of Filled Polymers. Similarities and Differences with Random Ionomers*. Macromolecules, 1995. **28**(18): p.6067.
258. A M Mayes, *Softer at the boundary*. Nature Materials, 2005. **4**(9): p.651.
259. F W Starr, T B Schroder, and S C Glotzer, *Effects of a Nanoscopic Filler on the Structure and Dynamics of a Simulated Polymer Melt and the Relationship to Ultrathin Films*. Physical Review E, 2001. **64**(2): p.021802(1).
260. J Schuller, Y B Melnichenko, B Yu, R Richert, E W Ficher, *Dielectric studies of the glass transition in porous media*. Physical Review Letter, 1994. **73**(16): p.2224.
261. D Morineau, Y D Xia, C Alba-Simionesco, *Finite-size and surface effects on the glass transition of liquid toluene confined in cylindrical mesopores*. Journal of Chemical Physics, 2002. **117**(19): p.8966.
262. M Xiong, G Gu, B You, L Wu, *Preparation and characterization of poly(styrene butylacrylate) latex/nano-ZnO nanocomposites*. Journal of Applied Polymer Science, 2003. **90**(7): p.1923.
263. W D Hiergeth, U J Steinau, H J Bittrich, G Simon, K Schmutzlet, *Polymerization in the presence of seeds. Part IV: Emulsion polymers containing inorganic filler particles*. Polymer, 1989. **30**(2): p.254.
264. Y M Cao, J Sun, D H Yu, *Preparation and properties of nano-Al_2O_3 particles/polyester/epoxy resin ternary composites*. Journal of Applied Polymer Science. **83**(1): p.70.

265. J Q Pham, C A Mitchell, J L Bahr, J M Tour, R Krishanamoorti, P F Green, *Glass transition of polymer/single-walled carbon nanotube composite films*. Journal of Polymer Science Part B: Polymer Physics, 2003. **41**(24): p.3339.

266. B J Ash, L S Schadler, R W Siegel, *Glass transition behavior of alumina/polymethylmethacrylate nanocomposites.* Materials Letters, 2002. **55** (1-2): p.83.

267. L Chen, K Zheng, X Tian, K Hu, R Wang, C Liu, Y Li, P Cui, *Double glass transitions and interfacial immobilized layer in in-situ-synthesized poly(vinyl alcohol)/silica nanocomposites*. Macromolecules, 2010. **43**(2): p.1076.

268. V Tomer, G Polizos, E Manias, and C A Randall, *Epoxy-based nanocomposites for electrical energy storage. I: Effects of montmorillonite and barium titanate nanofillers*. Journal of Applied Physics, 2010. **108**(7): p.074116.

269. Y Sun, Z Zhuqing, and C P Wong, *Study and characterization on the nanocomposite underfill for flip chip applications.* IEEE Transactions on Components and Packaging Technologies, 2006. **29**(1): p.190.

270. K C Cheng, W Y Chiu, *Monte Carlo Simulation of Polymer Network Formation with Complex Chemical Reaction Mechanism: Kinetic Approach on Curing of Epoxides with Amines*. Macromolecules, 1994. **27**(12): p.3406.

271. C C Wu, S L C Hsu, *Preparation of epoxy/silica and epoxy/titania hybrid resists via a sol-gel process for nanoimprint lithography*. Journal of Physical Chemistry C, 2010. **114**(5): p.2179.

272. H Yin, H Chen, D Chen, *Hydrogen bond interaction in poly(acrylonitrile-co-methylacrylate)/attapulgite nanocomposites*. Polymer Engineering & Science, 2010. **50**(2): p.312.

273. H Pan, Z Qiu, *Biodegradable poly(l-lactide)/polyhedral oligomeric silsesquioxanes nanocomposites: enhanced crystallization, mechanical properties, and hydrolytic degradation*. Macromolecules, 2010. **43**(3): p.1499.

274. A K Barick, D K Tripathy, *Thermal and dynamic mechanical characterization of thermoplastic polyurethane/organoclay nanocomposites prepared by melt compounding*. Materials Science and Engineering A, 2010. **527**(3): p.812.

275. A J Crosby, J Y Lee, *Polymer Nanocomposites: The "nano" effect on mechanical properties*. Polymer Reviews, 2007. **47**(2): p.217.

276. S Kripotou, P Pissis, Y V Savelyev, L P Robota, T V Travinskaya, *Polymer dynamics in polyurethane/clay nanocomposites studied by dielectric and thermal techniques*. Journal of Macromolecular Science, Part B: Physics, 2010. **49**(1): p.86.
277. A Wurm, M Ismail, B Kretzschmar, D Pospiech, C Schick, *Retarded crystallization in polyamide/layered silicates nanocomposites caused by an immobilized interphase*. Macromolecules, 2010. **43**(3): p.1480.
278. Y Xiong, X Lü, *Microstructure and properties of novel ReO_2 /polyimide nanocomposite films*. Journal of Polymer Research, 2010. **17**: p.273.
279. C F Ou, M C Shiu, *Epoxy composites reinforced by different size silica nanoparticles*. Journal of Applied Polymer Science, 2010. **115**(5): p.2648.
280. S Singha, M J Thomas, *Dielectric properties of epoxy nanocomposites*. IEEE Transactions on Dielectrics and Electrical Insulation, 2008. **15**(1): p.12.
281. M G Prolongo, F J Martinez-Casado, R M Masegosa, C Salom, *Curing and dynamic mechanical thermal properties of epoxy/clay nanocomposites*. Journal of Nanoscience and Nanotechnology, 2010. **10**(4): p.2870.
282. E Petrovicova, R Knight, L S Schadler, T E Twardowski, *Nylon 11/silica nanocomposite coatings applied by the HVOF process. II. Mechanical and barrier properties*. Journal of Applied Polymer Science, 2000. **78**(13): p.2272.
283. M Z Rong, M Q Zhang, Y X Zheng, H M Zeng, K Friedrich, *Improvement of tensile properties of nano-SiO_2/PP composites in relation to percolation mechanism*. Polymer, 2001. **42**(7): p.3301.
284. Y Kojima, A Usuki, M Kawasumi, A Okada, Y Fukushima, T Kurauchi, *Mechanical properties of nylon 6-clay hybrid*. Journal of Materials Research, 1993. **8**(5): p.1185.
285. H Zhang, Z Zhang, K Friedrich, C Eger, *Property improvements of in situ epoxy nanocomposites with reduced interparticle distance at high nanosilica content*. Acta Materialia, 2006. **54**(7): p.1833.
286. S Wu, *Phase structure and adhesion in polymer blends: A criterion for rubber toughening*. Polymer, 1985. **26**(12): p.1855.
287. S Wu, *A generalized criterion for rubber toughening: The critical matrix ligament thicknes*. Journal of Applied Polymer Science, 1988. **35**(2): p.549.

288. Gallot-Lavallee, G Teyssedre, C Laurent adn S Rowe, *Space charge behaviour in an epoxy resin: the influence of fillers, temperature and electrode material*. Journal of Physics D: Applied Physics, 2005. **38**(12): p.2017.
289. J K Nelson, J C Fothergill, L A Dissado, W Peasgood, *Towards an understanding of nanometric dielectrics*. IEEE Annual Report Conference on Electrical Insulation and Dielectric Phenomena, 2005.
290. A Hajiyiannis, G Chen, *Space Charge Formation in Epoxy Resin Including Various Nanofillers*. IEEE Annual Report Conference on Electrical Insulation and Dielectric Phenomena, 2008.
291. D Ma, T A Hugener, R W Siegel, A Christerson, E Martensson, C Onneby, L Schadler, *Influence of nanoparticle surface modification on the electrical behavior of polyethylene nanocomposites*. Nanotechnology, 2005. **16**(6): p.724.
292. P J Kim, C Simon, P J Hotchkiss, N Joshua, B Kippelen, S R Marder, J W Perry, *Phosphonic acid-modified barium titanate polymer nanocomposites with high permittivity and dielectric strength*. Advanced Materials, 2007. **19**(7): p.1001.
293. J Li, J Claude, L E Norena-Franco, S I Seok, Q Wang, *Electrical energy storage in ferroelectric polymer nanocomposites containing surface-functionalized BaTiO3 nanoparticles.* Chemistry of Materials, 2008. **20**(20): p.6304.
294. G Chen, A E Davies, *The influence of defects on the short-term breakdown characteristics and long-term dc performance of LDPE insulation*. IEEE Transactions on Dielectrics and Electrical Insulation, 2000. **7**(3): p.401.
295. Y Shen, Y Lin, M Li, C W Nan, *High dielectric performance of polymer composite films induced by a percolating interparticle barrier layer*. Advanced Materials, 2007. **19**(10): p.1418.
296. Y Sun, Z Zhang, C P Wong, *Influence of interphase and moisture on the dielectric spectroscopy of epoxy/silica composites*. Polymer, 2005. **46**(7): p.2297.
297. J C Fothergill, J K Nelson, M Fu, *Dielectric properties of Epoxy nanocomposites containing TiO2, Al2O3, and ZnO fillers*. IEEE Annual Report Conference on Electrical Insulation and Dielectric Phenomena, 2004.
298. N Tagami, Y Ohki, *Interface between Filler and Resin in Epoxy Nanocomposites Cured with Acid Anhydride*. The international Conference on Electrical Engineering, 2008.

299. P Barber, S Balasubramanian, Y Anguchamy, S Gong, A Wibowo, H Gao, H J Ploehn, H C Loye, *Polymer Composite and Nanocomposite Dielectric Materials for Pulse Power Energy Storage*. Materials, 2009. **2**(4): p.1697.
300. S Singha, M J Thomas, A Kulkarni, *Complex permittivity characteristics of epoxy nanocomposites at low frequencies*. IEEE Transactions on Dielectrics and Electrical Insulation, 2010. **17**(4): p.1249.
301. R Hackam, *Outdoor HV composite polymeric insulators*. IEEE Transactions on Dielectrics and Electrical Insulation, 1999. **6**(5): p.557.
302. L H Meyer, E A Chernry and S H Jayaram, *The role of inorganic fillers in silicone rubber for outdoor insulation-alumina tri-hydrate or silica*. IEEE Electrical Insulation Magazines, 2004. **20**(4): p.13.
303. B Ma, S M Gubanski, A Krivda, L E Schmidt, R Hollertz, *Dielectric properties and resistance to corona and ozone of epoxy compositions filled with micro- and nano-fillers*. IEEE Annual Report Conference on Electrical Insulation and Dielectric Phenomena, 2009.
304. G Chen, Y Tanaka, T Tanaka, L Zhong, *Effect of Polyethylene Interface on Space Charge Formation.* IEEE Transactions on Dielectrics and Electrical Insulation, 2004. **11**(1): p.113.
305. Z Xu, and G Chen, *Interfacial Characteristics of Space Charge in Multi-layer LDPE*. IEEE Conference on Condition Monitoring and Diagnosis, 2008.
306. J Hao, G Chen, R Liao, L Yang, C Tang, Influence of Moisture on Space Charge Dynamics in Multilayer Oil-Paper Insulation. IEEE Transactions on Dielectrics and Electrical Insulation, 2012. **19**(4): p.1456.
307. J Park, *Effect of nano-silicate on the mechanical, electrical and thermal properites of epoxy/micro-silica composite*. IEEE Transactions on Electrical and Electronic materials, 2012. **13**(3): p.153.
308. G Iyer, R S Gorur, R Richert, A Krivda, L E Schmidt, *Dielectric Properties of Epoxy based Nanocomposites for High Voltage Insulation*. IEEE Transactions on Dielectrics and Electrical Insulation, 2011. **18**(3): p.659.
309. P Tiemblo, M Hoyos, J M Gomez-Elvira, J Guzman, N Garcia, A Dardando, and F Guastavino, *The development of electrical treeing in LDPE and its nanocomposites with spherical silica and fibrous and laminar silicates.* Journal of Physics D - Applied Physics, 2008. **41**(12).

310. F Guastavino, A Dardano, G C Montanari, L Testa, and F Bellicci, *Electrical Treeing in EVA-Boehmite and EVA-Montmorillonite Nanocomposites*. IEEE Electrical Insulation Conference, 2009.

311. D Pitsa, G Vardakis, M G Danikas, and M Kozako, *Electrical Treeing Propogation in Nanocomposites and the Role of Nanofillers: Simulation with the Aid of Cellular Automata*. Journal of Electrical Engineering-Elektrotechnicky Casopis, 2010. **61**(2): p.125.

312. F Guastavino, A Dardano, G C Montanari, F Deorsola, and M Di Lorenzo del Casale, *A study about electrical treeing in different EVA-layered silicate nanostructured compounds*. Conference Record of the IEEE International Symposium on Electrical Insulation, 2006.

313. J V Champion, S J Dodd, Y Zhao, A S Vaughan, M Brown, A E Davies, S J Sutton, and S G Swingler, *Morphology and the growth of electrical trees in a propylene/ethylene copolymer.* IEEE Transactions on Dielectrics and Electrical Insulation, 2001. **8**(2): p.284.

314. J Holto, and E Ildstad, *Electrical tree growth in extruded s-polypropylene.* Proceedings of the 10th IEEE International Conference on Solid Dielectrics, 2010.

315. M D Noskov, A S Malinovski, M Sack, and A . Schwab, *Self-consistent modeling of electrical tree propagation and PD activity.* IEEE Transactions on Dielectrics and Electrical Insulation, 2000. **7**(6): p.725.

316. G E Vardakis, M G Danikas, and I Karafyllidis, *Simulation of space-charge effects in electrical tree propagation using cellular automata.* Materials Letters, 2002. **56**(4): p.404.

317. S J Dodd, *A deterministic model for the growth of non-conducting electrical tree structures.* Journal of Physics D-Applied Physics, 2003. **36**(2): p.129.

318. L A Dissado, and PI Williams, *Physical Origin for Differences in Electrical Tree Structures.* IEEE Annual Report Conference on Electrical Insulation and Dielectric Phenomena, 1994.

319. L A Dissado, and P J J Sweeney, *Physical Model for Breakdown Structures in Solid Dielectrics.* Physical Review B, 1993. **48**(22): p.16261.

320. S J Dodd, L A Dissado, J V Champion, and J M Alison, *Evidence for deterministic chaos as the origin of electrical tree breakdown structures in polymeric insulation.* Physical Review B, 1995. **52**(24): p.16985.
321. L A Dissado, J C Fothergill, N Wise, A Willby, and J Cooper, *A deterministic model for branched structures in the electrical breakdown of solid polymeric dielectrics.* Journal of Physics D-Applied Physics, 2000. **33**(19): p.L109.
322. L A Dissado, *Deterministic chaos in breakdown - Does it occur and what can it tell us?* IEEE Transactions on Dielectrics and Electrical Insulation, 2002. **9**(5): p.752.
323. J H Mason, *Assessing the Resistance of Polymers to Electrical Treeing.* IEE Proceedings-a-Science Measurement and Technology, 1981. **128**(3): p.193.
324. J V Champion and S J Dodd, *Simulation of partial discharges in conducting and non-conducting electrical tree structures*. Journal of Physics D: Applied Physics, 2001. **34**(8): p.1235.
325. K Wu, Y Suzuoki, T Mizutani and H Xie, *Model for partial discharges associated with treeing breakdown: II. Tree growth affected by PDs*. Journal of Physics D: Applied Physics, 2000. **33**(10): p.1209.
326. O P Poznansky, *Bush region in the propagation of electrical degradation in polymers.* Computational and Theoretical Polymer Science, 2001. **11**(1): p.81.
327. M H Ahmad, H Ahmad, N Bashir, Z A Malek, Y Z Arief, and R Kurnianto, *Statistical study on tree inception voltage of silicone rubber and epoxy resin.* International Conference on Electrical Engineering and Informatics, 2011.
328. R Sarathi, and K Sridhar, *Investigation in to growth of electrical trees in XLPE cables under transient voltages*. Proceedings of the IEEE 6th International Conference on Conduction and Breakdown in Solid Dielectrics, 1998.
329. H Mitsui, T Yoshimitsu, Y Mizutani, and K Umemoto, *Electrical Failure Properties of Cast Epoxy-resins.* IEEE Transactions on Electrical Insulation, 1981. **16**(6): p.533.
330. J Laserna, *An Introduction to Raman Spectroscopy, http://www.spectroscopynow.com/coi/cda/detail.cda?page=2&id=1882&type=EducationFeature&chId=6*. [29/04/09].
331. A M Macdonald, *Raman Spectroscopy and the Conservation of Historic Painted* Textiles. PhD thesis, University of Southampton, UK, 2004.

332. R Tabaksblat, R J Meier, and B J Kip, *Confocal Raman Microspectroscopy – Theory and Application to Thin Polymer Samples.* Applied Spectroscopy, 1992. **46**(1): p.60.
333. J P Tomba, and J A Pastor, *Confocal Raman micro spectroscopy with dry objectives: A depth profiling study on polymer films.* Vibrational Spectroscopy, 2007. **44**(1): p.62.
334. J P Tomba, and J M Pastor, *Confocal Raman Microspectroscopy: A Non-Invasive Approach for in-Depth Analyses of Polymer Substrates.* Macromolecular Chemistry and Physics, 2009. **210**(7): p.549.
335. T Wilson, *Confocal Microscopy*. Academic Press: London. 1994
336. D V Martyshkin, R C Ahuja, A Kudriavtsev, and S B Mirov, *Effective suppression of fluorescence light in Raman measurements using ultrafast time gated charge coupled device camera.* Review of Scientific Instruments, 2004. **75**(3): p.630.
337. J V Champion and S J Dodd, *The effect of absorbed water on electrical treeing in epoxy resin.* IEE Conference on Dielectric Materials Measurements & Applications, 1996.
338. T Tanaka, *Similarity between Treeing Lifetime and PD Resistance in Aging Mechanisms for Epoxy Nanocomposites*. Proceedings of the 9th International Conference on Properties and Applications of Dielectric Materials, 2009.
339. S Raetzke, Y Ohki, T Imai, J Kindersberger and T Tanaka, *Enhanced Performance of Tree Initiation V-t Characteristics of Epoxy /Clay Nanocomposite in Comparison with Neat Epoxy Resin*. IEEE Annual Report Conference on Electrical Insulation and Dielectric Phenomena, 2008.
340. N A Freebody, *The use of Raman microprobe spectroscopy in the analysis of electrically aged polymeric insulators*. PhD thesis, University of Southampton, UK, 2012.
341. K J Kingma, and R J Hemley, *Raman-Spectroscopic Study of Microcrystaline Silica.* American Mineralogist, 1994. **79**(3-4): p.269.